5-1-2014

Finite Difference Modeling of Surface-~Wave Scattering for Shallow Cavity Detection

Heston Travis Norcott
University of Nevada, Las Vegas, Heston.Norcott@gmail.com

FINITE DIFFERENCE MODELING OF SURFACE-WAVE SCATTERING FOR SHALLOW CAVITY DETECTION

By

Heston T. Norcott

Bachelor of Science in Civil and Environmental Engineering
University of Nevada, Las Vegas
2008

A thesis submitted in partial fulfillment
of the requirements for the

Master of Science in Engineering – Civil and Environmental Engineering

Department of Civil and Environmental Engineering and Construction
Howard R. Hughes College of Engineering
The Graduate College

University of Nevada, Las Vegas
May 2014

UNLV
UNIVERSITY OF NEVADA LAS VEGAS

THE GRADUATE COLLEGE

We recommend the thesis prepared under our supervision by

Heston T. Norcott

entitled

Finite Difference Modeling of Surface-Wave Scattering for Shallow Cavity Detection

is approved in partial fulfillment of the requirements for the degree of

Master of Science in Engineering -- Civil and Environmental Engineering

Department of Civil and Environmental Engineering and Construction

Barbara Luke, Ph.D., Committee Chair

Carlos Calderon-Macias, Ph.D., Committee Member

Moses Karakouzian, Ph.D., Committee Member

Yitung Chen, Ph.D., Graduate College Representative

Kathryn Hausbeck Korgan, Ph.D., Interim Dean of the Graduate College

May 2014

ABSTRACT

FINITE DIFFERENCE MODELING OF SURFACE-WAVE SCATTERING FOR SHALLOW CAVITY DETECTION

by

Heston T. Norcott

Dr. Barbara Luke, Examination Committee Chair

Professor, Department of Civil and Environmental Engineering and Construction

University of Nevada, Las Vegas

Data collection and analysis of scattering of Rayleigh-type surface waves are investigated for locating shallowly buried cavities. Surface-based seismic experiments conducted by others at the University of Nevada, Las Vegas (UNLV) Engineering Geophysics Test Site (EGTS) demonstrate scattering of Rayleigh waves caused by buried empty barrels (essentially air-filled cavities). The interpretation of the data is complicated by factors such as the presence of a high-velocity geologic layer just below the cavity.

This research uses a finite-difference seismic wave propagation code to compute time histories for a model that represents the Engineering Geophysics Test Site. By adding cavities to a background model, the time histories show scattering of surface waves due to the cavity. Complications in the wave train are caused by the high velocity layer. Starting by modeling a through-going cavity in an otherwise homogeneous soil model allows for identification of essential characteristics of time histories that reveal the presence of the cavity. The same homogeneous model without a cavity serves as a baseline to compare time histories and their frequency content. Layers are added and cavity length is reduced to create a more realistic model for comparing synthetic data with experimental data. This research compares experimental data to synthetic data in the forms of time histories, overtone images, and stacks of overtone images. The stacks of overtone images succeed for complex situations where the other approaches fail.

Comparing the synthetic data from the model that represents the EGTS, using a convolved real source, to the experimental data from the EGTS, the stacks of overtone images demonstrate similarities. Variations in amplitude mark the locations of the cavities in both cases. Power spectrums and a cavity characterization parameter proposed by others are also studied for their capacity to indicate the presence and location of the cavities.

ACKNOWLEDGMENTS

I especially thank my advisor, Dr. Barbara Luke, for mentoring in applied geophysics and for her guidance through graduate college. Dr. Carlos Calderón-Macías provided me with tutorials on signal processing, the E3D program, finite difference modeling techniques, and MATLAB. I also thank my other committee members Dr. Moses Karakouzian and Dr. Yi-Tung Chen. I would like to thank Dr. William Savage, Ms. Julie Longo, and the graduate students at the Applied Geophysics Center at the University of Nevada, Las Vegas for their assistance with processing data and editing my prospectus, thesis, posters, and presentations.

Thanks to Dr. Shawn Larsen at Lawrence Livermore National Laboratory (LLNL) for providing me the E3D source code and instructions on using it. Thanks to Lawrence Livermore National Laboratory for providing me with the WPP source code.

I acknowledge my family for their love and support throughout the duration of my research. To my mother and father, Jim and Cathy Norcott, for unconditionally loving and supporting me throughout my research. Thank you for your guidance and teaching me to never give up. To my son, Tristan Rhys, for being such a good boy while I spent many hours on my research. Thank you for making me play and laugh when I needed it, daddy loves you. To the mother of my child, my friend, my partner, my love, Sunnie Villalobos, thank you for taking care of our son and me throughout my research. And thank you for being so patient and understanding, I love you.

I greatly appreciated having the opportunity to add to the methodology of identifying buried cavities that can be used to address important and useful geotechnical engineering questions.

TABLE OF CONTENTS

ABSTRACT iii

ACKNOWLEDGMENTS v

TABLE OF CONTENTS vii

LIST OF TABLES x

LIST OF FIGURES xi

LIST OF ACRONYMS, SYMBOLS AND ABBREVIATIONS xviii

CHAPTER 1 INTRODUCTION 1

1.1 PURPOSE 1
1.2 RESEARCH HYPOTHESIS AND OBJECTIVES 4
1.3 STUDY SITE 7
1.4 ORGANIZATION OF THESIS 8
CHAPTER 2 LITERATURE REVIEW: STATE OF THE PRACTICE 12

2.1 SURFACE WAVE METHODS 13
2.2 SEISMIC METHODS FOR CAVITY DETECTION: TIME DOMAIN 14
2.3 SEISMIC METHODS FOR CAVITY DETECTION: FREQUENCY DOMAIN. 17
2.3.1 CAVITY CHARACTERIZATION PARAMETERS 20
2.3.2 SEISMIC TESTING FOR CAVITY DETECTION AT UNLV's APPLIED GEOPHYSICS CENTER 23
2.4 DISCUSSION 25
CHAPTER 3 METHODOLOGY 28

3.1 SYNTHETIC MODEL PARAMETERS 29
3.1.1 Tasks 31
3.1.1.1 Task 1 31
3.1.1.2 Synthetic Cavity Properties 33
3.1.1.3 Task 2 36

3.1.1.4 Methodology Used for the Sensitivity Studies 38
3.1.1.5 No Free Surface and Free Surface Models 40
3.1.2 Models and Cavities Setup 42
3.1.3 Source Location and Parameters 43
3.1.4 Residual Calculation 44
3.1.5 Overtone Images 45
3.1.6 Cavity Characterization Parameter 46
3.1.7 Signal to Noise Ratio 46
3.2 REPLICATING THE EXPERIMENTAL DATA 47
CHAPTER 4 FINDINGS OF THE SYNTHETIC STUDY 72
4.1 THE NO FREE SURFACE (NFS) MODEL AND THE FREE SURFACE (FS) MODEL 73
4.2 MODEL A – HOMOGENEOUS MODEL OF SOIL 76
4.3 MODEL B – SINGLE-LAYER MODEL INCLUDING CAVITY 79
4.4 MODEL C – TWO LAYER MODEL WITHOUT CAVITY 80
4.5 MODEL D – TWO LAYER MODEL INCLUDING CAVITY 81
4.6 NORMALIZED ENERGY DISTANCE (NED) CAVITY CHARACTERIZATION PARAMETER AND PoWER SPECTRUMS 84
4.7 MAXIMUM AMPLITUDES OF TIME HISTORIES 89
CHAPTER 5 NUMERICAL MODELING OF THE ENGINEERING GEOPHYSICS TEST SITE EXPERIMENT 120
5.1 MODEL E – FOUR-LAYER MODEL 120
5.2 MODEL F AND MODEL F* – FOUR-LAYER MODEL INCLUDING CAVITIES 124
CHAPTER 6 DISCUSSION, CONCLUSIONS, AND RECOMMENDATIONS 150
6.1 DISCUSSION 150
6.2 CONCLUSIONS 153
6.3 RECOMMENDATIONS 156
BIBLIOGRAPHY 158

APPENDIX 1 OVERTONE IMAGES FOR MODELS D AND F AND STACKS OF OVERTONE IMAGES USING A 50 HZ RICKER WAVELET SOURCE 167

APPENDIX 2 NORMALIZED-ENERGY-DISTANCE CAVITY CHARACTERIZATION PARAMETER FOR MODEL E, MODEL F, AND THE ENGINEERING GEOPHYSICS TEST SITE 168

APPENDIX 3 EXAMPLE OF WPP INPUT FILE 170

APPENDIX 4 TIME HISTORIES WITH ARRIVAL TIMES MATLAB SCRIPT 175

APPENDIX 5 OVERTONE IMAGE MATLAB SCRIPT 181

APPENDIX 6 STACK OF OVERTONE IMAGE MATLAB SCRIPT 187

APPENDIX 7 POWER SPECTRUM MATLAB SCRIPT 195

APPENDIX 8 DECONVOLUTION MATLAB SCRIPT 197

APPENDIX 9 CONVOLUTION MATLAB SCRIPT 204

APPENDIX 10 MATLAB FUNCTION PlotWigClip.m 209

APPENDIX 11 MATLAB FUNCTION applyBpFilter.m 217

APPENDIX 12 POWER SPECTRUMS FOR DECONVOLUTION AND CONVOLUTUION 224

APPENDIX 13 GLOSSARY 225

VITA 238

LIST OF TABLES

Table 2.1 Experiment setup at the Engineering Geophysics Test Site on the UNLV campus. Courtesy of B. Luke; Luke and Calderón-Macías (2007). 27

Table 3.1 Summary of synthetic model information for Model A, B, C, and D. 52

Table 3.2 Summary of synthetic model information for Model E, F, NFS, and FS. 53

Table 3.3 Summary of tests to select density of cavity for modeling with WPP. 54

Table 3.4 Comparison of cavity density versus typical densities of soils. 55

Table 3.5 Layer configuration from Jin (2006). 56

Table 3.6 Layer configurations used for WPP soil profiles. 56

LIST OF FIGURES

Figure 1.1 Engineering Geophysics Test Site map showing the locations of the buried barrels and boreholes. Modified from http://agc.unlv.edu/egts/SiteMap. 9

Figure 1.2 Simplified interpretation of borehole logs from the Engineering Geophysics Test Site. Borehole locations are shown on Figure 1.1. The nearest borehole to the cavities is displayed on the far left and the farthest on the far right. The water table is at 3.5 meters (11.5 feet) in depth. (Modified from http://agc.unlv.edu/egts/SoilTrenchLogs) 10

Figure 1.3 Experimental setup at the Engineering Geophysics Test Site on the UNLV campus, on February 8, 2007. View is toward the north, over the barrels. 11

Figure 1.4 Steel barrel buried at the Engineering Geophysics Test Site on the UNLV campus in 2001. Location is noted in Figure 1.1. 11

Figure 3.1 Synthetic models: describing experiment configuration and *X*, *Y*, and *Z* directions for all models. The coordinate origin is at (0, 15, 0) in this research which is at the center of the *Y* axis and the origination of the *X* and *Z* axis. 57

Figure 3.2 Task #1: *X* direction (in-plane of test array) cross sections of 3-D models used for sensitivity studies (Model A, Model B, Model C, and Model D). Layers and cavities drawn to scale (horizontal width = 30 m) where 1 in.=12 m. 58

Figure 3.3 Cross sectional view of cavity location. Grid illustrates 0.2-m grid spacing of the model. 59

Figure 3.4 Calculation for cavity size. 60

Figure 3.5 Task #2: *X* direction sections of 3-D models created to replicate the experimental data (Model E and Model F). Layers and cavities drawn to scale (horizontal width = 30 m) where 1”=12 m. 61

Figure 3.6 Plan view of synthetic model setup showing the primary source location which is used in Models A, B, C, and D. Point (0, 15, 0) refers to the origin in this research. Only Model F contains the cavity at x = 20 m. 62

Figure 3.7 The no free surface (NFS) and free surface (FS) models setup using E3D. ... 63

Figure 3.8 Time history used for convolution from a hammer source applied on an aluminum plate placed on the surface at UNLV’s Engineering Geophysics Test Site

(EGTS). The black square symbol is the picked P-wave arrival time at 0.0235 seconds. 64

Figure 3.9 Normalized frequency spectrum of hammer blow recorded on the EGTS. Created from the time history in Figure 3.8. 65

Figure 3.10 Setup of experimental data (EGTS) collection when compared to the synthetic models with the location of the trace picked for real source convolution. The 31st receiver with the 5th source location (red circle; (7, 15.2, 0)) is the picked trace for convolution. 66

Figure 3.11 Plan view of synthetic model setup showing multiple source locations used in Models D, E, and F. 67

Figure 3.12 Example EGTS experiment time histories, displaying vertical sensors for source location 5 out of 30. Source coordinates are (7, 15.2, 0). 68

Figure 3.13 Example of a set of EGTS time histories and the corresponding overtone image. Red line indicates steel barrel, blue line indicates plastic barrel. Source location 30 (out of 30 source locations). Source coordinates are (32, 15.2, 0). 69

Figure 3.14 Stack of overtone images according to velocity from the EGTS (Luke and Calderón-Macías (2008)). Locations of steel and plastic barrels are indicated by red and blue lines, respectively. 70

Figure 3.15 Stack of overtone images according to frequency from the EGTS (Luke and Calderón-Macías (2008)). Locations of steel and plastic barrels are indicated by red and blue lines, respectively. 71

Figure 4.1 Vertical direction time histories from the No Free Surface (NFS) model computed with E3D. The cavity is located beneath receiver numbers 16 and 17. The first red line according to time is calculated P-wave arrival time and the second red line according to time is calculated S-wave arrival time. This same pattern applies to the blue lines which represent the scattered wave theoretical arrival times. The model used a Ricker wavelet 50 Hz source which is located at (3, 1) and which initiated at 0.25 seconds. Receiver number 1 is located at (5, 0) and receiver number 72 is located at (28.7, 0). 90

Figure 4.2 Vertical direction time histories from the Free Surface (FS) model computed with E3D. Parameters are as described in Figure 4.1. 91

Figure 4.3 Vertical direction time histories from the residual of the No Free Surface (NFS) model subtracted from the Free Surface (FS) model. Parameters are as described in Figure 4.1. 92

Figure 4.4 Overtone image created from the No Free Surface (NFS) model corresponding to the time histories in Fig. 4.1. The black lines were chosen to start at 25 Hz..... 93

Figure 4.5 Overtone image created from the Free Surface (FS) model corresponding to the time histories in Fig. 4.2. The black line was chosen to start at 25 Hz..... 94

Figure 4.6 Overtone image created from the residual of the No Free Surface (NFS) model subtracted from the Free Surface (FS) model corresponding to the time histories in Fig. 4.3. The black line was chosen to start at 25 Hz..... 95

Figure 4.7 Model A time history from the first receiver in the array with calculated arrival times using a Ricker wavelet 50 Hz source located at (3, 15, 1). The calculated arrival times are shifted by a 17-millisecond (0.017 second) negative delay (earlier in time). ... 96

Figure 4.8 The power spectrum created from Model A's time history from the first receiver in the array using a Ricker wavelet 50 Hz source located at (3, 15, 1)..... 97

Figure 4.9 Model A time history from the last receiver in the array with calculated arrival times using a Ricker wavelet 50 Hz source located at (3, 15, 1). The red square is the calculated P-wave arrival time, the black square is the calculated S-wave arrival time, and the green square is the calculated Rayleigh-wave arrival time. The calculated arrival times are shifted by a 17-millisecond (0.017 second) negative delay (earlier in time). ... 98

Figure 4.10 Model A vertical direction time histories using a Ricker wavelet 50 Hz source. First red line according to time is calculated P-wave arrival time, second is S-wave arrival time, and third is Rayleigh wave arrival time. The source is located at (3, 15, 1), offset 1 is located at (5, 15, 0), and offset 72 is located at (28.7, 15, 0). The calculated arrival times are shifted by a 17-millisecond (0.017 second) negative delay (earlier in time). 99

Figure 4.11 Overtone image created from Model A corresponding to the time histories in Fig 4.10. The black line with X marker symbols is the calculated fundamental mode theoretical dispersion curve, which forms a horizontal line at the velocity of 187.6 m/s. The dispersion curve was chosen to start at 25 Hz. 100

Figure 4.12 Model B vertical direction time histories. Parameters are as described in Fig. 4.10. First blue line according to time is calculated arrival time of P energy for scattering due to the cavity (located beneath offsets 16 and 17) from incident P-wave, second is for

S energy from incident S-wave, and third is for R energy from incident Rayleigh wave. 101

Figure 4.13 Overtone image created from Model B corresponding to the time histories in Fig. 4.12. Parameters are as described in Figure 4.10. The dispersion curve was chosen to start at 25 Hz. 102

Figure 4.14 Residual of Model A subtracted from Model B, vertical direction time histories. Parameters are as described in Fig 4.10 and 4.12. 103

Figure 4.15 Overtone image created from the residual of Model A subtracted from Model B corresponding to the time histories in Fig 4.14. Parameters are as described in Fig. 4.10 and 4.11. The dispersion curve was chosen to start at 25 Hz. 104

Figure 4.16 Model C vertical direction time histories. Parameters are as described in Fig. 4.10..... 105

Figure 4.17 Overtone image created from Model C corresponding to the time histories in Fig. 4.16. The black line with X marker symbols is the calculated fundamental mode theoretical dispersion curve and the red line with X marker symbols is the calculated first higher order mode dispersion curve..... 106

Figure 4.18 Model D vertical direction time histories. Parameters are as described in Fig. 4.10 and 4.12..... 107

Figure 4.19 Residual of Model C subtracted from Model D. Parameters are as described in Fig. 4.10 and Fig. 4.12..... 108

Figure 4.20 Overtone image created from Model D corresponding to the time histories in Fig. 4.18. Parameters are as described in Fig. 4.10 and 4.17..... 109

Figure 4.21 Overtone image created from the residual of Model C subtracted from Model D corresponding to the time histories in Fig. 4.19. Parameters are as described in Fig. 4.10 and 4.17..... 110

Figure 4.22 Overtone images from Model D in the positive *X* direction which is used to create stacks of overtone images. Model D uses a 50 Hz Ricker wavelet source in multiple source locations and a pseudo-2D cavity. The first source location is on the left, the last source location is on the right. The cavity is located at source location 8, which is at (10, 15.5, 1). The arrows indicate stacking according to frequency, which yields a 2-D plot of offset as a function of velocity. 111

Figure 4.23 Stack of overtone images according to velocity using Model D with a 50 Hz Ricker wavelet source in multiple source locations and a pseudo-2D cavity. The cavity is located at source location 8, which is at (10, 15.5, 1). 112

Figure 4.24 Stack of overtone images according to frequency using Model D with a 50 Hz Ricker wavelet source in multiple source locations and a pseudo-2D cavity. The cavity is located at source location 8, which is at (10, 15.5, 1). 113

Figure 4.25 Comparing horizontal-radial and vertical (*X* and *Z*) direction time histories used for NED parameter calculation using Model A with a superimposed 25 Hz and 100 Hz Ricker wavelet source located at (3, 15, 1). The top figure is horizontal time histories, and the bottom figure is vertical time histories. Parameters are as described in Fig.4.10. 114

Figure 4.26 Normalized Energy-Distance (NED) parameter for Model A and Model B. The cavity in Model B is located beneath receiver numbers 16 and 17 as marked by the green lines. 115

Figure 4.27 Normalized Energy-Distance (NED) parameter for Model C and Model D. The cavity is located beneath receiver numbers 16 and 17 as marked by the green lines. 116

Figure 4.28 Power spectrums for Models A, B, C, D, E, and F for selected receivers. . 117

Figure 4.29 Power spectrums for Model A and Model B. The cavity is located under receivers 16 and 17 in Model B. 118

Figure 4.30 Maximum amplitudes from all models' time histories in the vertical direction using a superimposed 25 Hz and 100 Hz Ricker wavelet source. 119

Figure 5.1 Model E vertical direction time histories using a Ricker wavelet 50 Hz source (Shot 1 of 27). The first, second, and third red lines according to time are, respectively, the calculated P-wave arrival time, the calculated S-wave arrival time, and the calculated Rayleigh wave arrival time. The source is located at (3, 15.5, 1), receiver number 1 is located at (5, 15, 0), and receiver number 72 is located at (28.7, 15, 0). The calculated arrival times are shifted by a 17-millisecond (0.017 second) negative delay (earlier in time). 130

Figure 5.2 Residual of Model C subtracted from Model E vertical direction time histories. Parameters are as described in Fig. 5.1. The amplitudes are not scaled. 131

Figure 5.3 Model E vertical direction time histories for a filtered convolution of a real source (Shot 1 of 27). The red line is picked P-wave arrival time, where the first receiver is picked at 0.0235 seconds. Parameters are as described in Fig. 5.1. 132

Figure 5.4 Overtone image created from Model E corresponding to the time histories in Fig. 5.1. The data are not normalized. The black line and red line with X marker symbols are the calculated fundamental mode theoretical dispersion curve and the calculated first-higher order mode dispersion curve, respectively. 133

Figure 5.5 Overtone image from Model E using a filtered convolution of the real source (Shot 1 of 27). Parameters are as described in Fig. 5.1.. The overtone image for Model E using a convolved real source ranges in frequency from 38 Hz to 114 Hz, with a low amplitude section between 66 Hz and 75 Hz. 134

Figure 5.6 Stack of overtone images according to velocity using Model E with a convolved real hammer source in multiple source locations. 135

Figure 5.7 Stack of overtone images according to frequency using Model E with a convolved real hammer source in multiple source locations. 136

Figure 5.8 Model F vertical direction time histories using a Ricker wavelet 50 Hz source (Shot 1 of 27). The first, second, and third red lines according to time are, respectively, the calculated direct P-wave arrival, the calculated direct S-wave arrival, and the calculated direct Rayleigh wave arrival. The same pattern applies to the blue lines which are calculated scattered wave arrival times caused by interaction with the cavities (located beneath receiver number 16, 17, 46, and 47) in this synthetic model. Parameters are as described in Fig. 5.1. 137

Figure 5.9 Residual of Model E subtracted from Model F, vertical direction time histories. Parameters are as described in Fig. 5.1 and 5.8. 138

Figure 5.10 Model F filtered time histories from convolution of real source (Shot 1 of 27). The red line is picked P-wave arrival time. Parameters are as described in Fig. 5.1. 139

Figure 5.11 Overtone image created from Model F data corresponding to the time histories in Fig. 5.8. The data are not normalized. Parameters are as described in Fig. 5.1 and 5.4. 140

Figure 5.12 Overtone image residual of Model E subtracted from Model F corresponding to the time histories in Fig. 5.9. The data are not normalized. Parameters are as described in Fig. 5.1 and 5.4. 141

Figure 5.13 Model F filtered convolution of real source overtone image (Shot 1 of 27). The data are not normalized. Parameters are as described in Fig. 5.1 and 5.4. 142

Figure 5.14 Overtone images in the positive *X* direction using Model F* with a convolved real source in multiple source locations and a finite cavity. The figures are arranged from left to right where the top left is source location 1 and the bottom right is source location 26. In all overtone images the *X* axis is frequency in Hz, and the *Y* axis is velocity in m/s. The cavities are located at source locations 8 at (10, 15.5, 1) and 18 at (20, 15.5, 1). These are the images used to create the stack shown in Figures 5.17 and 5.18. 143

Figure 5.15 Stack of overtone images according to velocity using Model F with a convolved real source in multiple source locations and a pseudo-2D cavity. The cavities are located at source locations 8 at (10, 15.5, 1) and 18 at (20, 15.5, 1). 144

Figure 5.16 Stack of overtone images according to frequency using Model F with a convolved real source in multiple source locations and a pseudo-2D cavity. The cavities are located at source locations 8 at (10, 15.5, 1) and 18 at (20, 15.5, 1). 145

Figure 5.17 Stack of overtone images according to velocity using Model F* with a convolved real source in multiple source locations and a finite cavity. The cavities are located at source locations 8 at (10, 15.5, 1) and 18 at (20, 15.5, 1). 146

Figure 5.18 Stack of overtone images according to frequency using Model F* with a convolved real source in multiple source locations and a finite cavity. The cavities are located at source locations 8 at (10, 15.5, 1) and 18 at (20, 15.5, 1). 147

Figure 5.19 Comparison of stacks of overtone images according to velocity from Model E (does not contain a cavity) using a convolved real source, Model F* (two cavities located at source location 8 and 18) using a convolved real source, and the EGTS (two cavities located at 10 m and 20 m from the first receiver) using a hammer source. Model E is displayed at the top, Model F is displayed at the center, and the EGTS is displayed at the bottom. 148

Figure 5.20 Comparison of stacks of overtone images according to frequency from Model E (does not contain a cavity) using a convolved real source, Model F* (two cavities located at source location 8 and 18) using a convolved real source, and the EGTS (two cavities located at 10 m and 20 m from the first receiver) using a hammer source. Model E is displayed at the top, Model F is displayed at the center, and the EGTS is displayed at the bottom. 149

LIST OF ACRONYMS, SYMBOLS AND ABBREVIATIONS

CRS – Convolved Real Source

DC – Dispersion Curve

E3D – Wave propagation modeling software from LLNL (Larsen, S. & Schultz, C.A. 1995)

EGTS – Engineering Geophysics Test Site

FS – Free Surface

HVL – High Velocity Layer

LLNL – Lawrence Livermore National Laboratory

MASW – Multichannel Analysis of Surface Waves

MATLAB – MATLAB 7.13.0.564, The MathWorks Inc., Natick, MA, 2011

NED – Normalized Energy-Distance parameter

NFS – No Free Surface

NMO – Normal Move Out

ReMi – Refraction Microtremor

SASW – Spectral Analysis of Surface Waves

SWAMI - Surface Wave Modal Inversion

UNLV – University of Nevada, Las Vegas

USGS – United States Geological Survey

VP – Compressional wave Velocity

VS – Shear wave Velocity

WPP – Wave propagation modeling software from LLNL – also known as Serpentine Wave Propagation (Petersson, & Sjogreen 2011)

CHAPTER 1 INTRODUCTION

1.1 PURPOSE

The purpose of this research is to improve capabilities for cavity detection and characterization using Rayleigh-type seismic surface waves by studying patterns of diffraction on the ground surface from shallow buried cavities. Data collection and analysis of the scattering of surface waves are being investigated for locating shallowly buried hollow features, such as natural cavities, abandoned mines, and tunnels. Some engineering field applications of scattering of surface waves include engineering site investigations, environmental studies, archaeological site evaluations, removal of scatter ("noise") for determining subsurface characteristics at greater depth, as for oil or gas exploration, and ahead-of-drill exploration.

The cavities studied in this research consist of steel- and plastic-skinned, air-filled drums that were shallowly buried, empty, and synthetic model representations of these drums. This research encompasses numerical simulations and analyses of seismic wave propagation that are complementary to geotechnical field experiments conducted by others at the University of Nevada, Las Vegas (UNLV) Engineering Geophysics Test Site (EGTS), which contains the drums mentioned above. This research presents synthetic time histories that display scattering of surface waves caused by models of the buried drums. Discrete heterogeneities such as these are responsible for scattering of surface waves (Luke and Calderón-Macías (2007), Luke and Calderón-Macías (2008), Gelis et al (2005), Ivanov et al. (2003)).

Carbonate-cemented soil layers commonly encountered in the Las Vegas Valley are known locally as 'caliche'. The challenge of cavity detection in the presence of caliche is one unique aspect of this research when compared to other research on detecting cavities, such as Gucunski and Woods (1992), Gelis et al. (2005), and Nasseri-Moghaddam et al. (2005). The presence of caliche, which is manifested in this research as a high-velocity geologic layer below the EGTS drums, will be demonstrated to have a significant effect on the time histories; the additional wave partitioning caused by the caliche makes interpretation of the data challenging. The caliche layer must be considered to properly model wave propagation around the barrels at the EGTS.

The complex layering of the EGTS can be studied through synthetic modeling. To study fundamental wave propagation phenomena, the layer system can be simplified by removing some layers. In this research, simplified models are examined through sensitivity studies; these show the effect of each layer in the complex layer system of the EGTS. Layers manifest in Rayleigh wave data through the phenomenon of dispersion. "Dispersion" means that Rayleigh waves of different frequencies travel at different velocities in a layered system. Surface waves such as the Rayleigh wave, which is also referred to as ground roll, are distinct from body wave which include the P-wave, which is also known as the compression wave, and the S-wave, which is known as the shear wave.

This research depicts the surface-based seismic data by summing or stacking overtone images. The overtone image is the calculated amplitude spectra of wave velocity as a function of frequency for a linear sensor (geophone) array (e.g., Casto et al. 2009). Stacking overtone images along the frequency or velocity axis provides condensed maps of amplitude variation along the array (Luke and Calderón-Macías 2008). Such a plot summarizes the energy distribution along the array and, as will be shown, exhibits a distinctive energy pattern in the presence of a cavity.

Nasseri-Moghaddam et al. (2005) introduced parameters known as normalized energy-distance parameter (NED) and normalized amplified logarithmic decrement (NALD) to indicate and describe cavities in the frequency domain. The authors demonstrated the use of these parameters to determine the location and the embedment depth of a cavity. This procedure is based on the attenuation analysis of Rayleigh waves.

Methods used in this research for detecting and/or characterizing cavities using surface-based seismic data include:

1) Residual calculations obtained by subtracting time histories for different models from one another to see the differences between them;
2) Direct analysis of signal attenuation determined from time histories;
3) Overtone images;
4) Cavity characterization parameter NED of Nasseri-Moghaddam et al. (2005); and
5) Stacks of overtone images.

1.2 RESEARCH HYPOTHESIS AND OBJECTIVES

This research addresses detection of underground cavities above a high-velocity layer focusing on Rayleigh-type surface wave energy. One hypothesis is that the predominant energy propagated is Rayleigh wave energy and the predominant scattered energy is also Rayleigh wave energy; this is addressed in Chapter 4 using synthetic time histories created in this research.

The main hypothesis is that Rayleigh waves in stacks of overtone images and the cavity characterization parameters of Nasseri-Moghaddam et al. (2005) are diagnostic of the presence, placement and geometry of the cavities studied, even in layered ground having strong impedance contrasts. Other researchers have looked for scattered wave arrivals in time histories produced from a cavity (Gelis et al (2005), Ivanov et al. (2003), Luke and Calderón-Macías (2007), Luke and Calderón-Macías (2008), Sloan et al. (2011), Sloan et al. (2012)). This thesis tests whether the effect of cavities (modeled shallowly-buried drums) on synthetic, noise-free, surface-based seismic data is visually apparent in time histories and also in the frequency domain as visualized in stacks of overtone images. Then this thesis goes a step further to investigate experimental results, given the expectations from the synthetic analyses.

The main objectives of this research are:

- Use synthetic modeling to demonstrate whether it is possible to identify the presence of shallowly buried drums over caliche at the EGTS by observing stacks of overtone images.
- Use synthetic modeling to test whether the cavity characterization parameters of Nasseri-Moghaddam et al. (2005) can be used to identify the location and depth of the buried drums at the EGTS.
- Demonstrate the effects that a simple cavity has in the time domain and frequency domain by studying homogeneous and layered geologic models and using different types of seismic sources.
- Demonstrate differences in detectability for a continuous cavity (pipe) versus a discrete cavity (drum).
- Consider the signal-to-noise ratios necessary for cavity detection using seismic methods under the scenario presented.
- Demonstrate, using time histories, that the predominant energy that scatters from the cavity is from the incident Rayleigh wave .

The activities described below have been carried out to achieve the objectives listed above. Comparisons of theoretical and experimental data to seek approaches that show the presence and location of cavities are made in this research. This is a stepwise process of comparing synthetic propagation through simple geologic models with real wave propagation through real ground. Expectations are that real buried hollow features can be more readily located and characterized in a real-life setting using techniques and

procedures developed by gaining experience with what to look for by testing with synthetic time histories derived using simple geologic models.

In order to achieve the anticipated outcomes:

1) The frequency content within the field experiment is investigated in the form of power spectrums which display the frequency range of the source used, in this instance a sledgehammer. A similar frequency range for synthetic sources is chosen based on this.
2) Suites of synthetic time histories are generated for eight different geologic models that range in complexity from a homogenous halfspace to one that imitates the layering and the cavities of the EGTS field experiment.
3) Synthetic time histories are compared to experimental time histories collected at the EGTS.
4) Stacks of overtone images of synthetic data are compared to stacks of overtone images of experimental data presented by Luke and Calderón-Macías (2007).
5) Synthetic results are compared against each other; for example a homogeneous model without a cavity is compared to a model with the same parameters and a cavity added to the model to demonstrate the effect of the cavity. Another example is a two layer model compared to a homogeneous model to see the difference the added layer makes.
6) Synthetic stacks of overtone images are compared to comparable experimental stacks of overtone images. The amplitude pattern surrounding the cavities' locations in the stacks of overtone images is examined.

7) The Normalized Energy Density (NED) cavity detection parameter of Nasseri-Moghaddam et al. (2005) is computed and analyzed for cavities in a homogeneous model, a two-layer model with a high velocity layer (HVL), a four-layer model with a HVL, and the experimental data collected at the EGTS (Luke and Calderón-Macías 2008).

1.3 STUDY SITE

The EGTS is located on the UNLV campus, directly south of the engineering buildings (Figure 1.1). A simplified interpretation of five borehole logs from the EGTS is shown in Figure 1.2. Two of the boreholes are drilled to a depth of 20 feet, and the other three are drilled to a depth of 30 feet. As seen in the figure, the top layer of the EGTS mostly consists of different types of sands (clayey sand, silty sand and sandy gravel), the middle layer consists mostly of caliche (caliche, cemented sand and cemented gravel), and beneath that are different types of clays and sands (clayey sand, sandy clay, clayey gravel, clayey silt and sandy silt). There is imported fill at the surface that is covered by irrigated turf.

Figure 1.3 displays a picture of the experiment setup at the EGTS. The experimental data from the EGTS was collected on February 8, 2007 by Prof. Barbara Luke with assistance from UNLV students and Applied Geophysics Center staff member Chris Cothrun. The steel drum is shown in Figure 1.4. The drums were buried in 2001, on their sides such that the lowest edges are 1.5 m below the ground surface (Luke and Calderón-Macías

2008). The two drums are 0.3 m^3 (55 gallons); 0.9 m long by 0.6 m in diameter (Luke and Calderón-Macías 2008).

1.4 ORGANIZATION OF THESIS

Chapter 2 reviews the state of the practice of remote cavity detection by first addressing published literature from sources other than the UNLV Applied Geophysics Center and then reviewing directly relevant literature from UNLV Applied Geophysics Center researchers. Chapter 3 describes the methodology used for analyses conducted in this research. Section 3.1 contains a description of the synthetic model parameters, Section 3.2 addresses sensitivity studies, and Section 3.3 addresses replicating the experimental data with synthetic models. Chapter 4 presents the results of the sensitivity studies. Chapter 5 presents the results of synthetic modeling conducted to replicate the experimental dataset that was collected by others, and also presents a comparison of model to experimental results. Chapter 6 discusses the results and presents the conclusions and recommendations of this thesis.

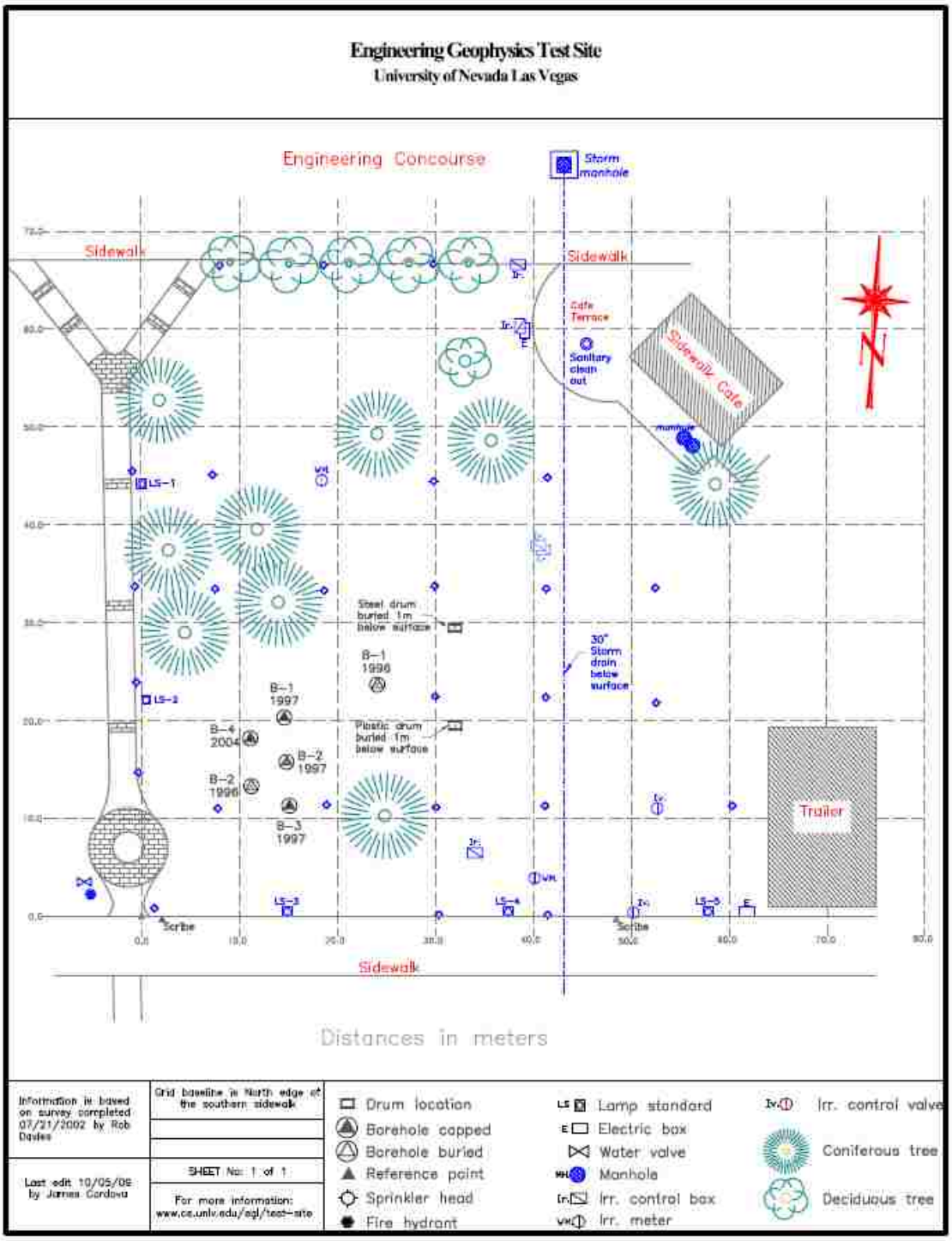

Figure 1.1 Engineering Geophysics Test Site map showing the locations of the buried barrels and boreholes. Modified from http://agc.unlv.edu/egts/SiteMap.

Figure 1.2 Simplified interpretation of borehole logs from the Engineering Geophysics Test Site. Borehole locations are shown on Figure 1.1. The nearest borehole to the cavities is displayed on the far left and the farthest on the far right. The water table is at 3.5 meters (11.5 feet) in depth. (Modified from http://agc.unlv.edu/egts/SoilTrenchLogs)

Figure 1.3 Experimental setup at the Engineering Geophysics Test Site on the UNLV campus, on February 8, 2007. View is toward the north, over the barrels.

Figure 1.4 Steel barrel buried at the Engineering Geophysics Test Site on the UNLV campus in 2001. Location is noted in Figure 1.1.

CHAPTER 2 LITERATURE REVIEW: STATE OF THE PRACTICE

Geophysical methods that have been used to detect and delineate cavities include seismic, electrical resistivity, electromagnetic (EM) including ground penetrating radar, and gravimetric (microgravity) methods (Sloan et al. 2012, Sloan et al. 2011, Butler 2008, Conyers 2011). Nazarian (2012) states seismic methods' main application in geotechnical engineering has been shear wave velocity (VS) profiling for geotechnical earthquake engineering analysis. Sloan et al. (2012) and Sloan et al. (2011) mention the application of active-source seismic surface-based methods for cavity detection which rely on data collection at the ground surface in the area containing the cavity.

The literature review for this thesis focuses on an examination of seismic methods used to detect and delineate cavities. It emphasizes the numerical simulation and application of Rayleigh-wave-based seismic methods, starting with typical ways that surface-based seismic data collection and analysis methods are used. Then specific seismic methods that use time histories, overtone images, the NED cavity characterization parameter (Nasseri-Moghaddam et al. 2005), and stacks of overtone images are reviewed.

One application of Rayleigh waves is determining layering of soil. Several approaches are used to implement this, including Spectral Analysis of Surface Waves (SASW), Multichannel Analysis of Surface Waves (MASW), and Refraction Microtremor (ReMi) (Nazarian 2012). These methods involve collecting time histories, then transforming these data into the frequency domain (using a one-dimensional Fourier transform). Sets of time histories collected along a linear array are most commonly displayed in the

MASW method as a plot of frequency versus wave velocity which is known as an overtone image or dispersion image. A fundamental mode dispersion curve and higher order mode dispersion curves are then identified (higher order modes are identified when possible) and inverted in order to obtain the VS profile of the site; except for the SASW method, which computes a single "effective" dispersion curve. The VS profile of the site provides a way to identify the sediment layers in the earth by showing what the VS is at a given depth and thus how it varies with depth.

2.1 SURFACE WAVE METHODS

The MASW style is used in this research for data collection and analysis of synthetic data, and also applies to the data collection and analysis of the experimental data from the EGTS. The SASW method is a two-receiver approach and was the first method developed. The MASW method is a multichannel approach, using 12 or more receivers, that builds from the SASW method. Nazarian (2012) states that MASW, using a sledge hammer as a source, is quite effective for VS profiling down to 10 to 15 meters below the ground surface. By changing the source characteristics, surface wave methods can provide a dispersion curve that covers from near the surface to depths of several hundred meters (Nazarian 2012). The SASW and MASW methods often use an active source, such as a sledge hammer as previously stated. Murvosh et al. (2013) used the SASW method in an urban environment with paired active sources, an IVI Inc. "minivib" Vibroseis and an instrumented hammer. They observed that the combination of sources allowed VS profiles to be developed to 100 m and deeper without sacrificing resolution at shallow depths.

The MASW method has the option of using a passive (ambient) source, such as traffic noise. Park et. al. (2007) discuss the use of passive source with the MASW method. The authors state that passive surface waves generated from natural (such as wind and tree movement) or cultural (such as people walking, airplanes, and road traffic) sources are usually of a low frequency (1-30 Hz) with wavelengths that range from multiple km (natural sources) to a few tens or hundreds of meters (cultural sources), accessing a wide range of depths and therefore providing a strong motivation to utilize them. The ReMi method uses the passive source. It successfully captured VS profiles down to the depth of 100 meters in tests at the Reno/Tahoe international airport in Nevada and the Newhall fire station in southern California (Louie 2001). Passive-source methods are particularly useful where noise is extreme, such as urban sites and other areas of heavy traffic.

The SASW, MASW, and ReMi methods have been used to define geometry of layered systems, such as soils and pavements, by utilizing dispersion of Rayleigh waves in layered systems. All three methods consist of three phases: 1) data collection, 2) evaluation of dispersion curve, and 3) inversion of the dispersion curve to obtain the VS profile (e.g., Gucunski and Woods 1992). An advantage of all three methods is that they are performed entirely from the ground surface.

2.2 SEISMIC METHODS FOR CAVITY DETECTION: TIME DOMAIN

The SASW and MASW methods have been tested for cavity detection. Gucunski et al. (1996) used a finite element model to test the detection of underground obstacles using

the SASW method and found it can be used effectively for shallow obstacle detection. However, when the SASW method was tested experimentally for cavity detection by Phillips et al. (2002) and by Luke and Chase (1997), results were mixed. Nasseri-Moghaddam et al. (2007) and Nolan et al. (2011) used the MASW method for cavity detection.

When surface-wave energy meets an object, backscattered surface waves are created, and energy scatters back toward the source (Sloan et al. 2011). The backscattered energy, as opposed to the dominant forward-propagating surface wave energy (background or incident field), is used to indicate the location of a cavity (Sloan et al. 2011). Sloan et al. (2011) present a technique which focuses on the backscatter energy and filtering the body- and surface-wave energy to identify anomalous changes in seismic properties that are indicative of a cavity. The authors detected a 9.1-m deep tunnel, 1.5 m by 1.2 m in cross section, dug horizontally in soil to represent a clandestine tunnel, using ground-surface based seismic techniques. The site consisted of unconsolidated sand, silt, and clay with very little soil moisture, which the authors note is typical of a southwestern desert environment. An accelerated weight drop source was used to acquire data with geophones configured in a 24-station land streamer. The authors present synthetic and experimental time histories and tomography plots that allow the identification of a cavity using two seismic techniques: body-wave diffractions and surface-wave backscatter.

Sloan et al. (2011) claim that body-wave diffractions are useful to detect subsurface cavities too small to be detected reliably by reflection methods. They consider four types

of diffractions: P, S, P-S conversions, and S-P conversions, where each is unique with respect to polarity and velocity. The authors conclude that only pure P- or S- diffractions can be used to make accurate depth and velocity measurements. They further found that S-P diffractions produce depths and velocities that are too deep and low, whereas P-S diffractions produce the opposite.

Sloan et al. (2011) tested changes in reflection moveout velocities to indicate cavities created through dissolution mining. They used the technique to identify cavities with potential of roof failure through the buildup of stress in the roof rock and walls, which is linked directly to increased VS because of increased load in load-bearing sidewalls. The authors stated that this method of observing VS increases in the surrounding media, in its current state, is applicable to large cavities at depths that are not plausible for the conventional MASW method using a sledgehammer source, however it is not appropriate for small, shallow cavities because the host sediments are not as likely to exhibit observable increases in stress.

When a seismic wave arrives at a surface separating two beds where the lower bed is stiffer than the upper bed, part of the energy is reflected and remains in the same medium as the original energy; the balance of the energy is refracted into the other medium (e.g., Sheriff and Geldart 1995). Tomography is imaging by sections using a penetrating wave, such as seismic waves, and is used in other scientific fields besides geophysics. Refraction tomography has been used to detect cavities; for example, Hickey et al. (2009), Riddle et al. (2010), and Nolan et al. (2011) detected cavities using refraction

tomography. Reflection tomography was used by Di Fiore (2013), Inazaki et al. (2005), and Miller et al. (1991) to detect cavities. The goal of this research is not to use refraction analysis; instead surface-wave backscatter analysis and overtone image stacking are considered.

2.3 SEISMIC METHODS FOR CAVITY DETECTION: FREQUENCY DOMAIN

Gelis et al. (2005) studied seismic response for different cavity shapes and different cavity depths, and for the presence of an altered zone through synthetic modeling and frequency-domain analyses. They computed time histories using a 2-D finite difference code to model elastic seismic wave propagation. The code had a perfectly-matched-layer absorbing-boundary condition to avoid reflections from the edges of the numerical model and allow the wavefield to propagate parallel to the edges. The purpose of an absorbing-boundary layer is to minimize the amplitudes of waves reflected from the artificial boundary (Engquist and Majda 1977). The absorbing boundary must prevent waves from reflecting by absorbing the waves that strike it. One of the first practically useful absorbing boundary conditions was derived by Clayton and Enguist (1977), whereas a perfectly-matched-layer absorbing boundary condition is a more recent development which has superior non-reflecting properties (Petersson and Sjogreen 2009).

To study the effect a cavity had in the frequency domain, Gelis et al. (2005) computed time histories from two synthetic models that were identical except for the presence of a cavity in one of the models. Each model was processed in MATLAB to create an overtone image. The overtone image for the model with the cavity was subtracted from

the model without a cavity; the authors referred to the result as the 'differential image'. The temporal differential seismogram isolates the cavity effects, at least to first order. A homogenous background was used with a P-wave velocity (VP) of 888 m/s, a VS of 431 m/s, and a density of 1600 kg/m^3 to model subsurface containing an underground railway structure in the north of France. The authors modeled an explosive source by a Ricker wavelet with a central frequency of 88.8 Hz, embedded at 1 m depth. The authors used a receiver spacing of 1 m, a source-to-receiver distance of 5 m, a grid spacing of 0.1 m, a grid size of 451 X 251 grid nodes, and a time step of 5 X 10^{-5} s with a total of 10,000 time steps, i.e., 0.5-s duration, in a 2-D model. The authors performed five different tests with models that contain cavities: three tests were performed with circular cavities of different depths, one with a rectangular cavity, and one with a circular cavity surrounded with an altered zone. The circular cavity was 3.6 m in diameter, and the rectangular cavity had 4 m width and 2.5 m depth. The depth to the top of each cavity was 2 m for all cavities except for the two deeper circular cavities at 5 and 8 m depths. The altered zone had a VP of 444 m/s, a VS of 200 m/s, and a density of 1600 kg/m^3.

Gelis et al. (2005) observed that differential time histories showed a non-symmetrical diffraction pattern and overtone images showed localized scattering from cavities. They presented overtone images for models with cavities that contain a band of non-coherent energy whose range depends on the cavity depth and shape. They found that the cavity had a stronger effect on time histories when it was shallower and that a rectangular cross section generated more severe perturbations than a circular section of similar size and location, due to non-symmetrical back-scatter. Furthermore, they found that low-velocity

zones around the cavity trapped waves, leading to increased Rayleigh wave attenuation and strong footprints in overtone images, possibly masking the cavity signature. The authors stated that when the altered zone extended to the surface as a cone (also a low-velocity zone), the trapping phenomena completely dominated the time histories, thereby masking the cavity. The authors observed that the ability to detect such altered zones was useful in natural hazard assessment, making it possible to distinguish the signature of a 'safe' cavity from a potentially dangerous one. It is notable that Gelis et al. (2005) report low-velocity zones around the cavity in shallow depths in the specific geologic conditions they studied, in contrast to Sloan et al. (2011) who reported velocity increases surrounding the cavity they studied, which was deeper and in a stiffer medium.

Other researchers have studied frequency domain data for cavity detection. Phillips et al. (2002) computed power spectral density from laboratory data and field data from an underground mine site and found amplification of energy = for certain wavelengths in receivers located directly above the cavity: for cavity depths to 50 m, frequencies in the power spectral density plots were amplified over the range of 13 Hz to 15 Hz. Shokouhi and Gucunski (2003) observed similar results in a finite element model with a concentration of energy in power spectral surfaces (power spectral amplitudes as functions of frequency and receiver location) slightly in front of a cavity in certain frequency bands.

Methods that have been used for cavity embedment depth detection include the following.

- Xia et al. (2006) uses the travel time equation to solve for phase velocity of the host medium and depth of a cavity and apply it in synthetic and experimental examples. This equation of surface-wave diffractions is based on properties of surface waves; two diffraction times were necessary to define the depth and phase velocity. When the solution is plotted over time histories it appears similar to hyperbolas shown later in this research in sections 4.3, 4.5, and 5.2 for the scattered arrival times. The apex of the hyperbola indicates the cavity location; another way to say this is the earliest arrival time of the scattered waves indicates the location of the cavity.
- Zhao and Rector (2010) use the cavity characterization parameters of Nasseri-Moghaddam et al. (2006) to investigate a septic tank. The authors claim success in determining the cavity location using the normalized energy distance parameter (NED). A cumulative summation of normalized amplified logarithmic decrement values (NALD) indicated that the top was at 0.9 m and the bottom at 4 m, whereas the true values are 0.5 m and 3.8 m, respectively. The following section discusses these cavity characterization parameters further.

2.3.1 CAVITY CHARACTERIZATION PARAMETERS

Nasseri-Moghaddam et al. (2005) introduced parameters for detecting cavities in the frequency domain. According to the authors, most of the seismic methods used for cavity detection at the time could successfully locate a cavity but not its embedment depth. The seismic methods the authors refer to are the SASW and the MASW.

A hypothesis of Nasseri-Moghaddam et al. (2006) is that part of the incident energy is trapped within the cavity and the trapped energy bounces inside the cavity until it is attenuated by radiation. The authors state the effect of the cavity is seen as a concentration of energy over the cavity region in the frequency domain.

Nasseri-Moghaddam et al. (2005) compared recorded energy at each receiver in a linear array by frequency content and by signal attenuation determined from time histories. The authors proposed an analysis procedure to determine not only the location of the surface projection but also embedment depth of a cavity; this procedure was based on what they termed as the attenuation analysis of Rayleigh waves. The authors use the frequency spectra of recorded signals to compute a spectral-energy parameter and a modified logarithmic-decrement parameter. The authors used a finite difference numerical model (FLAC2D, Itasca, 2000) to simulate the MASW test in the presence of a cavity. The proposed method for detecting a cavity was to calculate the signal energy at each receiver location and then to normalize the energy spectrum to compute a value known as the normalized energy-distance parameter (NED). These NED values were then plotted versus distance. According to the authors, the boundaries of the cavity are distinguished by peaks and valleys of the NED parameter. The amplified logarithmic decrement and its normalized value (NALD) are also calculated and then the NALD values are plotted versus normalized wavelength. The wavelength at the peak in the NALD plot gives a good estimation for the average depth of the cavity according to the authors. This parameter is not explored in this research for reasons that will be presented in section 4.6.

Nasseri-Moghaddam et al. (2005) tested a 2-D homogeneous model and six other 2-D models that include a square cavity. The cavity varied in embedment depth from 0.080 m to 0.160 m and also varied in size from 0.08 m to 0.64 m. The authors state if the geometrical damping is eliminated, the cumulative energy at each receiver is the same. This is shown by the homogeneous model which shows identical NED values at all receivers. In all cases that include a cavity, the NED plots start to fluctuate in the proximity of the cavity, and peaks and valleys of the NED parameter indicate the edges of the cavity. The authors state the horizontal component has a better resolution than the vertical, and also that wider cavities produce more conspicuous peaks and valleys in the NED parameter. Their results show smaller NED parameter values past the cavity location.

According to the authors (Nasseri-Moghaddam et al. 2005), in order for the fluctuations in the NED parameter to be sufficiently large, maximum wavelength must be greater than five times the embedment depth (depth to top of cavity). Another limitation is possible contamination of surface wave energy with body wave energy which the authors check by calculating the group velocity and comparing it with the phase velocity. They found that the difference in group velocity with respect to phase velocity was negligible, and therefore cross-contamination was not a concern, if maximum wavelength is less than 10 times the embedment depth. In summary, the maximum wavelength should be between five and ten times the embedment depth for successful application of the NED parameter.

Nasseri-Moghaddam et al. (2006) tested the NED parameter using experimental data. The data were collected at an abandoned mine site with known layout and surface conditions in the Crawford Mountains, Utah. The authors concluded that the NED parameter is a promising tool for the experimental data because it showed a peak amplitude at the center of the cavity and two smaller local maximums at the boundaries of the cavity.

Nasseri-Moghaddam et al. (2007) tested the parameters further in an experiment and numerical model of a mining site and concluded that the optimum wavelength for detection of cavities is 3 through 5 times the embedment depth.

2.3.2 SEISMIC TESTING FOR CAVITY DETECTION AT UNLV'S APPLIED GEOPHYSICS CENTER

This part of the literature review covers relevant work done at the Applied Geophysics Center of the University of Nevada, Las Vegas (UNLV). As previously noted, cavities and buried anomalies were studied by using surface-based seismic datasets, computing overtone images (as in surface-wave testing for VS modeling), then summing or stacking them into what is being named in this research stacks of overtone images. This stacking yields a 3-D data compilation in frequency, velocity and offset. Stacking overtone images along the frequency axis or velocity axis provides condensed maps of amplitude variation along the array (Luke and Calderón-Macías 2008). This thesis tests whether, in a noise-free environment, such stacks show a distinct energy signature that is diagnostic of the cavity.

Luke and Calderón-Macías (2008) collected experimental data at the Engineering Geophysics Test Site (EGTS) to test the ability of stacks of overtone images to indicate cavities. The sensors used were geophones with 4.5-Hz resonant frequency, paired to record vertical and horizontal (radial) components of motion (Luke and Calderón-Macías 2008). The test included 72 geophone pairs, using a 1/3-meter spacing, for a total of 144 channels as seen in Figure 1.3 and described further in Table 2.1. The test was collected over a buried steel drum and a plastic drum, respectively 10 m and 20 m south of the northernmost geophone pair. The source was a sledgehammer swung on an aluminum plate, at 1 m intervals starting 2 m beyond the north end of the geophone array. The water table is assumed to be at 3.5 meters (11.5 feet) in depth, based on the center of the caliche layer in the borehole logs from Figure 1.2. The drums lie on their sides, major axes parallel to one another, and the receiver line is perpendicular to their major axes.

Four source stacks were collected at each source location (Luke and Calderón-Macías 2008). This means four separate hammer hits were recorded and the results superimposed, matching trigger timing. Stacking the results of each hammer hit causes redundancy of the data, which improves the signal-to-noise ratio. The hammer source was applied at one meter spacing, starting 2 m beyond the north end of the geophone array and ending 3.3 m beyond the south end. The source location was offset 0.2 meters to the side of the receiver line. A Geometrics Geode seismograph was used to record the data, with a 1-second recording length and 0.25-millisecond sampling rate.

Luke and Calderón-Macías (2008) display stacks of overtone images created from data collected at the EGTS. The stacks of overtone images were created by first calculating the overtone image for each source location. Data from the receivers to the south of the source were summed, next the receivers to the north of the source were summed separately, and finally data from all receivers in both directions were summed. The overtone images were stacked according to both frequency and velocity. In the stacks of overtone images according to frequency, the authors observed a pattern of high amplitude responses flanking a low amplitude response with velocities concentrated in the range of 100 to 200 m/s. In stacks according to velocity, the authors observed lateral changes in frequency in the range of 50 Hz through 80 Hz. The authors found that compared to the frequency stacks, velocity stacks display more coherency and higher amplitude. The authors found higher resolution with vertical receivers than with horizontal. They noted the same trends of lower energy concentrations at the cavities with highs on either side over both barrels, but the effect was more pronounced for the steel barrel.

2.4 DISCUSSION

This current research evaluates the use of stacks of overtone images to detect cavities, and is based on methods examined in the literature review. The synthetic models used in this research provide the opportunity to compare modeled data with ground truth to verify the applicability of stacks of overtone images for cavity detection. Synthetic data aids in the interpretation, comparison, and analysis of cavities in experimental data.

This research displays 'differential images' similar to Gelis et al. (2005) as described in Section 2.2; here, the tool is applied to three different layer systems so that comparisons can be made. The cavity characterization parameter (NED) of Nasseri-Moghaddam et al. (2005; discussed in Section 2.3) is tested using the same synthetic models and also on the experimental data from the EGTS.

This research attempts to replicate stacks of overtone images obtained experimentally by Luke and Calderón-Macías (2008), using synthetic models. The synthetic models have known ground conditions (because they are defined in the synthetic model) and are free of noise, whereas at the field test site, the exact ground conditions in every possible location are not known and not free of noise (for example, because of natural variations such as layer depth and material uniformity). The synthetic models provide a method to demonstrate in controlled conditions to what extent stacks of overtone images can be useful for cavity detection. Results can be compared to the stacks of overtone images derived experimentally at the EGTS.

The next chapter describes the synthetic model parameters, the methodology used for the numerical model sensitivity studies, and the methodology used for replicating the experimental data at the EGTS.

Table 2.1 Experiment setup at the Engineering Geophysics Test Site on the UNLV campus. Courtesy of B. Luke; Luke and Calderón-Macías (2007).

Source:	hammer on aluminum plate
Source spacing:	1 m
Source line:	~30 m
Sensors:	2-C 4.5-hz geophones
Sensor spacing:	0.33 m
Receiver line:	~25 m
Sample rate:	0.25 ms
Barrels:	
Burial depth (bottom):	1.5 m
Length:	0.9 m
Diameter:	0.6 m
Steel :	at 10 m
Plastic:	at 20 m

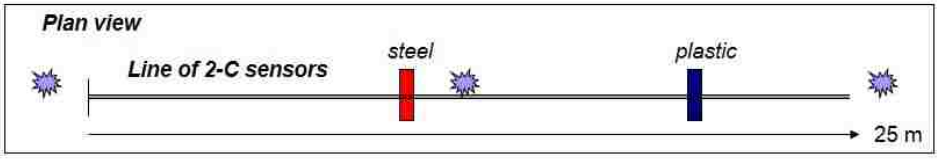

CHAPTER 3 METHODOLOGY

This chapter describes the synthetic model parameters in Section 3.1, the methodology used for the numerical model sensitivity studies in Section 3.2, and the methodology used for replicating the experimental data at the EGTS in Section 3.3.

Section 3.1 addresses the synthetic model parameters and also introduces the computer programs used. Section 3.1.1 covers tasks, which is comprised of the following. Section 3.1.1.1 includes the models used for sensitivity studies, how the reference axes of the synthetic models are defined, and the size of the 3-D models. Section 3.1.1.2 includes how the VS and density inside of the cavity were chosen for modeling purposes. Section 3.1.1.3 includes the models used to attempt to replicate the experimental data from the EGTS. The layer system used is explained in Section 3.1.1.4. Section 3.1.1.5 includes the 2-D models used as sensitivity studies. Section 3.1.2 includes the model and cavities layout. Section 3.1.3 includes the source location and parameters. Section 3.1.4 includes the method to calculate time domain and frequency domain residuals. Section 3.1.5 includes the method to calculate overtone images. Section 3.1.6 includes the method to calculate the cavity characterization parameters. A peak signal-to-noise ratio appropriate for cavity detection using seismic methods is discussed in Section 3.1.7. Section 3.2 includes the test setup used in the models that attempt to replicate the EGTS test. How the hammer source is simulated and replicated is also in Section 3.2.

3.1 SYNTHETIC MODEL PARAMETERS

The main task of this research is to create stacks of overtone images from synthetic data that replicate conditions under which experimental data were collected over buried drums at the EGTS for the purpose of detecting the locations of the cavities. In this research, a computer program for simulating seismic wave propagation is used to generate time histories for each synthetic model. The next step involves transforming sets of time histories into overtone images. Then the overtone images are summed according to direction from the source to create stacks of overtone images. Finally, the two stacks of overtone images from each direction are summed to create the final, composite stack of overtone images.

This research applies two advanced geophysics computer applications, which were designed for a super computer at Lawrence Livermore National Laboratory (LLNL), to the study of cavities. After creating synthetic time histories with this application, the data are processed using MATLAB software to produce plots and process further.

Synthetic models in this research are created using two computer programs that simulate seismic wave propagation: WPP and E3D. WPP is a computer program written by Anders Petersson and Bjorn Sjogreen at LLNL. E3D is a computer program written by Shawn Larsen at LLNL. The version of E3D used was published on 10-27-2004 (Shawn Larsen, personal communication, 2011), and the version of WPP used was published on 12-19-2011 (WPP 2.1.5 User Manual, 2011; software, 2011). WPP is in current use by

others at LLNL (Sjogreen and Petersson 2011). E3D is used by others such as Jin (2006) and, as a recent example, Mangriotis et al. (2013). This research uses WPP for most studies. E3D was used to compute 2-D synthetic data for a No Free Surface (NFS) and Free Surface (FS) sensitivity study. This research used two similar operating systems to compile WPP, Red Hat Enterprise Linux and The Community Enterprise Operating System (CentOS) Linux. Cygwin was used to compile E3D. The synthetic seismograms created with WPP are outputted in United States Geological Survey (USGS) format as a text file, and also in Seismic Analysis Code format as a binary file. This research uses the USGS format, which is inputted into MATLAB for processing.

Modeled time histories use a total duration of 1 sec or 0.5 sec. A 1 sec duration was used initially, after which it was determined that 0.5 sec would be sufficient for analysis while significantly decreasing the amount of time required for computation. Shot 1 of 27 from a two layer model with a cavity takes about 168 minutes of computation time using an AMD Phenom™ 9550 quad-core processor using a 0.5 sec total duration. This computation time is using only one core of the processor; four models were run at the same time in this research. WPP is able to run on multiple processors at the same time if desired.

A custom-built Linux machine, costing roughly $1000 at the time it was built, was used to compute models. This hardware has an AMD Phenom 9550 Quad-Core Processor at 2.20 GHz and 4 GB RAM, running Linux. VMware software was used to virtualize this

machine for the convenience of being able to use two different operating systems at the same time on the same machine (Linux and Windows).

3.1.1 Tasks

To better understand seismic wave propagation in the presence of discrete anomalies, for this research, six different subsurface models are developed, from which synthetic data are computed for purposes of comparison.

The research is separated into two different tasks, based on the layers used in the models. Task #1 is to create models to be used for sensitivity studies, and task #2 is to create models to attempt to replicate the experimental data at the EGTS.

3.1.1.1 Task 1

Task #1 involved computing time histories corresponding to four simplified subsurface models, named A, B, C, and D, as a sensitivity study and to establish baseline data for comparison to computations using more detailed models of the EGTS and experimental data from the EGTS.

Figure 3.1 displays the *X*, *Y*, and *Z* direction of the synthetic models created with WPP in an oblique view; the *X* direction is in-plane with the receiver line, the *Y* direction is out-of-plane of the receiver line, and the *Z* direction is positive downwards. When comparing

the model orientation to the EGTS experiment configuration, south is in the positive *X* direction and north is in the negative *X* direction. Models A, B, C, and D are 3-D models created with WPP. These models are illustrated in Figure 3.2. All 3-D models extend 30 meters in the *X* direction, 30 meters in the *Y* direction and 20 meters in the *Z* direction. The models use 72 receivers, which is the same for all models created in this research.

The grid spacing in all models is 0.2 meters. The best way of checking accuracy in a numerical solution is to repeat the calculation on a finer mesh and look for the same solution (WPP users guide version 2.1). Many grid spacing options were tested using Model B to find a reasonable computation time that was possible using the hardware available. Grid spacings considered included 1, 0.5, 0.2 and 0.1 m. Grid spacings of 1m and above were too large for the cavity, and the others produce the same results. Thus for the 0.2-m grid spacing chosen, the same solution was found with a finer mesh.

All models created with WPP share the same boundary conditions, which consists of a free surface condition on the top boundary (also known as a stress-free boundary) and a non-reflecting far-field boundary condition (also known as a supergrid boundary) on all other boundaries. A non-reflecting far-field boundary condition is a type of absorbing boundary condition. This boundary condition is used to minimize reflections from the boundary. All models in this research use absorbing boundary conditions on the sides and bottom of the models. Petersson and Sjogreen (2013) state the supergrid technique depends on coordinate stretching with the addition of a dissipation operator. Next they

state the dissipation operator is added in layers near the boundaries, which damps out waves that are poorly resolved because of coordinate stretching. A free-surface boundary condition is used to attempt to replicate the ground surface, which allows for surface wave propagation. The non-absorbing boundary used with these models (computed using WPP) is different from the one used with the Free Surface (FS) and No Free Surface (NFS) models (computed using E3D) described in section 3.1.1.4 due to availability within the different programs.

Table 3.1 and Table 3.2 summarizes most model parameters for all synthetic models created. Model A is homogeneous with body wave velocities (P and S) representing the near-surface conditions at the EGTS on the UNLV campus (described below). Model B is identical to Model A except that it includes a cavity. Model C is a two-layer system, with the top layer having the same VP and VS as Model A and Model B. The lower layer (halfspace) in Model C represents the caliche layer at the EGTS. Model D is identical to Model C except that it includes a cavity in the first layer.

3.1.1.2 Synthetic Cavity Properties

The cavities in models B and D are identical. It extends the entire width (y-direction; 30 m) of the 3-D model so that the situation is comparable to 2-D models of similar cavity cross-section. A cavity that is the entire width of the model clearly has a greater chance for detection by seismic methods compared to a finite sized cavity because there is an increased chance for the wave train to interact with the cavity.

The top of the cavity is buried 0.97 m from the surface and it is 0.53 m by 0.53 m in *X-Z* cross-section. Its corners are at (10, 0, 0.97), (10, 0, 1.5), (10.53, 0, 0.97), (10.53, 0, 1.5), (10.53, 30, 1.5), (10.53, 30, 0.97), (10, 30, 1.5), and (10, 30, 0.97). (Refer to Figure 3.1 for the coordinate system.) The *X-Z* cross-section contains 9 grid nodes (Figure 3.3). The cavity is square and contains 1359 grid nodes. The receiver spacing is 0.33 m, so the cavity is below two receivers.

Figure 3.3 displays a cross-sectional view of the cavity location in the models. When the layer boundaries do not align with the grid nodes, which is the case for the cavity defined in this research, WPP uses bi-linear interpolation in the horizontal directions and linear interpolation in the depth direction (WPP users guide version 2.1). For practical reasons, the modeled cavity was square in cross-section. This is in contrast to the cavities at the EGTS, whose shape in the *X-Z* plane is round. Although a circular shape would better match the results of the experimental study, a rectangular shape should produce a stronger signature (Gelis et al. 2005). Within this constraint of unmatched shape, to make the synthetic model best represent the EGTS cavities, the cross-sectional surface area and the depth of the cavity in the model were matched to the barrels. The calculation for the cavity size used in the synthetic models can be seen in Figure 3.4.

The cavity has a VP of 330 m/s, approximately the speed of sound in air. The VS inside a cavity would ideally be zero because S-waves do not travel through fluids. However,

setting the VS to zero results in numerically unstable results. The WPP program will allow for a VS no lower than 1 m/s. The accuracy of the program depends, among other things, on the parameter *P*, which is equal to the number of grid points for the shortest wavelength. The parameter *P* is therefore a normalized measure of how accurately a solution is resolved on the computational grid (WPP users guide version 2.1). The parameter *P* is a function of the VS and the grid spacing of the model: $P = (VS_{min})/(h*f_{max})$, where *h* is the grid spacing and f_{max} is the largest significant frequency in the time function; for practical purposes, the frequency where the amplitude of the Fourier transform falls below 5% of its maximum value (WPP users guide version 2.1). The f_{max} is calculated by 2.5 * f_0, where f_0 is the fundamental frequency, which equals the source frequency when a Ricker wavelet is used (WPP users guide version 2.1); 50 Hz in this research. So f_{max} is equal to 125 Hz in this research. The VS inside of the cavity for this research is assigned a low value of 30 m/s found using a trial and error approach. In initial tests a VS of 10 m/s with a grid spacing of 1 m failed to run, a VS of 20 m/s with a grid spacing of 2 m failed to run, and a VS of 30 m/s with a grid spacing of 3 m worked correctly. From these initial trial and error tests, a VS of 30 m/s inside of the cavity is used. For the models that include a cavity, *P* is equal to 1.2, and for the models without a cavity *P* is equal to 8. (Calculations apply to the grid spacing selected for use in all analyses, 0.2 m). A value of *P* greater than or equal to 15 can be relied upon to give accurate results; however, a lower number can be used in some practical situations, depending on the distance between the source and the receiver (WPP users guide version 2.1).

For VS of the cavity equal to 30 m/s, the ratio of VS of background stratum to VS of cavity is approximately seven. Considering VP of 330 m/s, the Poisson's ratio of the cavity is 0.50, which implies (incorrectly) that the cavity is incompressible.

Ideally, the model would use the density of air inside of the cavity. However, such a low density cannot be implemented in WPP. Table 3.3 displays how the cavity density for the synthetic models was selected. A trial-and-error approach was used to locate the lowest usable value. The lowest useable density was found to be 250 kg/m^3; values below this result in time histories with infinite amplitudes. This value is reasonable considering the surrounding material has a density of 1700 kg/m^3. The density in the cavity is compared to some typical dry densities of soils in Table 3.4. The lowest density reported in this table is a range of 612 to 816 kg/m^3 for a soft organic clay. The density for the cavities in the synthetic models is less than half of this minimum value. Comparing to a dry density, instead of a moist density, is conservative because adding moisture adds mass.

3.1.1.3 Task 2

Task #2 is an attempt to replicate the experimental data using 3-D models created with WPP, as shown in Figure 3.5. Models E and F are introduced. Model E has a multiple layer system (4 layers) to represent the soil conditions from the surface to 20 m depth at the ETGS. (Recall Figure 1.2.) Model F uses the layer system from Model E, but also includes two cavities to represent the steel and plastic barrels buried at the ETGS.

Model F is computed using two different cavity setups, for the purpose of comparison. One cavity setup is 0.53 m by 0.53 m, and extends the entire 30-m width of the model, thereby representing a 2-D scenario of a buried pipe or tunnel. The other cavity setup, designated Model F*, is 0.53 m by 0.53 m by 0.9 m, to imitate the actual size of the plastic and steel barrels at the UNLV EGTS (however the synthetic models' cavities are rectangular, while the actual cavities are cylinders; recall Figure 3.4). Thus, Model F* is a three-dimensional model with a three-dimensional, finite cavity.

Recall that the top of the cavity is buried 0.97 m from the surface and its corners are as described in chapter 3.1.1.2. The added cavity is at the same depth and has corners located at (20, 0, 0.97), (20, 0, 1.5), (20.53, 0, 0.97), (20.53, 0, 1.5), (20.53, 30, 1.5), (20.53, 30, 0.97), (20, 30, 1.5), and (20, 30, 0.97). The pipe-shaped cavity stretches all the way across the model in the *Y* direction.

The finite cavities (3-D barrels, as opposed to 2-D pipes) in model F* are 0.53 m in the *X* direction by 0.9 m in the *Y* direction by 0.53 m in the *Z* direction. For one of the finite cavities its corners are at (10, 14.5, 0.97), (10, 14.5, 1.5), (10.53, 14.5, 0.97), (10.53, 14.5, 1.5), (10.53, 15.4, 1.5), (10.53, 15.4, 0.97), (10, 15.4, 1.5), and (10, 15.4, 0.97). The other finite cavity has corners located at (20, 14.5, 0.97), (20, 14.5, 1.5), (20.53, 14.5, 0.97), (20.53, 14.5, 1.5), (20.53, 15.4, 1.5), (20.53, 15.4, 0.97), (20, 15.4, 1.5), and (20, 15.4, 0.97).

3.1.1.4 Methodology Used for the Sensitivity Studies

The layer system (geometry, velocities, density) used in this research was derived from the borehole logs from the EGTS and from a profile described by Jin (2006) which is presented in Table 3.5. Jin (2006) states that the profile is loosely based on sediment properties typical in Las Vegas Valley, Nevada and more specifically around conditions existing at the UNLV EGTS. The layer systems used for Models A through D can be seen in Table 3.6.

Model A host-material parameters represent the upper layer of native material at the EGTS (clayey sand, silty sand, and sandy gravel) described in the borehole logs (Figure 1.2). Models A and B (without and with cavity) have only one medium, for which the VR was calculated to be 184 m/s and the Poisson's ratio is 0.3 (This along with assigned VS fixes VP). Sharma (1997) states VP for dry sand alluvium between 300 m/s and 1000 m/s, and Burger (1992) states VP of unsaturated sand 200 m/s to 1000 m/s. The chosen VP of 370 m/s falls into these ranges.

Models C and D have two layers: 1) an upper layer with the same VP and VS as Model A; and 2) a buried layer representing the caliche at the EGTS. Stone and Luke (2001) tested the density and Poisson's ratio of cemented material cored at the EGTS. The density was found to be 2500 kg/m^3 and the Poisson's ratio was 0.23. Tecle et al. (2003) found the Poisson's ratio for a carbonate-cemented layer at 3.25 meter depth on the

EGTS to be 0.33 using a seismic downhole measurement. The difference between these two outcomes can be attributed to the fact that the sample tested in the lab was intact and very well cemented, while the field measurements would have been affected by discontinuities, a variable degree of cementation, and other heterogeneities occurring on the macro scale (Tecle et al. (2003) and personal communication, Barbara Luke 2013). Based on these test results, the density and Poisson's ratio of cemented soils for this study were set to 2200 kg/m^3 and 0.25, respectively.

Models E and F have a four-layer system: 1) an upper layer with the same VP and VS as Model A; 2) a buried layer representing the caliche at the EGTS with the same VP and VS as Model C; 3) a buried layer representing the material beneath the caliche at the EGTS; and 4) a halfspace. The Poisson's ratio for the uncemented layers below the water table (and below the cemented layer) was back-calculated to be 0.46. The uncemented layers have a gradually increasing VS of 200 m/s, 400 m/s, and 600 m/s which Jin (2006) selected as a normally dispersive profile. The four layer model seen in this research is similar to the HVL profile used by Jin (2006) where a HVL is inserted between the 200 m/s and 400 m/s layers of the normally dispersive profile.

The theoretical travel times were calculated using $t_p = d / VP$, $t_s = d / VS$, and $t_r = d / VR$, where t_p is the P-wave travel time, t_s is the S-wave travel time, t_r is the Rayleigh wave travel time, d is the straight-line distance between the source and receiver, and VR is the Rayleigh wave velocity. The theoretical travel times for reflected (scattered) energy were

calculated using $t_p = d_y / VP$, $t_s = d_y / VS$, and $t_r = d_y / VR$, where d_y is the distance from the source to the cavity plus the distance from the cavity to each receiver.

3.1.1.5 No Free Surface and Free Surface Models

A No Free Surface (NFS) synthetic model, created using E3D, is a two-dimensional model representing a completely buried space. E3D was used because when the NFS model was calculated in WPP the time histories had zero amplitude indicating a modeling error most likely caused by the change in boundary condition at the surface. The time history residual of the NFS model subtracted from Model B was computed but yielded spurious results (not shown). This is because the NFS model is two dimensional and created in E3D; whereas Model B is three dimensional and created in WPP. So in this case it would require subtracting two dimensional data from three dimensional data, which does not make sense (although it would make sense to subtract 2-D data from a vertical slice of the 3-D model). There are also differences in the way these two programs handle boundaries and the amount of delay needed in the time histories. In this research for data computed with E3D and WPP a delay (time shift) is applied to align the calculated arrival time at the first non-zero value of the Ricker wavelet (personal communication, Carlos Calderón-Macías, 2013). The magnitude of the shift needed depends on the frequency of the wavelet (personal communication, Carlos Calderón-Macías, 2013). The delay applied with WPP is negative 17 milliseconds (earlier in time) and with E3D is negative 6 milliseconds.

The NFS model allows computation of data that contain only body waves, which can be compared to a Free Surface (FS) model with the same material properties. The FS model allows body waves and surface waves to propagate, whereas the NFS model should allow only body waves. Thus, time histories and overtone images with and without surface waves can be compared. Residual time histories and overtone images can be created by subtracting the NFS data from the FS data. In theory, the residual contains only Rayleigh wave energy and body wave energy that results from Rayleigh scattering. The FS model is a 2-D replication of Model B which is 3-D. The main difference between the FS model and Model B is one is 2-D and one is 3-D. They have the same material properties, same receiver layout in *X* and *Z* direction, same source location in *X* and *Z* direction, same cavity location in *X* and *Z* direction, and same time parameters.

The NFS model is implemented to compare cavity detection with body waves versus detecting a cavity with surface waves as seen in Models B, D, and F. The NFS model has an absorbing boundary condition at all boundaries. It lacks a free surface boundary condition so surface waves will not propagate within the model. As mentioned previously, an absorbing-boundary layer is used to minimize the amplitudes of waves reflected from the artificial boundary (Engquist and Majda 1977). A Clayton and Engquist boundary condition (Clayton and Engquist 1977) is used as the absorbing boundary condition in the NFS and FS models.

In the NFS and FS models there are 2911 time steps at a time interval of 0.000343 seconds; therefore, the simulation lasts for 1 second total. The VP, VS, and density are chosen to match Model A and Model B. The cavity has the same dimensions, placement and material properties described earlier for models B and D. A 50-Hz Ricker wavelet source in the NFS and FS models is located three meters from the origin and one meter deep, which is the same distance as used for Models A, B, C, and D. The source, receiver and cavities locations can be seen in Figure 3.6 which displays the primary source location (also used in Models A, B, C, and D) in plan view. The setup for the two-dimensional NFS and FS models is displayed in Figure 3.7. Both of these figures are described further in the next section.

3.1.2 Models and Cavities Setup

Figure 3.6 displays the receiver and primary source location (used in Models A, B, C, and D) in plan view for the synthetic data computations. As stated previously, when comparing the model orientation to the EGTS experiment configuration, south is in the positive *X* direction and north is in the negative *X* direction. Point (0, 15, 0) in the figure refers to the origin in this research. (Refer to Fig. 3.1.) There is a cavity located 5 m from the first receiver, or 10 m from the *y*-axis of the models containing cavities (Models B, D and F). The second cavity of model F is located 15 m from the first receiver or 20 m from the *y*-axis. The cavity in Model B and D is located below receivers 16 and 17 at the same position described for the no-free-surface model. The cavities in Model F and F* are located below receivers 16 / 17 and 46 / 47.

The setup for the two-dimensional NFS and FS models is displayed in Figure 3.7. The *X* direction is in-plane with the receiver line, and the *Z* direction is positive downwards. The setup is the same as the mid-line (y=15 m) *X*-*Z* plane of the 3-D models (A through F). The NFS and FS models are the same dimensions in the *X* and *Z* direction as all other synthetic models in this research. There are the same number of vertical receivers and placed at the same locations as all other models in this research, distributed from (5, 0) to (28.7, 0). The grid spacing in the NFS and FS models is 0.25 m, compared to 0.20 m in the rest of the models. The NFS and FS models uses a source initiation time of 0.25 s. Both models have a cavity that is the same as Model B in the *X* and *Z* directions, with the same overburden. The properties of the host medium of the models are the same as for Model A.

3.1.3 Source Location and Parameters

A vertically-applied point force using a Ricker wavelet is the source in the synthetic models. The primary source location used for models A, B, C, and D is (3, 15, 1), that is 2.24 m straight-line distance from the first receiver which is located on the surface at (5, 15, 0). (Refer to Fig. 3.6.) In the primary source location setup (used in Models A, B, C and D) the source is inline with the receivers, whereas in the multiple source location setup (used in Models D, E, F, and F* and later described in section 3.2) the source is offset from the line of receivers by 0.5 m. This setup differs from the experimental data collected at the EGTS in that the source offset is only 0.2 m in the experiment. Similarly, the NFS and FS models used a source location of (3, 1), which is also 2.24 m from the first receiver which is located on the surface at (5, 0). All 3-D models (A through F) use

a forcing function that has model parameters of Fx=1, Fy=1, and Fz=1, where Fx, Fy, and Fz are the Cartesian components of the force vector which is scaled by the force amplitude. For the 2-D models, the source is applied at the corresponding location (3, 1) using a corresponding forcing function that has model parameters of Fx=1 and Fz=1. The source is applied at a depth of 1 m so it will not be directly on the surface, which reduces the chance for numerical instability (inaccuracy) caused by the boundary (personal communication, Carlos Calderón-Macías). Having the source location buried 1m also ensures most of the energy released from the source propagates through the synthetic model. Recall that Gelis et al. (2005) also buried the source 1 m in their numerical model.

3.1.4 Residual Calculation

Residuals are calculated for the following sets of time histories: Model A subtracted from Model B, Model C subtracted from Model D, Model E subtracted from Model F, Model C subtracted from Model E, and the NFS model subtracted from the FS model. The residual is used for direct observation of the difference caused by modifying a model, for example adding a cavity or a layer. To differentiate between effects of Rayleigh waves and body waves the NFS data is subtracted from the FS data. Creating a time histories residual such as this allows for filtering of the direct wave arrivals (e.g., Sloan et al. 2011). Residuals in the frequency domain are also calculated.

3.1.5 Overtone Images

Overtone images are generated by first performing a slant stack or frequency-slowness transformation followed by performing a fast Fourier transform on the data, where slowness is the inverse of phase velocity (Jin (2006), Luke and Calderón-Macías (2008)). In this research, the processing of these overtone images is completed using MATLAB. The results are plotted as an image that varies in color based on amplitude. The slant stack or frequency-slowness spectrum analysis from McMechan and Yedlin (1981) was used in this research, by using a MATLAB script written by Sacchi (2003). Jin (2006) describes slant stack as a process to stack traces by shifting them in time proportional to physical offsets of the sensors on the ground surface. The slant stack process differs from the frequency-wave number method; in the frequency-wave number method the record is translated from the time-space domain to the frequency-wavenumber domain by two successive applications of a one-dimensional fast Fourier transform algorithm (Jin 2006). After slant stacking, the data are transformed from the time domain into the frequency domain, where dispersion curves (DC) are imaged in the form of slowness as a function of frequency (Jin 2006). In the case of complex profiles such as the carbonate-cemented layer (caliche), multiple DCs may appear, demonstrating multi-modal wave propagation (e.g. Jin et al. 2009).

In the overtone images in this research, a dark blue color represents a zero amplitude value, and a dark red color represents a high amplitude value. The data were not normalized among overtone images in this research. A forward modeling algorithm from Rix and Lai (1998) called Surface Wave Modal Inversion (SWAMI) was used to

calculate dispersion curves, which were then superimposed upon the overtone images using MATLAB.

3.1.6 Cavity Characterization Parameter

The normalized energy distance (NED) cavity characterization parameter from Nasseri-Moghaddam et al. (2005) is tested in this research using synthetic models and experimental data. The NED parameter is calculated using the following equations given by the authors: $NED_z = \frac{E_z}{\max(E_z)}$, where $E_z = \sum_f |A_{f,z}|^2$. In these equations $|A_{f,z}|$ is the amplitude of the spectrum at frequency f for receiver z, E_z is the signal energy, and NED_z is the spectrum energy normalized to the maximum energy across the array. NED parameters range from zero through one and are dimensionless.

Nasseri-Moghaddam et al. (2006) correct the NED parameter for geometrical attenuation using a gain function. The gain function is defined as: $g_z = \sqrt{(d_z/d_1)}$ where g_z is the value of the gain function at the location of receiver z, d_1 is the distance of receiver number 1 from the source, and d_z is the distance of receiver number z from the source.

3.1.7 Signal to Noise Ratio

In this current study, signal attenuation was observed from time histories to determine the threshold signal-to-noise ratio needed for cavity detection. Determining the threshold signal to noise ratio is one goal of this research. It was found by comparing the

maximum amplitudes of time histories from synthetic models. Application-specific details are given in Section 4.7.

3.2 REPLICATING THE EXPERIMENTAL DATA

Currently, WPP does not allow a text file to be inputted as a source. This option is desirable because it would allow data from a real source collected at the EGTS to be used during model data computation. This current study used a 50-Hz Ricker wavelet and superimposed 25-Hz and 100-Hz Ricker wavelets. A 25 Hz and 100 Hz superimposed Ricker wavelet source was chosen for studying the EGTS using synthetic models with E3D, to match work by Jin (2006). A 50 Hz Ricker wavelet was later chosen to simplify the source used by reducing the range of input frequencies. To input real data collected in the field, such as from a hammer strike on the ground at the EGTS, deconvolution and then convolution must be used on the synthetic data that contains a Ricker wavelet source. Convolution is an operation of replacing each element of an input with a scaled output function; it is the mathematical equivalent to filtering, such as occurs naturally in the passage of seismic waves through the earth (Sheriff and Geldart 1995). Deconvolution is convolving with an inverse filter (Sheriff and Geldart 1995). The goal of the process of deconvolution and then convolution is to replace the Ricker wavelet source with a real hammer source. A time history from the EGTS that was collected during the test previously described was used in this process (Figure 3.8). This signal was collected using a sledge hammer source that was applied vertically on a steel plate placed on the ground surface. The signal was captured from the 31st vertical geophone, located at (15, 15, 0) using the fifth source location at (7, 15.5, 0), so the source-to-receiver

distance is 8.02 m. The 31st vertical geophone happened to be located directly above the steel drum at the EGTS. This time history was chosen because when compared to other time histories collected it appeared to have low noise. A drawback of using this time history for convolution is that it was not a direct hammer output; it was filtered by passing through the ground.

To deconvolve data, the time history for the Ricker wavelet source is first transformed to the frequency domain. Then, the Ricker wavelet dataset is divided with a power spectrum that well represents that Ricker wavelet data. So, a 50 Hz Ricker wavelet source in the frequency domain is divided by a 50 Hz power spectrum. Then, to convolve this synthetic dataset, the deconvolved dataset is multiplied with the power spectrum from the data to be convolved. In this case, that would be the power spectrum corresponding to the time history of Figure 3.8, shown in Figure 3.9. The data used in deconvolution and convolution need to have the same sample length and the same spacing between samples. If the datasets' length and spacing differ, then one dataset needs to be resampled in order to match.

The real source input was used to attempt to replicate the experimental data from the EGTS (Luke and Calderón-Macías 2008) as closely as possible. The convolved real source (CRS) input was used with Models E, F, and F* for comparison of results to the EGTS data. The location of the trace chosen for convolution is displayed in Figure 3.10.

Filtering consisted of performing a fast Fourier transform and then multiplying by the complex conjugate to calculate a power spectrum to find the predominant frequency of the time history; next, bandpass-filtering was applied using cutoff frequencies of 1 Hz, 3 Hz, 100 Hz, and 125 Hz. This effectively removes low (between 1 Hz and 3 Hz) and high frequencies (between 100 Hz and 125 Hz) which the finite difference code may not accurately compute (personal communication, Carlos Calderón-Macías). The cutoff frequencies were selected by comparing the power spectrums of the signals before and after deconvolution and convolution. The goal is to more-or-less match the power spectrums before and after the deconvolution / convolution process. A figure in the appendix displays the power spectrums of receiver number 10 from Model F and the time history used for deconvolution. Another figure in the appendix displays the power spectrums of receiver number 10 from Model F, Model F after deconvolution, and Model F after deconvolution with filtering. Another trial using bandpass filtering at 1 Hz, 3 Hz, 250 Hz, and 275 Hz yielded high frequencies that caused very large values in the output.

Figure 3.11 displays the receiver and source location for Models D, E, and F. Models D, E, and F use the same multiple source locations to emulate and study the EGTS experiment. The multiple-source location setup is the same as the single-source setup described in Figure 3.6 except for the addition of source locations which are offset from the receiver line by 0.5 m to emulate the locations used in the EGTS experiment. (However, recall that the model differs from the experimental data collected at the EGTS because the source is offset from the line of receivers by only 0.2 m in the experiment.) For the experiment, 30 source locations were used. The 29th and 30th source locations

were outside of the model's dimensions, at (31, 15.5, 1) and (32, 15.5, 1). The model would need to be increased to 33 meters in the *X* direction to include these source locations. The 28th source location at (30, 15.5, 1) resulted in time histories of zero amplitude, indicating a modeling error caused by the boundary. Therefore, in all, 27 source locations are used for creating stacks of overtone images, from source location (3,15.5,1) to source location (29, 15.5,1).

Figure 3.12 displays example vertical time histories from the EGTS experiment, from the fifth source location out of thirty source locations used. This source location is at (7, 15.5, 0). The total time of recording is 0.5 seconds. The signal used for convolution (Figure 3.8) was captured from the 31st geophone in Figure 3.12 (coordinate (15, 15, 0)).

Figure 3.13 displays another set of time histories from the EGTS, with the corresponding overtone image for the 30th source location (32, 15.5, 0). The buried drums are located beneath receiver number 31 and 61, as shown by red and blue lines in the time histories. The time histories display strong resonance. The direct arrival times would be challenging to pick and the scattered arrival times do not appear to be obvious enough to pick. The high amplitudes in the overtone image range in frequency from 28 Hz to 41 Hz and in velocity from 138 m/s to 194 m/s. The Rayleigh wave velocity of 184 m/s in the top layer falls in this range. Luke and Calderón-Macías (2008) report for both vertical and radial components, the highest amplitude in the overtone images corresponds to the fundamental-mode surface wave observed in the frequency range of approximately 40 to

120 Hz and a velocity range of approximately 125 to 300 m/s. So this example falls into this range for velocity, but is lower than expected in the frequency range. Luke and Calderón-Macías (2008) also observe effects of energy from other wave types, possible body waves and higher-mode and scattered energy in the overtone images from the EGTS. The time histories and overtone images from the EGTS experiments like those shown in the figure can be compared to the synthetic time histories and overtone images generated from the models in this research.

Figure 3.14 displays the stacks of overtone images created by Luke and Calderón-Macías (2008) from the EGTS experimental data, stacked according to velocity. Figure 3.15 displays the same dataset, stacked according to frequency. Receivers to the south of the source and receivers to the north of the source are summed separately, then all receivers are summed.

The methodology explained in this chapter is used to obtain results such as time histories, overtone images, and stacks of overtone images; which are presented in Chapters 4 and 5.

Table 3.1 Summary of synthetic model information for Model A, B, C, and D.

	Model A	Model B	Model C	Model D
Code Used	WPP	WPP	WPP	WPP
3D or 2D	3D	3D	3D	3D
Number of Receivers	72	72	72	72
Receiver Spacing (m)	0.33	0.33	0.33	0.33
Number of Source Locations	1	1	1	27
Source Run No. 1 Ricker Wavelets	25 & 100 Hz	25 & 100 Hz	25 & 100 Hz	25 & 100 Hz
Source Run No. 2 Ricker Wavelet	50 Hz	50 Hz	50 Hz	50 Hz
Source Run No. 3	N/A	CRS*	CRS*	N/A
Number of Layers Including Halfspace	1	1	2	2
Extent in x Direction (m)	30	30	30	30
Extent in y Direction (m)	30	30	30	30
Extent in z Direction (m)	20	20	20	20
Grid Spacing (m)	0.2	0.2	0.2	0.2
Total Time Steps Run No. 1	2911	2911	20973	20973
Total Time Steps Run No.2	2911	2911	10487	10487
Total Time Steps Run No. 3	N/A	4096	N/A	N/A
Time Interval (s) Run No. 1	0.000344	0.000344	0.000048	0.000048
Time Interval (s) Run No. 2	0.000344	0.000344	0.000048	0.000048
Time Interval (s) Run No. 3	N/A	0.000244	N/A	N/A
Total Run Time (s) Run No. 1	1	1	1	1
Total Run Time (s) Run No. 2	1	1	0.5	0.5
Total Run Time (s) Run No. 3	N/A	1	N/A	N/A
Number of Cavities	0	1	0	1
Cavity Depth (m)	N/A	0.97	N/A	0.97
Cavity Length (m)	N/A	30	N/A	30
Cavity Width (m)	N/A	0.53	N/A	0.53
Cavity Height (m)	N/A	0.53	N/A	0.53
Cavity VP (m/s)	N/A	330	N/A	330
Cavity VS (m/s)	N/A	30	N/A	30
Cavity Poisson's Ratio	N/A	0.4958	N/A	0.4958
Cavity Density (kg/m^3)	N/A	250	N/A	250
*CRS: convolved real source				

Table 3.2 Summary of synthetic model information for Model E, F, NFS, and FS.

	Model E	Model F	NFS Model	FS Model
Code Used	WPP	WPP	E3D	E3D
3D or 2D	3D	3D	2D	2D
Number of Receivers	72	72	72	72
Receiver Spacing (m)	0.33	0.33	0.33	0.33
Number of Source Locations	27	27	1	1
Source Run No. 1 Ricker Wavelets	25 & 100 Hz	25 & 100 Hz	N/A	N/A
Source Run No. 2 Ricker Wavelet	50 Hz	50 Hz	50 Hz	50 Hz
Source Run No. 3	CRS*	CRS*	N/A	N/A
Number of Layers Including Halfspace	4	4	1	1
Extent in x Direction (m)	30	30	30	30
Extent in y Direction (m)	30	30	N/A	N/A
Extent in z Direction (m)	20	20	20	20
Grid Spacing (m)	0.2	0.2	0.2	0.2
Total Time Steps Run No. 1	20973	20973	2911	2911
Total Time Steps Run No.2	10487	10487	N/A	N/A
Total Time Steps Run No. 3	16384	16384	N/A	N/A
Time Interval (s) Run No. 1	0.000048	0.000048	0.000343	0.000343
Time Interval (s) Run No. 2	0.000048	0.000048	N/A	N/A
Time Interval (s) Run No. 3	0.000031	0.000031	N/A	N/A
Total Run Time (s) Run No. 1	1	1	1	1
Total Run Time (s) Run No. 2	0.5	0.5	N/A	N/A
Total Run Time (s) Run No. 3	0.5	0.5	N/A	N/A
Number of Cavities	0	2	1	1
Cavity Depth (m)	N/A	0.97	0.97	0.97
Cavity Length (m)	N/A	30 and 0.9	N/A	N/A
Cavity Width (m)	N/A	0.53	0.53	0.53
Cavity Height (m)	N/A	0.53	0.53	0.53
Cavity VP (m/s)	N/A	330	330	330
Cavity VS (m/s)	N/A	30	30	30
Cavity Poisson's Ratio	N/A	0.4958	0.4958	0.4958
Cavity Density (kg/m^3)	N/A	250	250	250
*CRS: convolved real source, NFS: No Free Surface, FS: Free Surface				

Table 3.3 Summary of tests to select density of cavity for modeling with WPP.

V_s of cavity (m/s)	ρ of cavity (kg/m^3)	Test result
0	1.2	fails to run
1	1.2	fails to run
10	1.2	fails to run
100	1.2	fails to run
200	1.2	fails to run
200	100	fails to run
200	175	fails to run
200	200	fails to run
225	200	fails to run
200	1000	works
200	500	works
200	250	works
100	250	works
10	250	works
1	250	works

Table 3.4 Comparison of cavity density versus typical densities of soils.

		Dry Density Minimum (kg/m^3)	Dry Density Maximum (kg/m^3)
This research	Cavity	250	
This research	Density of host medium	1700	
Budhu (2000)	Gravel	1531	1735
Budhu (2000)	Sand	1327	1633
Budhu (2000)	Silt	1429	1837
Budhu (2000)	Clay	1429	2143
Das (2002)	Loose uniform sand	1480	1480
Das (2002)	Soft clay	1173	1480
Das (2002)	Loess	1378	1378
Das (2002)	Soft organic clay	612	816

Table 3.5 Layer configuration from Jin (2006).

Soil Profile from Jin (2006)					
Layer Number	Thickness	Density	P Wave Velocity	S Wave Velocity	Poisson's Ratio
#	m	kg/m^3	m/s	m/s	
1	2	1700	370	200	0.3
2	1.5	2200	2600	1500	0.25
Water Table					
3	4	1700	1500	400	0.46
Halfspace		1700	2200	600	0.46

Table 3.6 Layer configurations used for WPP soil profiles.

Model A and B Soil Profile					
Layer Number	Thickness	Density	P Wave Velocity	S Wave Velocity	Poisson's Ratio
#	m	kg/m^3	m/s	m/s	
1	20	1700	370	200	0.3

Model C and D Soil Profile					
Layer Number	Thickness	Density	P Wave Velocity	S Wave Velocity	Poisson's Ratio
#	m	kg/m^3	m/s	m/s	
1	2.4	1700	370	200	0.3
2	17.6	2200	2600	1500	0.25

Model E and F Soil Profile					
Layer Number	Thickness	Density	P Wave Velocity	S Wave Velocity	Poisson's Ratio
#	m	kg/m^3	m/s	m/s	
1	2.4	1700	370	200	0.3
2	2.2	2200	2600	1500	0.25
Water Table					
3	2.9	1700	1500	400	0.46
Halfspace		1700	2200	600	0.46

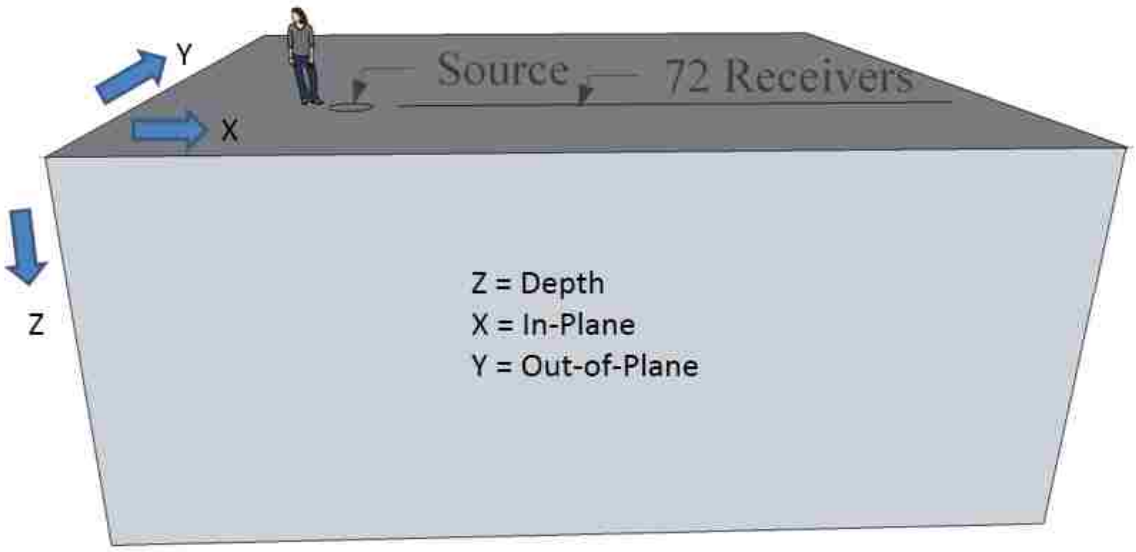

Figure 3.1 Synthetic models: describing experiment configuration and *X*, *Y*, and *Z* directions for all models. The coordinate origin is at (0, 15, 0) in this research which is at the center of the *Y* axis and the origination of the *X* and *Z* axis.

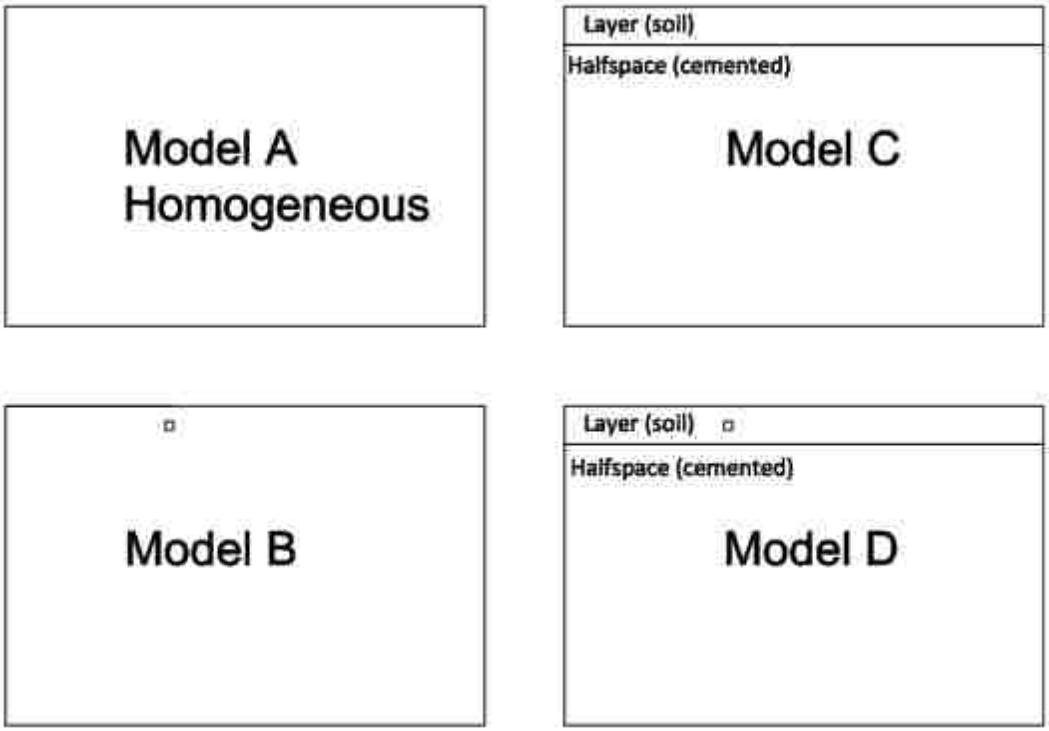

Figure 3.2 Task #1: *X* direction (in-plane of test array) cross sections of 3-D models used for sensitivity studies (Model A, Model B, Model C, and Model D). Layers and cavities drawn to scale (horizontal width = 30 m) where 1 in.=12 m.

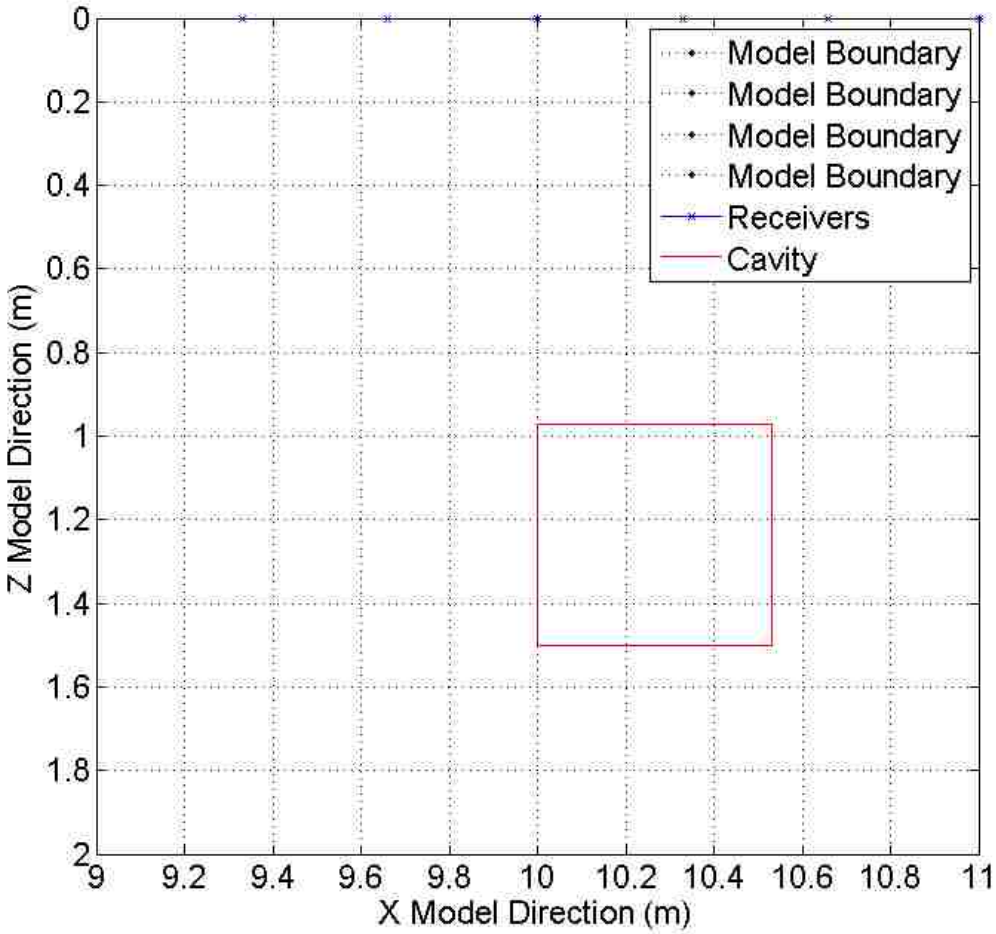

Figure 3.3 Cross sectional view of cavity location. Grid illustrates 0.2-m grid spacing of the model.

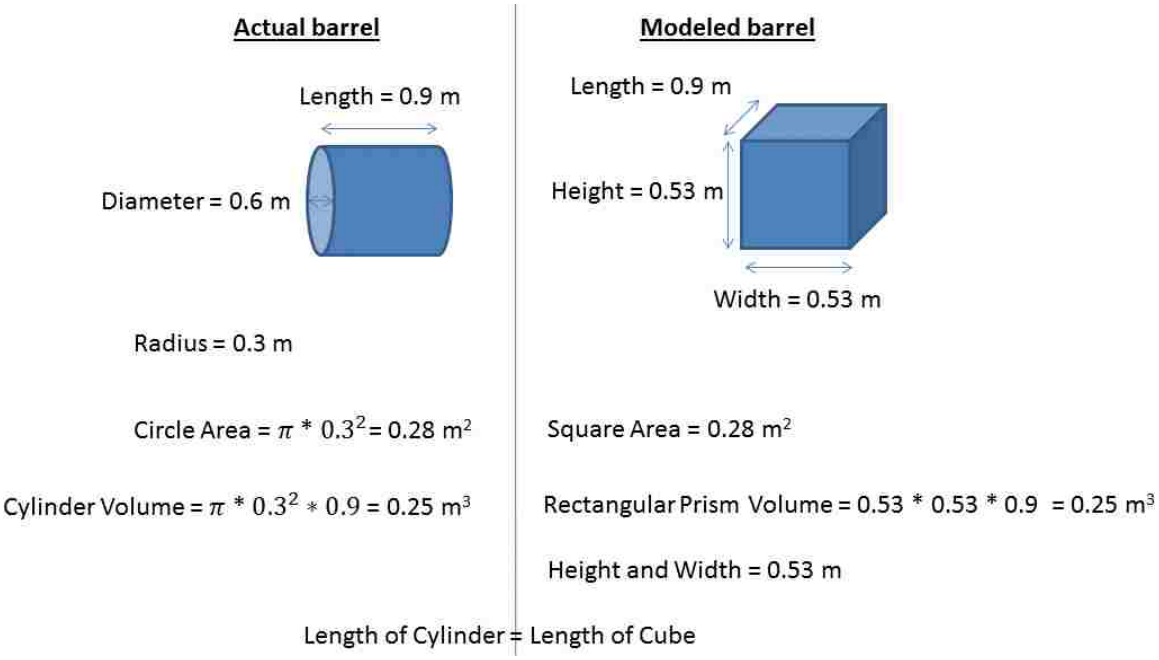

Figure 3.4 Calculation for cavity size.

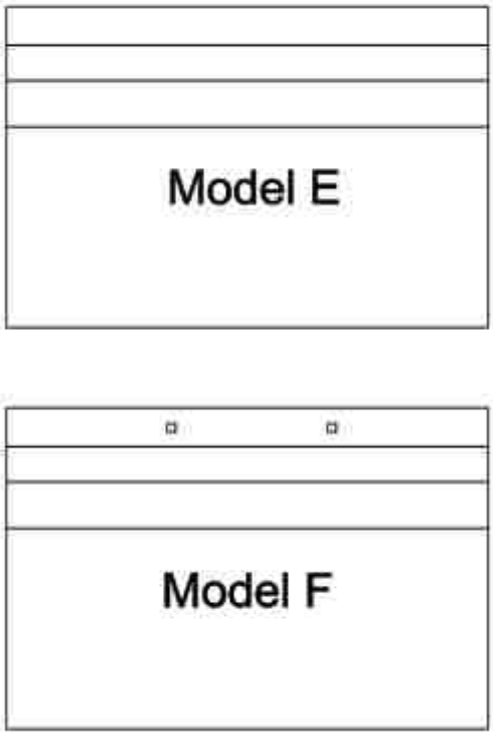

Figure 3.5 Task #2: *X* direction sections of 3-D models created to replicate the experimental data (Model E and Model F). Layers and cavities drawn to scale (horizontal width = 30 m) where 1”=12 m.

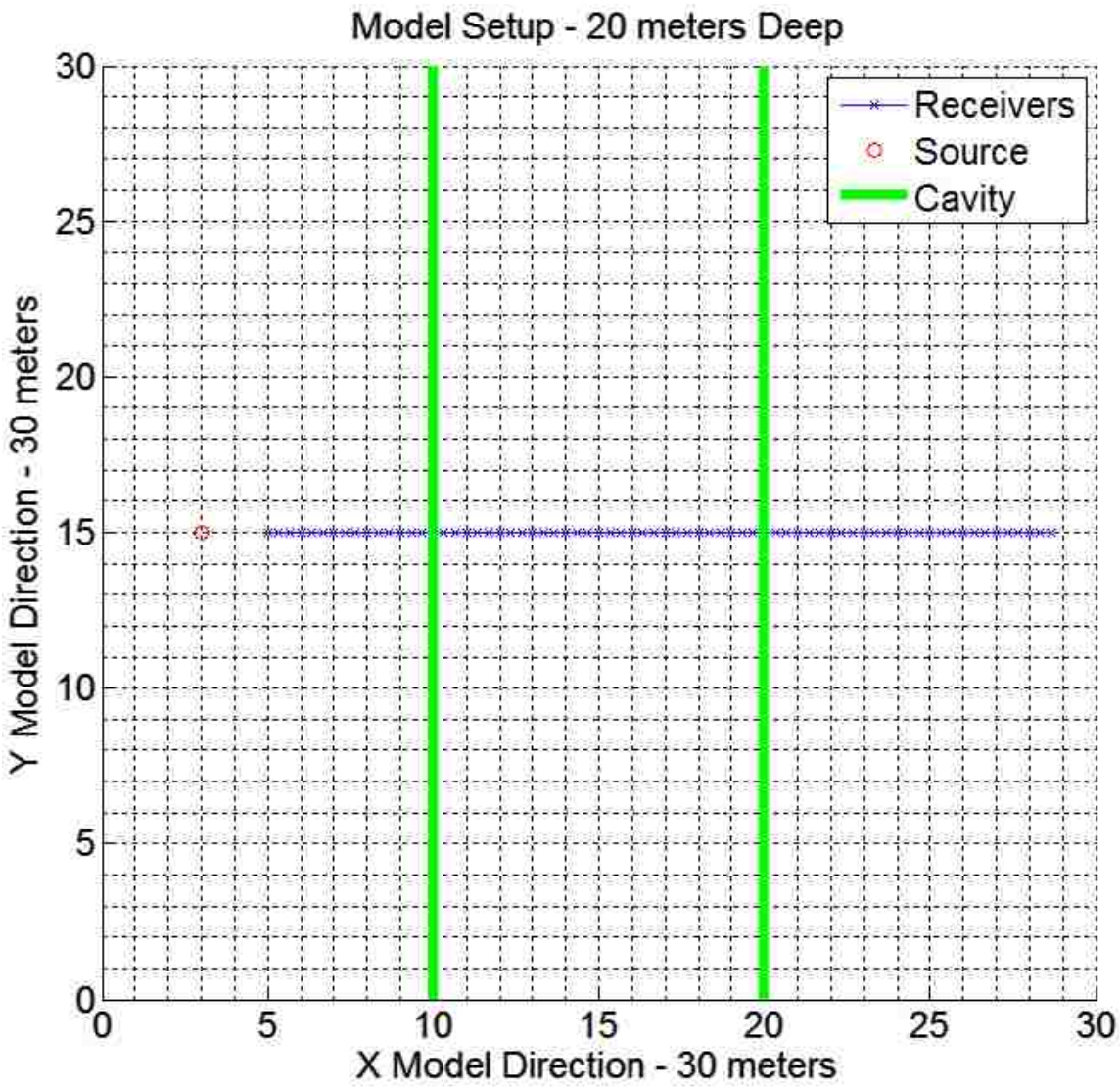

Figure 3.6 Plan view of synthetic model setup showing the primary source location which is used in Models A, B, C, and D. Point (0, 15, 0) refers to the origin in this research. Only Model F contains the cavity at x = 20 m.

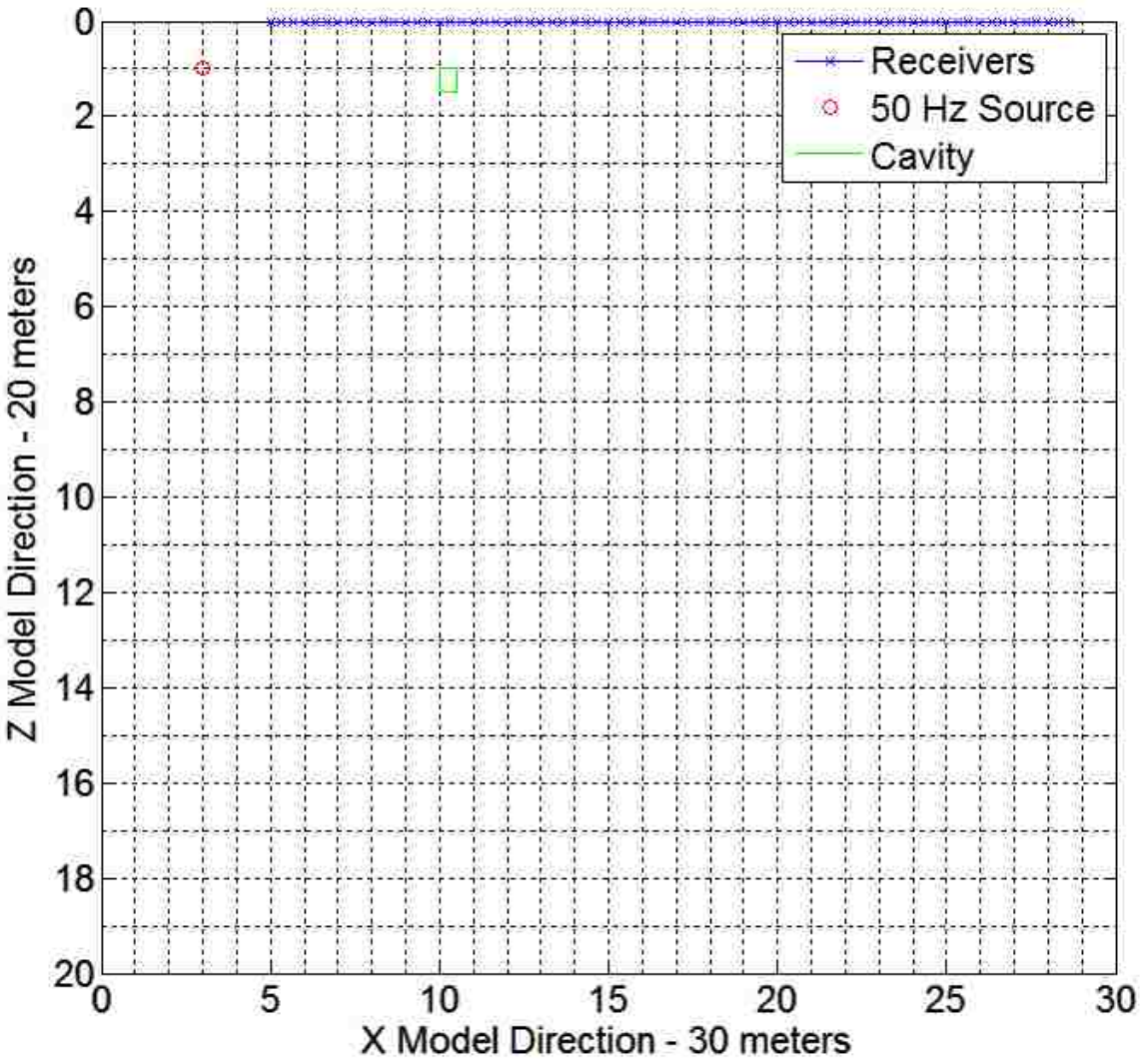

Figure 3.7 The no free surface (NFS) and free surface (FS) models setup using E3D.

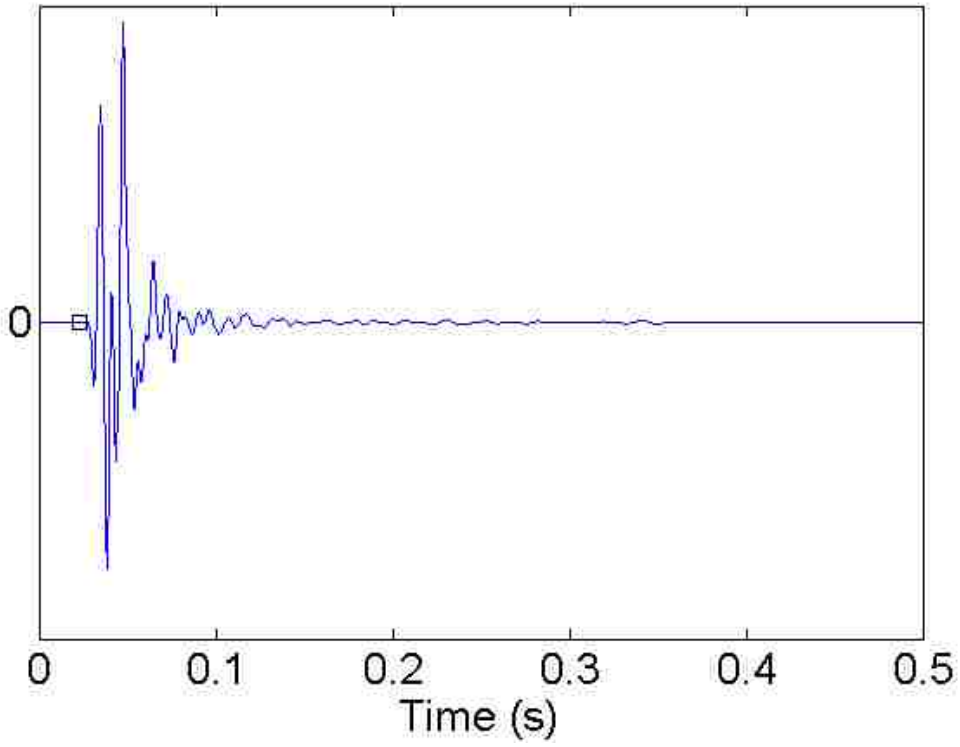

Figure 3.8 Time history used for convolution from a hammer source applied on an aluminum plate placed on the surface at UNLV's Engineering Geophysics Test Site (EGTS). The black square symbol is the picked P-wave arrival time at 0.0235 seconds.

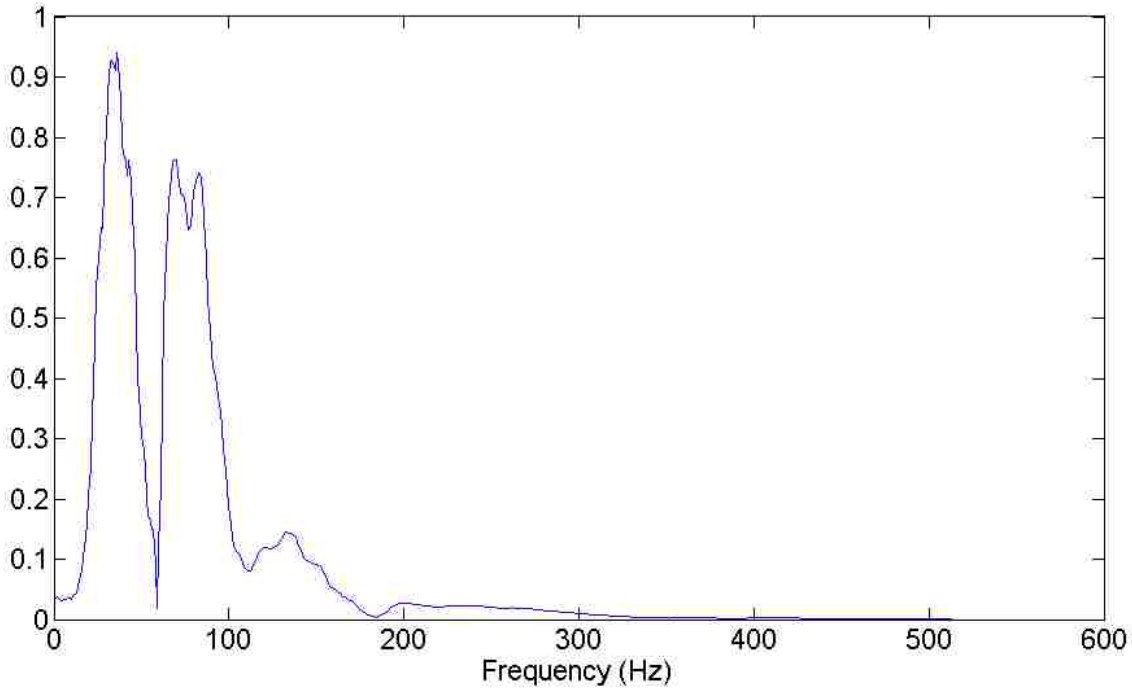

Figure 3.9 Normalized frequency spectrum of hammer blow recorded on the EGTS. Created from the time history in Figure 3.8.

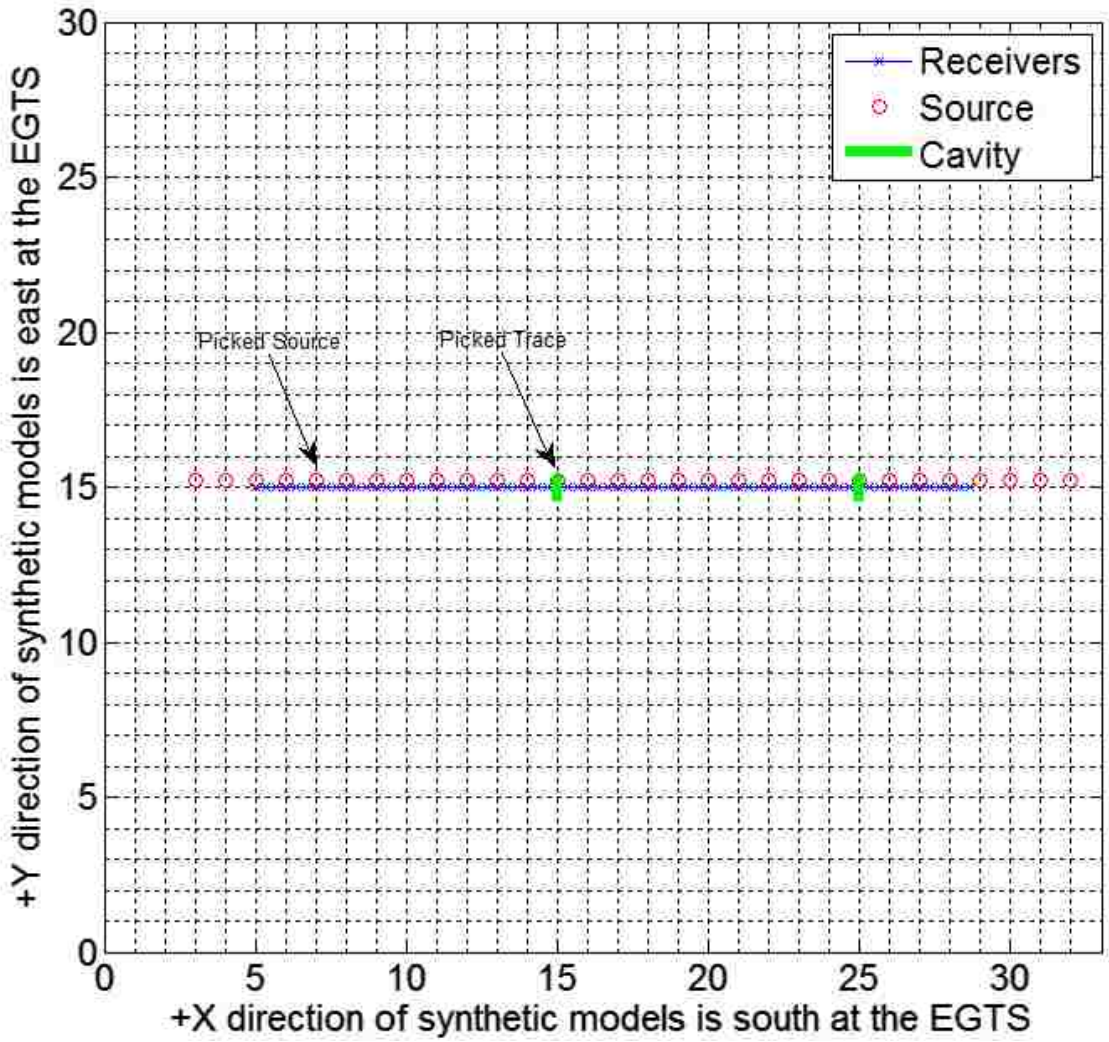

Figure 3.10 Setup of experimental data (EGTS) collection when compared to the synthetic models with the location of the trace picked for real source convolution. The 31st receiver with the 5th source location (red circle; (7, 15.2, 0)) is the picked trace for convolution.

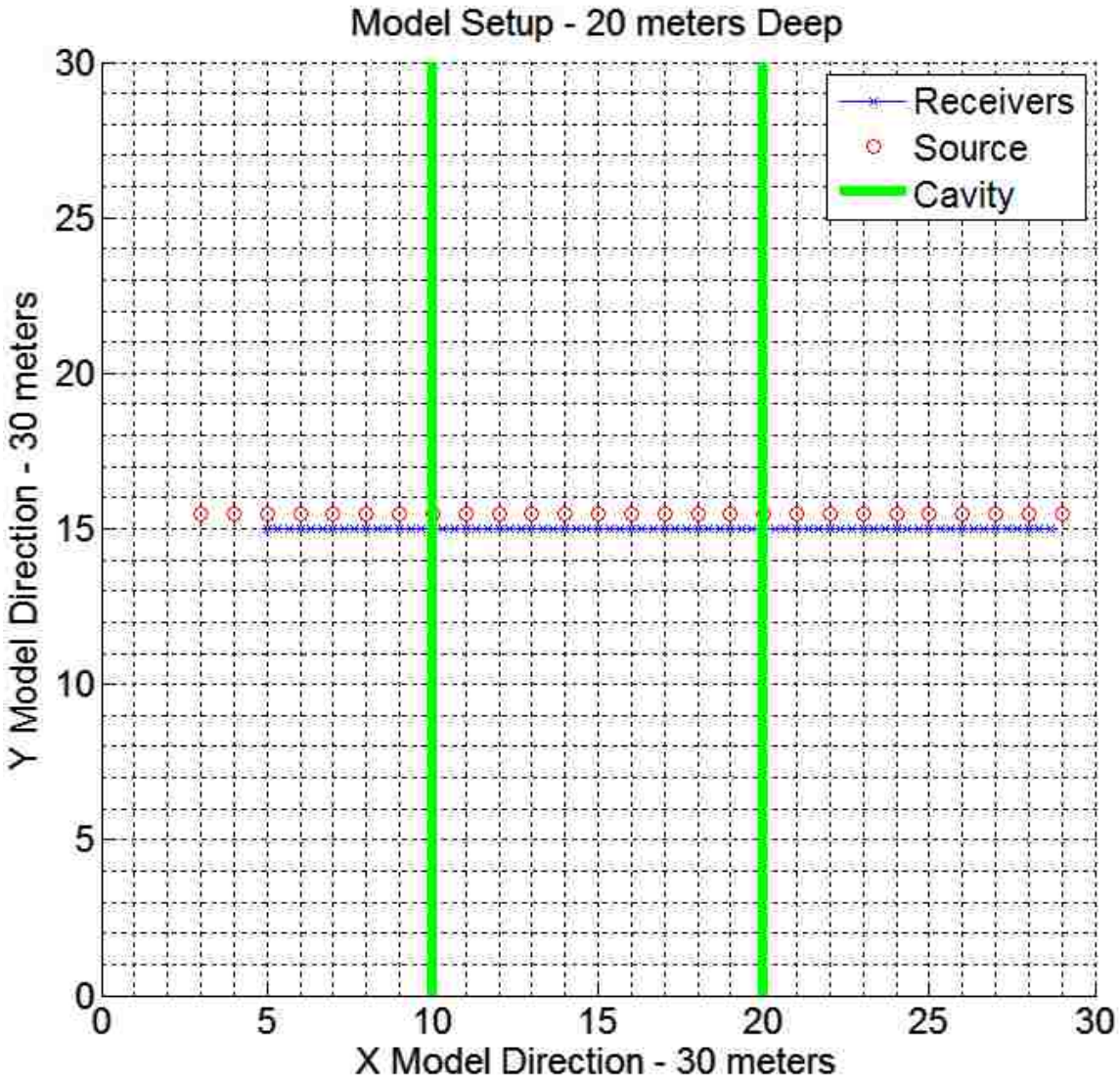

Figure 3.11 Plan view of synthetic model setup showing multiple source locations used in Models D, E, and F.

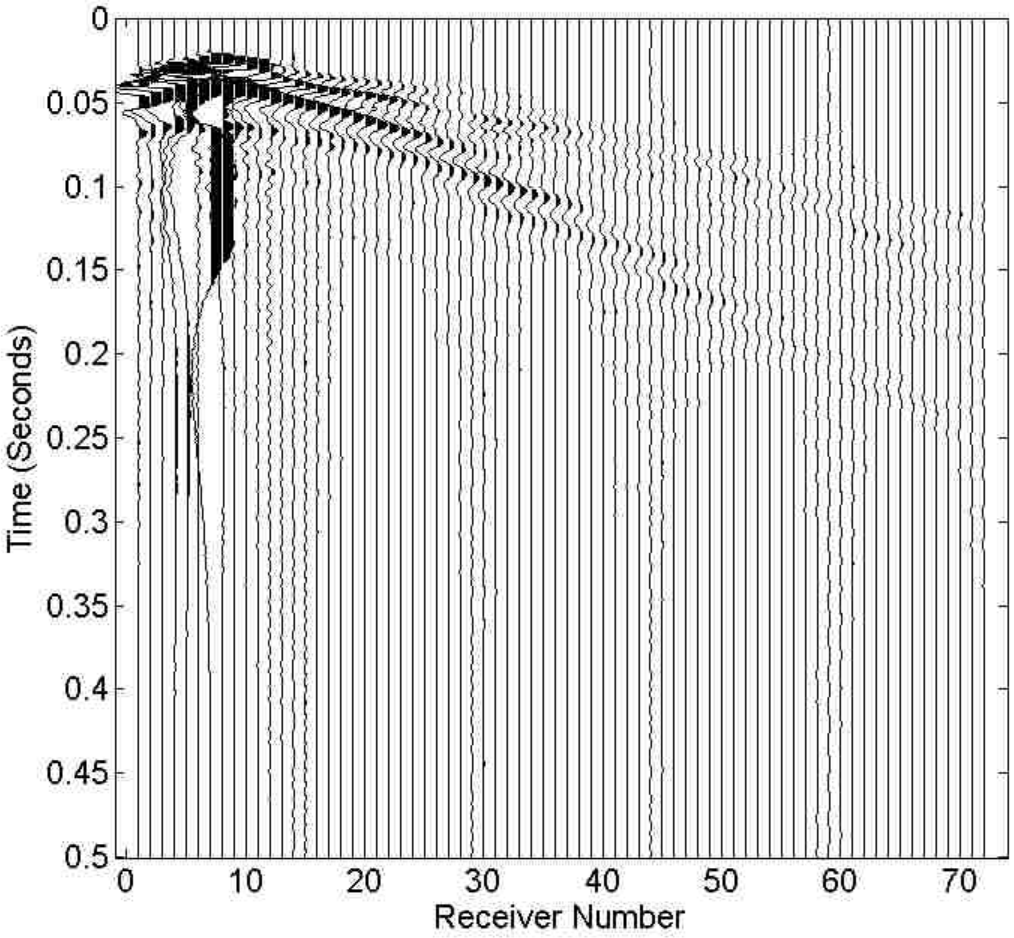

Figure 3.12 Example EGTS experiment time histories, displaying vertical sensors for source location 5 out of 30. Source coordinates are (7, 15.2, 0).

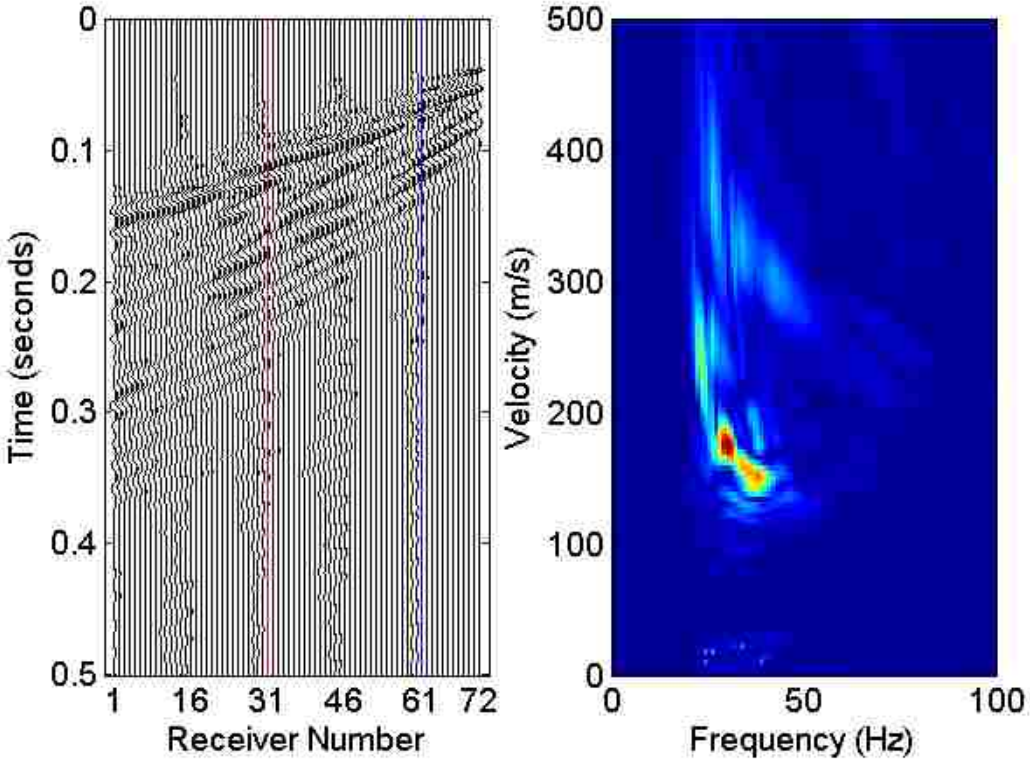

Figure 3.13 Example of a set of EGTS time histories and the corresponding overtone image. Red line indicates steel barrel, blue line indicates plastic barrel. Source location 30 (out of 30 source locations). Source coordinates are (32, 15.2, 0).

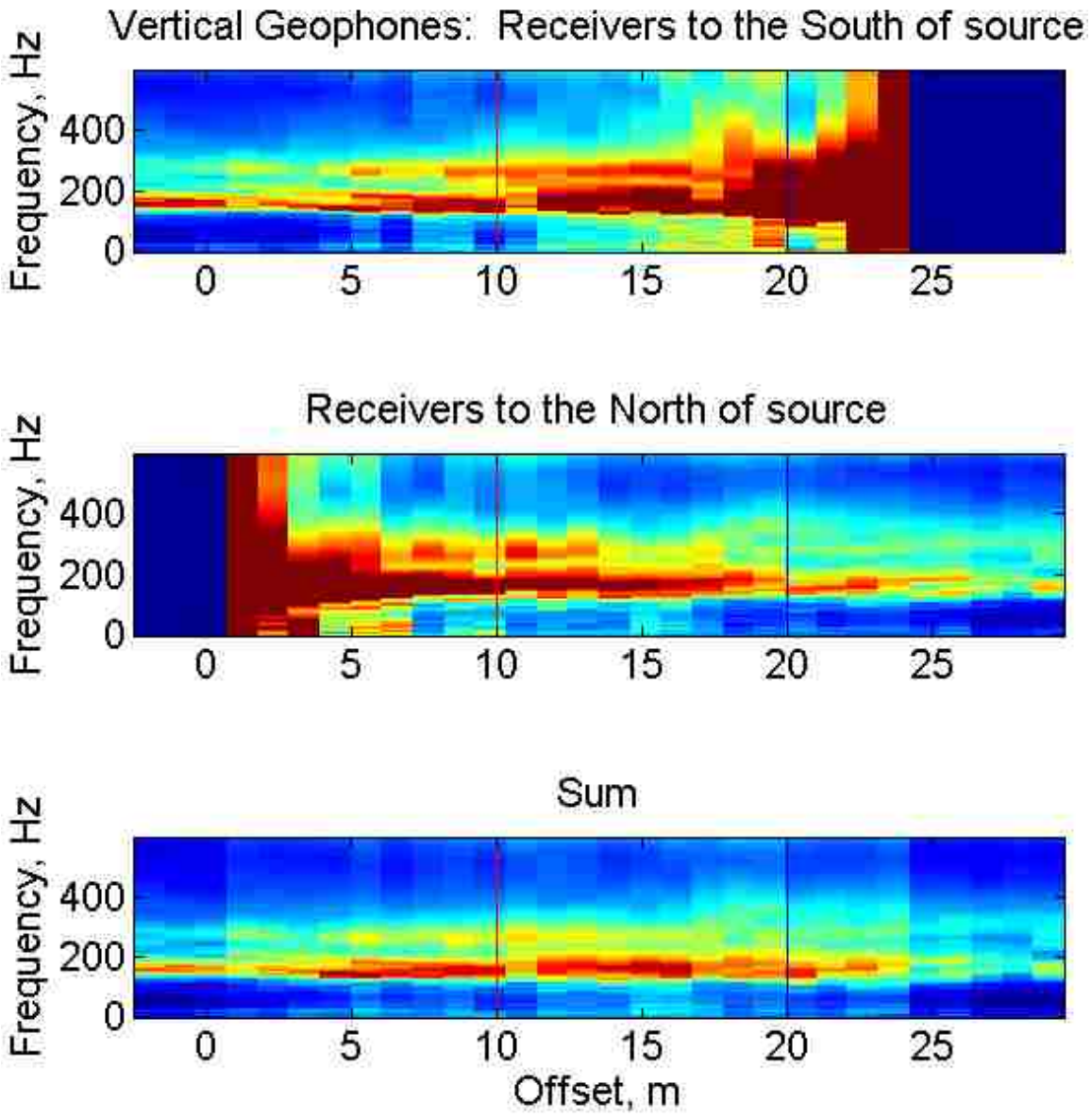

Figure 3.14 Stack of overtone images according to velocity from the EGTS (Luke and Calderón-Macías (2008)). Locations of steel and plastic barrels are indicated by red and blue lines, respectively.

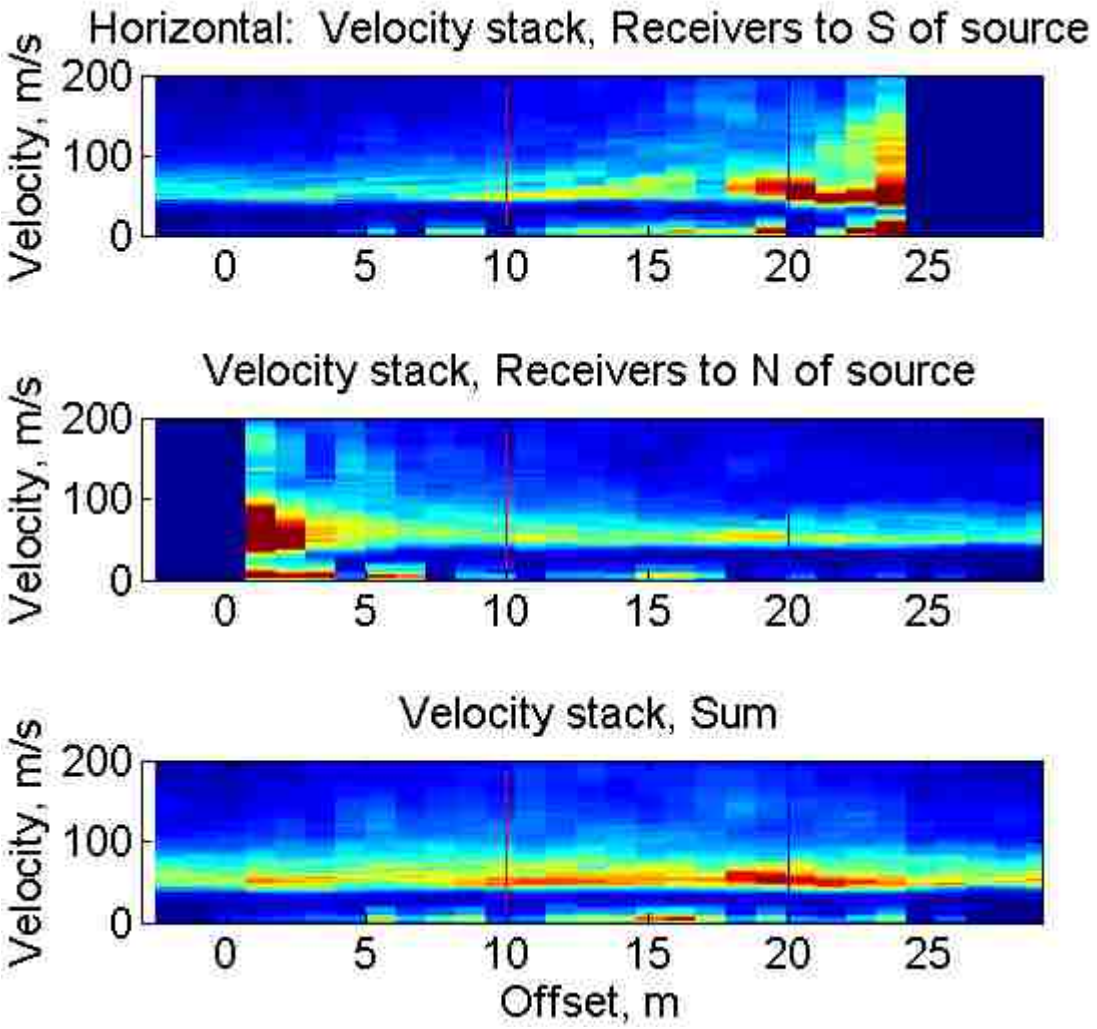

Figure 3.15 Stack of overtone images according to frequency from the EGTS (Luke and Calderón-Macías (2008)). Locations of steel and plastic barrels are indicated by red and blue lines, respectively.

CHAPTER 4 FINDINGS OF THE SYNTHETIC STUDY

This chapter contains results from the tests conducted using the No Free Surface (NFS) model, the Free Surface (FS) model and models A, B, C, and D. Analysis products include time histories, overtone images, stacks of overtone images, a comparison of maximum amplitudes of time series, the cavity characterization parameter of normalized energy-distance (NED), and power spectrums.

In models A and B the source is initiated at 0.25 s and data were computed for 1 s total. For the rest of the models, starting with Model C, the source is initiated at 0.1 s and the data were computed for 0.5 s total. Recall that the NFS model and FS model are two dimensional, 30 m in the *X* direction and 20 m in the *Z* direction (refer to Figure 3.7 for model configuration and orientation) and models A, B, C, and D are three dimensional, 30 m in the *X* direction, 30 m in the *Y* direction, and 20 m in the *Z* direction. A superimposed 25 Hz and 100 Hz Ricker wavelet was used initially, based on successful results with similar modeling techniques by Jin (2006), then a 50 Hz Ricker wavelet was used to simplify the source by removing one Ricker wavelet and choosing a single central frequency. All time histories and overtone images presented use the 50 Hz Ricker wavelet source, however, as will be explained later, the superimposed 25/100 Hz Ricker wavelet source was used to compute the NED parameter. All time histories presented in this research are in the vertical direction, except for one comparison of time histories in the vertical and horizontal directions. In all three-dimensional models' time histories receiver number 1 is located at (5, 15, 0) and the last receiver, number 72, is located at (28.7, 15, 0) (refer to Figure 3.6). Similarly, in all two-dimensional models' time

histories, receiver number 1 is located at (5, 0) and receiver number 72 is located at (28.7, 0) (refer to Figure 3.7).

4.1 THE NO FREE SURFACE (NFS) MODEL AND THE FREE SURFACE (FS) MODEL

The time histories and overtone images from the No Free Surface (NFS) model and the Free Surface (FS) model are used as a starting point for comparison with Models A and B. The time histories and overtone image from the NFS models are compared against one another.

The time histories for the NFS model, the FS model and their residual are presented in Figure 4.1, Figure 4.2, and Figure 4.3 respectively. The NFS model should contain only body waves and not surface waves, since the model does not contain a free surface. The cavity is located beneath receiver numbers 16 and 17. The calculated arrival times for direct and reflected P- and S- waves are overprinted. The calculated arrival times are shifted by a 6 millisecond (0.006 second) positive delay (later in time). The time shift is found by comparing the calculated time to the time found with the earliest non-zero amplitude in the first trace.

Scattered body waves, most likely to be primarily S-type, due to interaction with the cavity, are seen on traces 1 through 16. The P and S wave arrivals are consistent with the modeled velocities. The effect of the cavity is seen in the time histories (scattered

waves); therefore, the cavity is readily detected with body waves, in a homogenous, noise-free medium and in the absence of surface waves.

The time histories of the FS model are displayed in Figure 4.2. The cavity location and the overlaid calculated arrivals are as described for Figure 4.1, with additional curves for theoretical Rayleigh wave arrivals (direct and reflected). Scattered waves, due to interaction with the cavity, are again seen on traces 1 through 16. The wave arrivals are consistent with the modeled velocities. The effect of the cavity is seen in the time histories (scattered waves); therefore, the cavity can be detected by the combined field of surface waves and body waves. The effect of the cavity is more pronounced with the FS model than the NFS model, indicating that the Rayleigh waves are valuable for cavity detection. The maximum amplitude of the NFS model is about 41% higher than that of the FS model (2.6230e-017 versus 6.3620e-017). Reflections from incident body wave energy are obscured by surface wave energy. This limits their direct usefulness for cavity detection; however, they contribute to the rise in energy (amplitude) between the source and the cavity. This contribution appears to be of secondary importance with respect to the scattering resulting from the incident Rayleigh wave energy.

The residual time histories of the NFS model subtracted from the FS model are displayed in Figure 4.3. The cavity location and the overlaid theoretical arrival times are as described for Figure 4.2. Again, scattered waves, due to interaction with the cavity, are seen on traces 1 through 16. The Rayleigh wave arrivals are consistent with the modeled

velocities. The effect of the cavity is seen in the time histories (scattered waves); therefore, the cavity can be detected with only surface waves.

The overtone image created from the NFS model time histories (Figure 4.1) is displayed in Figure 4.4. How overtone images were calculated was described in chapter 3. A black, horizontal line with 'X' markers represents the model's VS, which lies at the velocity of 200 m/s. The low-frequency cutoff for the VS line was chosen as 25 Hz. The energy in the NFS model overtone image lines up with the VS as expected.

The overtone image created from the FS model vertical direction time histories (Figure 4.2) is displayed in Figure 4.5. A black line with circle markers represents the Rayleigh wave velocity, which forms a horizontal line at the velocity of 184 m/s, again with low-frequency cutoff at 25 Hz. The energy in the FS model overtone image lines up with the Rayleigh wave velocity as expected.

The residual overtone image created by subtracting the NFS model from the FS model time histories (Figure 4.3) and then creating an overtone image from the data is displayed in Figure 4.6. A black line with 'X' marker symbols represents the Rayleigh wave velocity, which forms a horizontal line at the velocity of 184 m/s, starting at 25 Hz. The energy concentration lines up with the Rayleigh wave velocity. The field is otherwise relatively clear, indicating that only Rayleigh waves are present. The residual overtone image appears almost identical to the FS model overtone image, which confirms that the

wave field is dominated by Rayleigh wave energy. The residual overtone image presented in the figure is the same type as the 'differential image' presented by Gelis et al. (2005).

4.2 MODEL A – HOMOGENEOUS MODEL OF SOIL

Figure 4.7 displays the theoretical first arrival times with the time history for the first receiver in the array in Model A. The source starting time in Model A is 0.25 s. The figure displays how direct arrival times for the Ricker wavelet appear in the wavetrain; this pattern is expected in all time histories presented in this chapter. The P-wave arrival time was calculated to be 0.2560 s, the S-wave arrival time was calculated to be 0.2612 s, and the Rayleigh-wave arrival was calculated to be 0.2622 s. The calculated arrival times are shifted by a 17-millisecond (0.017 second) negative delay (earlier in time) in all figures for Models A, B, C, D, E and F. All calculated arrival times and source starting times reported in this thesis are before the 17-millisecond negative delay is added.

Figure 4.8 displays the power spectrum corresponding to the time history in Figure 4.7. The maximum amplitude is approximately 50 Hz, as is expected for a 50 Hz Ricker wavelet source pulse. Separating the arrival times of the three waves is not possible at such a short offset; the body and surface waves interact and that produces a distortion of the wavelet (a phenomenon known as near-field effect (e.g., Yoon and Rix (2006)). This makes picking of all but the first arrival at near offset impossible. The situation improves with increasing distance from the source. Because the shear and Rayleigh waves travel at

a similar velocity, it is not expected to see a clear separation between those two, especially at small offsets. The time history and theoretical first arrival times for the last receiver in the array in Model A are displayed in Figure 4.9. The straight-line distance between the source and the receiver is 25.68 m. The P-wave arrival time was calculated to be 0.3194 s. There is more separation between the waves in the last receiver than the first receiver. The S-wave arrival time was calculated to be 0.3784 s. The Rayleigh wave arrival time was calculated to be 0.3895 s. The P-wave arrival appears as expected at the first non-zero amplitude in the trace. The S-wave arrival appears at the start of the second excursion. The Rayleigh wave arrival appears partially down the first sidelobe of the second Ricker wavelet shape, making its arrival indistinguishable. It is still impossible to distinguish between the S-wave arrival and the Rayleigh wave arrival at the last receiver, even though they are more separated in time than at the first receiver.

The time histories for Model A are displayed with the theoretical first arrival times in Figure 4.10. The time history plots for Model A have clipping turned on and the amplitudes are multiplied by 50 to make the arrivals easier to identify. The theoretical arrival times were calculated as described above. The time histories form linear wave arrival patterns. In Model A's time histories, the P-wave arrives first; the larger excursion after that is the S-wave arrival, and last to arrive is the Rayleigh wave, matching the overprinted theoretical arrival times. There is a reflection starting at approximately 0.4 s at the last receiver in the time histories; these waves have reflected off the boundary in the synthetic model. The plot was truncated to display only data recorded from 0.2 s to 0.45 s.

There was no cavity or other heterogeneity in Model A; its time histories display only direct transmission of P-, S-, and Rayleigh waves. Therefore, there are no scattered wave arrivals in Model A except for the boundary reflection. The boundary conditions appear to be functioning adequately. S-waves and Rayleigh waves have larger amplitudes than P-waves, so it is easier to see the S-waves and Rayleigh waves in the time histories than the P-waves. The difference in amplitudes is explained by how much energy each wave contains when compared to each other: according to Richart et al. (1970) the wave field generated by a circular footing undergoing vertical oscillations at the surface of a homogeneous half-space distributes as follows: the Rayleigh wave contains 67% of the total energy released, the S-wave contains 26% of the total energy released, and the P-wave contains 7% of the total energy released. Amplifying the signal increases capability to identify the arrival of the P-waves.

The overtone image created for Model A is displayed in Figure 4.11. In this figure, the calculated Rayleigh wave velocity is overprinted. This value is 188 m/s, forming a horizontal line. This is the expected result from Model A since the model contains a homogeneous medium. The theoretical dispersion curve matches the overtone image from approximately 25 Hz to 100 Hz, with the highest amplitudes centered around 50 Hz. This makes sense since a 50 Hz Ricker wavelet was used as source. Only fundamental-mode energy is expected, however some evidence of higher mode energy is seen in light blue color.

4.3 MODEL B – SINGLE-LAYER MODEL INCLUDING CAVITY

Figure 4.12 displays time histories from Model B with the anticipated arrival times added. The FS model time histories and overtone image (Figure 4.2 and Figure 4.5) are almost identical to Model B's (Figure 4.12 and Figure 4.13), which indicates that 2-D modeling is sufficient for the pipeline/tunnel case studied. However for more complex cavity shapes and sizes 3-D modeling may lead to better accuracy; different cavity sizes are compared with model F and model F* in Chapter 5.2.

Comparing Model A's time histories in Figure 4.10 to Model B's time histories in Figure 4.12, the effect of adding a cavity to the model can be seen. Scattered wave arrivals produced from the cavity in Model B's time histories are seen, considering matches to computed arrival times for scatterers (blue lines), but only direct wave arrivals in Model A's time histories are seen indicated by computed direct arrival times (red lines). As shown earlier with the FS/NFS models, the observed scattered wavefield enables identification of a cavity in the otherwise homogeneous model. The largest amplitudes in the time histories that are caused by the cavity occur after the incidence of the Rayleigh wave on the cavity. In other words, the most visible scattered waves in the time histories are attributable to the Rayleigh waves whose energy dominates the incident signal. The time histories from Model B display a similar pattern to the synthetic time histories presented by Sloan et al. (2011) and Sloan et al. (2012) which are reviewed in Section 2.2 (both demonstrate scattering of energy produced from the cavity).

The time histories residual of Model A subtracted from Model B with calculated arrival times added is displayed in Figure 4.14. The computed arrival times shown in Model B's time histories are repeated to facilitate comparison. The cavity is located at the earliest wave arrival, under receivers 16 and 17. The time histories in the figure show a wave pattern that forms an arrow when the time arrivals are traced. The arrow points at the location of the cavity. The figure is truncated in time the same way as Model B's time histories.

The overtone image created for Model B is displayed in Figure 4.13. Models A and B have the same Rayleigh wave velocity. The difference between Model A and Model B is difficult to determine when looking at the overtone images, but can be seen by plotting the residual overtone image of Model A data subtracted from Model B data (Figure 4.15). The true Rayleigh wave velocity is shown in the frequency range 25 to 100 Hz, where the highest amplitudes are located. The image demonstrates that the difference between the models is greatest in the frequency range 40 to 100 Hz. In other words, the effect of the cavity is greatest in this frequency range.

4.4 MODEL C – TWO LAYER MODEL WITHOUT CAVITY

The time histories from Model C with calculated arrival times added are displayed in Figure 4.16. Model C's time histories displays resonance and dispersion caused by the strong impedance contrast. The amplitude of the resonance pulses with respect to the

initial pulses is large. The resonance is masking the wavetrain needed to detect cavity location. Dispersion is seen in the time histories as an initial sharp pulse at the first receiver that broadens and separates from the P-wave arrival towards the last receiver.

The overtone image created for Model C is displayed in Figure 4.17. The calculated fundamental mode and first higher mode dispersion curves are overprinted. In contrast to the time domain data which are dominated by resonances, the overtone plot is clear. At 36 Hz, the first higher mode dispersion curve almost intersects the fundamental mode dispersion curve. The complexity of the layered system has increased the complexity of the theoretical dispersion curve and overtone image. It would be possible to correctly hand-pick the fundamental- mode dispersion curve between 60 Hz and 100 Hz, but in the range of 40 Hz through 60 Hz hand-picking would lead to values that are too high. No picks can be made below 40 Hz. The first higher order mode dispersion curve would not be possible to pick in any frequency range.

4.5 MODEL D – TWO LAYER MODEL INCLUDING CAVITY

The time histories from Model D, with calculated arrival times added, are displayed in Figure 4.18. The time histories for Model D again display resonance caused by the added caliche layer. A cavity cannot be identified without filtering because its effects are masked by the resonance. Comparing time histories for Model C to Model D, it is difficult to see the effect caused by the added cavity.

The time histories residual of Model C subtracted from Model D, with calculated arrival times superimposed, is displayed in Figure 4.19. The amplitudes in the figure are multiplied by 50, which is the same factor used for the time histories in Models C and D. The earliest wave "arrival" appears at the location of the cavity. Similar to the residual from models A/B, the time history has a wave pattern that forms an arrow that points to the location of the cavity. The resonances are still strongly apparent. It is unclear why the resonances do not cancel one another, unless these are resonances of scattered waves.

The overtone image created for Model D is displayed in Figure 4.20. The calculated dispersion curves are the same as shown for Model C (Figure 4.17). If the dispersion curve were hand-picked it would provide nearly identical results to Model C.

The residual overtone image of Model C subtracted from Model D is displayed in Figure 4.21. The residual emphasizes the difference between Model C and Model D, which is mainly in the frequency range 40 through 70 Hz. The calculated dispersion curves are the same as shown for Model C (Figure 4.17). As noted earlier, the color scales for the overtone plots are not uniform among images. The maximum amplitudes in the overtone images for Model D and this differential image are of the same order of magnitude (9.4 x 10^{-9} and 2.8 x 10^{-9}, respectively). This further demonstrates that the scattered waves are similar in amplitude to the direct (non-scattered) waves, as was observed in the time histories.

This study of Models C and D indicates that identifying cavities from time histories that include a HVL by inspecting the time histories is difficult if not impossible. As discussed earlier, Luke and Calderón-Macías (2008) suggest stacking of overtone images might be used to illuminate buried features. The framework for creating stacks of overtone images presented by Luke and Calderón-Macías (2008) is applied to these synthetic datasets.

Figure 4.22 displays the overtone images from Model D in the positive *X* direction which are used to create stacks of overtone images. The first source location is on the left, the last source location is on the right. The cavity is located at source location 8, which is at (10, 15.5, 1). This figure is to help conceptualize how a stack of overtone images is created. The arrows in the figure indicate the direction the data are summed if stacked according to velocity. Stacking allows the 3-D dataset shown in this figure to be turned into a 2-D image that can be read as position versus either velocity or frequency. The overtone images shown in this figure are used to create the stacks of overtone images shown in the next two figures in this section.

Stacks of overtone images are created from summing the overtone images from the 27 source locations in this research. The receivers in the positive *X* direction from the source were summed separately from the receivers in the negative *X* direction from the source and then both directions were added together. Figure 4.23 displays a stack of overtone images according to velocity containing the sum from all receivers for the 27 source-location tests of Model D and Figure 4.24 displays the same data stacked

according to frequency. All of the data provided in Figure 4.20 appear in a vertical band at source location one in both figures. The high amplitudes at source location 8 occur at the location of the cavity. The cavity is 10 m from the *X* axis in Model D, which is 5 m from the first receiver. The highest amplitudes center around 50 Hz because a 50-Hz source was used to generate the time histories. This study demonstrates a synthetic case where stacks of overtone images can be observed to visually locate a cavity along a line of receivers. The stacks of overtone images correctly identified the cavity location even when the model included a HVL beneath the cavity. For Model D, stacks of overtone images clearly and correctly indicate the cavity location, whereas analyses of time histories or individual overtone plots do not.

4.6 NORMALIZED ENERGY DISTANCE (NED) CAVITY CHARACTERIZATION PARAMETER AND POWER SPECTRUMS

Time histories in the horizontal radial and vertical (*X* and *Z*) direction were used for calculation of the NED parameter according to Nasseri-Moghaddam et al. (2005) for Models A through D. The time histories in the *X* and *Z* direction from Model A using a superimposed 25 Hz and 100 Hz Ricker wavelet source, with calculated arrival times added, are compared side-by-side in Figure 4.25. Recall that a superimposed 25 Hz and 100 Hz Ricker wavelet was used initially based on successful results with similar modeling techniques by Jin (2006), then a 50 Hz Ricker wavelet was used to simplify the source by removing one Ricker wavelet and choosing a central frequency. The cavity characterization parameter work was carried out before the source was simplified. The

source is at (3, 15, 1), which is located 2.24 m from the first receiver at (5, 15, 0) in the array.

Recall that according to Nasseri-Moghaddam et al. (2005), the boundaries of the cavity are distinguished by peaks and valleys of the NED parameter; the NED starts to fluctuate in the proximity of the cavity; the horizontal component has a better resolution than the vertical; wider cavities produce more conspicuous peaks and valleys in NED; and NED values decline beyond the cavity location.

A reliable frequency range over which to evaluate E_z needs to be identified. Virieux (1986) states the minimum reliable wavelength for correct modeling is 10 times the grid size. Following these guidelines, for the case tested by Nasseri-Moghaddam et al. (2005) the minimum reliable wavelength is 0.08 m. Then, using 64 m/s as the Rayleigh wave velocity, the maximum reliable frequency is 800 Hz. Following these guidelines for the current research, the minimum reliable wavelength is 2 m. Then, using 184 m/s as the Rayleigh wave velocity, the maximum reliable frequency is 92 Hz. Further, we consider the range of frequencies in the overtone images for Models A through D that display a high amplitude, which is 40 through 80 Hz. In that high amplitude range the velocity is approximately 185 m/s. Using this frequency range and velocity the calculated minimum reliable wavelength range is 2.3 m, close to the minimum calculated using the guidelines of Virieux (1986), and the maximum reliable wavelength is 4.6 m. Nasseri-Moghaddam et al. (2005) use the maximum reliable wavelength in comparison to embedment depth to

determine effectiveness of the NED parameter. According to the authors, in order for the fluctuations in the NED parameter to be sufficiently large, the maximum wavelength must be greater than five times the embedment depth (depth to top of cavity). For the current research, the maximum wavelength (4.6 m) is slightly less than five times the embedment depth (4.85 m). So according to this guideline, the NED parameter will be only marginally effective for locating a cavity in the current research.

As mentioned earlier, Nasseri-Moghaddam et al. (2005) found that the difference in group velocity with respect to phase velocity was negligible, and therefore cross-contamination of the Rayleigh energy with body wave energy was not a concern, if maximum wavelength is less than 10 times the embedment depth. The maximum wavelength (4.6 m) is significantly less than 10 times the embedment depth (9.7 m) in this research.

Nasseri-Moghaddam et al. (2007) conclude that the optimum wavelength for detection of cavities is 3 through 5 times the embedment depth. In the current research, the minimum wavelength is 2.3 m, which is slightly less than the minimum end of the optimum wavelength range, and the maximum wavelength is 4.6 m which falls in the optimum range.

The NED parameter was calculated, including the energy correction, as explained in Chapter 3.1. Figure 4.26 displays the NED parameter for Model A and Model B; the

cavity is shown by the green lines. The NED parameter fluctuates near the location of the cavity in Model B, which contains a cavity, and not for Model A which does not. If a cavity location was picked from the figure the location chosen would be at the local maximum in Model B vertical direction at receiver number 15. Receiver number 15 is 0.33 m from the front edge of the cavity (with respect to source location). The NED parameters indicate the approximate location of the cavity in Model B; therefore it is effective at locating the cavity using the local fluctuations of the NED parameter. According to the authors the horizontal data display better resolution for deeper cavities than the vertical data. In this case, the horizontal (in-plane) data and the vertical data are both useful in identifying the location of the cavity since both display local fluctuations.

The NED parameter for Model C (no cavity) and Model D is displayed in Figure 4.27. There is a local maximum in Model D vertical direction at receiver number 10, and local minimums at receivers number 6 and 16. Nasseri-Moghaddam et al. (2006) observed a local maximum, followed by a local minimum, and then again followed by a local maximum in their synthetic results. The NED parameters calculated for Model D indicate the approximate location of the cavity but not as precisely as for Model B; following the procedure proposed by Nasseri-Moghaddam et al. (2006) the data suggest that the cavity boundaries are located approximately at receiver numbers 6 and 16; when it is actually at receivers number 16 and 17, which are at 3.33 m and 0.33 m, respectively, in the positive *X* direction. The results are not as precise because of multiple local fluctuations. So one might conclude from the NED plot that a cavity exists, but the location is uncertain. Another observation is that the horizontal data do not fluctuate in

this case; the cavity cannot be identified using horizontal data. There are no large local fluctuations in the NED plot for Model C, which is appropriate for this model which is laterally homogeneous.

The NED calculation leads to picking a location just in front of the cavity in Model B and Model D. Overall this study of the NED parameter achieves similar results to that of Nasseri-Moghaddam et al (2006) for Model B, but the process is successful but not precise with Model D. The NALD cavity characterization parameter from the authors is not tested in this research because of limited success found while testing the NED parameter.

Recall that Phillips et. al. (2002) observed that in the power spectrums of data from receivers located directly above a cavity, certain frequency ranges were amplified. The power spectrums for all models are displayed in Figure 4.28, and the power spectrums for Model A and Model B only are displayed in Figure 4.29. The power spectrums were created using the 25-Hz and 100-Hz superimposed Ricker wavelet source. From looking at these two figures, a cavity cannot be readily located. For example, power spectrums for Model B have consistently larger peak amplitudes, and peaks in the spectrums for Model B are consistently at slightly lower frequency than for Model A. So the cavity is causing higher amplitudes and downward shifts in the frequency response which might be used as a diagnostic tool. However this occurs at all receivers so it might be said to

indicate that a cavity exists but does not point to the location. Overall, using power spectrums to locate a cavity in this research is not productive.

4.7 MAXIMUM AMPLITUDES OF TIME HISTORIES

The maximum amplitudes of each time history in each synthetic model created are displayed in Figure 4.30. The residual of Model A subtracted from Model B represents the amplitude of the scattered waves, whereas Model A represents the amplitude of the direct waves. By comparing these amplitudes the percent of the signal that is scattered waves is found. If the noise level is higher than the amplitude of the scattered waves it will be hard to detect a cavity. The maximum amplitude residual of Model A subtracted from Model B divided by the maximum amplitude of Model A is about 20%. This indicates that it would be difficult to detect a cavity if the noise in the field is more than 20% of the signal. This is a general indicator only; if the events occur in different parts of the frequency spectrum then one doesn't necessarily mask the other.

This chapter has covered the results from the sensitivity studies of the No Free Surface (NFS) model, the Free Surface (FS) model, and the numerical models A, B, C, and D. The next chapter (chapter 5) covers the results from attempting to replicate the experimental data collected at the EGTS in models E and F.

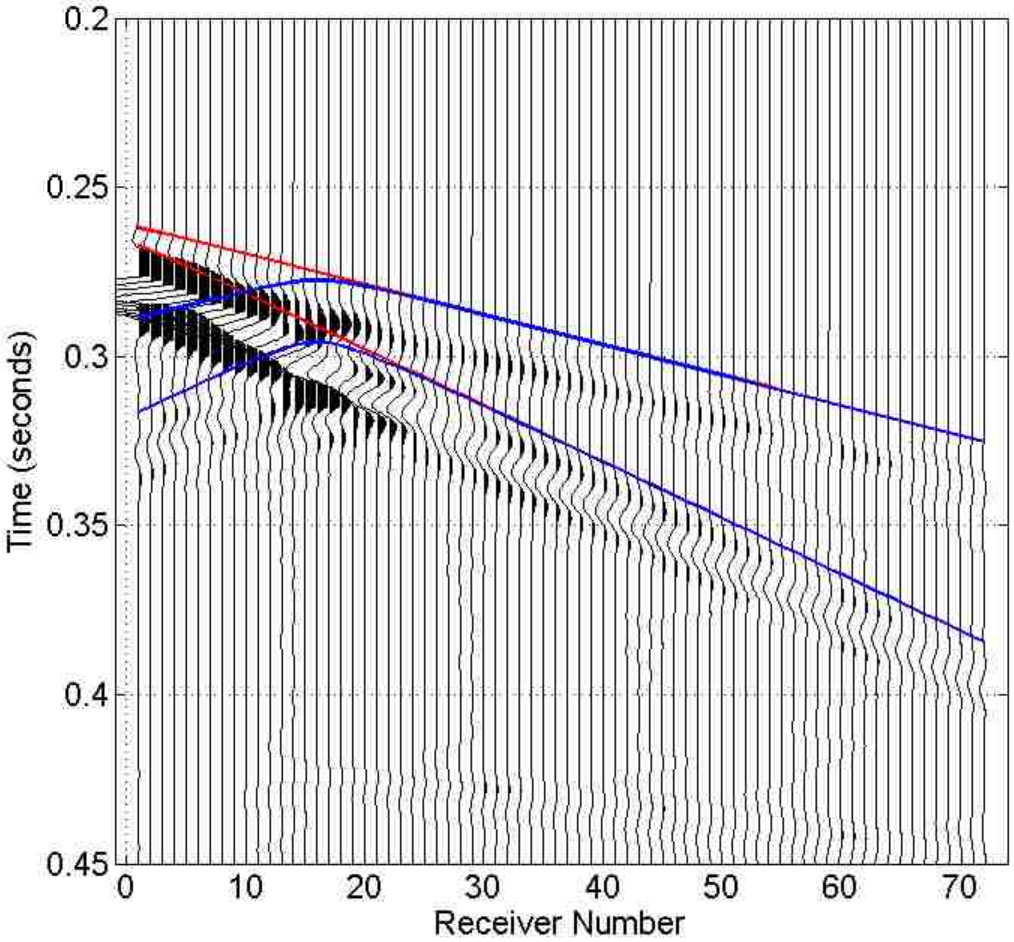

Figure 4.1 Vertical direction time histories from the No Free Surface (NFS) model computed with E3D. The cavity is located beneath receiver numbers 16 and 17. The first red line according to time is calculated P-wave arrival time and the second red line according to time is calculated S-wave arrival time. This same pattern applies to the blue lines which represent the scattered wave theoretical arrival times. The model used a Ricker wavelet 50 Hz source which is located at (3, 1) and which initiated at 0.25 seconds. Receiver number 1 is located at (5, 0) and receiver number 72 is located at (28.7, 0).

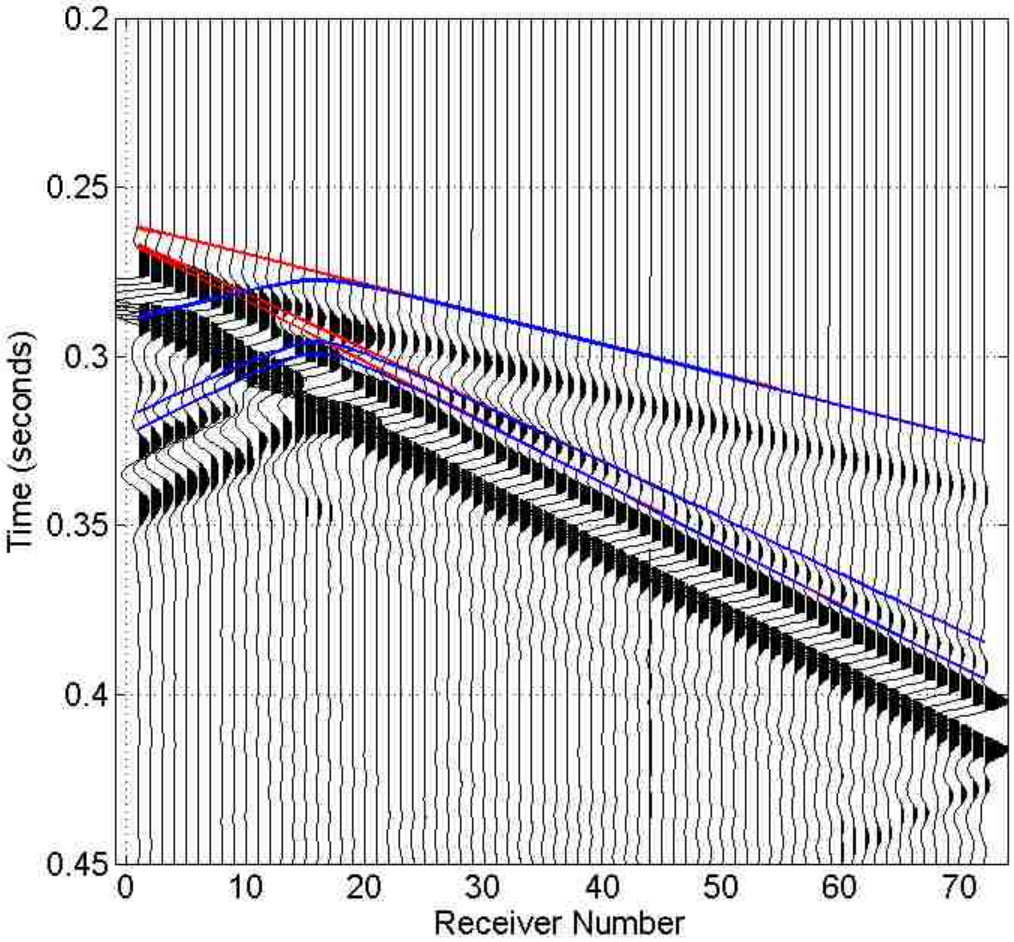

Figure 4.2 Vertical direction time histories from the Free Surface (FS) model computed with E3D. Parameters are as described in Figure 4.1.

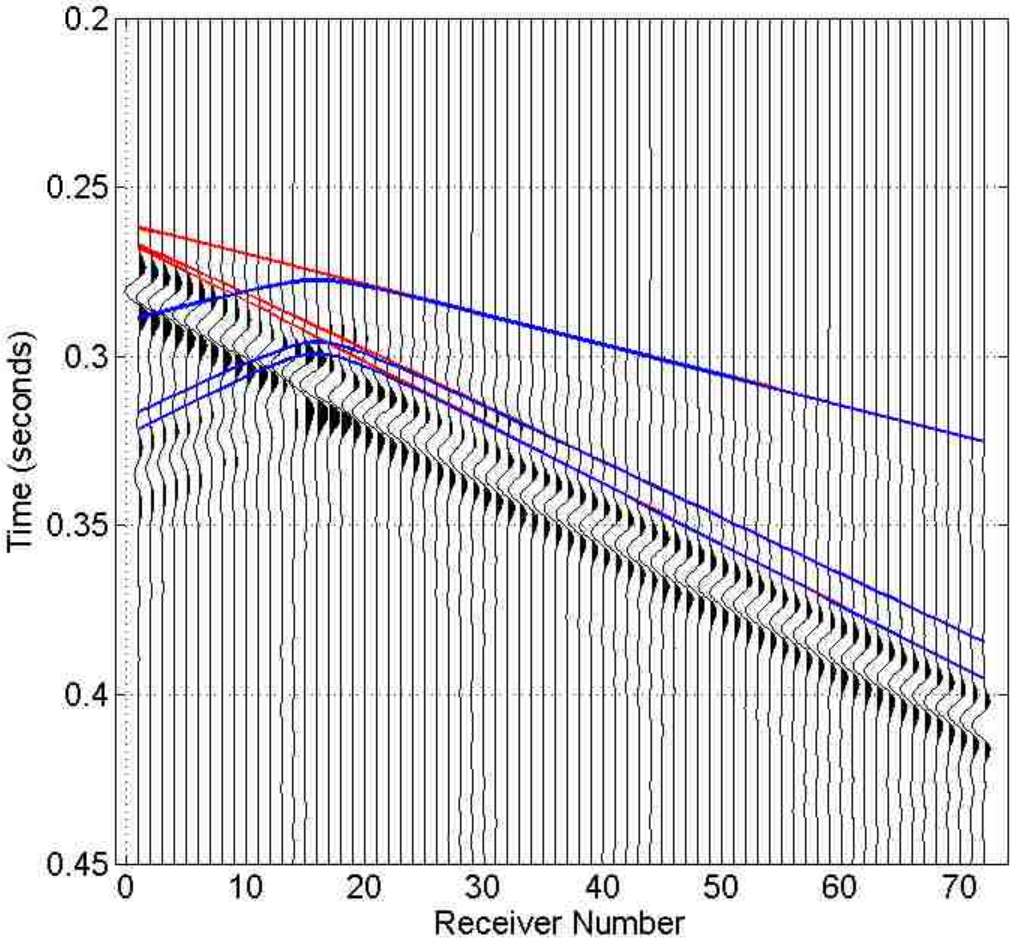

Figure 4.3 Vertical direction time histories from the residual of the No Free Surface (NFS) model subtracted from the Free Surface (FS) model. Parameters are as described in Figure 4.1.

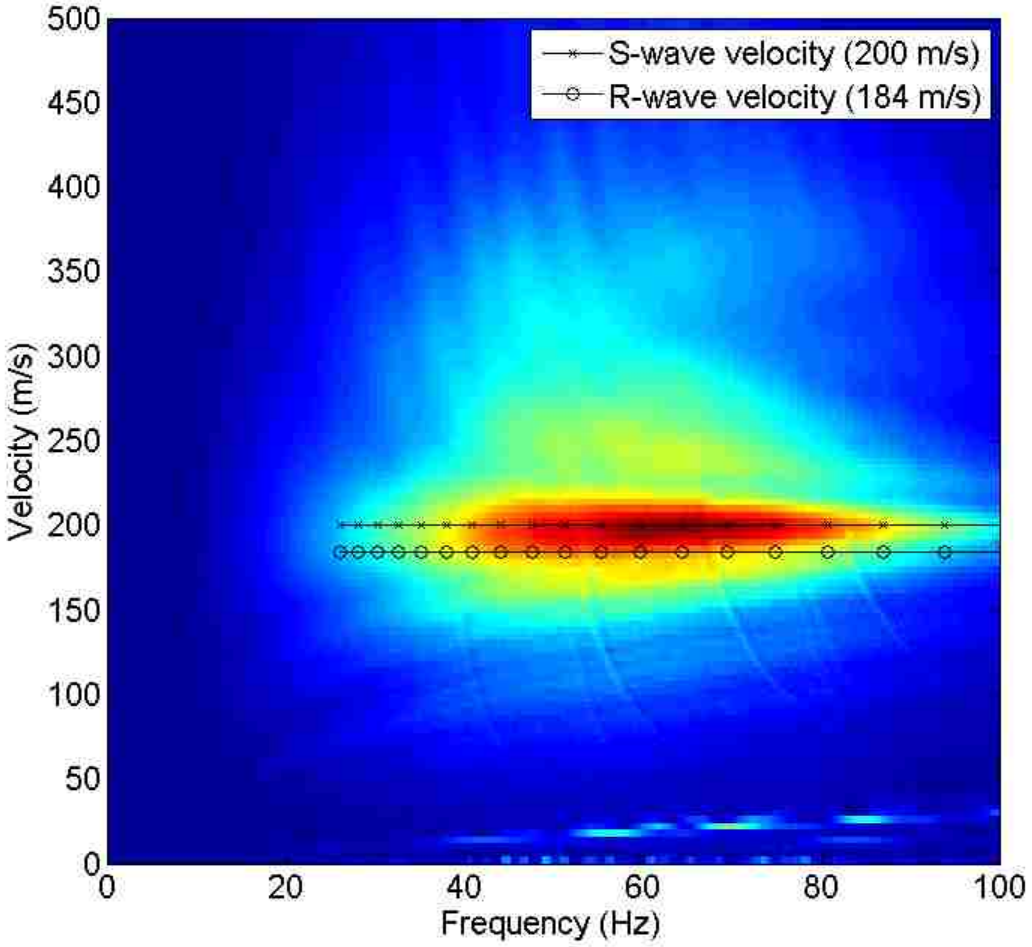

Figure 4.4 Overtone image created from the No Free Surface (NFS) model corresponding to the time histories in Fig. 4.1. The black lines were chosen to start at 25 Hz.

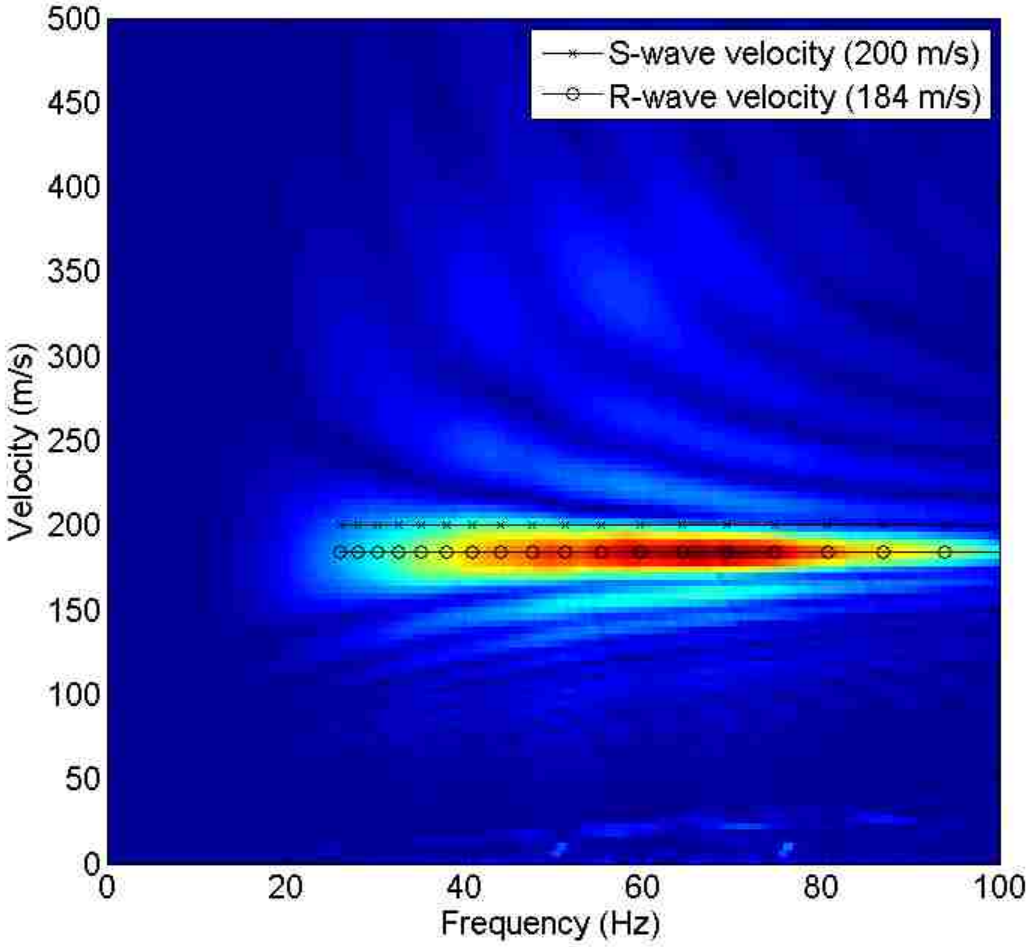

Figure 4.5 Overtone image created from the Free Surface (FS) model corresponding to the time histories in Fig. 4.2. The black line was chosen to start at 25 Hz.

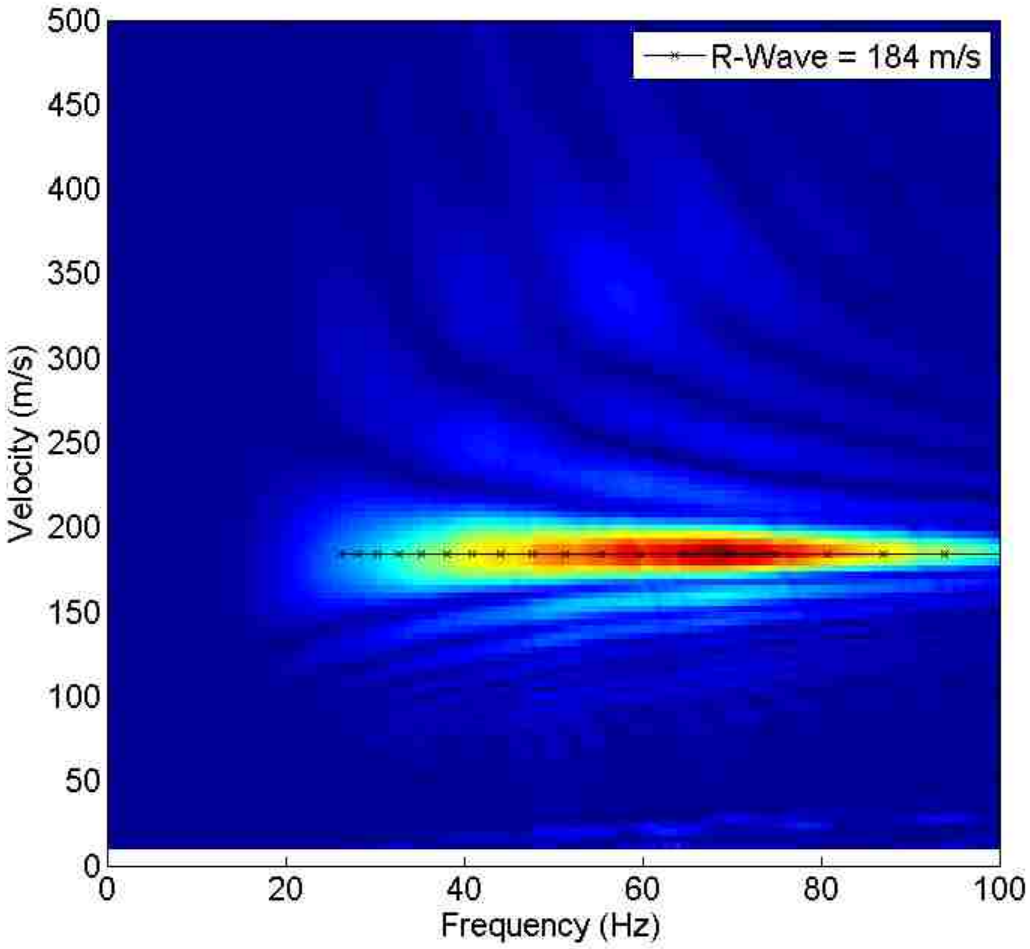

Figure 4.6 Overtone image created from the residual of the No Free Surface (NFS) model subtracted from the Free Surface (FS) model corresponding to the time histories in Fig. 4.3. The black line was chosen to start at 25 Hz.

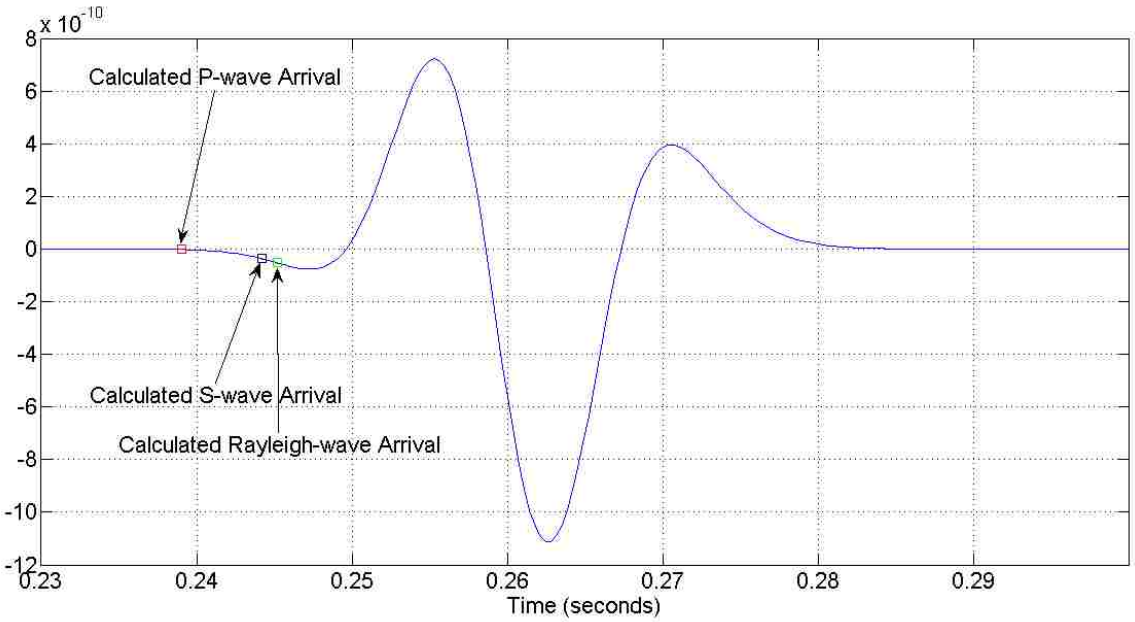

Figure 4.7 Model A time history from the first receiver in the array with calculated arrival times using a Ricker wavelet 50 Hz source located at (3, 15, 1). The calculated arrival times are shifted by a 17-millisecond (0.017 second) negative delay (earlier in time).

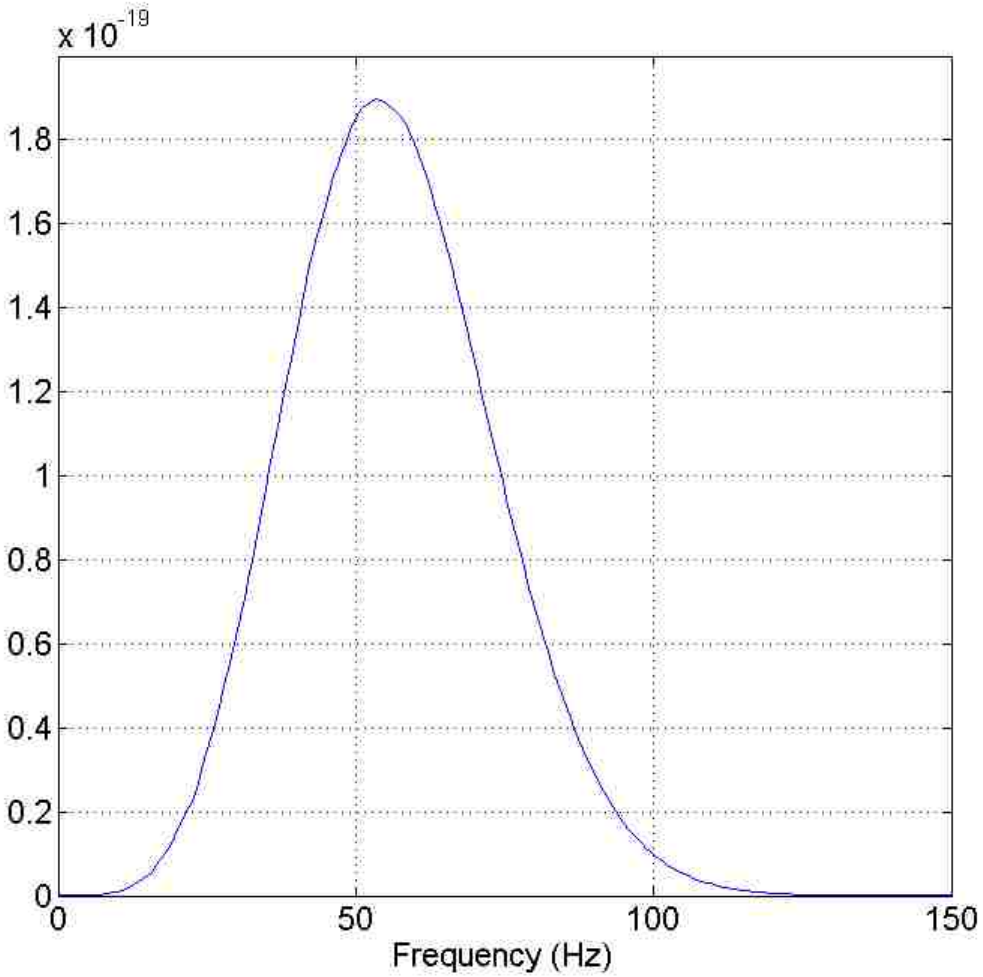

Figure 4.8 The power spectrum created from Model A's time history from the first receiver in the array using a Ricker wavelet 50 Hz source located at (3, 15, 1).

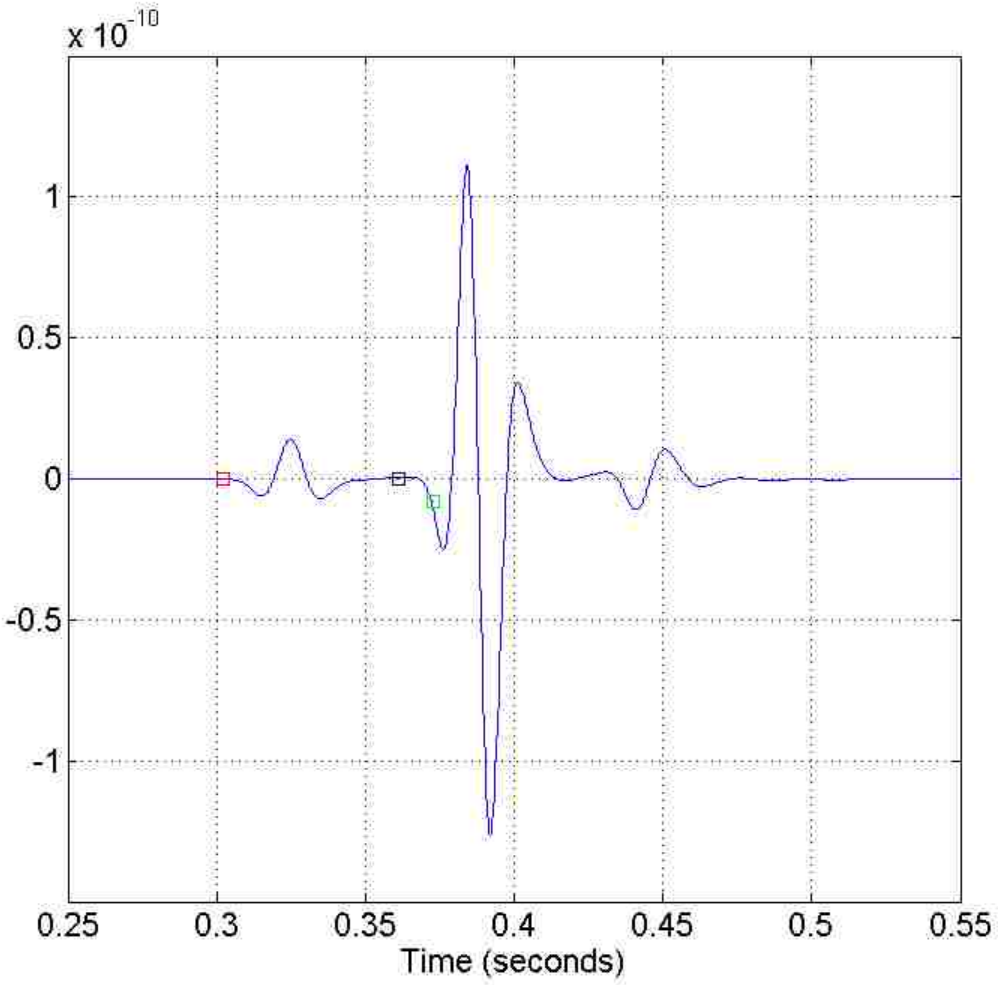

Figure 4.9 Model A time history from the last receiver in the array with calculated arrival times using a Ricker wavelet 50 Hz source located at (3, 15, 1). The red square is the calculated P-wave arrival time, the black square is the calculated S-wave arrival time, and the green square is the calculated Rayleigh-wave arrival time. The calculated arrival times are shifted by a 17-millisecond (0.017 second) negative delay (earlier in time).

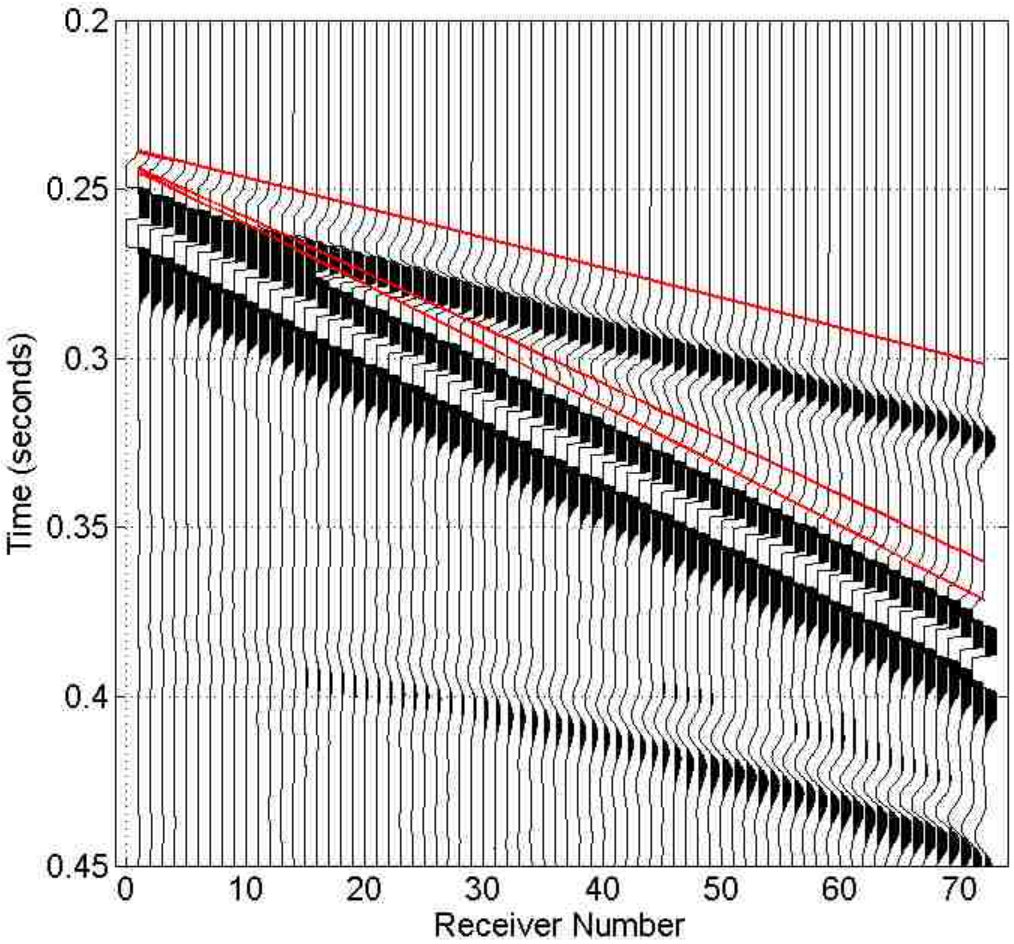

Figure 4.10 Model A vertical direction time histories using a Ricker wavelet 50 Hz source. First red line according to time is calculated P-wave arrival time, second is S-wave arrival time, and third is Rayleigh wave arrival time. The source is located at (3, 15, 1), offset 1 is located at (5, 15, 0), and offset 72 is located at (28.7, 15, 0). The calculated arrival times are shifted by a 17-millisecond (0.017 second) negative delay (earlier in time).

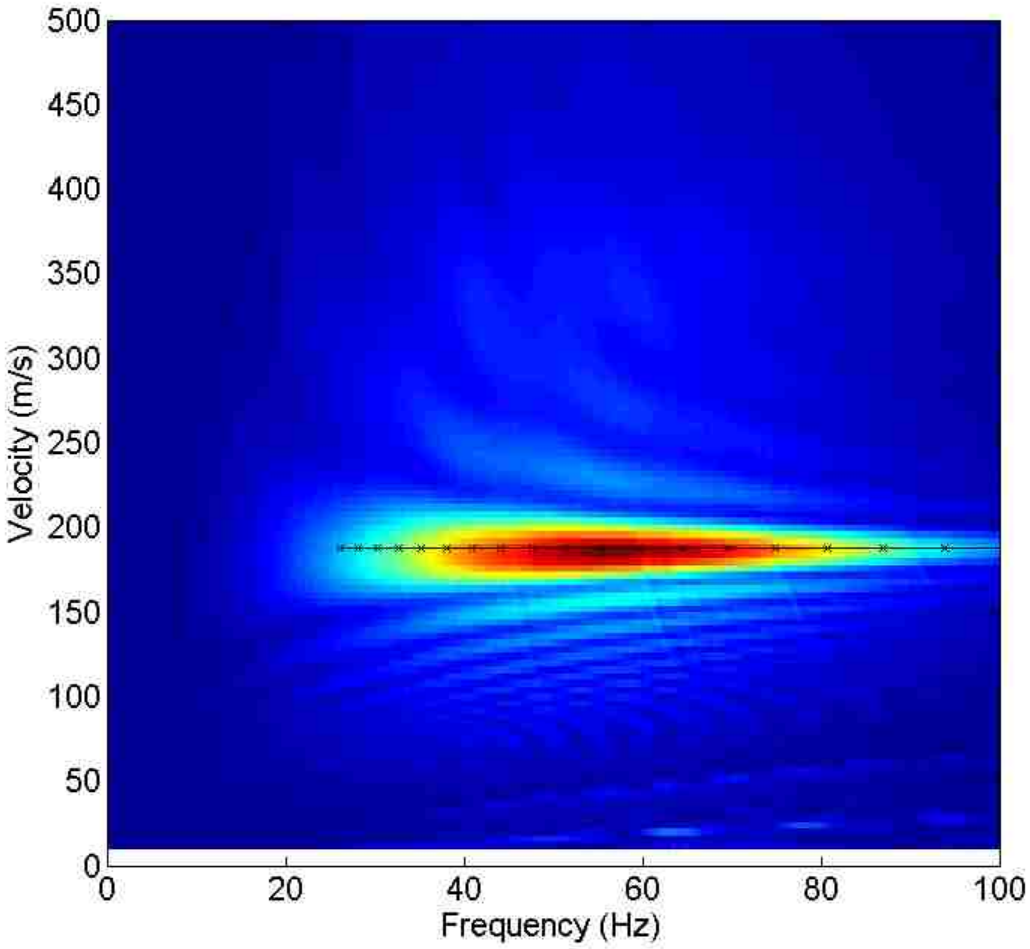

Figure 4.11 Overtone image created from Model A corresponding to the time histories in Fig 4.10. The black line with X marker symbols is the calculated fundamental mode theoretical dispersion curve, which forms a horizontal line at the velocity of 187.6 m/s. The dispersion curve was chosen to start at 25 Hz.

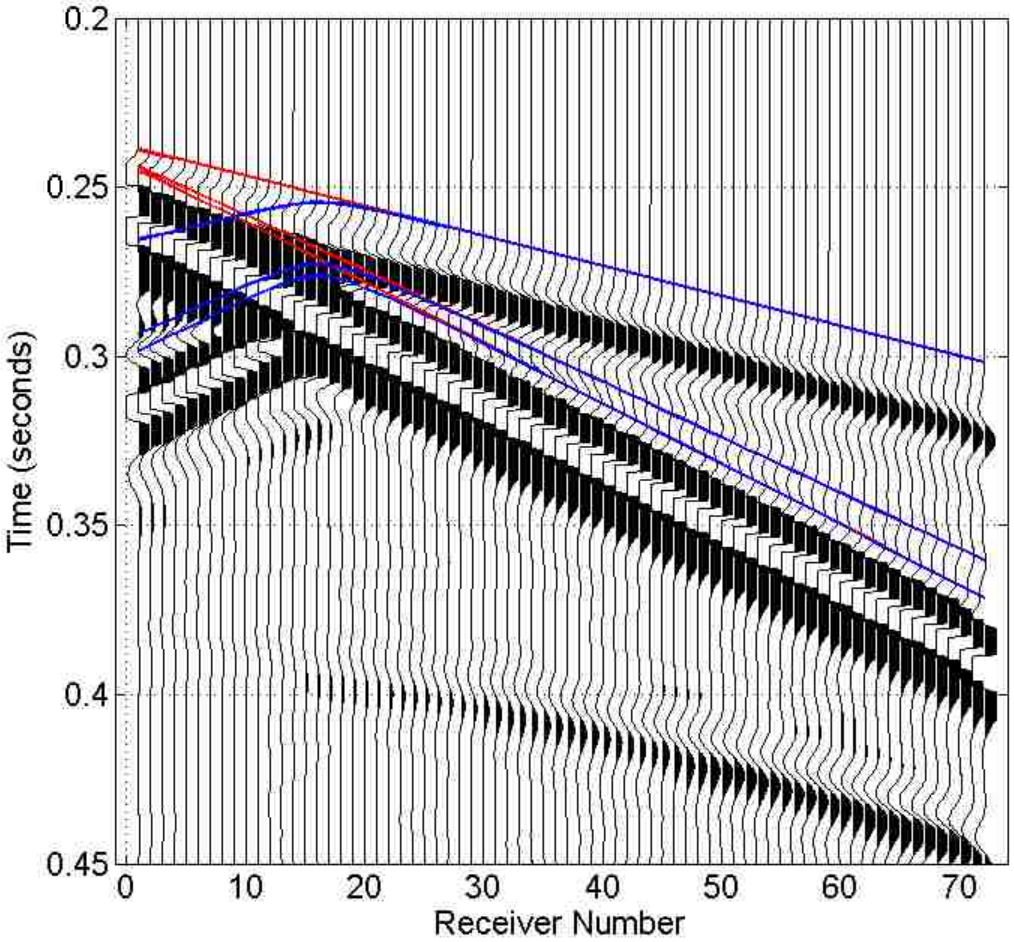

Figure 4.12 Model B vertical direction time histories. Parameters are as described in Fig. 4.10. First blue line according to time is calculated arrival time of P energy for scattering due to the cavity (located beneath offsets 16 and 17) from incident P-wave, second is for S energy from incident S-wave, and third is for R energy from incident Rayleigh wave.

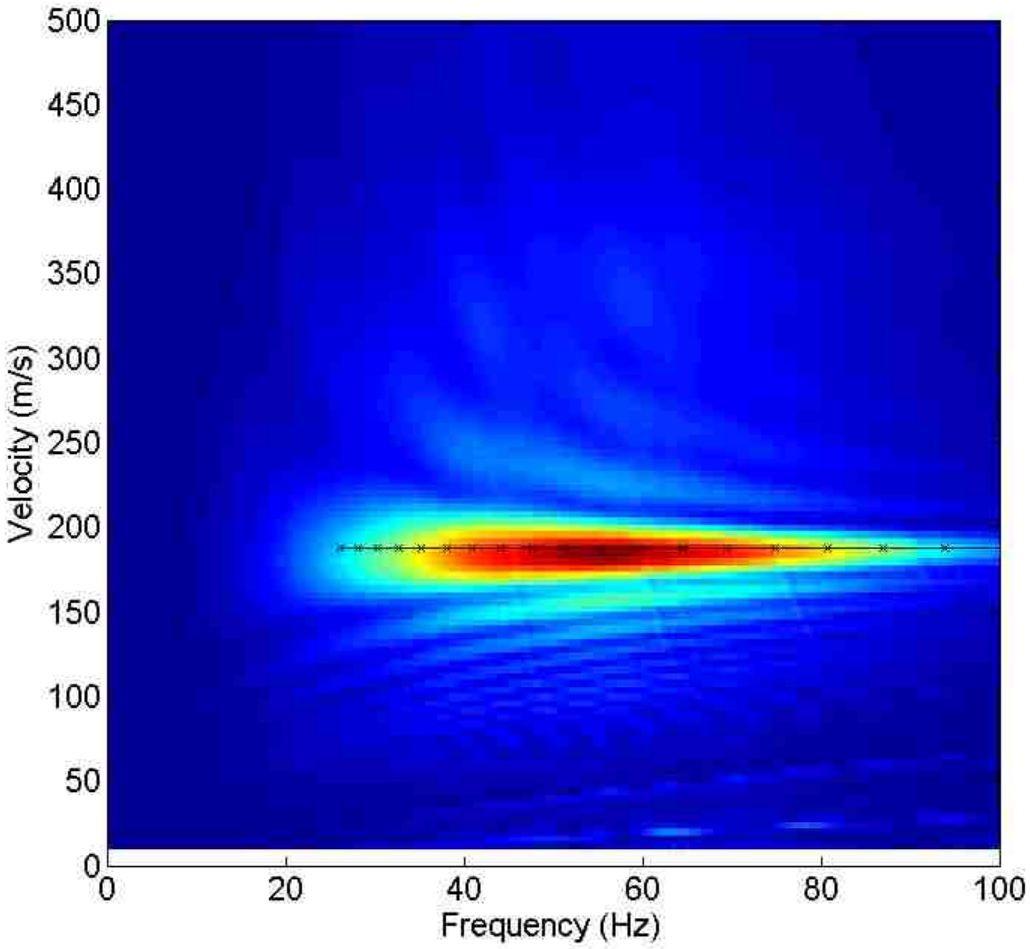

Figure 4.13 Overtone image created from Model B corresponding to the time histories in Fig. 4.12. Parameters are as described in Figure 4.10. The dispersion curve was chosen to start at 25 Hz.

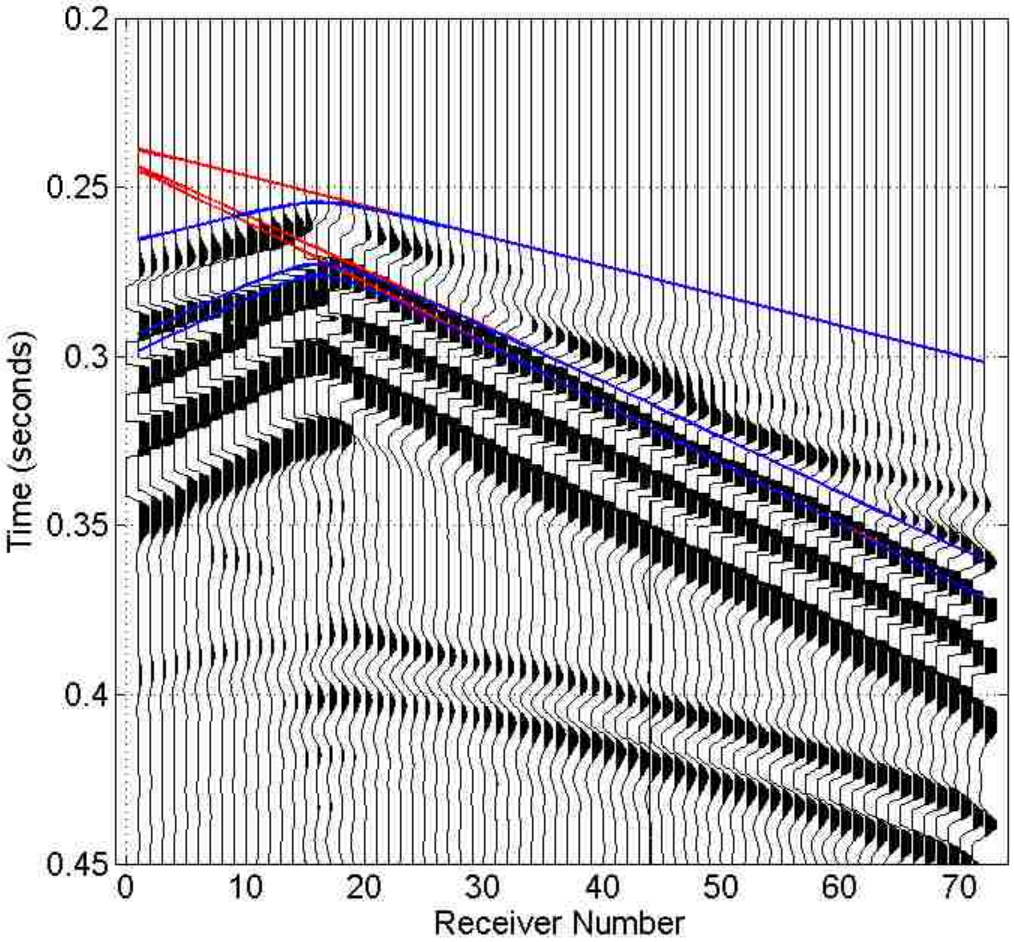

Figure 4.14 Residual of Model A subtracted from Model B, vertical direction time histories. Parameters are as described in Fig 4.10 and 4.12.

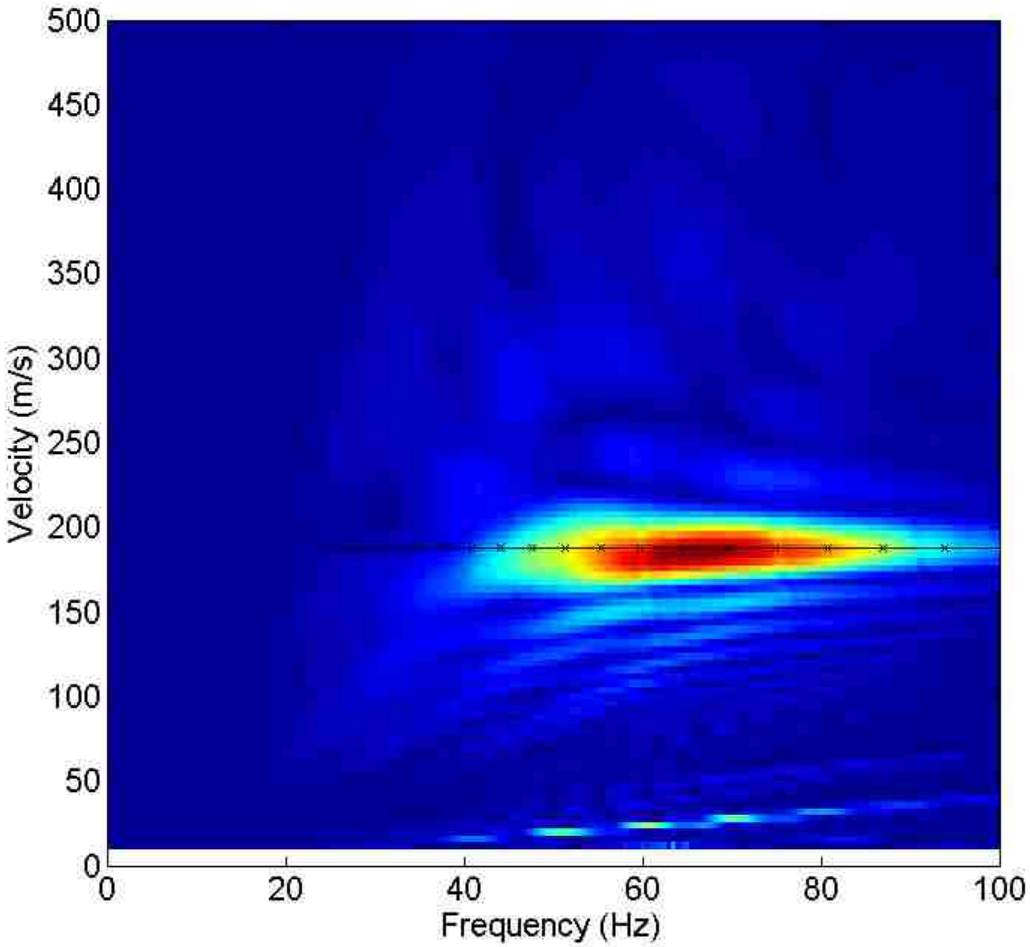

Figure 4.15 Overtone image created from the residual of Model A subtracted from Model B corresponding to the time histories in Fig 4.14. Parameters are as described in Fig. 4.10 and 4.11. The dispersion curve was chosen to start at 25 Hz.

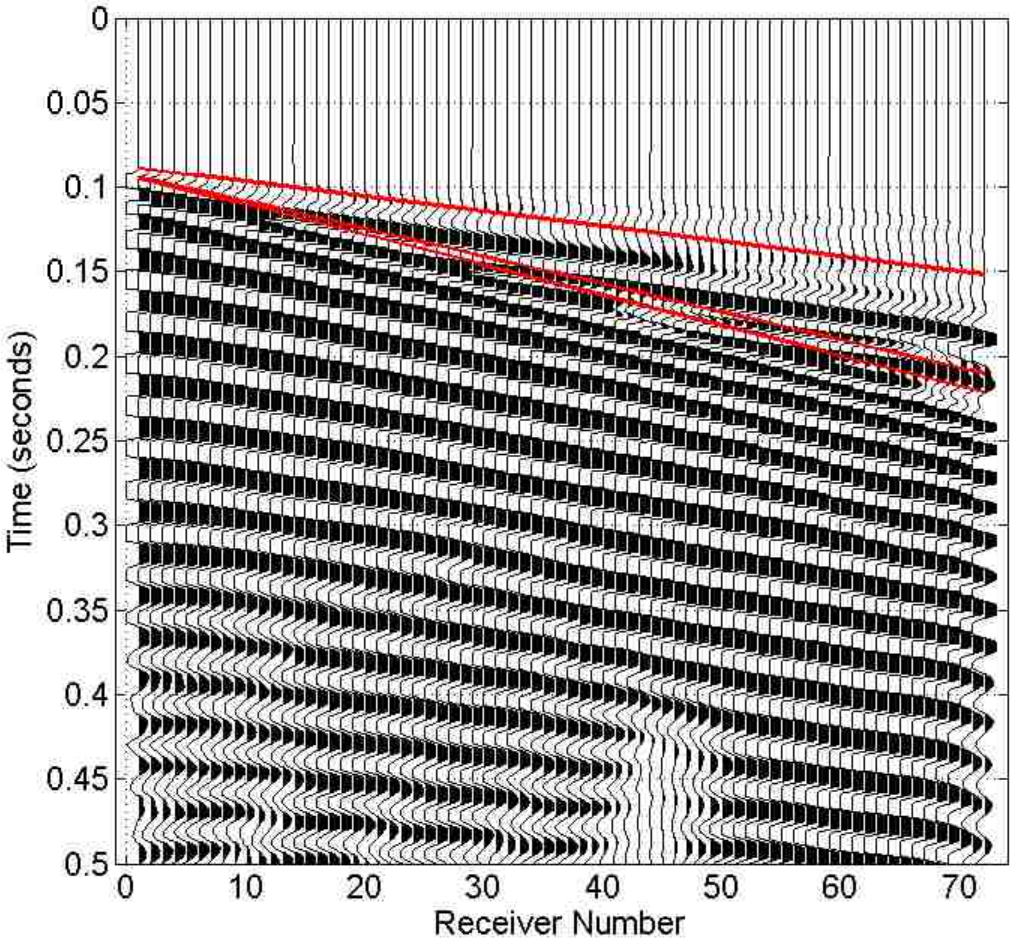

Figure 4.16 Model C vertical direction time histories. Parameters are as described in Fig. 4.10.

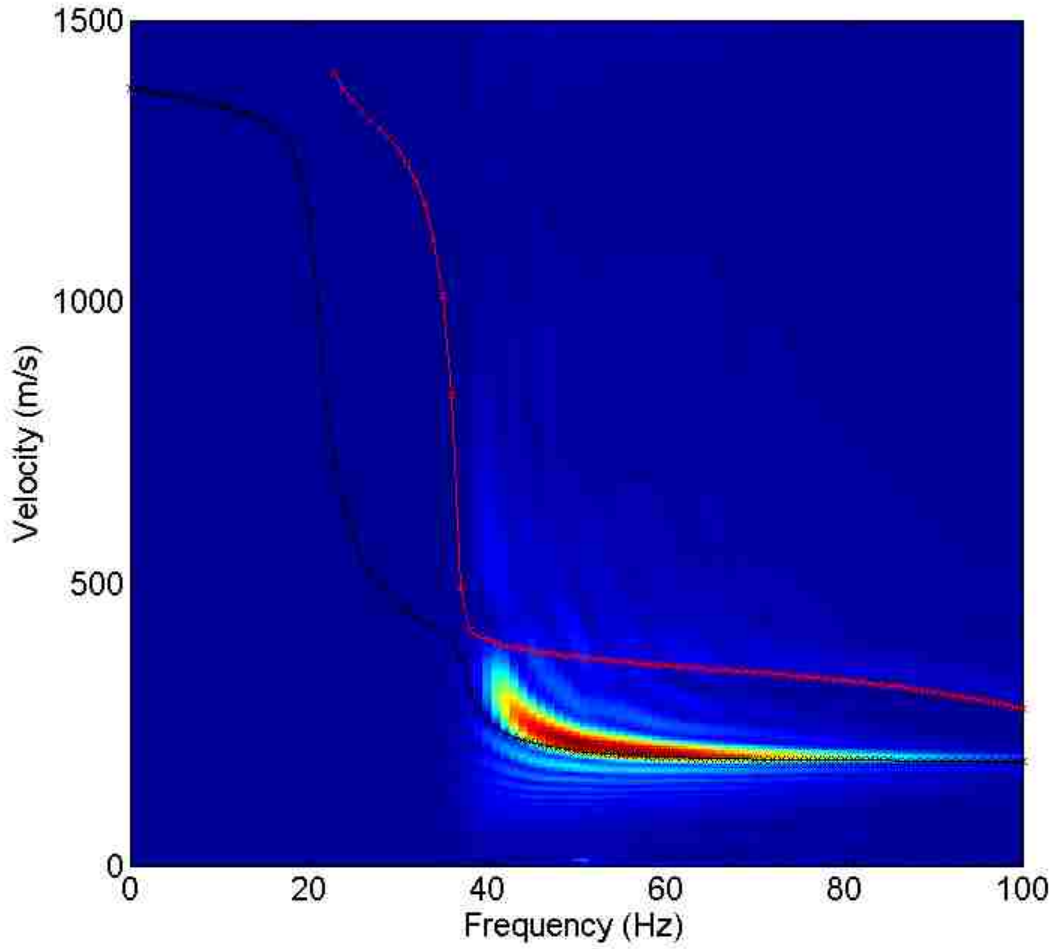

Figure 4.17 Overtone image created from Model C corresponding to the time histories in Fig. 4.16. The black line with X marker symbols is the calculated fundamental mode theoretical dispersion curve and the red line with X marker symbols is the calculated first higher order mode dispersion curve.

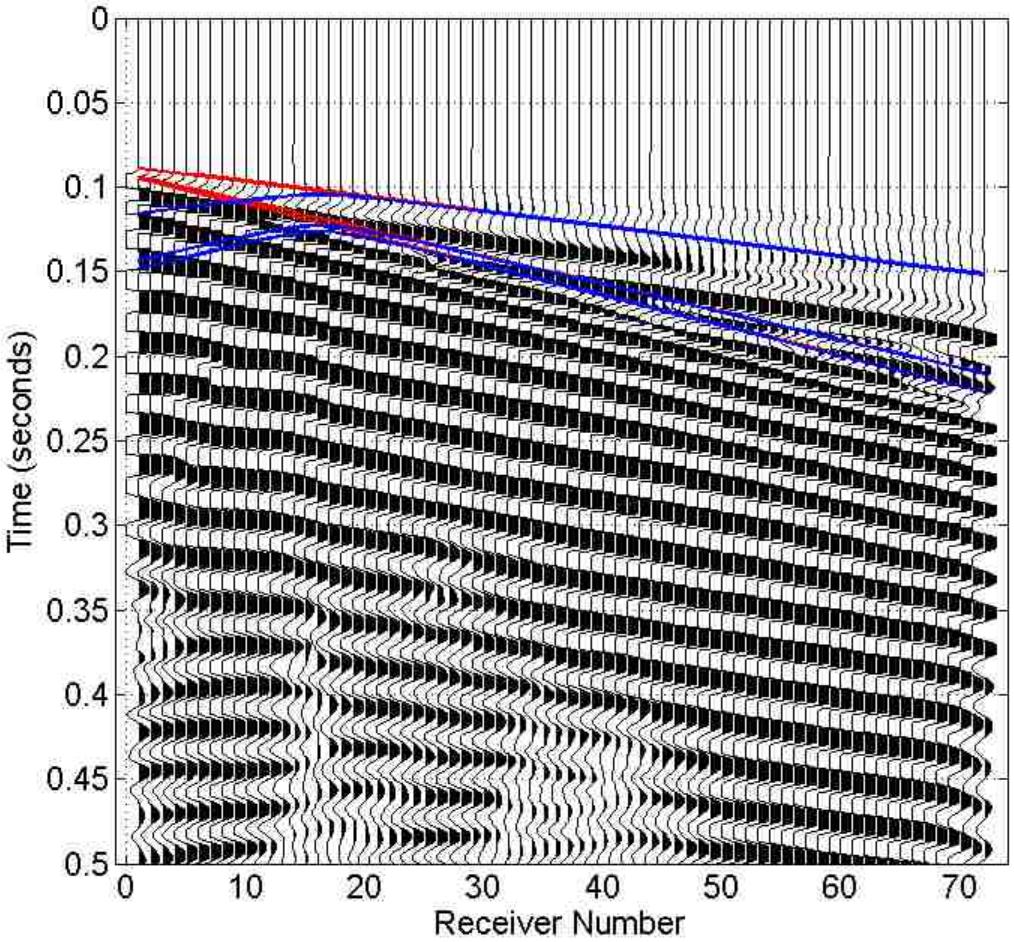

Figure 4.18 Model D vertical direction time histories. Parameters are as described in Fig. 4.10 and 4.12.

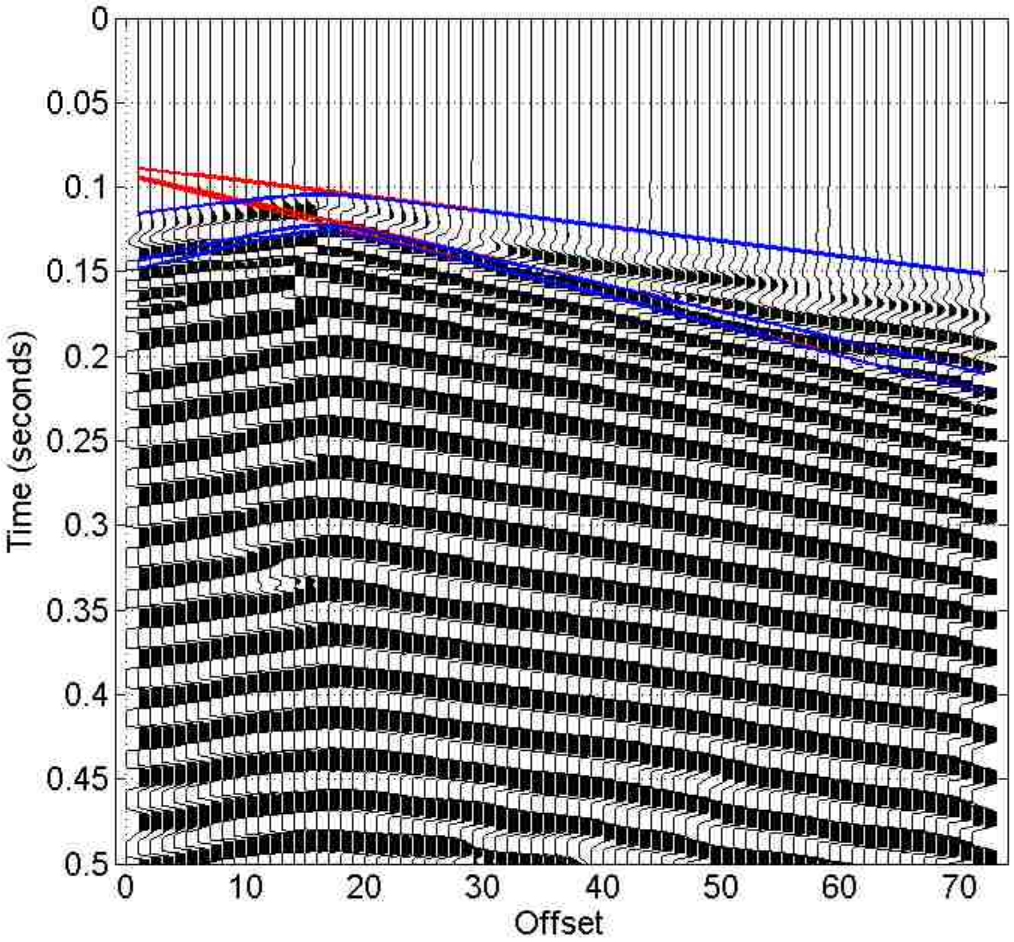

Figure 4.19 Residual of Model C subtracted from Model D. Parameters are as described in Fig. 4.10 and Fig. 4.12.

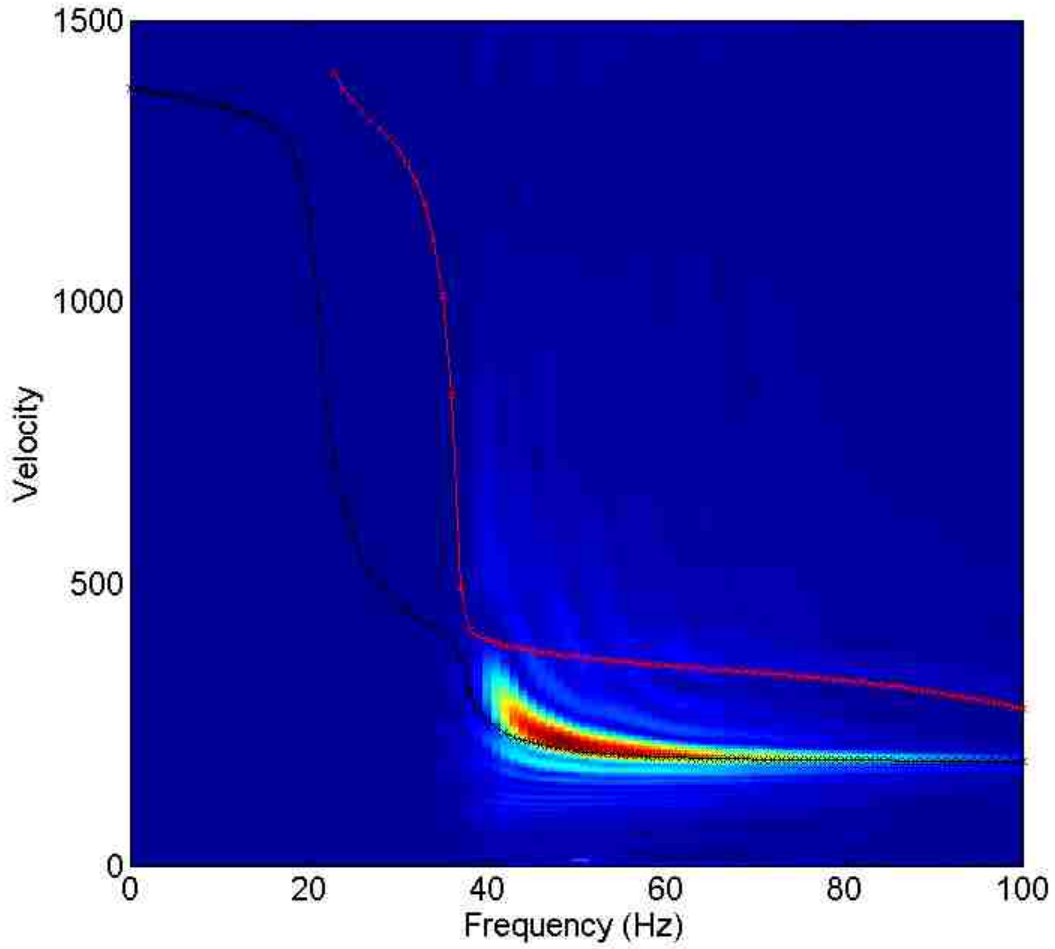

Figure 4.20 Overtone image created from Model D corresponding to the time histories in Fig. 4.18. Parameters are as described in Fig. 4.10 and 4.17.

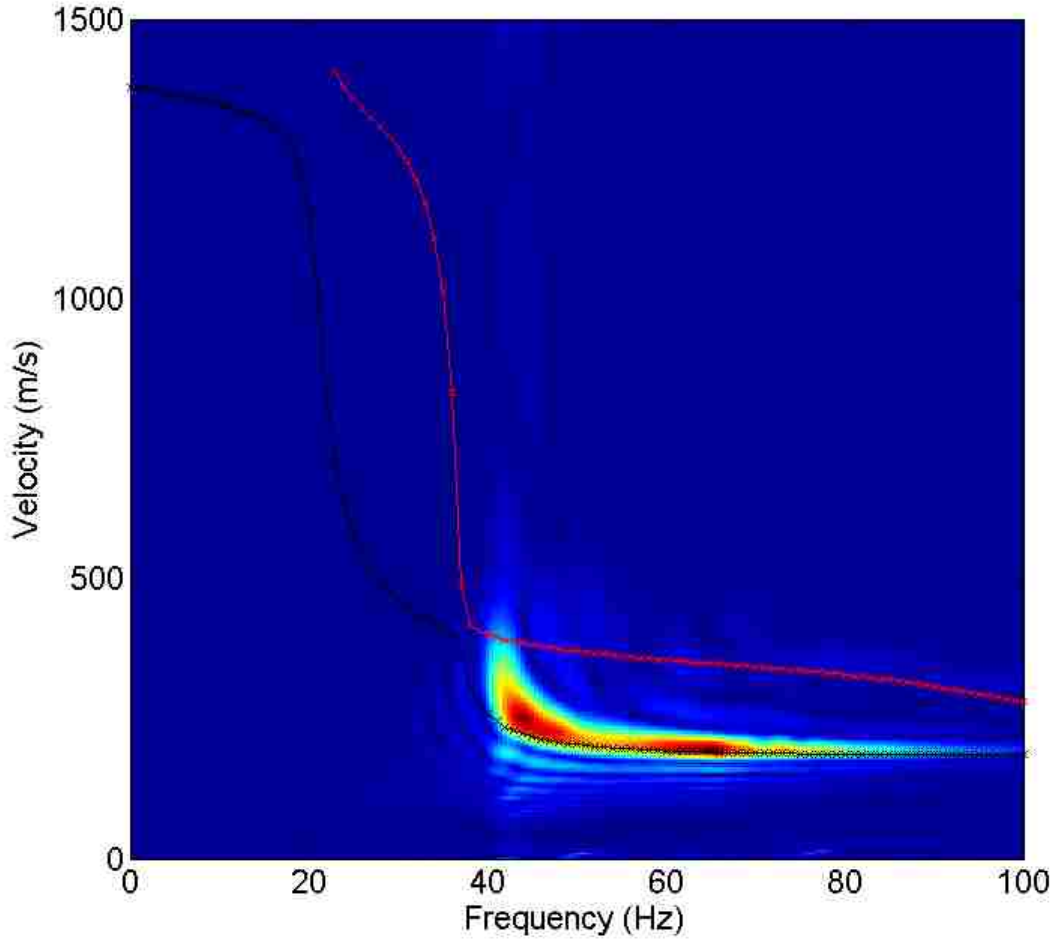

Figure 4.21 Overtone image created from the residual of Model C subtracted from Model D corresponding to the time histories in Fig. 4.19. Parameters are as described in Fig. 4.10 and 4.17.

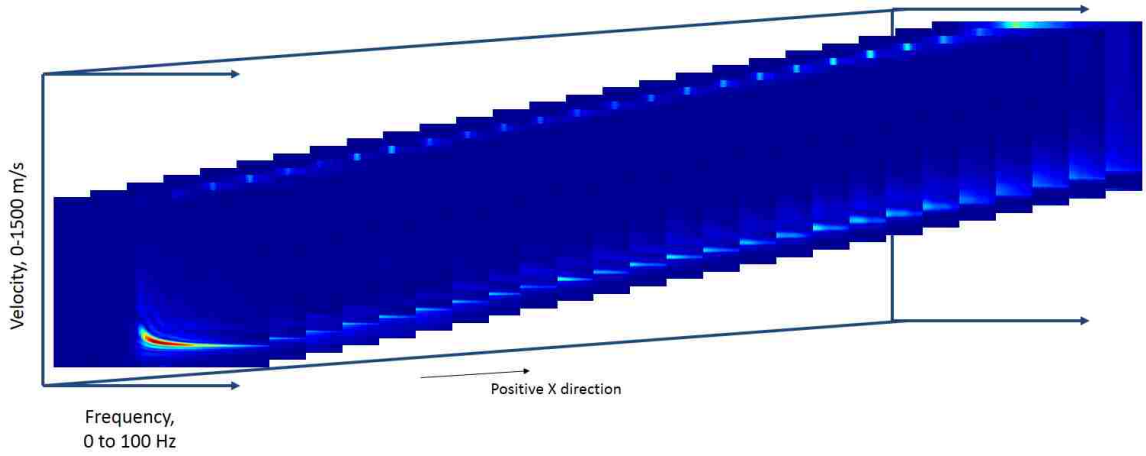

Figure 4.22 Overtone images from Model D in the positive *X* direction which is used to create stacks of overtone images. Model D uses a 50 Hz Ricker wavelet source in multiple source locations and a pseudo-2D cavity. The first source location is on the left, the last source location is on the right. The cavity is located at source location 8, which is at (10, 15.5, 1). The arrows indicate stacking according to frequency, which yields a 2-D plot of offset as a function of velocity.

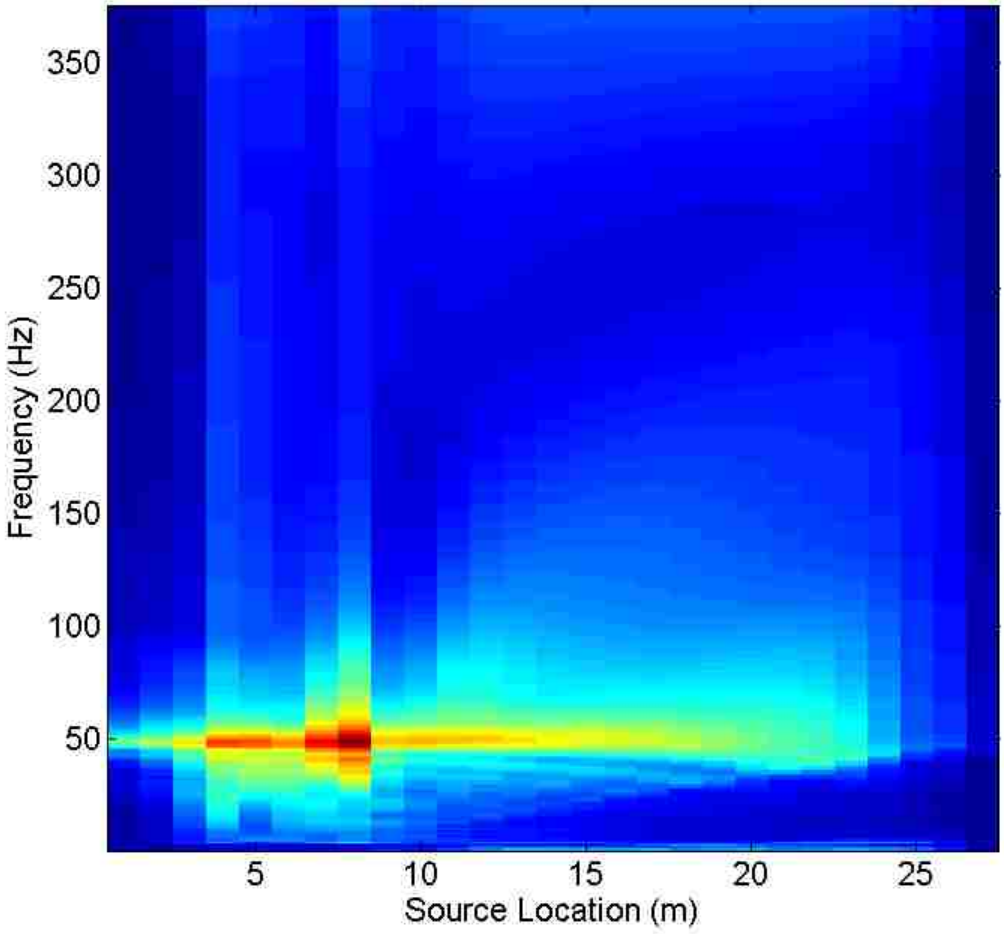

Figure 4.23 Stack of overtone images according to velocity using Model D with a 50 Hz Ricker wavelet source in multiple source locations and a pseudo-2D cavity. The cavity is located at source location 8, which is at (10, 15.5, 1).

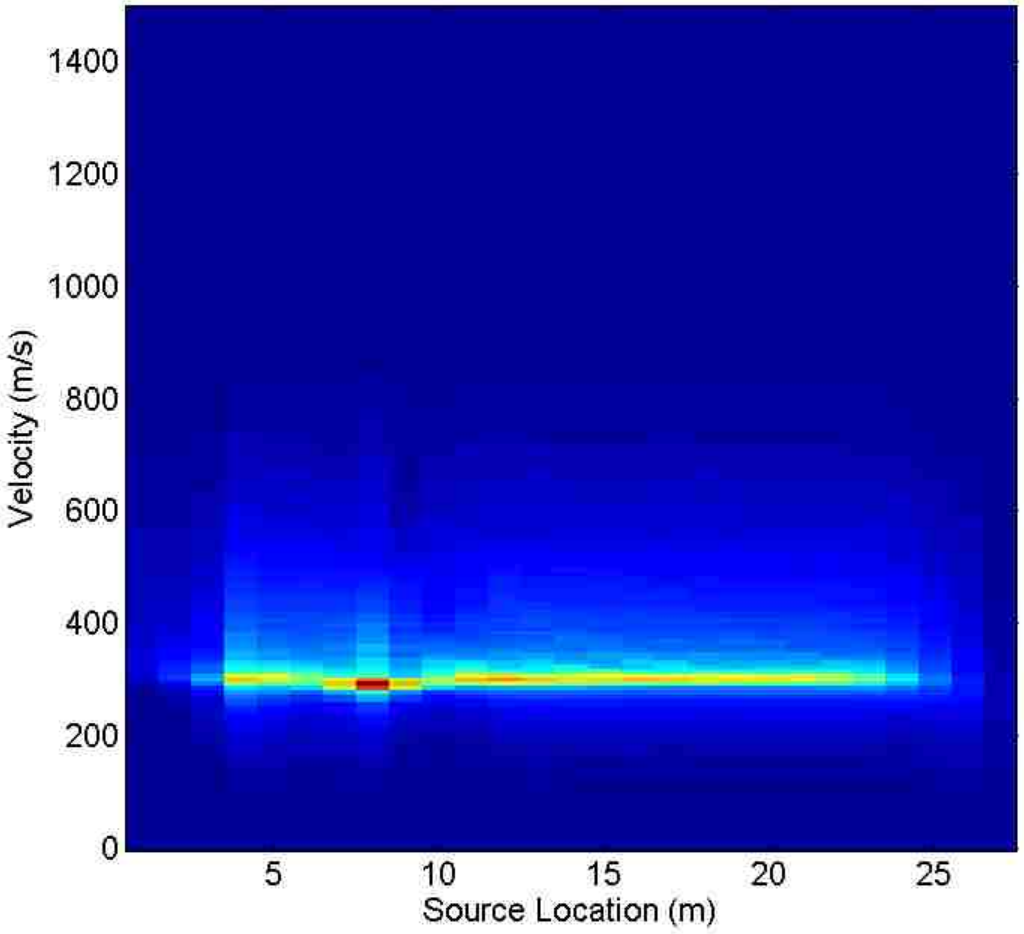

Figure 4.24 Stack of overtone images according to frequency using Model D with a 50 Hz Ricker wavelet source in multiple source locations and a pseudo-2D cavity. The cavity is located at source location 8, which is at (10, 15.5, 1).

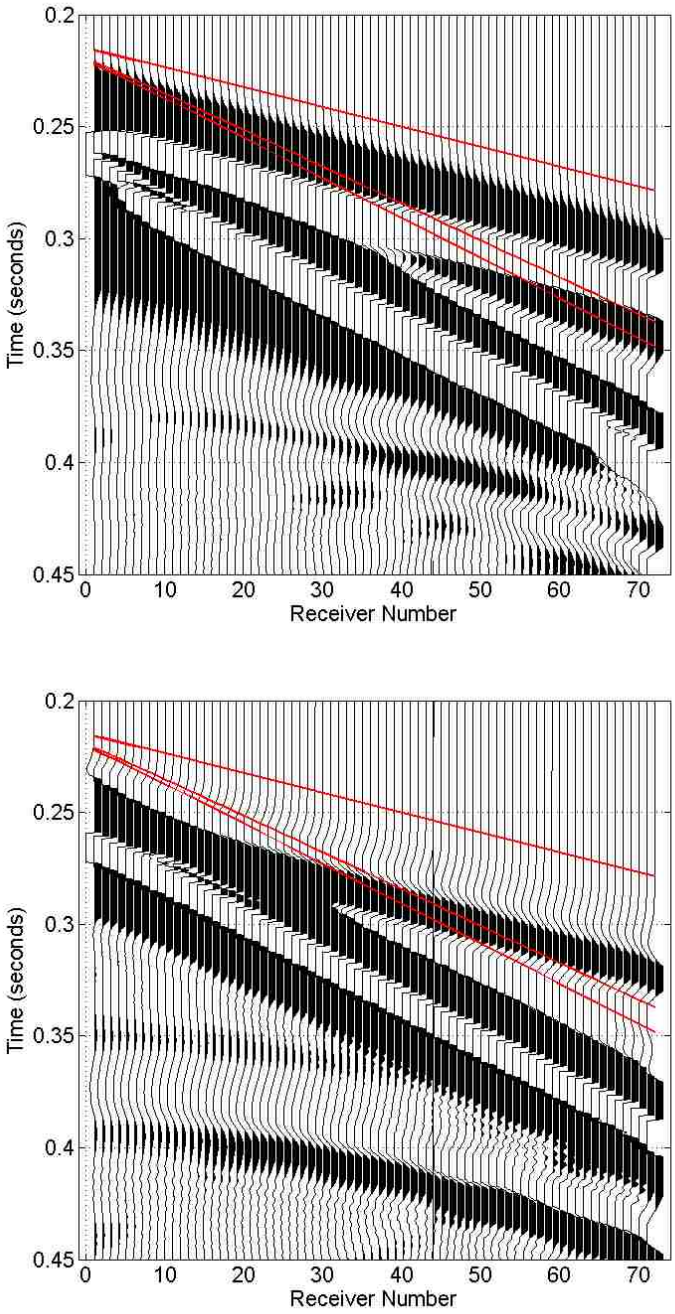

Figure 4.25 Comparing horizontal-radial and vertical (*X* and *Z*) direction time histories used for NED parameter calculation using Model A with a superimposed 25 Hz and 100 Hz Ricker wavelet source located at (3, 15, 1). The top figure is horizontal time histories, and the bottom figure is vertical time histories. Parameters are as described in Fig.4.10.

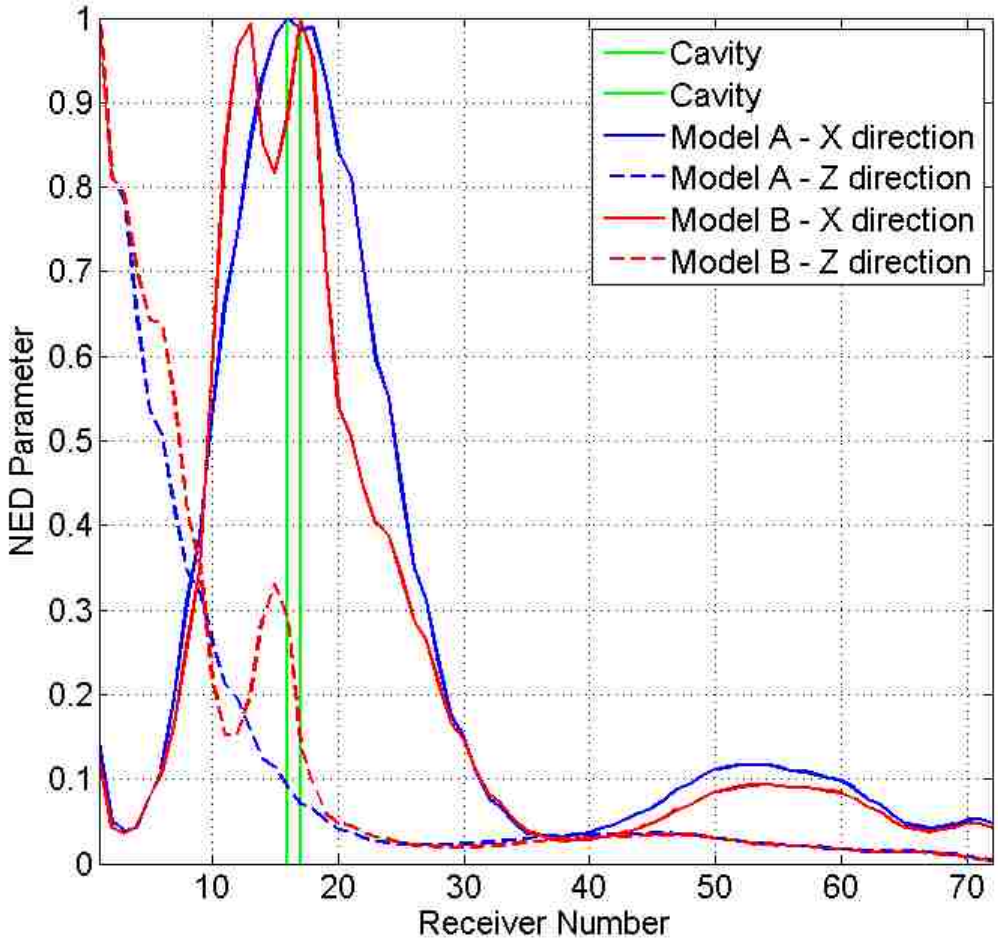

Figure 4.26 Normalized Energy-Distance (NED) parameter for Model A and Model B. The cavity in Model B is located beneath receiver numbers 16 and 17 as marked by the green lines.

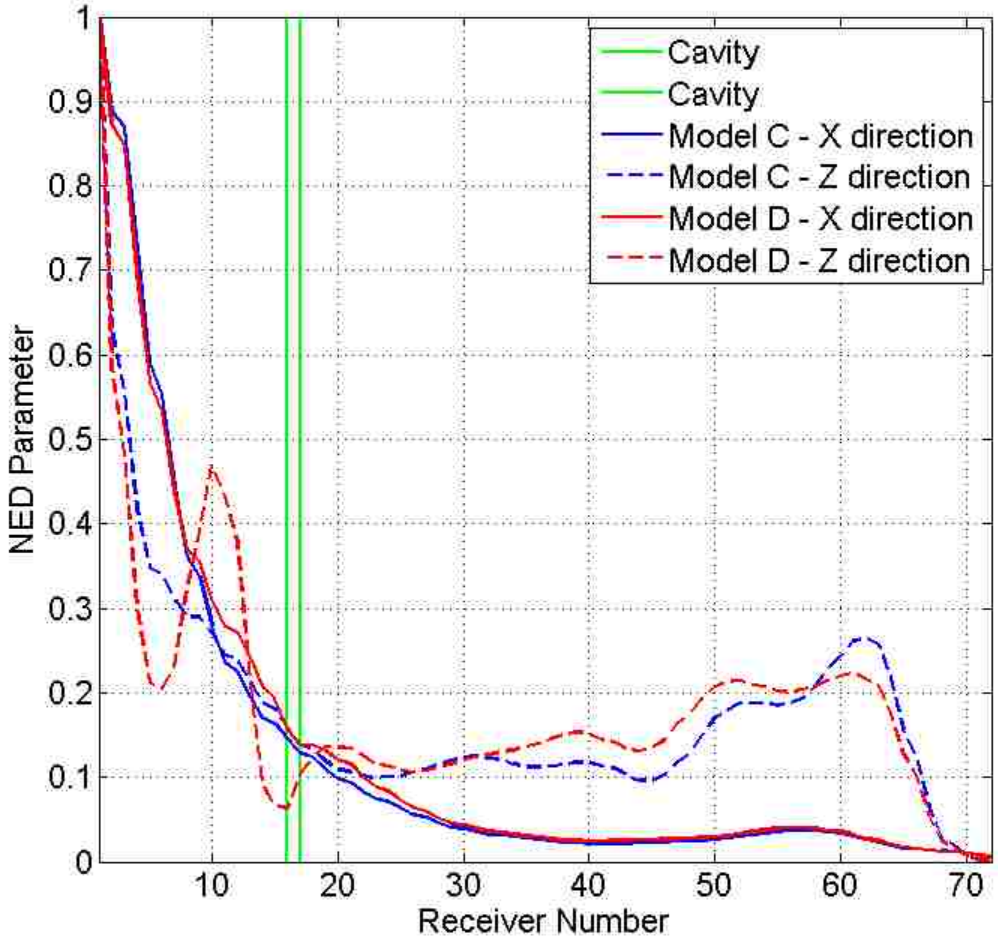

Figure 4.27 Normalized Energy-Distance (NED) parameter for Model C and Model D. The cavity is located beneath receiver numbers 16 and 17 as marked by the green lines.

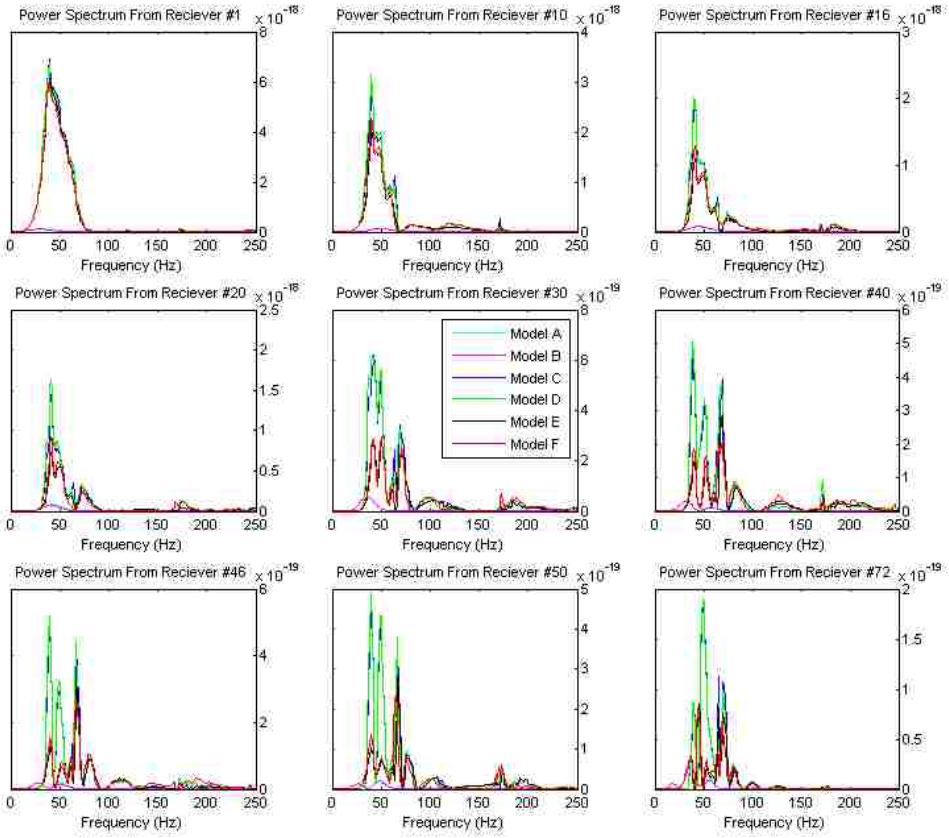

Figure 4.28 Power spectrums for Models A, B, C, D, E, and F for selected receivers.

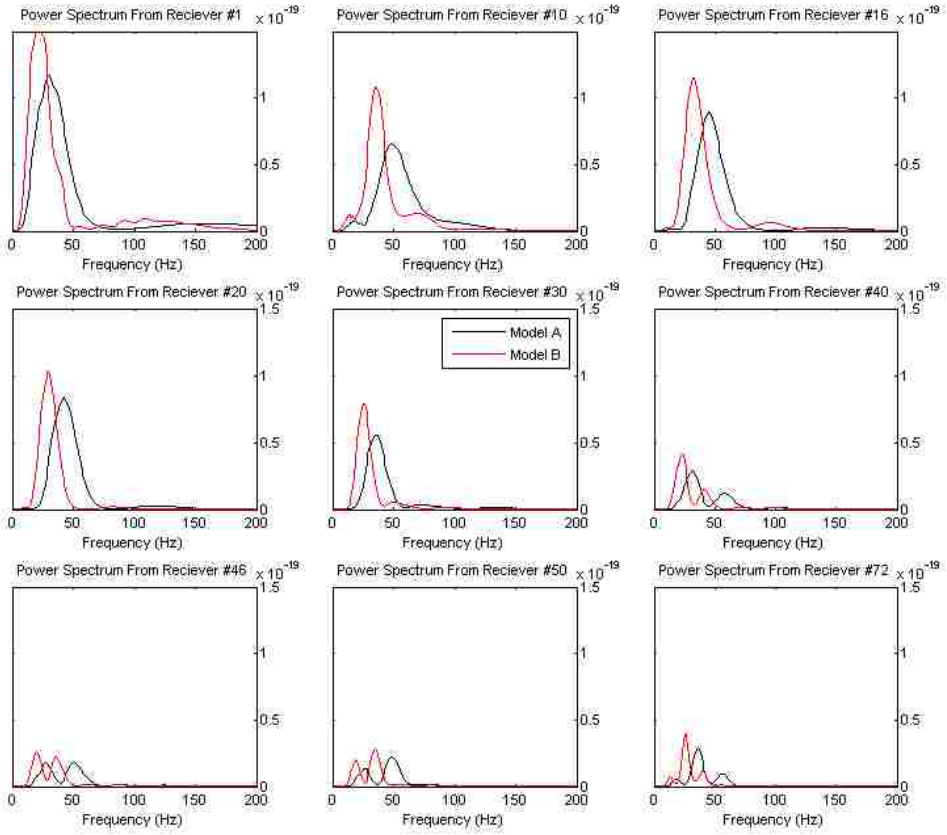

Figure 4.29 Power spectrums for Model A and Model B. The cavity is located under receivers 16 and 17 in Model B.

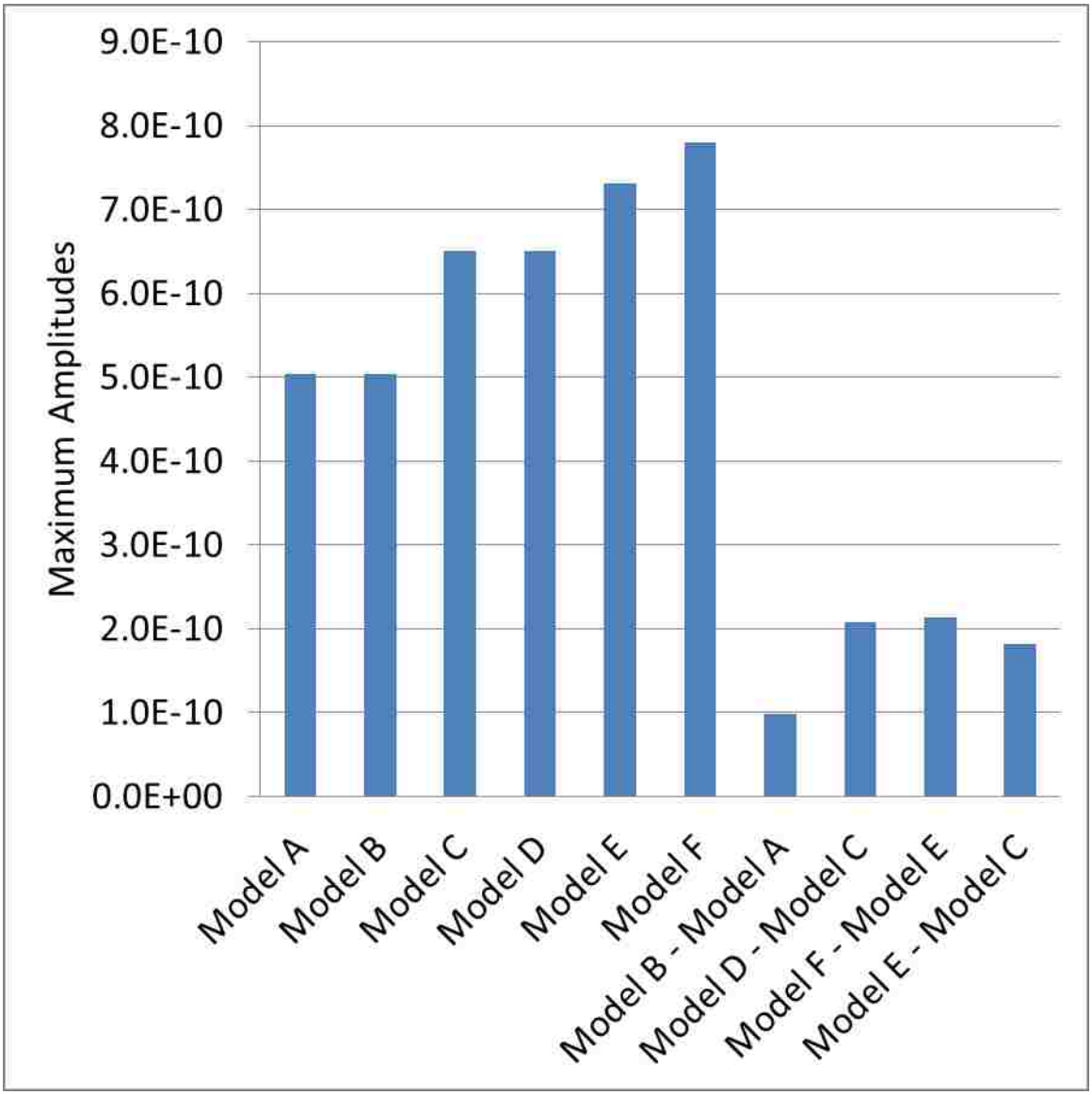

Figure 4.30 Maximum amplitudes from all models' time histories in the vertical direction using a superimposed 25 Hz and 100 Hz Ricker wavelet source.

CHAPTER 5 NUMERICAL MODELING OF THE ENGINEERING GEOPHYSICS TEST SITE EXPERIMENT

This chapter contains results from the tests to detect and delineate cavities conducted using synthetic data that attempts replicating EGTS experimental data (Luke and Calderón-Macías 2008), using Model E and Model F. Analysis products include time histories, time histories residuals, overtone images, overtone image residuals, stacks of overtone images from Model E using a convolved real hammer source, and stacks of overtone images from Model F using a convolved real hammer source.

Models E and F differ from Models C and D only in the following aspects: all time histories and overtone images presented use either a 50 Hz Ricker wavelet source or a convolved real hammer source, and Models E and F have four layers whereas Models C and D have two layers. Computations using a Ricker wavelet source are presented to give a simplified example of time histories and overtone images which can be compared to the convolved real hammer source time histories and overtone images. The patterns expected in the data are easier to follow when using a Ricker wavelet source with a single central frequency versus a convolved real hammer source. Refer to Figure 3.5, Figure 3.10, Table 3.1, and Table 3.5 for more information on how Model E and F are set up.

5.1 MODEL E – FOUR-LAYER MODEL

A set of time histories from Model E in source location 1 is displayed in Figure 5.1; the amplitudes are multiplied by 50. This was the first of 27 source locations used. The

calculated times of arrival are overlaid on the figure. The first, second, and third red line according to time are, respectively, the calculated P-wave arrival time, the calculated S-wave arrival time, and the calculated Rayleigh wave arrival time adjusted for negative delay. Model E time histories can be compared to Model C time histories. Model C is a two layer model, whereas Model E is a four layer model. The difference in layering is described in chapter 3. The layers Model E has, that Model C does not have, are hard to identify by comparing the time histories in the two figures. The time histories created from Model E data display dispersion and resonance, which also occurs in the time histories created from Model C. The amplitude of the resonance pulses with respect to the initial pulses is large. The resonance masks the part of the wavetrain that is needed to detect the cavity.

The time histories residual of Model E using a 50 Hz Ricker wavelet subtracted from Model C using a 50 Hz Ricker wavelet is displayed in Figure 5.2. The amplitudes in the figure are not scaled, whereas the amplitudes in Figure 5.1 are multiplied by 50. Model C and Model E do not contain cavities, so the difference in the time histories is caused only by adding layers to the model. The wave pattern displayed in this residual is caused by the added layers, which should make the synthetic model more closely resemble the experimental data. Any fluctuations caused by the additional layers appear to be masked by the resonances.

Convolution and deconvolution are covered in section 3.2. The time histories for Model E using the CRS are displayed in Figure 5.3, for the first of 27 source locations used. The red line in the figure is the P-wave arrival times, the slope of the arrivals is the same as the previously calculated arrival time line in Figure 5.1, and the first arrival of the first trace is handpicked. Recall that the time history from the EGTS in Figure 3.8 was used for convolution, and it has a picked P-wave arrival time of 0.0235 seconds. The picked P-wave arrival of the first receiver in the figure is 0.0235 seconds also, therefore the arrival times match what is predicted based on the real source. The predominant energy in the figure is Rayleigh wave energy; this statement is based on observation, backed by the demonstration by Richart et al. (1970) that showed the majority of the total energy released from a circular footing undergoing vertical oscillations at the surface of a homogeneous half-space is Rayleigh wave energy. Less resonance appears when using the CRS than the Ricker wavelet source.

Recall that how overtone images were calculated was described in section 3.1.5. The overtone image created for Model E source location 1 is displayed in Figure 5.4. Similar to Figure 4.17, in the overtone images a black line with X marker symbols is the calculated fundamental mode theoretical dispersion curve and the red line with X marker symbols is the calculated first-higher order mode dispersion curve. The two curves intersect at approximately 36 Hz. Measurable response in the overtone image for Model E ranges in frequency from 38 Hz to 100 Hz. The overtone image for Model E after filtering using a CRS is displayed in Figure 5.5. The anticipated bend in the dispersion curve occurs at a lower frequency in Figure 5.5. Measurable response in this overtone

image is from 38 Hz to 114 Hz, with a low amplitude section between 66 Hz and 75 Hz. From 75 Hz to 114 Hz the high amplitudes in the overtone image closely follow the theoretical dispersion curve, and from 38 Hz to 66 Hz the theoretical dispersion curve is slightly lower in velocity than the high amplitudes. The CRS overtone image more closely resembles (having a similar frequency range and velocity range) the experimental overtone image (Luke and Calderón-Macías 2008; Figure 3.12) than does the Ricker wavelet overtone image. The CRS is more useful for comparison to the experimental data so stacks of overtone images using the CRS will be presented in the rest of this chapter. Corresponding stacks of overtone images using the Ricker wavelet source are presented in the appendix.

Stacks of overtone images are created in the same way as described in section 4.5. Model E does not contain a cavity; therefore, these figures are an example of a stack of overtone images for a layered medium without cavities present. A stack of overtone images according to velocity containing the sum of all receivers for the multiple source location tests in Model E using a CRS is displayed in Figure 5.6. A similar stack of the same overtone images according to frequency is displayed in Figure 5.7. Similar stacks of overtone images for Model E using a 50 Hz Ricker wavelet source are presented in the appendix. In both figures, the number one on the *X* axis is the first (southernmost) source location, and 27 on the *X* axis is the last source location. The frequency range for heightened amplitude in Figure 5.6 is from 5 Hz to 114 Hz, similar to the measureable response in the single overtone image shown in Figure 5.5. In Figure 5.8 the higher mode is seen in the 600 m/s to 800 m/s range.

5.2 MODEL F AND MODEL F* – FOUR-LAYER MODEL INCLUDING CAVITIES

A set of time histories for Model F in the vertical direction using a 50 Hz Ricker wavelet source is displayed in Figure 5.8; this was the first of 27 source locations used. In the time histories presented in the figure Model F contains two pipe-shaped cavities (30 m in length). In the figure the direct arrival times follow the same pattern as Figure 5.1. In the figure the blue lines are the calculated scattered wave arrival times caused by interaction with the cavities (located beneath receivers number 16, 17, 46, and 47) in this synthetic model. Model F time histories in the figure should be compared to Model D time histories (Figure 4.18). The layers Model F has, that Model D does not have (as shown in Table 3.6), are hard to identify by comparing the time histories in the two figures. Model F's time histories also display strong resonance, similar to Model E's time histories.

Figure 5.9 displays the time histories residual of Model E subtracted from Model F in the vertical direction. The computed arrival times shown in Model F's time histories are repeated to facilitate comparison. One cavity is located at the earliest wave arrival, under receivers 16-17, and the other is located under receivers 46-47. The time histories in the figure show a wave pattern that forms an arrow over each cavity when the time arrivals are traced. The arrows point at the locations of the cavities. Residuals of time histories are useful for identifying the location of the cavities in Model F, however they are less practical to use in experimental data.

The time histories for Model F after filtering and convolution with the sledgehammer data are displayed in Figure 5.10. Figure 5.3 (no cavity) and Figure 5.10 can be more directly compared to experimental time histories from the EGTS since they use the same hammer source, instead of a synthetic Ricker wavelet source.

The overtone image created for Model F, source position 1 of 27, is displayed in Figure 5.11. It is overlaid by the same dispersion curves as the overtone image created for Model E. If the dispersion curve were hand-picked, a curve following the highest amplitudes would have been chosen; the curve could not be picked below a frequency of 40 Hz. Higher mode data do not appear in the overtone image. The overtone image residual of Model E subtracted from Model F (source position 1) is displayed in Figure 5.12. The residual demonstrates that the difference between Model E and Model F is mainly in the frequency range 40 through 100 Hz, and has slightly higher velocities than Model F (Figure 5.11). The residual also has a lower amplitude section with respect to Model F (Figure 5.11), between 51 Hz and 53 Hz. The black line depicts the fundamental mode dispersion curve, and the red line is the dispersion curve for the first higher mode. These are the same dispersion curves presented with Model E and Model F overtone images, to facilitate comparison. This residual plot implies that the effect of the cavities in the overtone images created for Model F should be looked for in the frequency and velocity range seen in Figure 5.12. The overtone image for Model F, source location 1, after filtering using a CRS is displayed in Figure 5.13. The signal ranges in frequency from 38 Hz to 114 Hz, with a low amplitude section between 66 Hz and 75 Hz. With

respect to Model E, the frequency range is the same and the low-amplitude section is also the same.

The overtone image for Model F* (finite cavity; Figure 5.14), source position 1, is visually indistinguishable from the overtone image for Model F (Figure 5.13). All of the overtone images to be stacked for Model F* are displayed sequentially in Figure 5.14. This figure is created from the receivers located in the positive *X* direction from the source position. The images are arranged from left to right where the top left is for source position 1 and the bottom right is for source position 26. There are 26 overtone images because the 27th source location is beyond the end of the receiver array, so it would contain only receivers in the negative *X* direction. The data in the overtone images in the figure are not normalized. Source locations 8 and 18 are at the locations of the cavities. By visual inspection, the overtone images for Model E (not shown) appear identical to those for Model F*, for all source locations.

The areas of highest amplitude in the stack of overtone images represent the locations of the cavities; in Model F, one is located at source location 8 and the second is located at source location 18. A stack of overtone images according to velocity containing the sum of all receivers for the multiple source location tests in Model F, using a CRS, is displayed in Figure 5.15. A similar stack of the same overtone images according to frequency is displayed in Figure 5.16. A stack of overtone images according to velocity containing the sum of all receivers for the multiple source location tests in Model F*,

using a finite cavity shape and a CRS, is displayed in Figure 5.17. A similar stack of the same overtone images according to frequency is displayed in Figure 5.18. High-amplitude values spreading over broader frequency ranges appear near the locations of the cavities (source location 8 and 18) in Figure 5.15 and Figure 5.17. The CRS response has higher frequency content than the 50 Hz Ricker wavelet source used (recall the power spectrum of the CRS; Figure 3.9). Stacks of overtone images visually locate cavities along a line of receivers in synthetic models D and F, whereas analyses of time histories for Model D in Figure 4.18 and for Model F in Figure 5.8 do not identify the cavity location. The location of the cavities is able to be observed in the stacks of overtone images, whereas it is not able to be observed in the individual overtone images.

Comparing Figure 5.15 to Figure 5.17 allows the difference to be seen between modeling with a pipe-shaped cavity (30 m in length) versus a finite cavity shape (0.9 m in length). A pipe-shaped cavity is simpler to detect (has a stronger response) than a finite-shaped cavity in a stack of overtone images, which is expected because of the large size. A pipe shaped cavity is closer in relation to what is expected in a 2-D model than a finite-shaped cavity which is closer in relation to what is expected in the experimental data, which targets buried barrels. Even though the barrel is a much smaller target the stacks of overtone images are still able to show the cavity location.

Figure 5.19 compares the stacks of overtone images according to velocity from Models E and F* using a CRS, and the experimental data at the EGTS (Luke and Calderón-Macías

2008). The same overtone images stacked according to frequency are displayed in Figure 5.20. The top stack of overtone images is Model E, which does not contain a cavity; the middle stack of overtone images is Model F*, using a CRS that contains two finite cavities at source location 8 and 18; the bottom stack of overtone images is from the EGTS experimental data (Luke and Calderón-Macías 2008) which contains two cavities at 10 m and 20 m from the first receiver. All stacks of overtone images in the figures are the sum of all receivers in the north and south or positive and negative *X* directions. The stack for Model E has a smooth shape in its high-amplitude area (red), while the stack for Model F* has a rougher shape in its high-amplitude area. For Model F*, the largest high-amplitude areas occur at the locations of the cavities. The stack of overtone images for the EGTS experiment has a distorted shape in its high-amplitude area; it demonstrates the effect of noise, and is more complex to identify cavity locations from. Comparing the synthetic Model F* data to the experimental data from the EGTS (Luke and Calderón-Macías 2008), the stacks of overtone images share similarities. High-amplitude values spreading over broader frequency ranges appear near the locations of the cavities in both cases.

Considering differences between the experiment and the model, the experiment has cavities with a circular cross section and uses a source offset with respect to the line of receivers of 0.2 m; whereas Model F* contains cavities with a square cross section and uses a source offset of 0.5 m. The difference in source offset is not expected to create a difference in recorded amplitude recorded, however, the effect was not investigated. The rectangular cross section in the synthetic model is a reason to expect larger amplitudes of

waves scattered from the cavity with respect to the experiment where the cavities have a circular cross section (Gelis et al. 2005). The impact of this difference remains to be explored.

This chapter covered the results from Models E, F and F* which attempt to replicate the experimental data at the EGTS (Luke and Calderón-Macías 2008). This chapter also includes time histories, time histories residuals, overtone images, overtone image residuals, stacks of overtone images from Model E using a convolved real hammer source, and stacks of overtone images from Model F using a convolved real hammer source. The next chapter (chapter 6) contains the discussion and conclusions to this research.

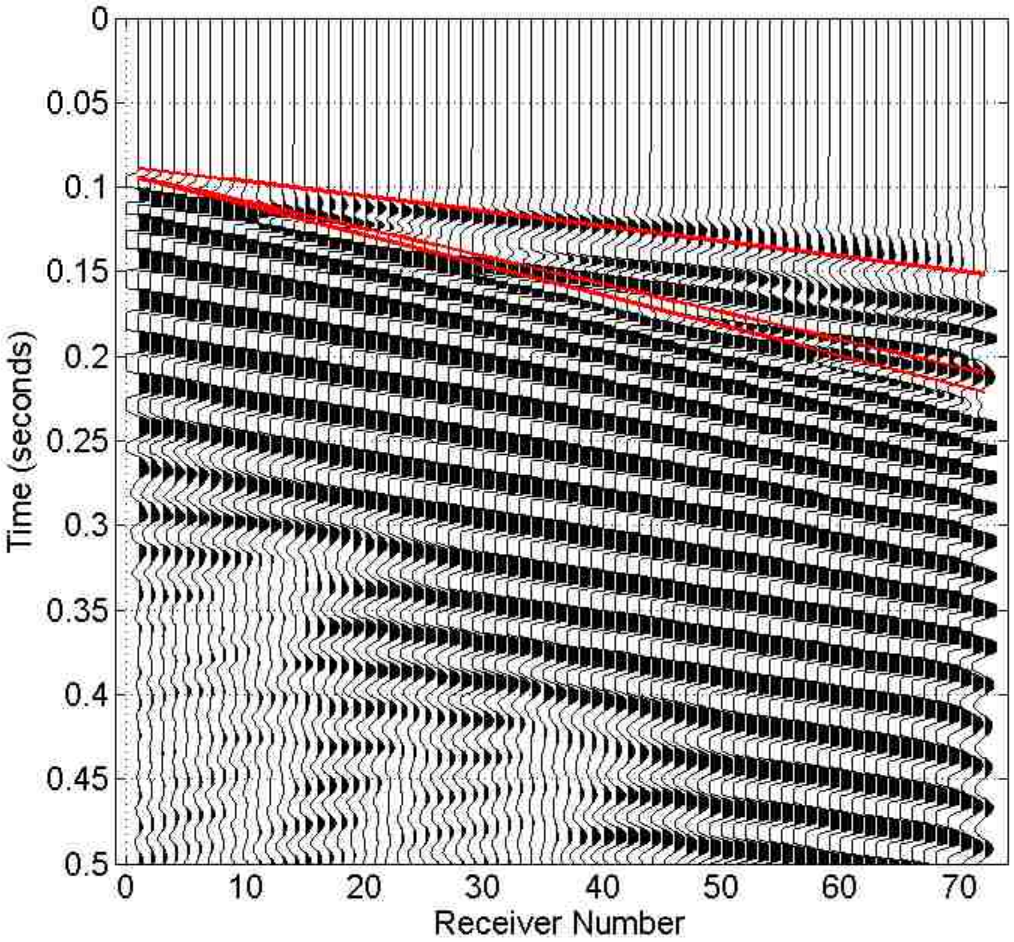

Figure 5.1 Model E vertical direction time histories using a Ricker wavelet 50 Hz source (Shot 1 of 27). The first, second, and third red lines according to time are, respectively, the calculated P-wave arrival time, the calculated S-wave arrival time, and the calculated Rayleigh wave arrival time. The source is located at (3, 15.5, 1), receiver number 1 is located at (5, 15, 0), and receiver number 72 is located at (28.7, 15, 0). The calculated arrival times are shifted by a 17-millisecond (0.017 second) negative delay (earlier in time).

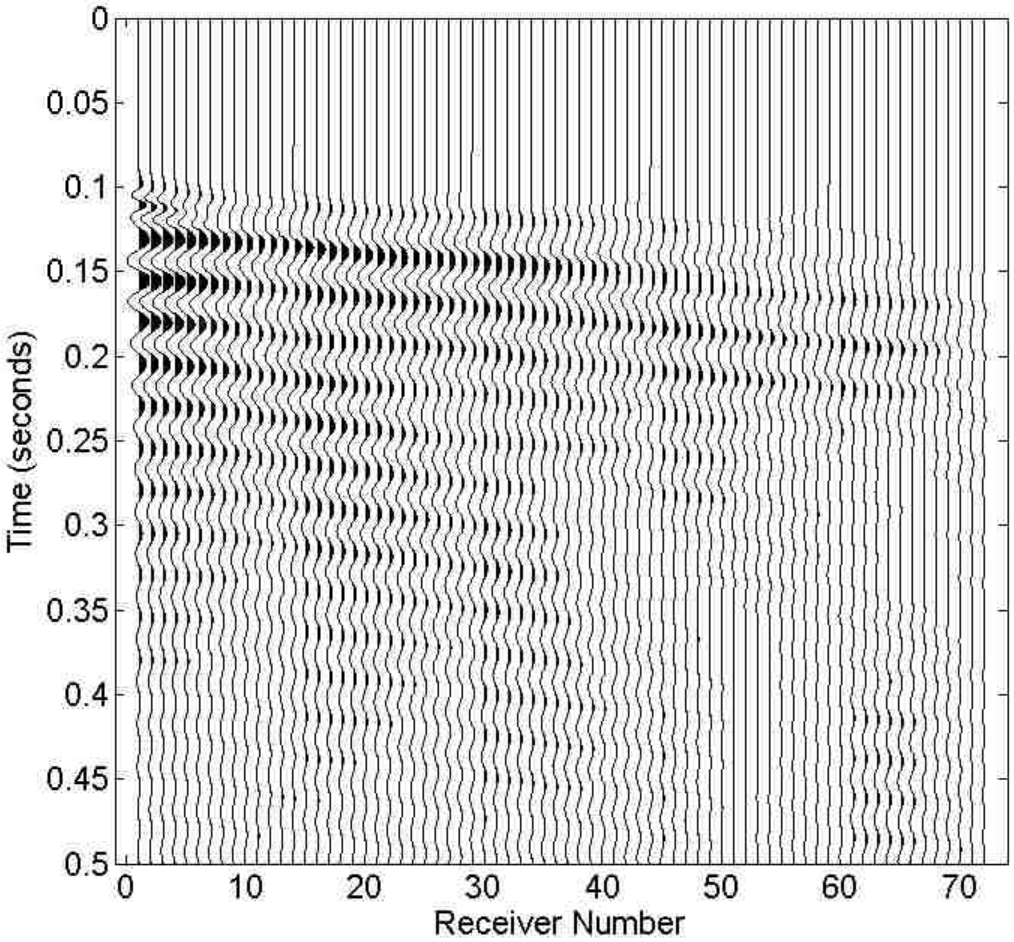

Figure 5.2 Residual of Model C subtracted from Model E vertical direction time histories. Parameters are as described in Fig. 5.1. The amplitudes are not scaled.

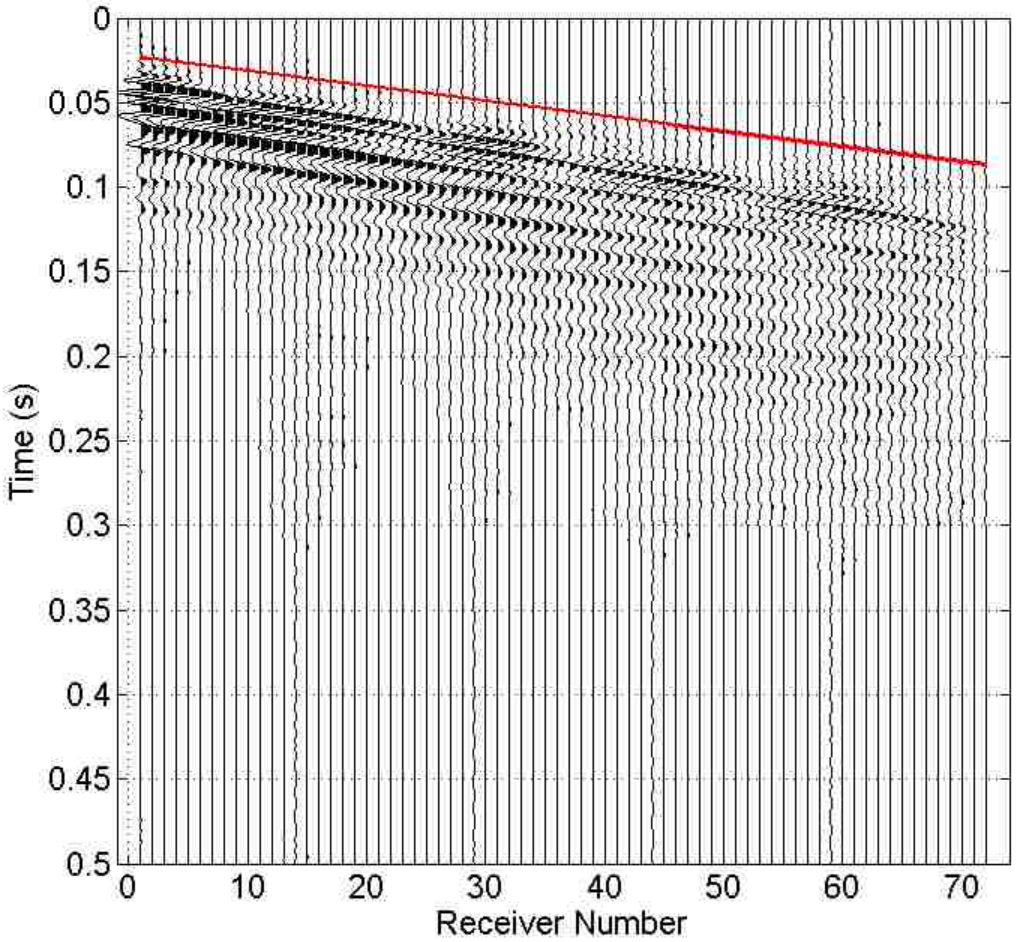

Figure 5.3 Model E vertical direction time histories for a filtered convolution of a real source (Shot 1 of 27). The red line is picked P-wave arrival time, where the first receiver is picked at 0.0235 seconds. Parameters are as described in Fig. 5.1.

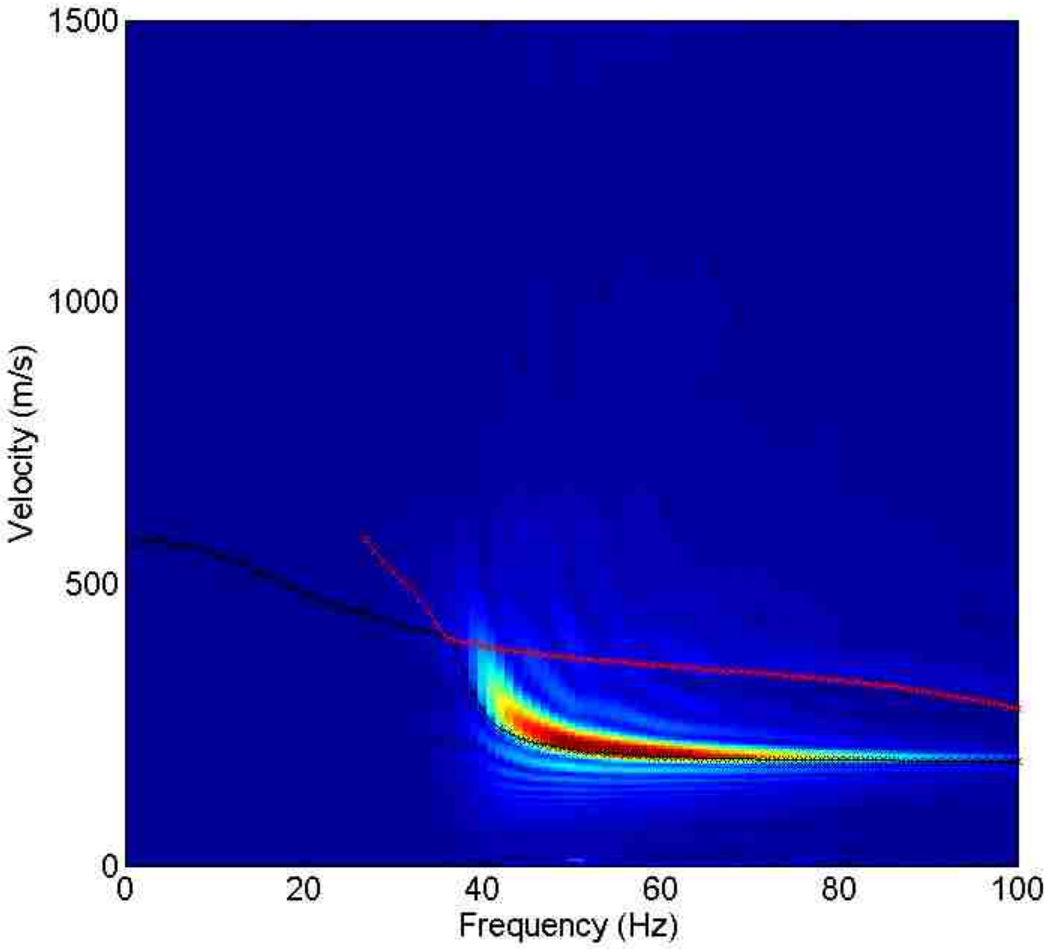

Figure 5.4 Overtone image created from Model E corresponding to the time histories in Fig. 5.1. The data are not normalized. The black line and red line with X marker symbols are the calculated fundamental mode theoretical dispersion curve and the calculated first-higher order mode dispersion curve, respectively.

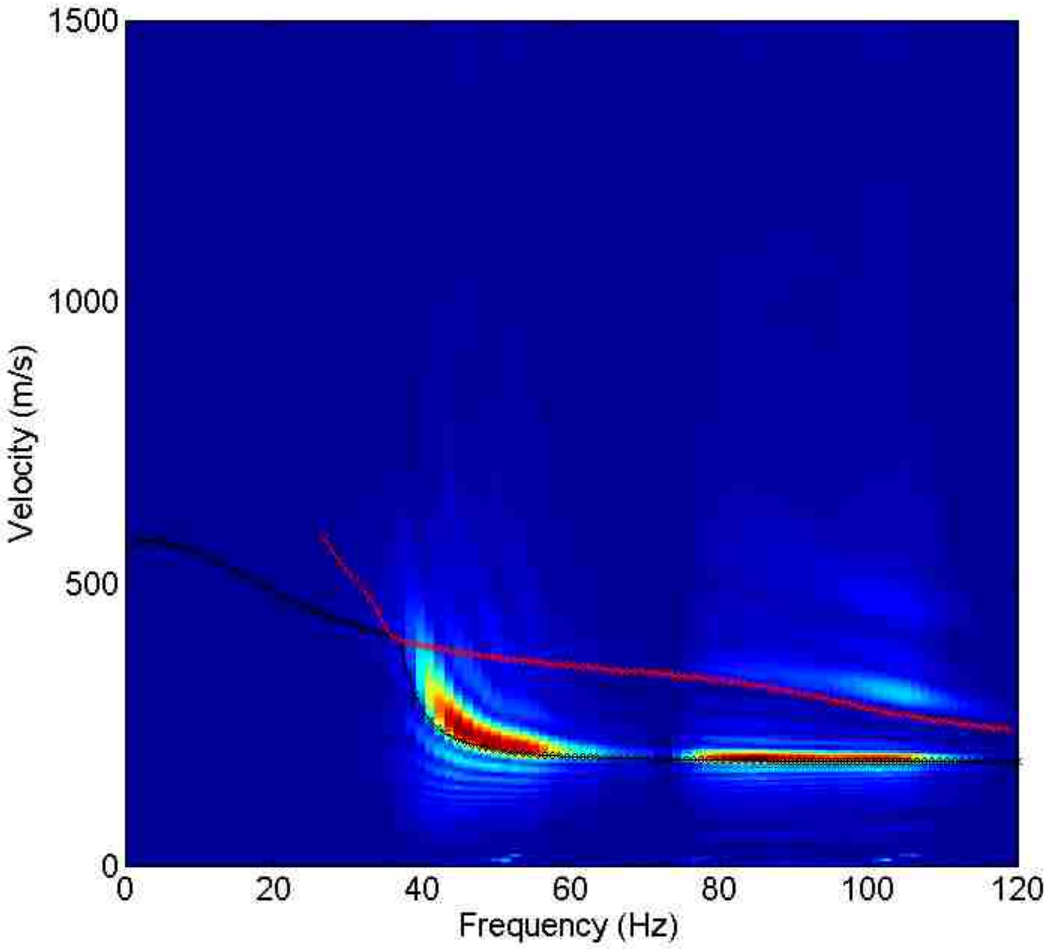

Figure 5.5 Overtone image from Model E using a filtered convolution of the real source (Shot 1 of 27). Parameters are as described in Fig. 5.1.. The overtone image for Model E using a convolved real source ranges in frequency from 38 Hz to 114 Hz, with a low amplitude section between 66 Hz and 75 Hz.

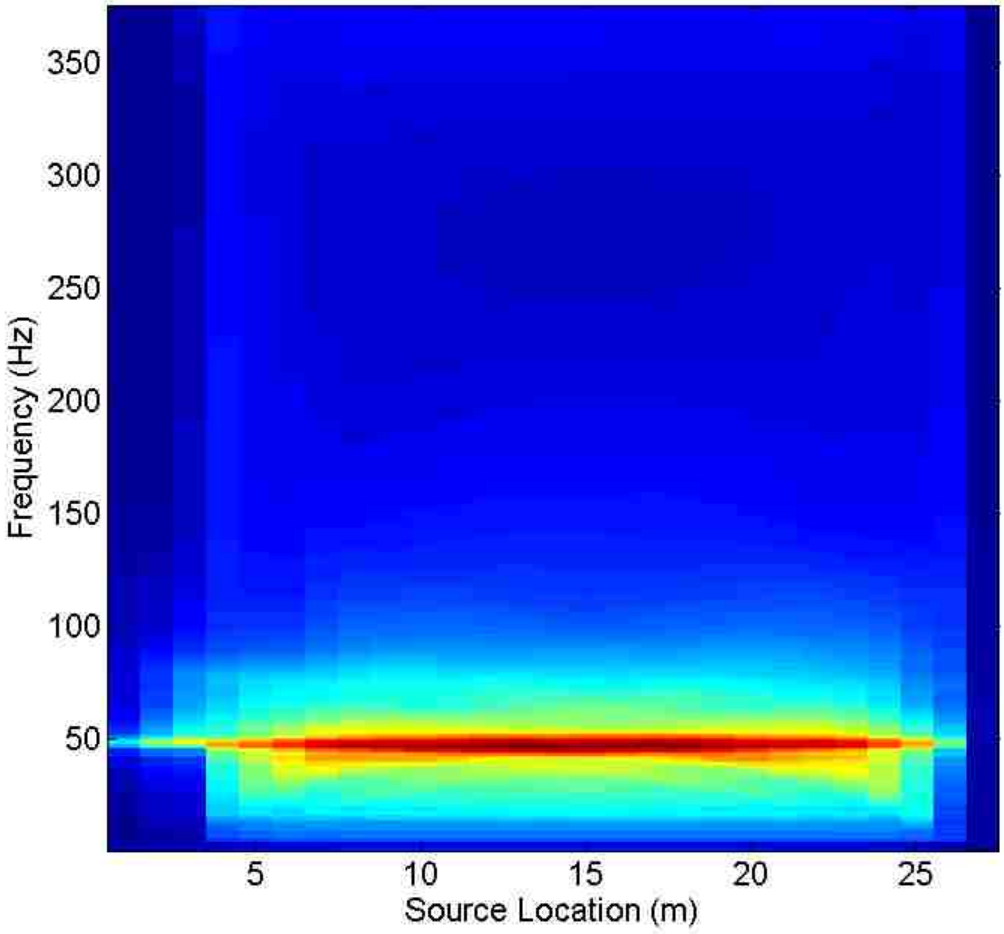

Figure 5.6 Stack of overtone images according to velocity using Model E with a convolved real hammer source in multiple source locations.

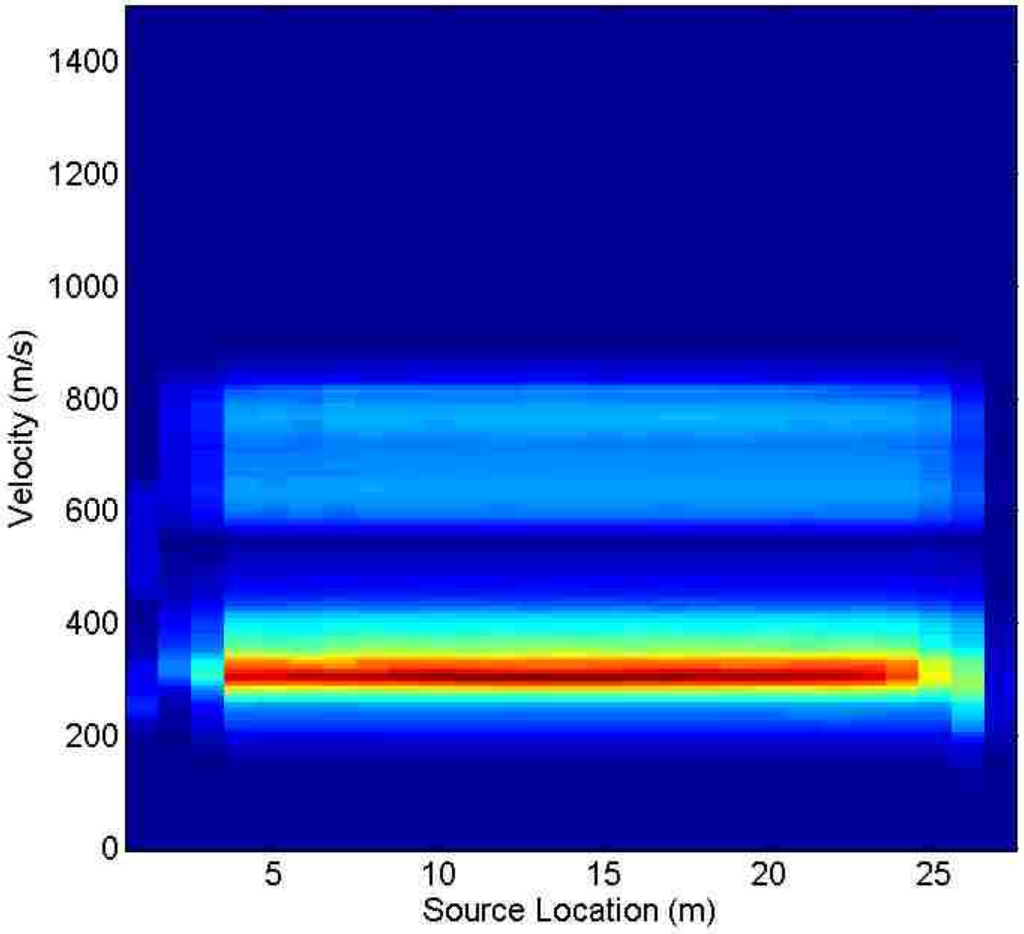

Figure 5.7 Stack of overtone images according to frequency using Model E with a convolved real hammer source in multiple source locations.

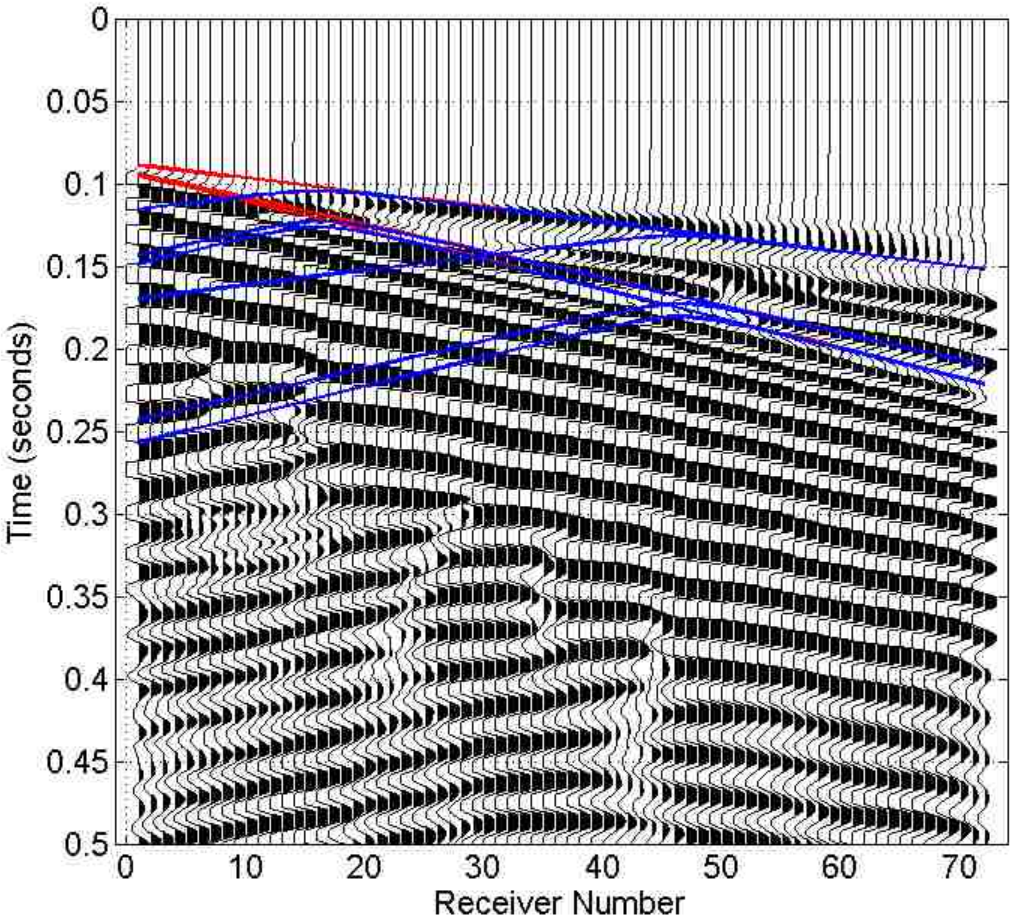

Figure 5.8 Model F vertical direction time histories using a Ricker wavelet 50 Hz source (Shot 1 of 27). The first, second, and third red lines according to time are, respectively, the calculated direct P-wave arrival, the calculated direct S-wave arrival, and the calculated direct Rayleigh wave arrival. The same pattern applies to the blue lines which are calculated scattered wave arrival times caused by interaction with the cavities (located beneath receiver number 16, 17, 46, and 47) in this synthetic model. Parameters are as described in Fig. 5.1.

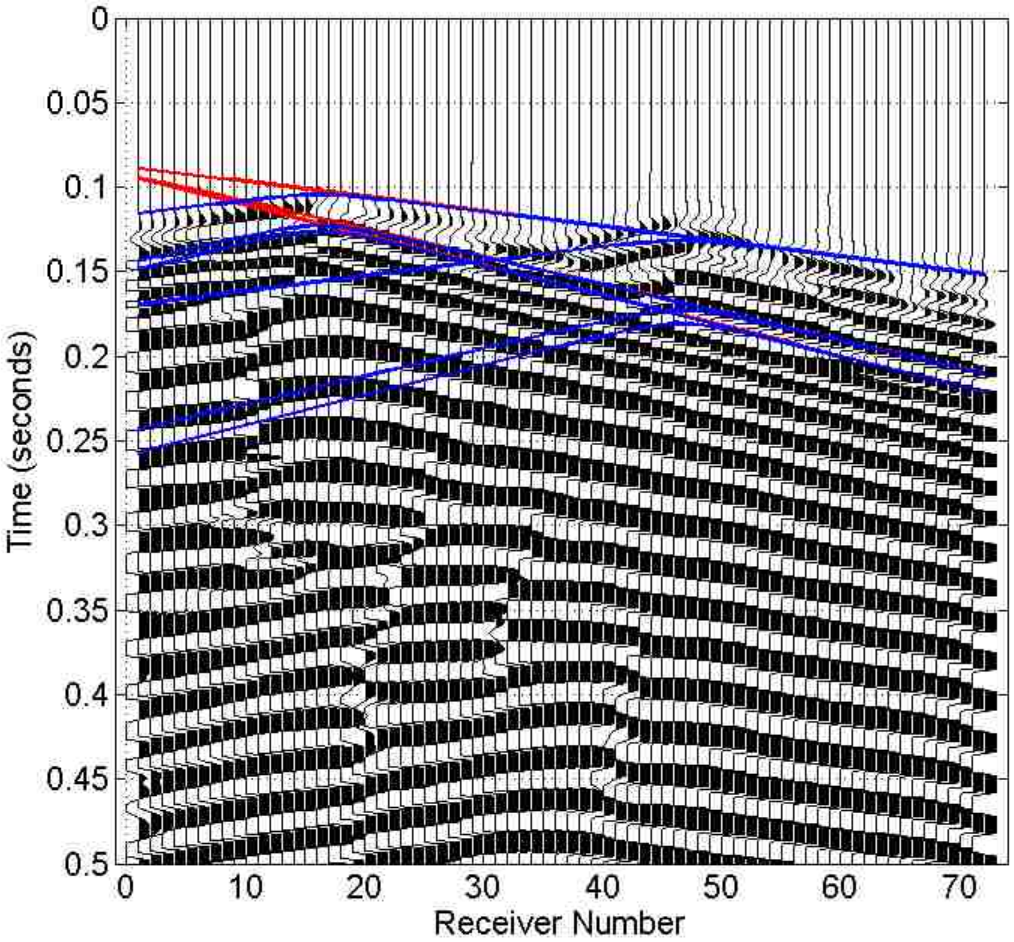

Figure 5.9 Residual of Model E subtracted from Model F, vertical direction time histories. Parameters are as described in Fig. 5.1 and 5.8.

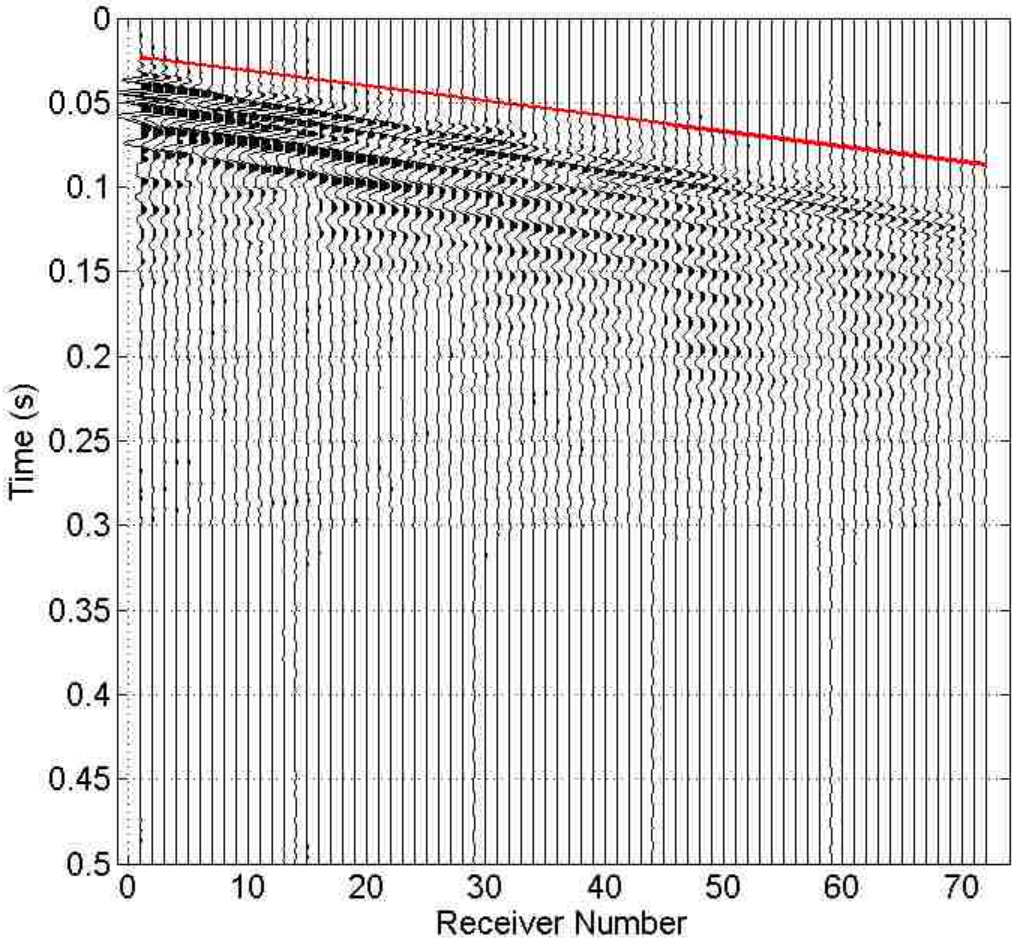

Figure 5.10 Model F filtered time histories from convolution of real source (Shot 1 of 27). The red line is picked P-wave arrival time. Parameters are as described in Fig. 5.1.

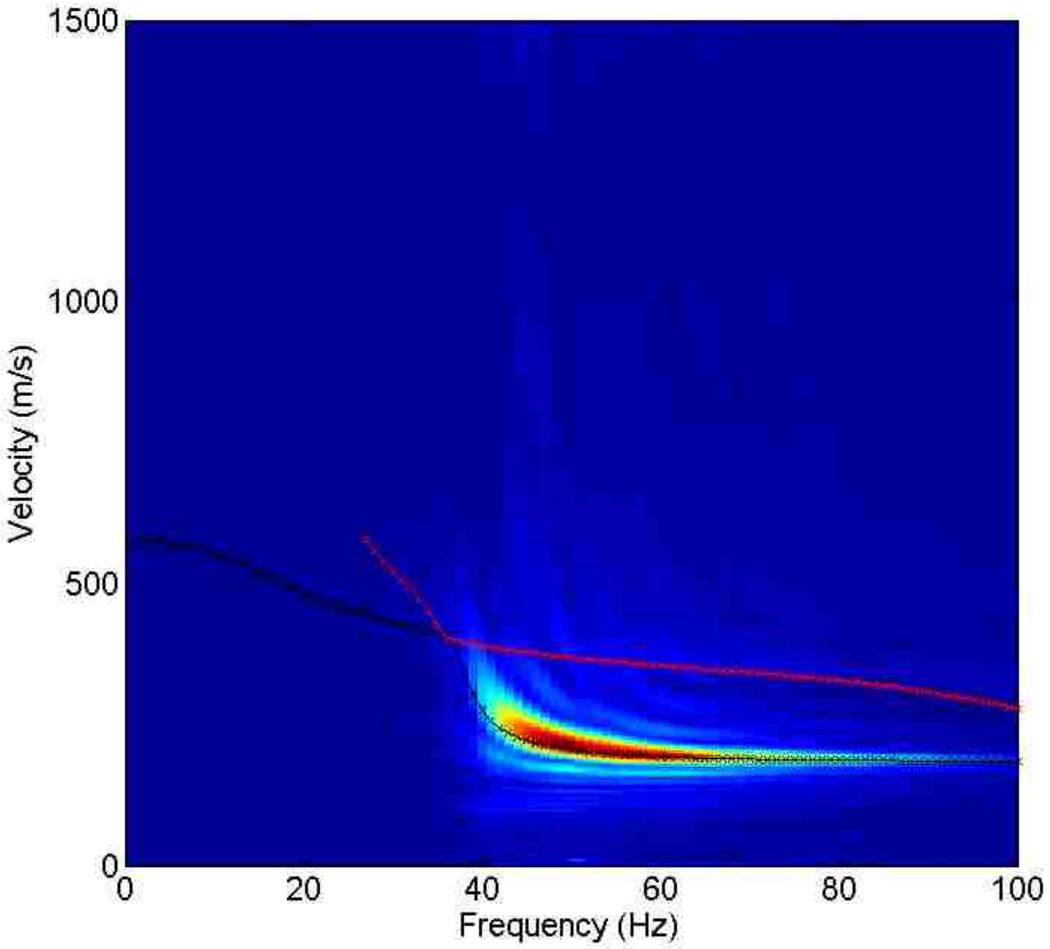

Figure 5.11 Overtone image created from Model F data corresponding to the time histories in Fig. 5.8. The data are not normalized. Parameters are as described in Fig. 5.1 and 5.4.

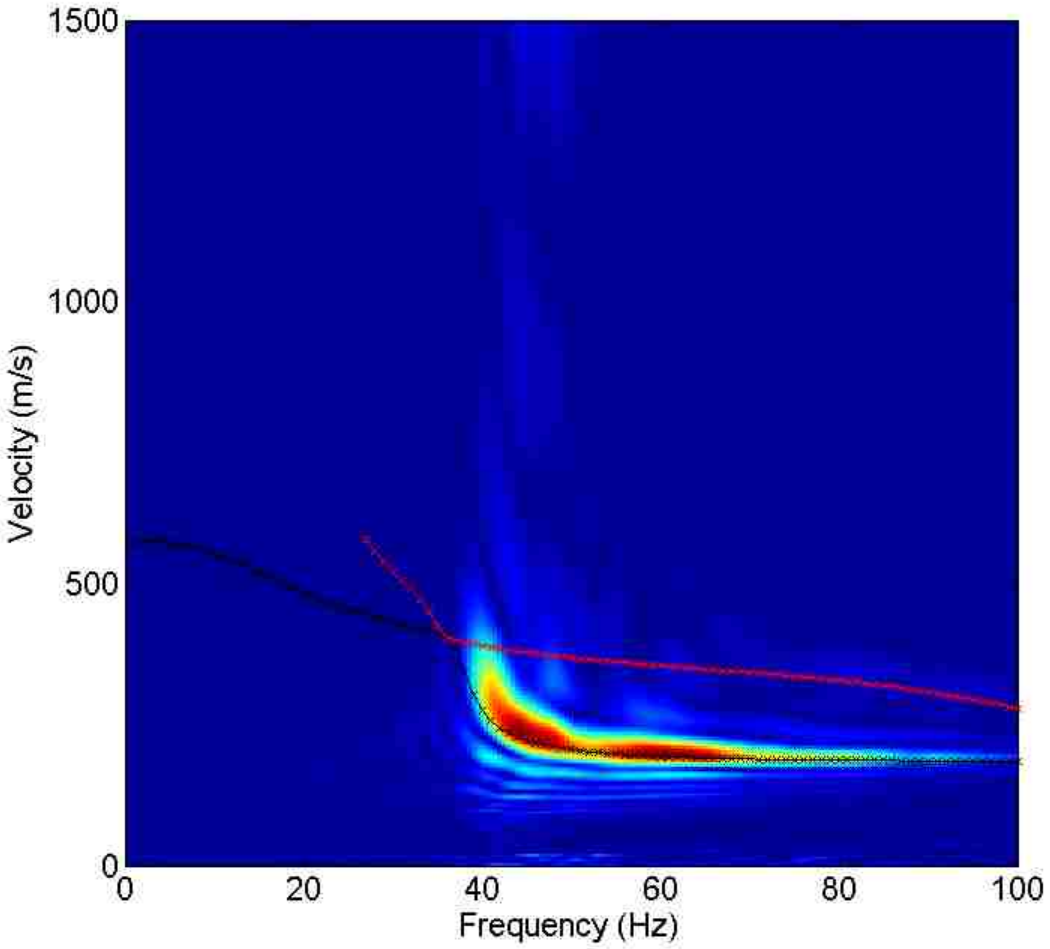

Figure 5.12 Overtone image residual of Model E subtracted from Model F corresponding to the time histories in Fig. 5.9. The data are not normalized. Parameters are as described in Fig. 5.1 and 5.4.

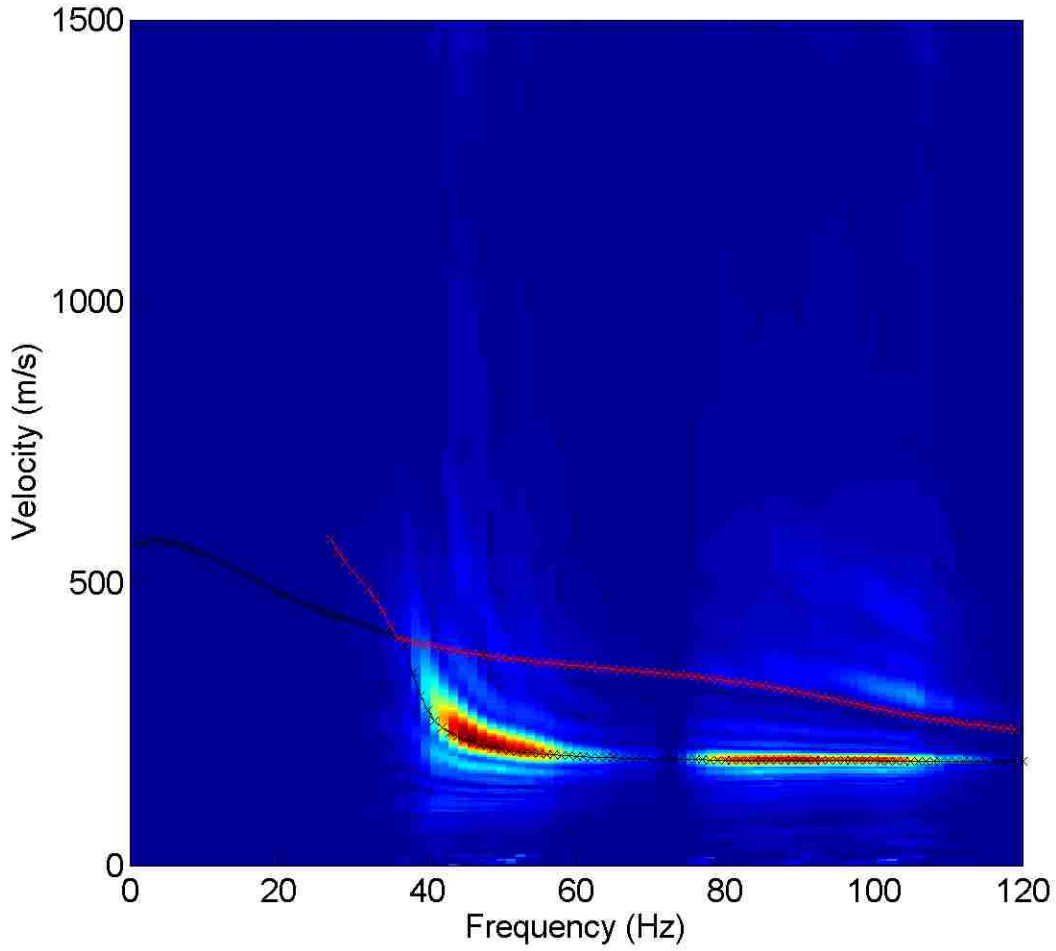

Figure 5.13 Model F filtered convolution of real source overtone image (Shot 1 of 27). The data are not normalized. Parameters are as described in Fig. 5.1 and 5.4.

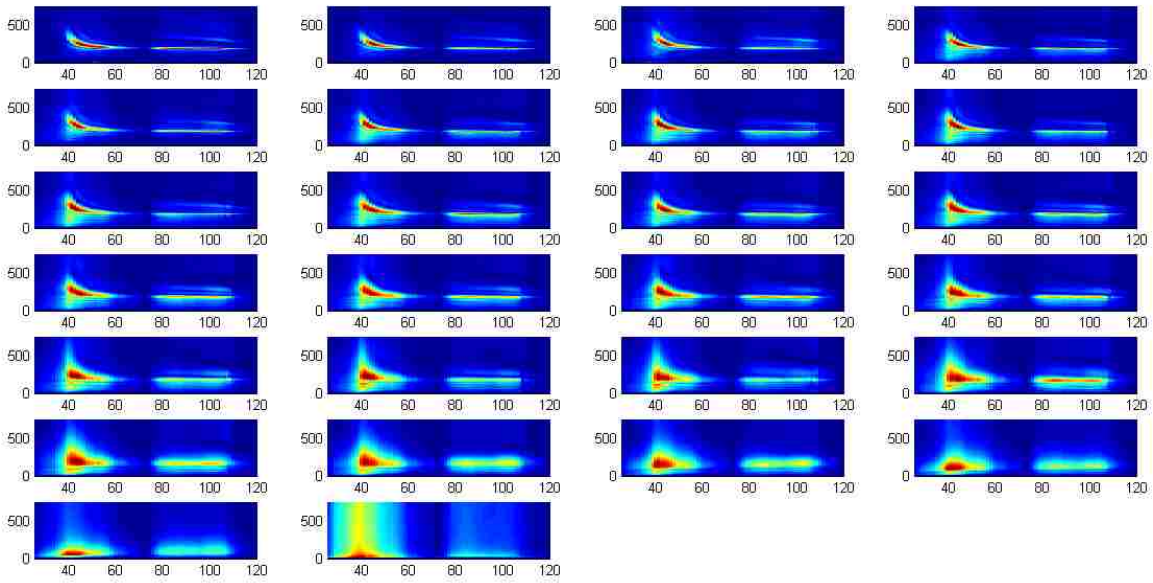

Figure 5.14 Overtone images in the positive *X* direction using Model F* with a convolved real source in multiple source locations and a finite cavity. The figures are arranged from left to right where the top left is source location 1 and the bottom right is source location 26. In all overtone images the *X* axis is frequency in Hz, and the *Y* axis is velocity in m/s. The cavities are located at source locations 8 at (10, 15.5, 1) and 18 at (20, 15.5, 1). These are the images used to create the stack shown in Figures 5.17 and 5.18.

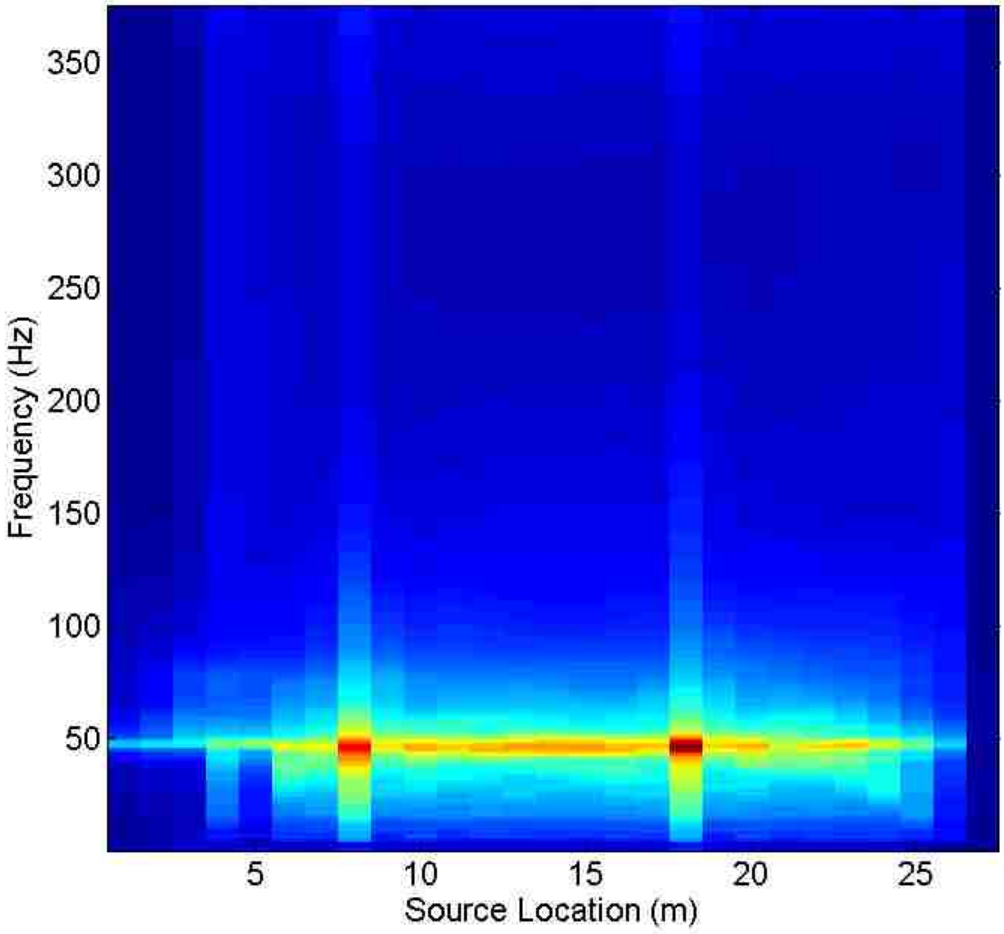

Figure 5.15 Stack of overtone images according to velocity using Model F with a convolved real source in multiple source locations and a pseudo-2D cavity. The cavities are located at source locations 8 at (10, 15.5, 1) and 18 at (20, 15.5, 1).

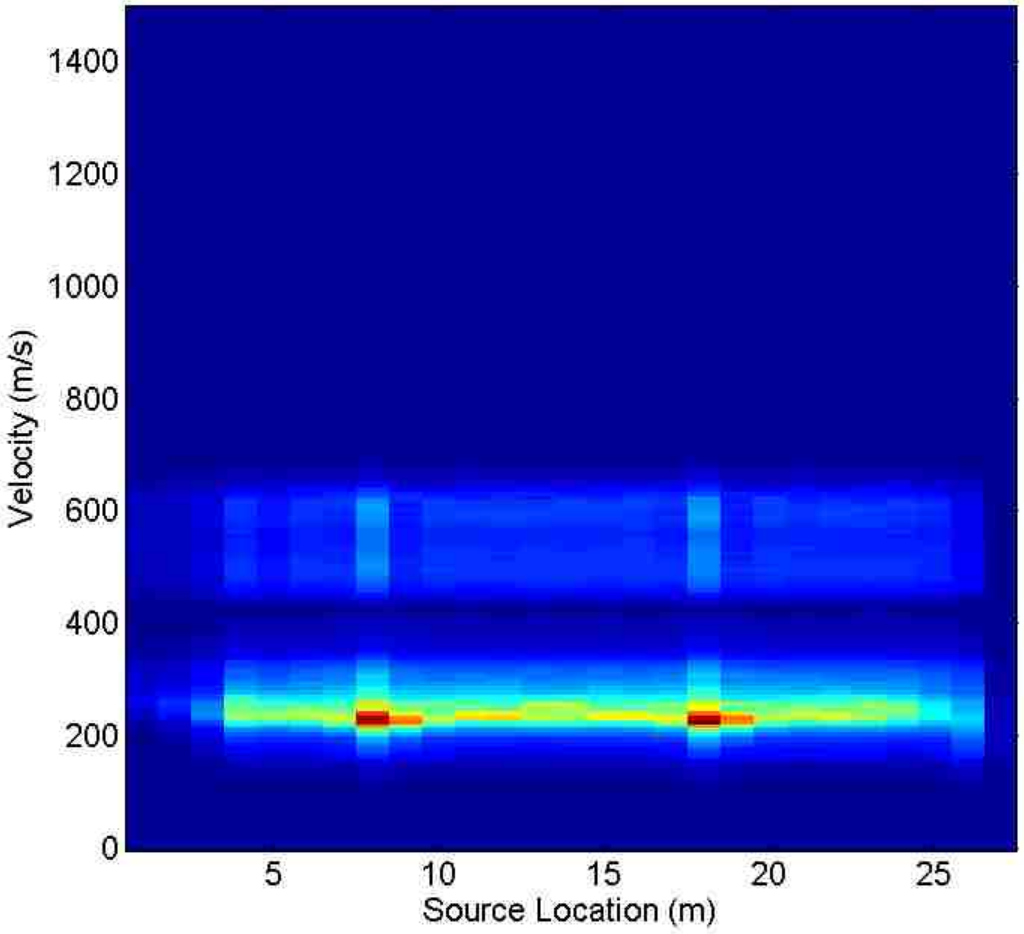

Figure 5.16 Stack of overtone images according to frequency using Model F with a convolved real source in multiple source locations and a pseudo-2D cavity. The cavities are located at source locations 8 at (10, 15.5, 1) and 18 at (20, 15.5, 1).

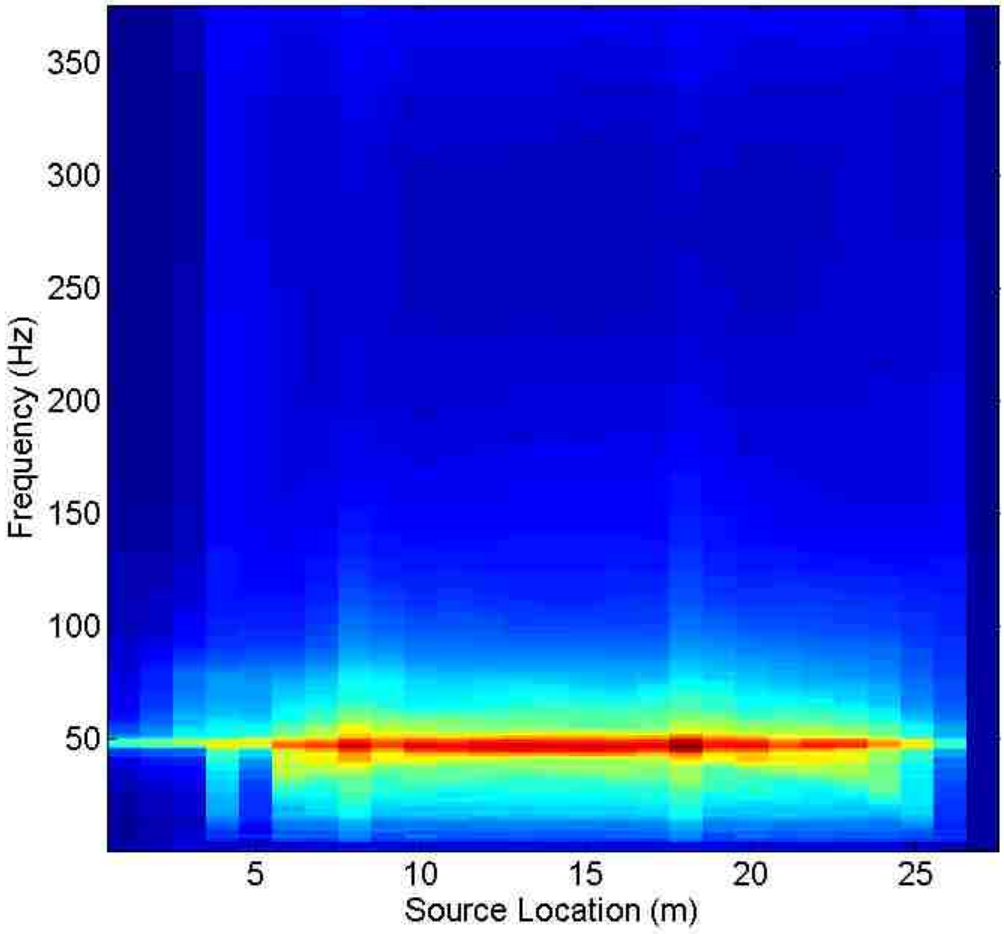

Figure 5.17 Stack of overtone images according to velocity using Model F* with a convolved real source in multiple source locations and a finite cavity. The cavities are located at source locations 8 at (10, 15.5, 1) and 18 at (20, 15.5, 1).

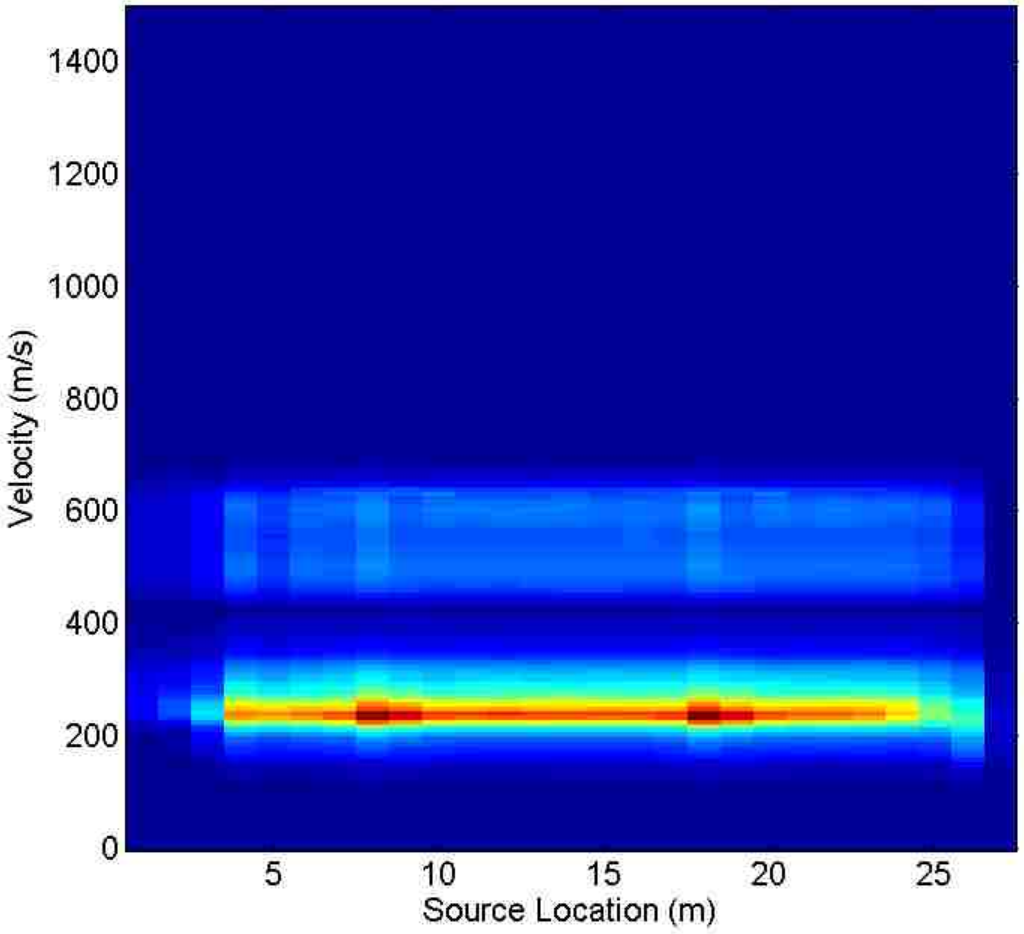

Figure 5.18 Stack of overtone images according to frequency using Model F* with a convolved real source in multiple source locations and a finite cavity. The cavities are located at source locations 8 at (10, 15.5, 1) and 18 at (20, 15.5, 1).

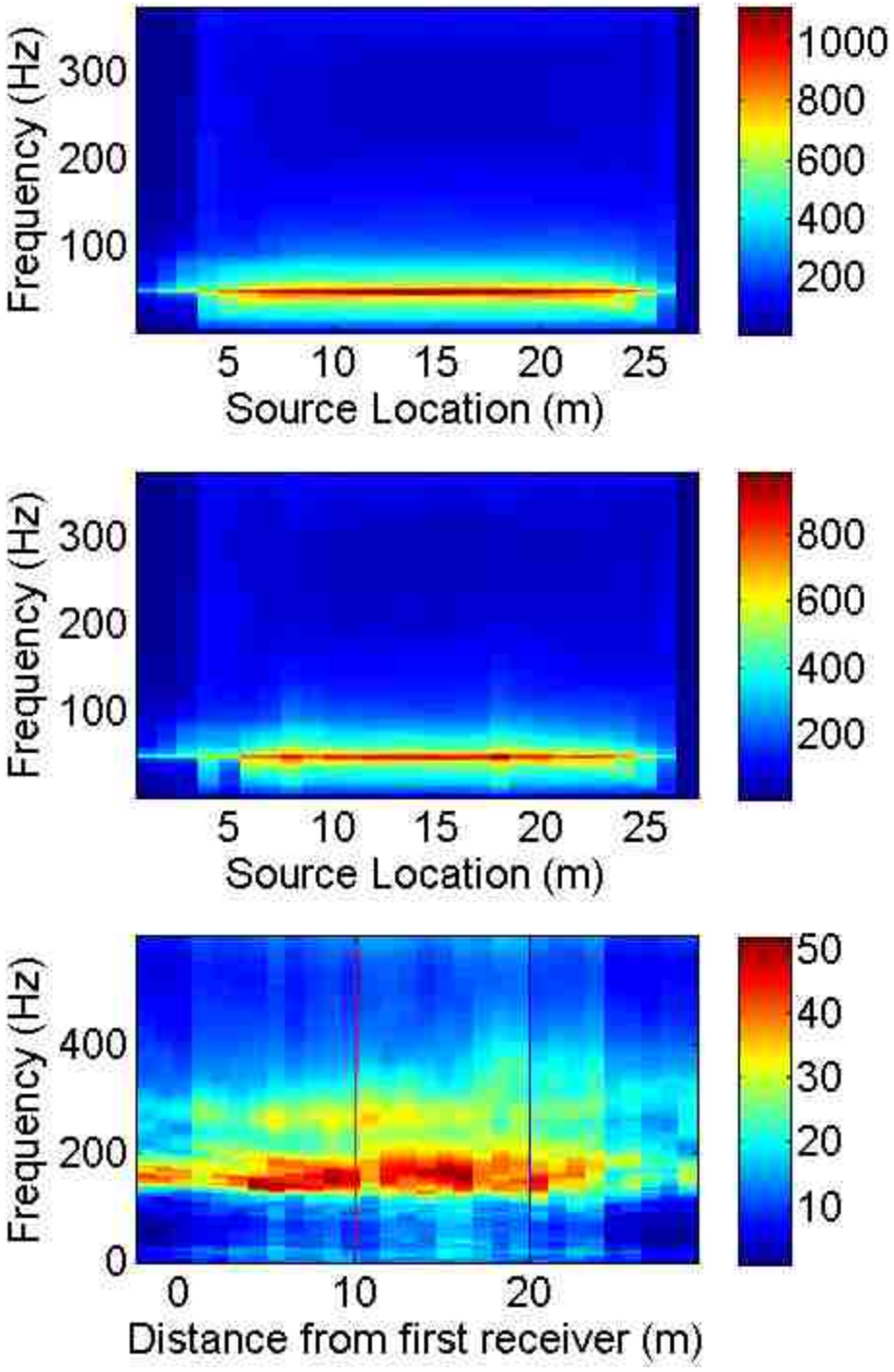

Figure 5.19 Comparison of stacks of overtone images according to velocity from Model E (does not contain a cavity) using a convolved real source, Model F* (two cavities located at source location 8 and 18) using a convolved real source, and the EGTS (two cavities located at 10 m and 20 m from the first receiver) using a hammer source. Model E is displayed at the top, Model F is displayed at the center, and the EGTS is displayed at the bottom.

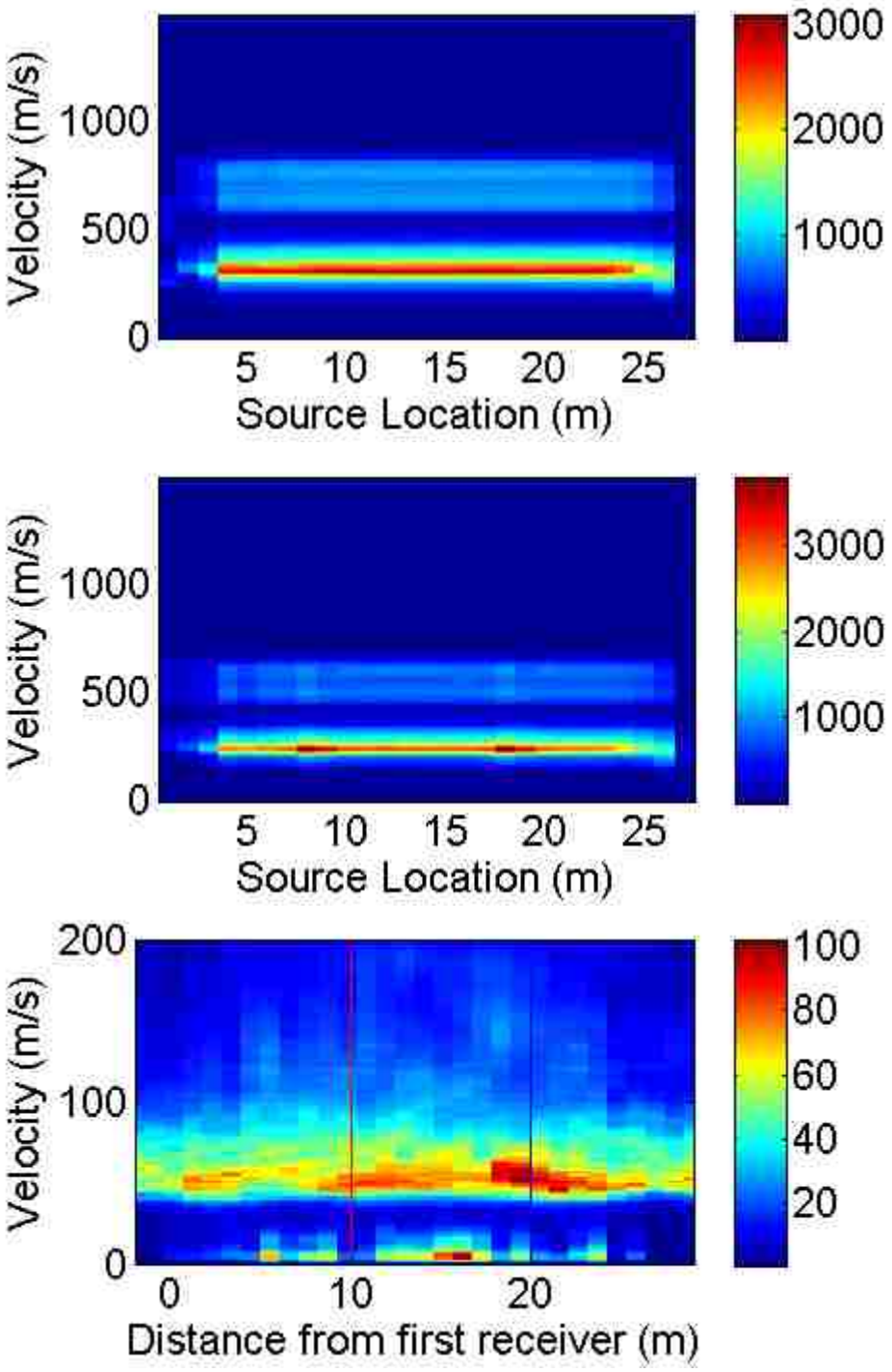

Figure 5.20 Comparison of stacks of overtone images according to frequency from Model E (does not contain a cavity) using a convolved real source, Model F* (two cavities located at source location 8 and 18) using a convolved real source, and the EGTS (two cavities located at 10 m and 20 m from the first receiver) using a hammer source. Model E is displayed at the top, Model F is displayed at the center, and the EGTS is displayed at the bottom.

CHAPTER 6 DISCUSSION, CONCLUSIONS, AND RECOMMENDATIONS

6.1 DISCUSSION

The capacity to share seismology knowledge and methods through the internet has provided an expanded overview of exploration seismology and exploration geophysics for this study. Geophysics and seismology literature shows that cavity detection and delineation methods are constantly being improved. This research advances the ability to detect cavities by using stacks of overtone images to identify the cavities' location. The synthetic models provide a method to demonstrate in controlled conditions whether stacks of overtone images can be useful for cavity detection. Synthetic model data can be compared to experimental data to gain an understanding of what to look for that would identify a cavity, what can be considered noise, and to validate results. The synthetic modeling applied in this research is an existing tool to improve the understanding of the stacking of overtone images for robust anomaly detection which is a new tool. Stacks of overtone images are used to identify cavities in the frequency domain. Nasseri-Moghaddam et al. (2005) present a different frequency domain method to detect cavities and this is also tested in the current research.

In order to identify cavities in a layer system that includes a HVL, this research tested stacks of overtone images using a Ricker wavelet source and also a convolved real hammer source. Stacks of overtone images are a new tool to visually identify cavities in the frequency domain. In the University of Nevada, Las Vegas (UNLV) Engineering Geophysics Test Site (EGTS) experimental data (Luke and Calderón-Macías 2008), a variety of field conditions added complexity to the data. The synthetic model of the

EGTS is based on geophysical data collected previously at the EGTS. A contribution of this research is it provides a mechanism (synthetic modeling) for establishing degree of resolution of the stacks of overtone images.

The normalized-energy-density (NED) cavity characterization parameter from Nasseri-Moghaddam et al. (2005) indicates the approximate (not precise) location of a cavity in an otherwise homogeneous soil system in the synthetic model created in this research. For the same cavity in a two-layer system that includes an HVL, analysis of the NED parameter enables identification of the presence of the cavity, but not its accurate location. The authors found better resolution with the horizontal component than the vertical. In this research, the horizontal (in-plane) data and the vertical data were equally useful in identifying the location of the cavity. The observation by Nasseri-Moghaddam et al. (2005) that wider cavities produce more conspicuous peaks and valleys in the NED parameter should lead to similar results in this research with respect to those authors because they tested square 2D cavities that range from 0.08 m to 0.64 m, whereas this research tests a square cross section that is 0.53 m on a side. Another condition, noted earlier, is that in order for the fluctuations in the NED parameter to be sufficiently large, maximum wavelength must be greater than five times the embedment depth (depth to top of cavity); according to this condition our test scenario (maximum wavelength approximately equal to five times the embedment depth) is only marginally effective for locating a cavity using the NED parameter.

A benefit of stacks of overtone images is they can correctly identify the horizontal location of a cavity or cavities in a multiple-layer system that includes a HVL, such as when caliche is present beneath the cavities, whereas inspections of time histories and individual overtone images are not successful under the same circumstances. In this research another advantage of stacks of overtone images is that multiple cavities can be identified within one test. Exact delineation of cavities was not achieved; however detection and approximate horizontal location of cavities is found by stacks of overtone images in the synthetic data examined in this research. Luke and Calderón-Macías (2008) found that compared to the frequency stacks, velocity stacks display more coherency and higher amplitude. In the synthetic models in this research, both frequency stacks and velocity stacks display high enough amplitudes to identify cavity locations. Another advantage is that after the MATLAB scripts have been written the stacks of overtone images are straightforward to produce. So stacks of overtone images are an efficient diagnostic tool.

Gelis et al. (2005) found that a cavity with a rectangular cross section generated more severe perturbations than a circular section of similar size and location, due to non-symmetrical back-scatter. This is a limitation of the synthetic models in this research because the synthetic cavity has a square cross section versus the barrels shaped cavities at the EGTS. This is a possible source of the differences between the synthetic and experimental results presented.

Two different finite difference codes are used in this research: E3D and WPP. When comparing outputs from the two codes, a time shift was needed to align calculated arrival times. An advantage of WPP found in this research is the ability to output synthetic seismograms in United States Geological Survey (USGS) format as a text file because this can be directly imported into MATLAB for processing. An advantage of E3D is the ability to compile the code in Cygwin, whereas WPP requires Linux with a specific version of GCC (the GNU compiler collection). In other words E3D can be run in a Windows environment using Cygwin, whereas WPP needs to be setup in a Linux virtual machine that contains the required version of GCC to be run in a Windows environment.

6.2 CONCLUSIONS

The purpose of this research is to improve capabilities for cavity detection and characterization using Rayleigh-type seismic surface waves by studying patterns of diffraction on the ground surface from shallow buried cavities. The main hypotheses are that Rayleigh wave data in stacks of overtone images and the cavity characterization parameters of Nasseri-Moghaddam et al. (2005) are diagnostic of the presence, placement and geometry of the cavities studied, even in layered ground having strong impedance contrasts.

The EGTS site studied and modeled is located on the UNLV campus where the top layer mostly consists of different types of sands (clayey sand, silty sand and sandy gravel), the middle layer consists mostly of caliche (cemented sand and cemented gravel), and

beneath that are different types of clays and sands (clayey sand, sandy clay, clayey gravel, clayey silt and sandy silt). There is imported fill at the surface that is covered by irrigated turf. A steel drum and plastic drum are buried in the top layer and serve as the cavities in the experiment.

The following series of notable observations are made.

1.) Inspecting synthetic time histories from a cavity placed within an otherwise homogeneous space enables identification of the cavity location because of energy scattering from the cavity. The most prominent scattering occurs after arrival at the cavity of the Rayleigh wave, whose energy dominates the incident wave.

2.) Inspecting synthetic time histories in a layer system that includes a HVL does not enable the identification of a shallow cavity placed above the HVL because of strong resonances.

3.) Time history residuals can clearly indicate the presence of the cavity in these models.

4.) Individual overtone images from these models do not enable the identification and location of the cavity.

5.) Stacks of overtone images from a two-layer model that includes a shallowly-buried full-model-width cavity (30 m long) over a HVL enabled identification of the cavity, whereas analyses of time histories or individual overtone images did not.

6.) Stacks of overtone images also enabled identification of cavities for a four-layer model that includes two full-model-width cavities over a HVL and two discrete 0.9 m-

long cavities under the same background conditions. The signature of the discrete cavities was less distinct, which is expected because of the difference in size.

7.) Results of an experiment conducted by others, to explore detection of shallowly buried cavities in a heterogeneous background using stacks of overtone images, were validated through numerical studies that generally replicated the test conditions. Under otherwise ideal conditions, the cavity should be detectable using the approach presented if the system noise is less than 20 percent of the signal.

This research contributes to the literature reviewed by supporting observations found by the following authors, with a couple of notable variations.

- This research demonstrates the presence of a cavity against a simple background using time histories, in agreement with the work of Sloan et al. (2011) and Sloan et al. (2012).
- This research demonstrated a downward shift in frequency and increase in amplitudes in frequency response in power spectrums at all receiver locations that overlie a cavity, in agreement with work by Phillips et al. (2002) and Shokouhi and Gucunski (2003).
- This research uses the NED parameter from Nasseri-Moghaddam et al. (2005) to approximately locate a cavity for a single layer model and enables identification of the presence of a cavity, but not its precise location, for a two layer model, despite experimental and numerical test design conditions that the authors would characterize as marginal for success.

- Analyses conducted for this research generally validate results of an experiment by Luke and Calderón-Macías (2008) using stacked overtone images to detect shallowly buried barrels in a complex layered environment.

This research improves capabilities for cavity detection and location by demonstrating in a noise-free environment that scattering from Rayleigh waves in stacks of overtone images is diagnostic of the presence and placement of the cavities studied. After the MATLAB scripts have been written the stacks of overtone images are straightforward to produce, making stacks of overtone images an efficient diagnostic tool.

6.3 RECOMMENDATIONS

In this research the results are limited to general location on the surface of cavities. Extensions of the method are needed to address depth, size and shape of discrete cavities. Synthetic modeling in 3-D offers ready access to such parametric studies. Another recommendation is to consider shape of the cavity when analyzing stacks of overtone images. Further testing of stacks of overtone images at various experimental sites that contain a HVL or otherwise would offer useful comparisons to this research.

Gelis et al. (2005) found that low-velocity zones around and above the cavity trapped waves and led to increased Rayleigh wave attenuation and strong footprints in overtone images, possibly masking the cavity signature. In contrast, Sloan et al. (2011) studied more competent media surrounding deeper cavities, with different results. Numerical

modeling of a cavity at different depths within backgrounds of different velocities could be employed to explore the transition between these endpoints.

BIBLIOGRAPHY

Burger, H. R., & Burger, D. C. (1992). *Exploration Geophysics of the Shallow Subsurface* Prentice Hall.

Butler, D. (2008). Detection and characterization of subsurface cavities, tunnels and abandoned mines. *Near-Surface Geophysics and Human Activity,* Science Press USA Inc. 578-584.

Casto, D. W., Luke, B., Calderon-Macias, C., & Kaufmann, R. (2009). Interpreting surface-wave data for a site with shallow bedrock. *Journal of Environmental & Engineering Geophysics, 14*(3), 115-127. doi:10.2113/JEEG14.3.115

Clayton, R., & Engquist, B. (1977). Absorbing boundary conditions for acoustic and elastic wave equations. *Bulletin of the Seismological Society of America, 67*(6), 1529-1540.

Conyers, L. B. (2011). Discovery, mapping and interpretation of buried cultural resources non-invasively with ground-penetrating radar. *Journal of Geophysics and Engineering, 8*(3), S13-S22. doi:10.1088/1742-2132/8/3/S02

Das, B. M. (2002). *Principles of Geotechnical Engineering* (5th ed.) Brooks Cole/Thompson Learning.

Di Fiore, V., Angelino, A., Passaro, S., & Bonanno, A. (2013). High resolution seismic reflection methods to detect near surface tuff-cavities: A case study in the Neapolitan

area, Italy. *Journal of Cave and Karst Studies, 75*(1), 51-59. doi:10.4311/2011ES0248

Engquist, B., & Majda, A. (1977). Absorbing boundary conditions for the numerical simulation of waves. *Mathematics of Computation, 31*(139), 629-651.

Gelis, C., Leparoux, D., Virieux, J., Bitri, A., Operto, S., & Grandjean, G. (2005). Numerical modeling of surface waves over shallow cavities. *Journal of Environmental & Engineering Geophysics, 10*(2), 111-121. doi:10.2113/JEEG10.2.111

Gucunski, N., Ganji, V., & Maher, M. H. (1996). SASW test in location of buried objects. *Proc., Symposium on the Application of Geophysics to Engineering and Environmental Problems,* 481-486.

Gucunski, N., & Woods, R. D. (1992). Numerical simulation of the SASW test. *Soil Dynamics and Earthquake Engineering, 11*(4), 213-227. doi:10.1016/0267-7261(92)90036-D

Hickey, C., Schmitt, D., Sabatier, J., & Riddle, G. (2009). Seismic measurements for detecting underground high-contrast voids. *Proc., Symposium on the Application of Geophysics to Engineering and Environmental Problems,* 929-936.

Inazaki, T., Kawamura, S., Tazawa, O., Yamanaka, Y., & Kano, N. (2005). Near-surface cavity detection by high-resolution seismic reflection methods using short-spacing

type land streamer. *Proc., Symposium on the Application of Geophysics to Engineering and Environmental Problems,* 959-970. doi:10.4133/1.2923554

Ivanov, J., Miller, R., Park, C., & Ryden, N. (2003). Seismic search for underground anomalies. [Abstract] *Society of Exploration Geophysicists Technical Program Expanded Abstracts*, 1223-1226 doi:10.1190/1.1817502

Jin, X. (2006). *Delineating anomalous layers in soil profiles using seismic surface wave methods.* Ph.D. Dissertation, The University of Nevada Las Vegas, Las Vegas, NV.

Jin, X., Luke, B., & Calderón-Macías, C. (2009). Role of forward model in surface-wave studies to delineate a buried high-velocity layer. *Journal of Environmental & Engineering Geophysics, 14*(1), 1-14. doi:10.2113/JEEG14.1.1

Larsen, S., & Schultz, C. A. (1995). *E3D 2D/3D Elastic Finite-Difference Wave Propagation Code.* Lawrence Livermore National Laboratory (Technical Report No. UCRL-MA-121792).

Louie, J. N. (2001). Faster, better: Shear-wave velocity to 100 meters depth from refraction microtremor arrays. *Bulletin of the Seismological Society of America, 91*(2), 347-364.

Luke, B., & Calderón-Macías, C. (2008). An experimental investigation of surface wave scattering over a site with shallow buried heterogeneities [Abstract]. *Symposium on the Application of Geophysics to Engineering and Environmental Problems, Extended Abstract, 21* 1166. doi:10.4133/1.2963226

Luke, B., & Calderón-Macías, C. (2008). Scattering of surface waves due to shallow heterogeneities [Abstract]. *Society of Exploration Geophysicists Technical Program Expanded Abstracts,* 1283-1287. doi:10.1190/1.3059151

Luke, B., & Calderón-Macías, C. (2007). Mapping near surface heterogeneities for geotechnical and environmental applications using seismic surface waves, *Eos Trans. AGU 88*(23), Jt. Assem. Suppl., Abstract NS33A-07. Washington, DC: American Geophysical Union.

Luke, B. and Chase, D. S. 1997. Detecting caves using seismic surface waves: A feasibility study. In B. F. Beck and J. B. Stephenson (eds.), *The Engineering Geology and Hydrogeology of Karst Terranes*, Proceedings, Multidisciplinary Conference on Sinkholes and the Engineering and Environmental Impacts of Karst. Rotterdam, the Netherlands: Balkema. pp 419-424.

Mangriotis, M., Rector, J., III, Herkenhoff, E., & Neu, J. (2013). Scattering versus intrinsic attenuation in the vadose zone: A VSP experiment. *Geophysics, 78*(2), B49-B63. doi:10.1190/geo2012-0174.1

McMechan, G. A., & Yedlin, M. J. (1981). Analysis of dispersive waves by wave field transformation. *Geophysics, 46*(6), 869-874.

Miller, R. D., & Steeples, D. W. (1991). Detecting voids in a 0.6 m coal seam, 7 m deep, using seismic reflection. *Geoexploration, 28*(2), 109-119.

Murvosh, H., Luke, B., & Calderón-Macías, C. (2013). Shallow-to-deep shear wave velocity profiling by surface waves in complex ground for enhanced seismic microzonation of Las Vegas, Nevada. *Soil Dynamics and Earthquake Engineering, 44*, 168-182.

Nasseri-Moghaddam, A. (2006). *Study of the effect of lateral inhomogeneities on the propagation of Rayleigh waves in an elastic medium.* Thesis, University of Waterloo.

Nasseri-Moghaddam, A., Cascante, G., Phillips, C., & Hutchinson, D. J. (2007). Effects of underground cavities on Rayleigh waves—Field and numerical experiments. *Soil Dynamics and Earthquake Engineering,* (27), 300-313.

Nasseri-Moghaddam, A., Cascante, G., & Hutchinson, J. (2005). A new quantitative procedure to determine the location and embedment depth of a void using surface waves. *Journal of Environmental and Engineering Geophysics, 10*(1), 51-64. doi:10.2113/JEEG10.1.51

Nazarian, S. (2012). Shear wave velocity profiling with surface wave methods. In K. Rollins, & D. Zekkos (Eds.), *Geotechnical Engineering State of the Art and Practice* (pp. 221-240). Reston, Virginia: American Society of Civil Engineers.

Nolan, J. J., Sloan, S. D., Broadfoot, S. W., McKenna, J. R., & Metheny, O. M. (2011). Near-surface void identification using MASW and refraction tomography techniques. [Abstract] *Society of Exploration Geophysicists Technical Program Abstracts, 1401-1405. doi:10.1190/1.3627464*

Park, C. B., Miller, R. D., Xia, J., & Ivanov, J. (2007). Multichannel analysis of surface waves (MASW)—active and passive methods. *The Leading Edge, 26*(1), 60-64.

Petersson, A., & Sjogreen, B. (2011). *WPP: Serpentine wave propagation user manual* (2.1.5 ed.) Lawrence Livermore National Laboratory.

Petersson, A., & Sjogreen, B. (2013). Super-grid modeling of the elastic wave equation in semi-bounded domains. *Communications in Computational Physics,* Manuscript submitted for publication.

Petersson, N. A., & Sjogreen, B. (2009). An energy absorbing far-field boundary condition for the elastic wave equation. *Communications in Computational Physics, 6*(3), 483.

Philips, C., Cascante, G., & Hutchinson, D. J. (2002). The innovative use of seismic surface waves for void detection and material characterization. *Proc., Symposium on the Application of Geophysics to Engineering and Environmental Problems,* 1-10.

Richart Jr., F. E., Hall Jr., J. R., & Woods, R. D. (1970). *Vibrations of Soils and Foundations*, Prentice-Hall Inc. 86-92.

Richart, F. E. (1962). Foundation vibrations. *Transactions of the American Society of Civil Engineers, 127*(1), 863-897.

Riddle, G. I., Hickey, C. J., & Schmitt, D. R. (2010). Subsurface tunnel detection using electrical resistivity tomography and seismic refraction tomography: A case study.

Proc., Symposium on the Application of Geophysics to Engineering and Environmental Problems, 552-562.

Rix, G. J., & Lai, C. G. (1998). *Simultaneous inversion of Rayleigh phase velocity and attenuation for near-surface site characterization.* (No. GIT-CEE/GEO-98-2).School of Civil and Environmental Engineering, Georgia Institute of Technology.

Sacchi, M.D. (2003) *SeismicLab Revision 1.2.* Signal Analysis and Imaging Group (SAIG), Department of Physics, University of Alberta, Canada.

Sharma, P. V. (1997). *Environmental and Engineering Geophysics* Cambridge University Press.

Sheriff, R. E., & Geldart, L. P. (1995). *Exploration Seismology* (2nd ed.) Cambridge University Press.

Shokouhi, P., & Gucunski, N. (2003). Application of wavelet transform in detection of shallow cavities by surface waves. *Proc., Symposium on the Application of Geophysics to Engineering and Environmental Problems, San Antonio, Texas,* 1582-1600.

Sloan, S. D., Peterie, S. L., Ivanov, J., Miller, R. D., & McKenna, J. R. (2011). Void detection using near surface seismic methods. In R. D. Miller, J. H. Bradford, K. Holliger & R. B. Latimer (Eds.), *Advances in near-surface seismology and ground-penetrating radar* (15th ed., pp. 201-218) Society of Exploration Geophysicists.

Sloan, S. D., Peterie, S. L., Miller, R. D., Ivanov, J., McKenna, J. R., Broadfoot, S. W., & Metheny, O. M. (2012). Tunnel detection using near-surface seismic methods [Abstract]. *Society of Exploration Geophysicists Technical Program Expanded Abstracts,* 1-5. doi:10.1190/segam2012-1442.1

Sloan, S. D., Peterie, S. L., Ivanov, J., Miller, R. D., & McKenna, J. R. (2010). Void detection using near-surface seismic methods. In R. D. Miller, J. H. Bradford, K. Holliger & R. B. Latimer (Eds.), *Advances in near-surface seismology and ground-penetrating radar* (15th ed., pp. 201-218) Society of Exploration Geophysicists.

Stone, R. C., & Luke, B. (2001). An overview of engineering with cemented soils in Las Vegas. *Proc., Symposium on the Application of Geophysics to Engineering and Environmental Problems,* Idaho State University, Pocatello. 135-144.

Tecle, M., Giorgis, A., & Luke, B. (2003). Comparison of seismic downhole to crosshole measurements in a complex-layered system. *Proc., Symposium on the Application of Geophysics to Engineering and Environmental Problems,* Idaho State University, Pocatello. 217-232.

Virieux, J. (1986). P-SV wave propagation in heterogeneous media: Velocity-stress finite-difference method. *Geophysics, 51*(4), 889-901. doi:10.1190/1.1442147

Xia, J., Nyquist, J., Xu, Y., & Roth, M. (2006). Feasibility of detecting voids with Rayleigh-wave diffraction. *Proc., Symposium on the Application of Geophysics to Engineering and Environmental Problems,* 1168-1180.

Yoon, S., & Rix, G. J. (2006). Evaluation of near-field effects on active surface wave measurements with multiple receivers. *Proc., Symposium on the Application of Geophysics to Engineering and Environmental Problems*

Zhao, Y., & Rector, J. W. (2010). Using seismic surface waves generated by motor vehicles to find voids: Field results [Abstract]. *Society of Exploration Geophysicists Technical Program Expanded Abstracts,* 2029-2033. doi:10.1190/1.3513243

APPENDIX 1 OVERTONE IMAGES FOR MODELS D AND F AND STACKS OF OVERTONE IMAGES USING A 50 HZ RICKER WAVELET SOURCE

This appendix contains individual overtone images for each source location for Model D, using a 50 Hz Ricker wavelet source and for Model F, using a CRS. These are the same images used to create stacks of overtone images presented in Chapters 4 and 5. This appendix also contains stacks of overtone images that are similar to those presented in Chapter 5 (Figure 5.6, Figure 5.7, Figure 5.15, Figure 5.16, Figure 5.17 and Figure 5.18) for Models E, F and F* except that the source pulse is a 50 Hz Ricker wavelet.

APPENDIX 2 NORMALIZED-ENERGY-DISTANCE CAVITY CHARACTERIZATION PARAMETER FOR MODEL E, MODEL F, AND THE ENGINEERING GEOPHYSICS TEST SITE

This appendix contains the normalized-energy-distance (NED) cavity characterization parameter for Model E, Model F, and the EGTS.

Recall that horizontal (in-plane) and vertical motions were used for calculation of the NED parameter from Nasseri-Moghaddam et al. (2005). Recall that a superimposed 25 Hz and 100 Hz Ricker wavelet was used initially, based on successful results with similar modeling techniques by Jin (2006), then a 50 Hz Ricker wavelet was used to simplify the source by removing one Ricker wavelet and choosing a central frequency. The cavity characterization parameter work was carried out before the source was simplified.

How the NED parameter is calculated was explained in section 3.1.6. The frequency range of 40 Hz to 80 Hz is used in Model E and F, because this is the range of highest amplitude in the overtone images. The NED parameters calculated are processed in the same fashion described previously for Models A, B, C, and D.

The Normalized Energy-Distance (NED) parameter for Models E and F is displayed in Figure A.2.1. Model F includes two cavities beneath receiver numbers 16 - 17 and 46 - 47 marked by green lines in the figure. Recall that according to Nasseri-Moghaddam et

al. (2005), the boundaries of the void are distinguished by peaks and valleys of the NED parameter. The horizontal (in-plane) direction for the NED parameter for Model E is similar to Model F. The NED parameter fluctuates near the location of the cavities for Model F, which has cavities, and not for Model E which does not. There are small local fluctuations in the NED parameter for Model E. There are many local maximums and minimums in the NED plot for Model F, making it not accurate to identify the location of a cavity, however this may indicate the existence of cavities. If interpreted blindly, there are many possible cavity locations in the NED parameter results in the figure.

The NED parameter computed for the Engineering Geophysics Test Site (EGTS) experimental data is displayed in Figure A.2.2. The frequency range of 20 Hz to 60 Hz is used because these are the highest amplitudes in the overtone images. Shot 1 of 30 is used for the NED parameter calculation for the EGTS. The NED parameter is close to zero near the first cavity at receiver number 30, and also the second cavity at receiver number 60. The NED parameter plot does not identify the location of the cavities in the EGTS experimental data.

The NED parameter does not successfully identify the cavities locations in Model F, however local fluctuations may indicate the existence of a cavity. Overall this study of the NED parameter is not accurate with Model F and not successful with the experimental data from the EGTS.

APPENDIX 3 EXAMPLE OF WPP INPUT FILE

This appendix consists of an example WPP input file for the first source location in Model F which uses a 50 Hz Ricker wavelet and a 0.9 m in length (finite) cavity.

```
FILENAME = ModelF50HzShot1Barrel.in

grid   h=0.2 x=30 y=30 z=20

time    t=0.5

fileio path=ModelF50HzShot1Barrel verbose=1 printcycle=10

block   vp=370 vs=200 rho=1700

block   vp=2600 vs=1500 rho=2200 z1=2.4 z2=4.6

block   vp=1500 vs=400 rho=1700 z1=4.6 z2=7.5

block   vp=2200 vs=600 rho=1700 z1=7.5 z2=20

block   vp=330 vs=30 rho=250 x1=10 x2=10.53 y1=14.5 y2=15.4 z1=0.97 z2=1.5

block   vp=330 vs=30 rho=250 x1=20 x2=20.53 y1=14.5 y2=15.4 z1=0.97 z2=1.5

source type=Ricker x=3 y=15.5 z=1 fx=1 fy=1 fz=1 freq=50 t0=0.1

sac     x=5 y=15 z=0 file=s1 usgsformat=1

sac     x=5.33 y=15 z=0 file=s2 usgsformat=1

sac     x=5.66 y=15 z=0 file=s3 usgsformat=1

sac     x=6 y=15 z=0 file=s4 usgsformat=1
```

```
sac    x=6.33 y=15 z=0 file=s5 usgsformat=1

sac    x=6.66 y=15 z=0 file=s6 usgsformat=1

sac    x=7 y=15 z=0 file=s7 usgsformat=1

sac    x=7.33 y=15 z=0 file=s8 usgsformat=1

sac    x=7.66 y=15 z=0 file=s9 usgsformat=1

sac    x=8 y=15 z=0 file=s10 usgsformat=1

sac    x=8.33 y=15 z=0 file=s11 usgsformat=1

sac    x=8.66 y=15 z=0 file=s12 usgsformat=1

sac    x=9 y=15 z=0 file=s13 usgsformat=1

sac    x=9.33 y=15 z=0 file=s14 usgsformat=1

sac    x=9.66 y=15 z=0 file=s15 usgsformat=1

sac    x=10 y=15 z=0 file=s16 usgsformat=1

sac    x=10.33 y=15 z=0 file=s17 usgsformat=1

sac    x=10.66 y=15 z=0 file=s18 usgsformat=1

sac    x=11 y=15 z=0 file=s19 usgsformat=1

sac    x=11.33 y=15 z=0 file=s20 usgsformat=1

sac    x=11.66 y=15 z=0 file=s21 usgsformat=1

sac    x=12 y=15 z=0 file=s22 usgsformat=1
```

```
sac     x=12.33 y=15 z=0 file=s23 usgsformat=1

sac     x=12.66 y=15 z=0 file=s24 usgsformat=1

sac     x=13 y=15 z=0 file=s25 usgsformat=1

sac     x=13.33 y=15 z=0 file=s26 usgsformat=1

sac     x=13.66 y=15 z=0 file=s27 usgsformat=1

sac     x=14 y=15 z=0 file=s28 usgsformat=1

sac     x=14.33 y=15 z=0 file=s29 usgsformat=1

sac     x=14.66 y=15 z=0 file=s30 usgsformat=1

sac     x=15 y=15 z=0 file=s31 usgsformat=1

sac     x=15.33 y=15 z=0 file=s32 usgsformat=1

sac     x=15.66 y=15 z=0 file=s33 usgsformat=1

sac     x=16 y=15 z=0 file=s34 usgsformat=1

sac     x=16.33 y=15 z=0 file=s35 usgsformat=1

sac     x=16.66 y=15 z=0 file=s36 usgsformat=1

sac     x=17 y=15 z=0 file=s37 usgsformat=1

sac     x=17.33 y=15 z=0 file=s38 usgsformat=1

sac     x=17.66 y=15 z=0 file=s39 usgsformat=1

sac     x=18 y=15 z=0 file=s40 usgsformat=1
```

sac x=18.33 y=15 z=0 file=s41 usgsformat=1

sac x=18.66 y=15 z=0 file=s42 usgsformat=1

sac x=19 y=15 z=0 file=s43 usgsformat=1

sac x=19.33 y=15 z=0 file=s44 usgsformat=1

sac x=19.66 y=15 z=0 file=s45 usgsformat=1

sac x=20 y=15 z=0 file=s46 usgsformat=1

sac x=20.33 y=15 z=0 file=s47 usgsformat=1

sac x=20.66 y=15 z=0 file=s48 usgsformat=1

sac x=21 y=15 z=0 file=s49 usgsformat=1

sac x=21.33 y=15 z=0 file=s50 usgsformat=1

sac x=21.66 y=15 z=0 file=s51 usgsformat=1

sac x=22 y=15 z=0 file=s52 usgsformat=1

sac x=22.33 y=15 z=0 file=s53 usgsformat=1

sac x=22.66 y=15 z=0 file=s54 usgsformat=1

sac x=23 y=15 z=0 file=s55 usgsformat=1

sac x=23.33 y=15 z=0 file=s56 usgsformat=1

sac x=23.66 y=15 z=0 file=s57 usgsformat=1

sac x=24 y=15 z=0 file=s58 usgsformat=1

sac x=24.33 y=15 z=0 file=s59 usgsformat=1

sac x=24.66 y=15 z=0 file=s60 usgsformat=1

sac x=25 y=15 z=0 file=s61 usgsformat=1

sac x=25.33 y=15 z=0 file=s62 usgsformat=1

sac x=25.66 y=15 z=0 file=s63 usgsformat=1

sac x=26 y=15 z=0 file=s64 usgsformat=1

sac x=26.33 y=15 z=0 file=s65 usgsformat=1

sac x=26.66 y=15 z=0 file=s66 usgsformat=1

sac x=27 y=15 z=0 file=s67 usgsformat=1

sac x=27.33 y=15 z=0 file=s68 usgsformat=1

sac x=27.66 y=15 z=0 file=s69 usgsformat=1

sac x=28 y=15 z=0 file=s70 usgsformat=1

sac x=28.33 y=15 z=0 file=s71 usgsformat=1

sac x=28.66 y=15 z=0 file=s72 usgsformat=1

APPENDIX 4 TIME HISTORIES WITH ARRIVAL TIMES MATLAB SCRIPT

This appendix consists of an example of the MATLAB script used to plot time histories with first arrival times and scattered arrival times from Model F.

```
% Clear All data and Close all Open Windows

clear all;

close all;

clc;


load z.mat

load time.mat


offset= 1:1:72;


%Plot Seismic Data

maxampmatrix = max(z)

maxamp = max(maxampmatrix)

PlotWigClip(z,50,offset,time,maxamp,1)

hold on
```

```
xreceiver1 = 5:0.33:28.66;

yreceiver1(1:72) = 15;

zreceiver1(1:72) = 0;


xcavity(1:72) = 10;

ycavity(1:72) = 15;

zcavity(1:72) = 0.97;


xcavity2(1:72) = 20;

ycavity2(1:72) = 15;

zcavity2(1:72) = 0.97;


sourcex(1:72) = 3;

sourcey(1:72) = 15.5;

sourcez(1:72) = 1;


sourceTocavity=sqrt((10-3)^2+(15-15.5)^2+(0.97-1)^2);
```

```
sourceTocavity2=sqrt((20-3)^2+(15-15.5)^2+(0.97-1)^2);

DirectDistance=sqrt((xreceiver1-sourcex).^2+(yreceiver1-sourcey).^2+(zreceiver1-
sourcez).^2);

ScatteredDistance=(sqrt((xcavity-xreceiver1).^2+(ycavity-yreceiver1).^2+(zcavity-
zreceiver1).^2))+sourceTocavity;

ScatteredDistance2=(sqrt((xcavity2-xreceiver1).^2+(ycavity2-yreceiver1).^2+(zcavity2-
zreceiver1).^2))+sourceTocavity2;


Vp=370;


DirectTimePwave=DirectDistance/Vp+0.1-0.0170;

ScatteredTimePwave=ScatteredDistance/Vp+0.1-0.0170;

ScatteredTimePwave2=ScatteredDistance2/Vp+0.1-0.0170;


Vs=200;


DirectTimeSwave=DirectDistance/Vs+0.1-0.0170;

ScatteredTimeSwave=ScatteredDistance/Vs+0.1-0.0170;

ScatteredTimeSwave2=ScatteredDistance2/Vs+0.1-0.0170;
```

```
Rayleigh=0.92*Vs;


DirectTimeRayleighwave=DirectDistance/Rayleigh+0.1-0.0170;

ScatteredTimeRayleighwave=ScatteredDistance/Rayleigh+0.1-0.0170;

ScatteredTimeRayleighwave2=ScatteredDistance2/Rayleigh+0.1-0.0170;


p1=plot(offset, DirectTimePwave)

set(p1,'Color','red','LineWidth',2)

grid on

hold on

p2=plot(offset, DirectTimeSwave)

set(p2,'Color','red','LineWidth',2)

hold on

p3=plot(offset, DirectTimeRayleighwave)

set(p3,'Color','red','LineWidth',2)

hold on

p4=plot(offset, ScatteredTimePwave)
```

```
set(p4,'Color','blue','LineWidth',2)

hold on

p5=plot(offset, ScatteredTimeSwave)

set(p5,'Color','blue','LineWidth',2)

hold on

p6=plot(offset, ScatteredTimeRayleighwave)

set(p6,'Color','blue','LineWidth',2)

p7=plot(offset, ScatteredTimePwave2)

set(p7,'Color','blue','LineWidth',2)

hold on

p8=plot(offset, ScatteredTimeSwave2)

set(p8,'Color','blue','LineWidth',2)

hold on

p9=plot(offset, ScatteredTimeRayleighwave2)

set(p9,'Color','blue','LineWidth',2)


xlabel('Receiver Number','FontSize',16)

ylabel('Time (seconds)','FontSize',16)
```

```
%title('Model F using a 50 Hz source : z direction')


%Set Figure units and size, and set font size

figure (1)

hFig = figure(1);

set(gcf,'PaperPositionMode','auto')

set(gcf,'Units','inches')

set(hFig, 'Position', [0 0 8 8])

set(gca,'FontSize',16)

axis([-1 74 0 0.50])

saveas(hFig,'Figure5.8_ModelF_TimeHistories.fig')
```

APPENDIX 5 OVERTONE IMAGE MATLAB SCRIPT

This appendix consists of an example of the MATLAB script used to create overtone images in this research.

```
clear all;

close all;

clc;

%%

% Load Model F time domain data

load z.mat

% location of receivers

xlocS = (0:1/3:23.67);


% time-freq sampling

nt   = 10487; % Number of time steps

dt = 0.5/10487; % time resolution

nfft = 2*nt; % Number of points used in fft

fs = 1/dt; % Sampling frequency - Number of samples obtained in one second

fn = 1/2/dt; % Nyquist Frequency or Maximum Frequency
```

```
df = fn/nfft*2; % frequency resolution

m  = nfft/2 + 1; %  Folding Variable

f  = 0 : df : fn*2;% this is the frequency axis

t  = 0: dt : (nt-1)*dt ; % Time Range to use


%% Processing -> computing freq-velocity dispersion maps

% phase velocity ranges

cmin = .1;

cmax = 1500;

dc = 4;

c = cmin : dc : cmax;


% ray parameter ranges

p     = 1./c;

muo   = 250;


% frequency ranges for transformation

flow = 3;
```

```
fhigh = 250;


   indxS = (1:1:72);


   d_S  = z(:,indxS);
%%
   % source receiver separation
   offsS =
[2.23606797700000,2.53859103500000,2.84800124800000,3.16227766000000,3.48010
217000000,3.80058475000000,4.12310562600000,4.44722135500000,4.7726070210000
0,5.09901951400000,5.42627353200000,5.75422550100000,6.08276253000000,6.41179
468700000,6.74124947200000,7.07106781200000,7.40120110400000,7.7316090030000
0,8.06225774800000,8.39311887500000,8.72416821900000,9.05538513800000,9.38675
189400000,9.71825315800000,10.0498756200000,10.3816076700000,10.713439120000
0,11.0453610200000,11.3773654400000,11.7094453800000,12.0415945800000,12.3738
074600000,12.7060790400000,13.0384048100000,13.3707807500000,13.703203190000
0,14.0356688500000,14.3681747100000,14.7007180500000,15.0332963800000,15.3659
074300000,15.6985491200000,16.0312195400000,16.3639169400000,16.696639720000
0,17.0293863700000,17.3621555200000,17.6949459200000,18.0277563800000,18.3605
858100000,18.6934331900000,19.0262975900000,19.3591781300000,19.692073980000
0,20.0249843900000,20.3579086500000,20.6908460700000,21.0237960400000,21.3567
```

```
579700000,21.6897313100000,22.0227155500000,22.3557101800000,22.688714770000
0,23.0217288700000,23.3547520700000,23.6877840100000,24.0208243000000,24.3538
726100000,24.6869286200000,25.0199920100000,25.3530624900000,25.686139800000
0;];


    % this is tau-p transformation

    maptp = inverse_radon(d_S, dt, offsS, p, 1, flow, fhigh, muo, 'ls');


    % transform to frequency-phase vel.

    temp_S = abs( fft( maptp, nfft)) ;

    mapvf_S(:,:,1) = temp_S( 1 : m , :);


     figure

     set(gca,'FontSize',16)

     imagesc( f, c +dc/2, temp_S');

     axis( [0 100 0 1500])

     axis('xy')

     xlabel('Frequency (Hz)','FontSize',16)

     ylabel('Velocity (m/s)','FontSize',16)
```

```
        hold on

        %saveas(gcf,'ModelFfrequencySouth.png')

        %saveas(gcf,'ModelFfrequencySouth.fig')


mapvf_S_shot1=mapvf_S

%save('mapvf_S_shot1', '-regexp', '^mapvf_S_shot1');


hold on

        load index_f_modelE.mat

        load vel_ref_f_modelE.mat

        plot(index_f,vel_ref_f, '-xk')

        load index_f2_modelE.mat

        load vel_ref_f2_modelE.mat

        load fr.mat

        plot(fr(index_f2:end),vel_ref_f2(index_f2:end), '-xr')


        %Set Figure units and size, and set font size

figure (1)
```

```
hFig = figure(1);

set(gcf,'PaperPositionMode','auto')

set(gcf,'Units','inches')

set(hFig, 'Position', [0 0 8 8])

set(gca,'FontSize',16)

%axis([-1 74 0 0.50])

saveas(hFig,'Figure5.6_ModelF_Overtone.fig')
```

APPENDIX 6 STACK OF OVERTONE IMAGE MATLAB SCRIPT

This appendix contains an example of the MATLAB script used to create stacks of overtone images in this research.

```
clear all;

close all;

clc;


load mapvf_S.mat;

load mapvf_N.mat;


%% plot phase velocity map stacked over all frequencies

% stack all frequencies

% Note: map_stackS is frequencies x phase velocities x number of shots

%       the sum is over the FIRST dimension, the frequencies

map_stackS = sum( mapvf_S,1);

%map_stackS = reshape( map_stackS, length(c), nshots)    ; % c=wave

%velocity range 375 points and nshots=number of shots used

map_stackS = reshape( map_stackS, 375, 27);
```

```
map_stackN = sum( mapvf_N,1);

map_stackN = reshape( map_stackN, 375, 27);


map_stackSUM = map_stackS + map_stackN ;


%a=x axis range, b=y axis range

a=1:1:27;

b=1:1:375;


figure

imagesc(a,b,map_stackS);

axis('xy')

%title('Vertical:  Receivers to the South of source')

ylabel('Frequency (Hz)','FontSize',16)

xlabel('Source Location (m)','FontSize',16)


%Set Figure units and size, and set font size
```

```
figure (1)

sFig = figure(1);

set(gcf,'PaperPositionMode','auto')

set(gcf,'Units','inches')

set(sFig, 'Position', [0 0 8 8])

set(gca,'FontSize',16)

%saveas(gcf,'ModelFstackedoverallfrequenciesSouth.png')

%saveas(gcf,'ModelFstackedoverallfrequenciesSouth.fig')



figure

imagesc(a,b,map_stackN);

axis('xy')

%title('Vertical:  Receivers to the North of source')

ylabel('Frequency (Hz)','FontSize',16)

xlabel('Source Location (m)','FontSize',16)



%Set Figure units and size, and set font size

figure (2)
```

```
nFig = figure(2);

set(gcf,'PaperPositionMode','auto')

set(gcf,'Units','inches')

set(nFig, 'Position', [0 0 8 8])

set(gca,'FontSize',16)

%saveas(gcf,'ModelFstackedoverallfrequenciesNorth.png')

%saveas(gcf,'ModelFstackedoverallfrequenciesNorth.fig')



figure

imagesc(a,b,map_stackSUM);

axis('xy')

%title('Vertical:  Sum of North and South Receivers')

ylabel('Frequency (Hz)','FontSize',16)

xlabel('Source Location (m)','FontSize',16)



%Set Figure units and size, and set font size

figure (3)

SUMFig = figure(3);
```

```
set(gcf,'PaperPositionMode','auto')

set(gcf,'Units','inches')

set(SUMFig, 'Position', [0 0 8 8])

set(gca,'FontSize',16)

%saveas(gcf,'ModelFstackedoverallfrequenciesSUM.png')

%saveas(gcf,'ModelFstackedoverallfrequenciesSUM.fig')


%% plot phase velocity map stacked over all velocities


% stack all velocities

map_stackvS = sum( mapvf_S,2);

%map_stackvS = reshape( map_stackvS, length(f), nshots);

map_stackvS = reshape( map_stackvS, 200, 27);


% stack all velocities

map_stackvN = sum( mapvf_N,2);

%map_stackvN = reshape( map_stackvN, length(f), nshots);

map_stackvN = reshape( map_stackvN, 200, 27);
```

```
% SUM

map_stackvSUM = map_stackvN + map_stackvS ;



%c=x axis range, d=y axis range

% source location

c=1:1:27;

% velocity range used for overtone images

d=0.1:4:1500;



figure

imagesc( c, d, map_stackvS);

axis('xy')

%title('Horizontal:  Velocity stack, Receivers to S of source')

xlabel('Source Location (m)','FontSize',16)

ylabel('Velocity (m/s)','FontSize',16)



%Set Figure units and size, and set font size
```

```
figure (4)

sFig = figure(4);

set(gcf,'PaperPositionMode','auto')

set(gcf,'Units','inches')

set(sFig, 'Position', [0 0 8 8])

set(gca,'FontSize',16)



figure

imagesc( c, d, map_stackvN);

axis('xy')

%title('Velocity stack, Receivers to N of source')

xlabel('Source Location (m)','FontSize',16)

ylabel('Velocity (m/s)','FontSize',16)



%Set Figure units and size, and set font size

figure (5)

sFig = figure(5);

set(gcf,'PaperPositionMode','auto')
```

```
set(gcf,'Units','inches')

set(sFig, 'Position', [0 0 8 8])

set(gca,'FontSize',16)



figure

imagesc( c, d, map_stackvSUM);

axis('xy')

%title('Velocity stack, Sum')

xlabel('Source Location (m)','FontSize',16)

ylabel('Velocity (m/s)','FontSize',16)



%Set Figure units and size, and set font size

figure (6)

sFig = figure(6);

set(gcf,'PaperPositionMode','auto')

set(gcf,'Units','inches')

set(sFig, 'Position', [0 0 8 8])

set(gca,'FontSize',16)
```

APPENDIX 7 POWER SPECTRUM MATLAB SCRIPT

This appendix contains an example of the MATLAB script used to create power spectrums in this research.

```
clear all;

close all;

load x.mat;

dt = 1/length(x);

fs = 1/dt; %Sample frequency (Hz)

m = length(x); % Window length

n = pow2(nextpow2(m)); %Transform length

t = (0:m-1)/fs % Time range for data

xfft = fft(x,n); %Discrete Fourier Transform
```

```
f = (0:n-1)*(fs/n);     % Frequency range

Nyquist=fs/2; %Nyquist frequency


xpower = xfft.*conj(xfft)/n;   % Power of the DFT


plot(f,xpower(:,1))

xlabel('Frequency (Hz)')

axis([0 500 0 .14E-19])
```

APPENDIX 8 DECONVOLUTION MATLAB SCRIPT

This appendix contains an example of the MATLAB script used for deconvolution in Model F.

```
%% Deconvolution

clear all;

close all;

clc;


load z.mat

load resamplezDecon.mat


% params

nt = 10487; % nt is the number of samples in time

npow = ceil( log2( nt)) ;

nfft = 2^npow ; % NNFT NOW APPROXIMATES THE CLOSES POWER OF 2 NUMBER TO NT

m  = nfft/2 + 1 ; % folding variable

%dtcheck = 0.50/10487; % Model F dt from WPP - Total time run / number of time steps
```

```
dt = 4.76826e-05; % Taken from WPP run

fs = 1/dt; % Sample frequency (Hz)

fn = 1/(2*dt) ; % this the maximum frequency of your data given by dt

df = 1/nfft/dt ; % this is the frequency sampling rate

fr = 0 : df : fn ; % this is the frequency axis


decon=fft(resamplezDecon, nfft);


%This reverses the direction of the wavelet in time

staticShiftresamplezDecon = staticShift( resamplezDecon, 2176, 1) ;


[n1 n2] = size(z) ;


PzF = fft(z, nfft) ;


%% Divide each power spectrum by the 'captured' power spectrum

d = 0*PzF ; % this creates d same size as PzF
```

```
% origianl signal in time

modelt = real( ifft( PzF)) ;


for k=1:n2


   %d(2:m,k) = PzF(2:m,k)./( decon1(2:m) + .000000001) ;

   d(2:m,k) = PzF(2:m,k)./( decon(2:m) + .000000001) ; %<- making this value smaller
changes how spiky the deconvolution looks


   for j=2:m-1,


      jj       = nfft - j + 2;


      d(jj,k)   = conj( d(j,k)) ;


   end


end
```

```
% go back to time

d_time = real( ifft( d)) ;



% remove lows and highs

%d_filter = applyBpFilter(d_time, [1,3,200,225], dt, 1) ;

d_filter = applyBpFilter(d_time, [1,3,100,125], dt, 1) ;



dff = fft( d_filter) ;



%% figures



figure

plot(resamplezDecon);

title('resamplezDecon');



figure

plot(decon);
```

```
title('resampled Captured 50 Hz wavelet from WPP homogeneous model (complex
numbers)')


figure
plot(staticShiftresamplezDecon);
title('resampled Time Domain of "captured" 50 Hz wavelet from WPP after staticShift')
xlabel('Time Steps')


figure
PlotWig (z)
title('Time Domain of Model F Shot 1')
xlabel('Offset #')


% plot spectra
figure
plot( abs( PzF(1:m,10))/max( max( abs(PzF(:,10)))) ) ;
hold on
plot( abs( decon(1:m)/max(abs(decon))), 'r-')
title('Sample Spectra')
```

```
legend('Model F fft','Deconvolution')

axis([0 500 0 1])

xlabel('Frequency (Hz)')


figure

PlotWig(d_time)

title('Deconvolved signal - Model F')

xlabel('Offset #')


figure

PlotWig(modelt)

title('Original signal - Model F')

xlabel('Offset #')


figure

PlotWig(d_filter)

title('Filtered Deconvolved signal - Model F')

xlabel('Offset #')
```

```
% compare spectra

figure

plot( abs( PzF(1:m,10))/max( max( abs(PzF(:,10)))) ) ;

hold on

plot( abs( d(1:m,10))/max( max( abs(d(:,10)))), 'r-' ) ;

plot( abs( dff(1:m,10))/max( max( abs(dff(:,10)))), 'k--' ) ;

title('Compare Spectra')

legend('Model F fft','Deconvolution','Deconvolution Filtered')

axis([0 500 0 1])

xlabel('Frequency (Hz)')
```

APPENDIX 9 CONVOLUTION MATLAB SCRIPT

This appendix contains an example of the MATLAB script used for convolution in Model F.

```
%%Convolution

clear all;

close all;

clc;


load d_filter.mat;

load resampleEGTS.mat


offset = [1:1:72] ;


nt = 16384; % Number of time steps

nfft = 2^nextpow2(nt); % Next power of 2 from length of nt

dt = 4.76826e-05; % Taken from WPP run

m  = nfft/2 +1;
```

```
FFTd_filter = fft(d_filter, nfft);

FFTresampleEGTS = fft(resampleEGTS, nfft);

time=[0:(1/(nfft-1))/2:0.5]

%%

for k2=1:72

   Convol(2:m,k2)  = FFTd_filter(2:m,k2).*(FFTresampleEGTS(2:m) + 0);

   for j=2:m-1,   % this is the conjugate part, it ensures that in output, the
                  % inverse transformed data is real

      jj       = nfft - j + 2;

      Convol(jj,k2)   = conj(Convol(j,k2));
```

```
    end
end


ConvolTime = real(ifft(Convol));
%ConvolTime = flipud(ConvolTime);


% remove lows and highs
ConvolTime_filter = applyBpFilter(ConvolTime, [1,3,200,225], dt, 1) ;


ConvolTime_filter_fft = fft( ConvolTime_filter) ;


%% figures
figure
plot(resampleEGTS) ;
title('Time Domain of Real Source from Engineering Geophysics Test Site')
xlabel('Time Steps')


figure
```

```
plot(FFTresampleEGTS)

title('FFT of resampleEGTS')


% check spectra

figure

plot( abs( FFTresampleEGTS(1:end))/max( max( abs(FFTresampleEGTS(:)))), 'r-' ) ;

title('Check Spectra of FFT of resampleEGTS')

axis([0 500 0 1])

xlabel('Frequency (Hz)')


figure

PlotWigClip(ConvolTime)

title('Convolution of Model F')


figure

PlotWigClip(d_filter)

title('d_filter - Filtered - Deconvolved Model F')
```

```
figure

PlotWigClip(ConvolTime_filter,1,offset,time)

title('Filtered Convolution of Model F')

xlabel('Offset')

ylabel('Time Steps')



% compare spectra

figure

plot( abs( d_filter(1:m,10))/max( max( abs(d_filter(:,10)))) ) ;

hold on

plot( abs( Convol(1:m,10))/max( max( abs(Convol(:,10)))), 'r-' ) ;

plot( abs( ConvolTime_filter_fft(1:m,10))/max( max( abs(ConvolTime_filter_fft(:,10)))),

'k--' ) ;

title('Compare Spectra')

legend('Deconvolution Model F fft','Convolution Model F fft','Filtered Convolution

Model F fft')

axis([0 500 0 1])

xlabel('Frequency (Hz)')
```

APPENDIX 10 MATLAB FUNCTION PlotWigClip.m

This appendix contains an example of the MATLAB script used for plotting time histories in the wiggle format in this research. This script was created by Xingong Li in December of 1995 and was obtained from Dr. Calderón-Macías.

```
function PlotWigClip (a,scal,x,z,amx, clip)
% PlotWig: plot section of traces in wiggle format
%  function PlotWigClip (a,scal,x,z,amx, clip)
%       1) 'a' is input matrix.
%       2) x direction is as trace number.
%       3) If only 'a' is enter, 'scal,x,z,amn,amx' are decided automatically;
%       otherwise, 'scal' is a scalar; 'x, z' are vectors for annotation in
%       offset and time, amx are the amplitude range.
% Author:
%       Xingong Li, Dec. 1995
% Changes:
%   Jan23,2008: add clip CC - based on PlotWig
%       Jun11,1997: add amx
%       May16,1997: updated for v5 - add 'zeros line' to background color
```

```
%       May17,1996: if scal ==0, plot without scaling

%       Aug6, 1996: if max(tr)==0, plot a line


if nargin == 0, nx=10;nz=10; a = rand(nz,nx)-0.5; end;


[nz,nx]=size(a);


trmx= max(abs(a));

if (nargin <=5); clip = 0; end;

if (nargin <= 4); amx=mean(trmx);  end;

if (nargin <= 2); x=[1:nx]; z=[1:nz]; end;

if (nargin <= 1); scal =1; end;


if nx <= 1; disp(' ERR:PlotWig: nx has to be more than 1');return;end;


 % take the average as dx

        dx1 = abs(x(2:nx)-x(1:nx-1));

        %dx = sum(dx1)/(nx-1);
```

```
        dx = median(dx1);


dz=z(2)-z(1);

xmx=max(max(a)); xmn=min(min(a));


if scal == 0; scal=1; end;

a = a * dx /amx;

a = a * scal;


fprintf(' PlotWig: data range [%f, %f], plotted max %f \n',xmn,xmx,amx);


% set display range

x1=min(x)-2.0*dx; x2=max(x)+2.0*dx;

z1=min(z)-dz; z2=max(z)+dz;


set(gca,'NextPlot','add','Box','on', ...

 'XLim', [x1 x2], ...

 'YDir','reverse', ...
```

```
 'YLim',[z1 z2]);



%rgray=flipud(gray); colormap(rgray); % Revert the Gray colormap


        % fillcolor = [0.5 .5 .5];

        % linecolor = [0.5 .5 .5];

        fillcolor = [0 0 0];

        linecolor = [0 0 0];

        linewidth = 0.1;


        z=z';    % input as row vector

        zstart=z(1);

        zend  =z(nz);


for i=1:nx,


 if trmx(i) ~= 0;    % skip the zero traces
```

```
        tr=a(:,i);          % --- one scale for all section


 % cc - do the clipping here
if( clip >0)
   for jt = 1:nz,
      if( abs(tr(jt)) > clip)
         tr(jt) = clip*sign( tr(jt));
      end
   end
end


 s = sign(tr) ;
        i1= find( s(1:nz-1) ~= s(2:nz) );         % zero crossing points
        npos = length(i1);



        %12/7/97
        zadd = i1 + tr(i1) ./ (tr(i1) - tr(i1+1)); %locations with 0 amplitudes
```

```
aadd = zeros(size(zadd));


[zpos,vpos] = find(tr >0);

[zz,iz] = sort([zpos; zadd]);    % indices of zero point plus positives

aa = [tr(zpos); aadd];

aa = aa(iz);


% be careful at the ends

        if tr(1)>0,        a0=0; z0=1.00;

        else,              a0=0; z0=zadd(1);

        end;

        if tr(nz)>0,       a1=0; z1=nz;

        else,              a1=0; z1=max(zadd);

        end;


zz = [z0; zz; z1; z0];

aa = [a0; aa; a1; a0];
```

```
            zzz = zstart + zz*dz -dz;

            patch( aa+x(i) , zzz,  fillcolor);

            line( 'Color',[1 1 1],'EraseMode','background',  ...
          'Xdata', x(i)+[0 0], 'Ydata',[zstart zend]); % remove zero line

%'LineWidth',linewidth, ...
%12/7/97 'Xdata', x(i)+[0 0], 'Ydata',[z0 z1]*dz);      % remove zero line

            line( 'Color',linecolor,'EraseMode','background',  ...
             'LineWidth',linewidth, ...
             'Xdata', tr+x(i), 'Ydata',z);      % negatives line

        else % zeros trace
            line( 'Color',linecolor,'EraseMode','background',  ...
             'LineWidth',linewidth, ...
```

```
        'Xdata', [x(i) x(i)], 'Ydata',[zstart zend]);

    end;

end;
```

APPENDIX 11 MATLAB FUNCTION applyBpFilter.m

This appendix contains an example of the MATLAB script used for applying a bandpass filter. This script was obtained from Dr. Calderón-Macías

```
%
%  Apply band-pass filter
%
%  function [datbp] = applyBpFilter( din, flims, dsam, powr)
%
%  INPUT:
%   din : input data (ns, ntr)
% flims : bandpass limits (f1,f2,f3,f4)
%  dsam : dt
%
% Optional:
%   powr : (=0.5) Power applied to hanning window for bp ramps
%
% OUTPUT:
%   datbp: filtered output (ns, ntr)
```

```
% CC - Jan 26, 2009
%


function [datbp] = applyBpFilter( din, flims, dsam, powr)


if( nargin<4)
  powr = 0.5 ;
end


% extract filter coefficients
f1 = flims( 1) ;
f2 = flims( 2) ;
f3 = flims( 3) ;
f4 = flims( 4) ;



[ns ntr] = size( din) ;
```

```
ns = length( din(:,1)) ;

% find nearest power of two

nlog = log2( ns) ;

npow = ceil( nlog) ;

nfft = 2^npow ;

m = nfft/2 + 1 ;

fn = 1/2/dsam ;

df = 1 / (nfft*dsam) ;

fr = 0 : df : fn ;
```

```
% design filter

bpfilt = zeros( m, 1) ;

% i0 and i4 are zero

% i1 and i3 correspond to hann windows

% i2 is the all pass band

%i0 = find( fr<f1) ;

i1 = find( fr>=f1 & fr<f2) ;

i2 = find( fr>=f2 & fr<=f3) ;

i3 = find( fr>f3 & fr<=f4) ;
```

```
%i4 = find( fr>f4) ;

nsf1  = length( i1) ;

nsf2  = length( i2) ;

nsf3  = length( i3) ;


wlp = hann( 2*nsf1).^powr ;

wlp = wlp( 1:nsf1) ;

whp = hann( 2*nsf3).^powr ;

whp = whp( nsf3+1:nsf3*2) ;
```

```
bpfilt( i1) = wlp ;

bpfilt( i2) = ones( length(nsf2), 1) ;

bpfilt( i3) = whp ;

% plot( fr, bpfilt)

datbp = 0*din ;

for k= 1 : ntr,

   aux  = fft( din(:,k), nfft);

   aux(1:m)  = aux(1:m).*bpfilt ;

   for j=2:m-1,
```

```
        jj      = nfft - j + 2;

        aux(jj)  = conj( aux(j));

    end

    auxi = ifft( aux);

    datbp(:,k) = real( auxi(1:ns));

end
```

APPENDIX 12 POWER SPECTRUMS FOR DECONVOLUTION AND CONVOLUTUION

This appendix contains power spectrums that are compared during the deconvolution and convolution process to match as closely as possible. Figure A.13.1 displays the power spectrums of receiver number 10 from Model F and the time history used for deconvolution. Figure A.13.2 displays the power spectrums of receiver number 10 from Model F, Model F after deconvolution, and Model F after deconvolution with filtering. Bandpass-filtering is useful for attempting to match the power spectrums as closely as possible; this can be seen in Figure A.13.2 in the reduction of amplitude in the range higher than approximately 100 Hz.

APPENDIX 13 GLOSSARY

Convolution – operation of replacing each element of an input with a scaled output function; it is the mathematical equivalent to filtering, such as occurs naturally in the passage of seismic waves through the earth. (Sheriff and Geldart 1995)

Deconvolution – convolving with an inverse filter. (Sheriff and Geldart 1995)

Dispersion Curve – a curve showing values of dispersive characteristics of a soil site with unit of frequency and velocity.

Dispersive –waves of different frequencies travel at different velocities.

Overtone Image – calculated amplitude spectra of wave velocity as a function of frequency (e.g., Casto et al. 2009)

Ricker Wavelet – the most common zero-phase wavelet (Sheriff and Geldart 1995)

Stack of Overtone Images –Stacking the overtone images across frequency or velocity results in 2D images that summarize energy distribution along the array. (Luke and Calderón-Macías 2008)

Time History - ground motion, such as displacement, measured at a set of fixed times. Also termed as time series. (http://earthquake.usgs.gov/learn/glossary/?term=time%20history)

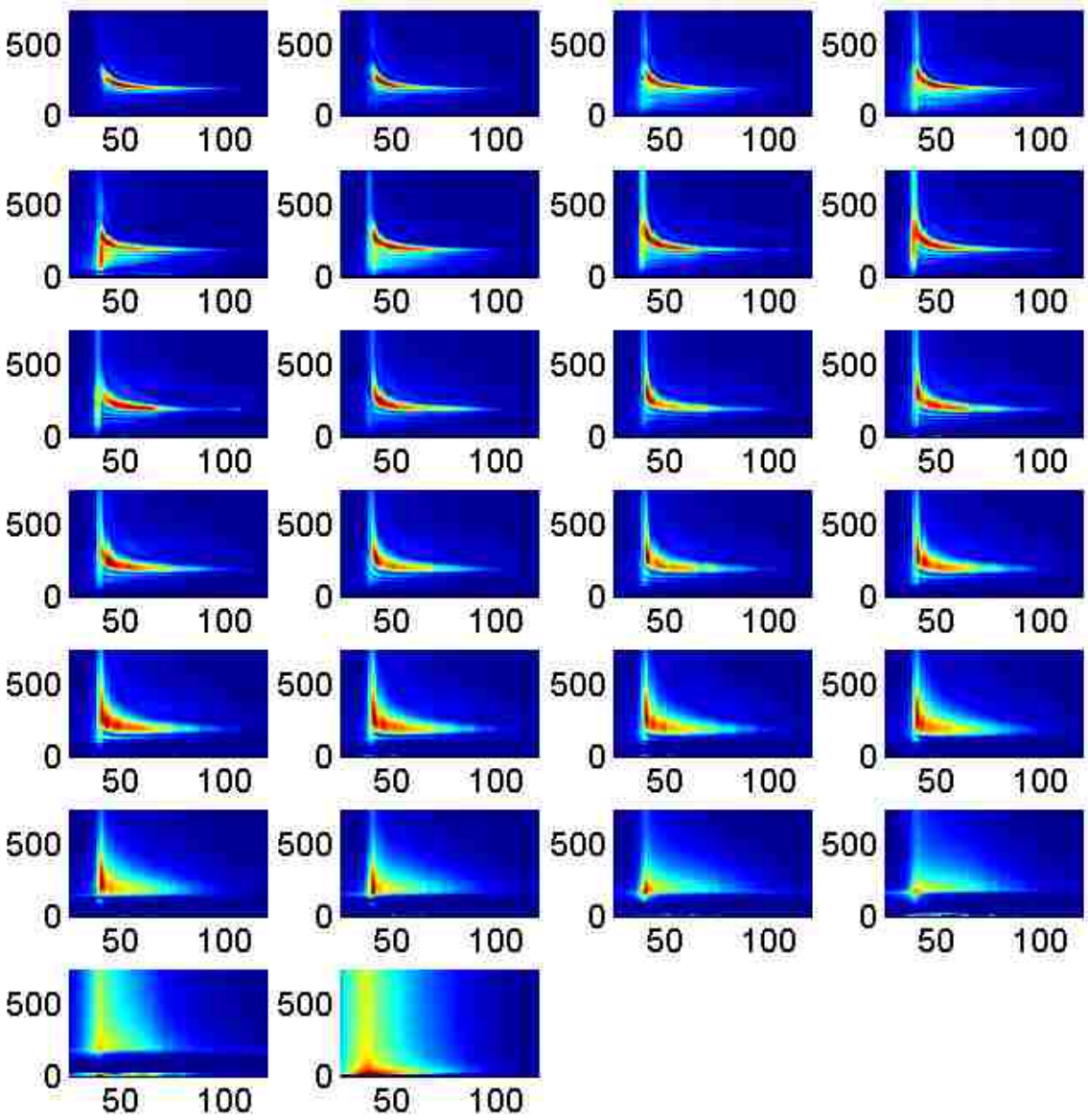

Figure A.1.a Overtone images in the positive X direction using Model D with a 50 Hz Ricker wavelet source in multiple source locations and a full width of model cavity. The figures are arranged from left to right where the top left is source location 1 and the bottom right is source location 26. In all overtone images the X axis is frequency in Hz, and the Y axis is velocity in m/s. The cavity is located at source locations 8 at (10, 15.5, 1). These are the same images as in Figure 4.22 and also used to create the stacks shown in Figures 4.23 and 4.24.

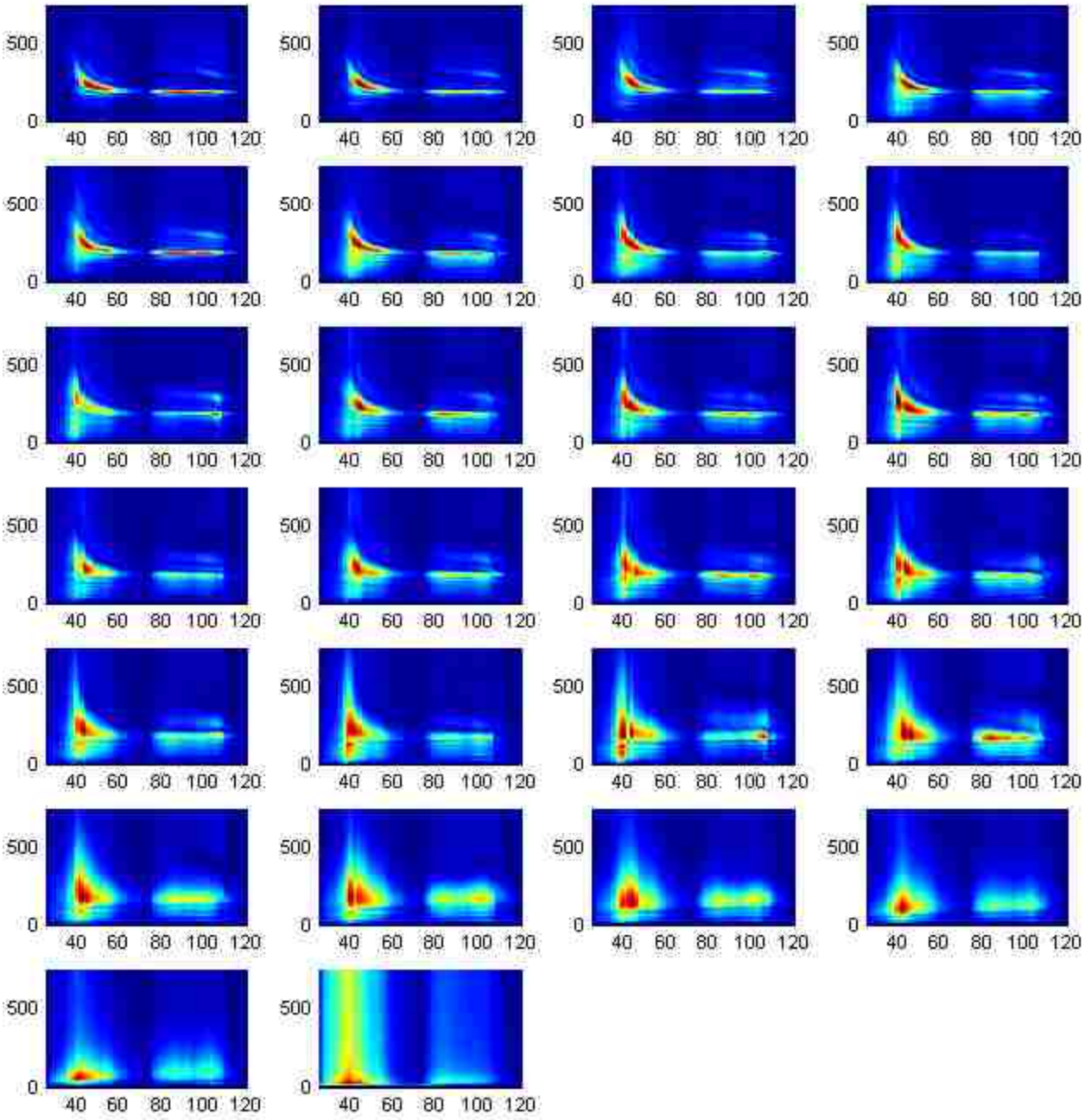

Figure A.1.b Overtone images in the positive X direction using Model F with a convolved real source in multiple source locations and a full width of model cavity. The figures are arranged from left to right where the top left is source location 1 and the bottom right is source location 26. In all overtone images the X axis is frequency in Hz, and the Y axis is velocity in m/s. The cavities are located at source locations 8 at (10, 15.5, 1) and 18 at (20, 15.5, 1). These are the images used to create the stacks shown in Figures 4.23 and 4.24.

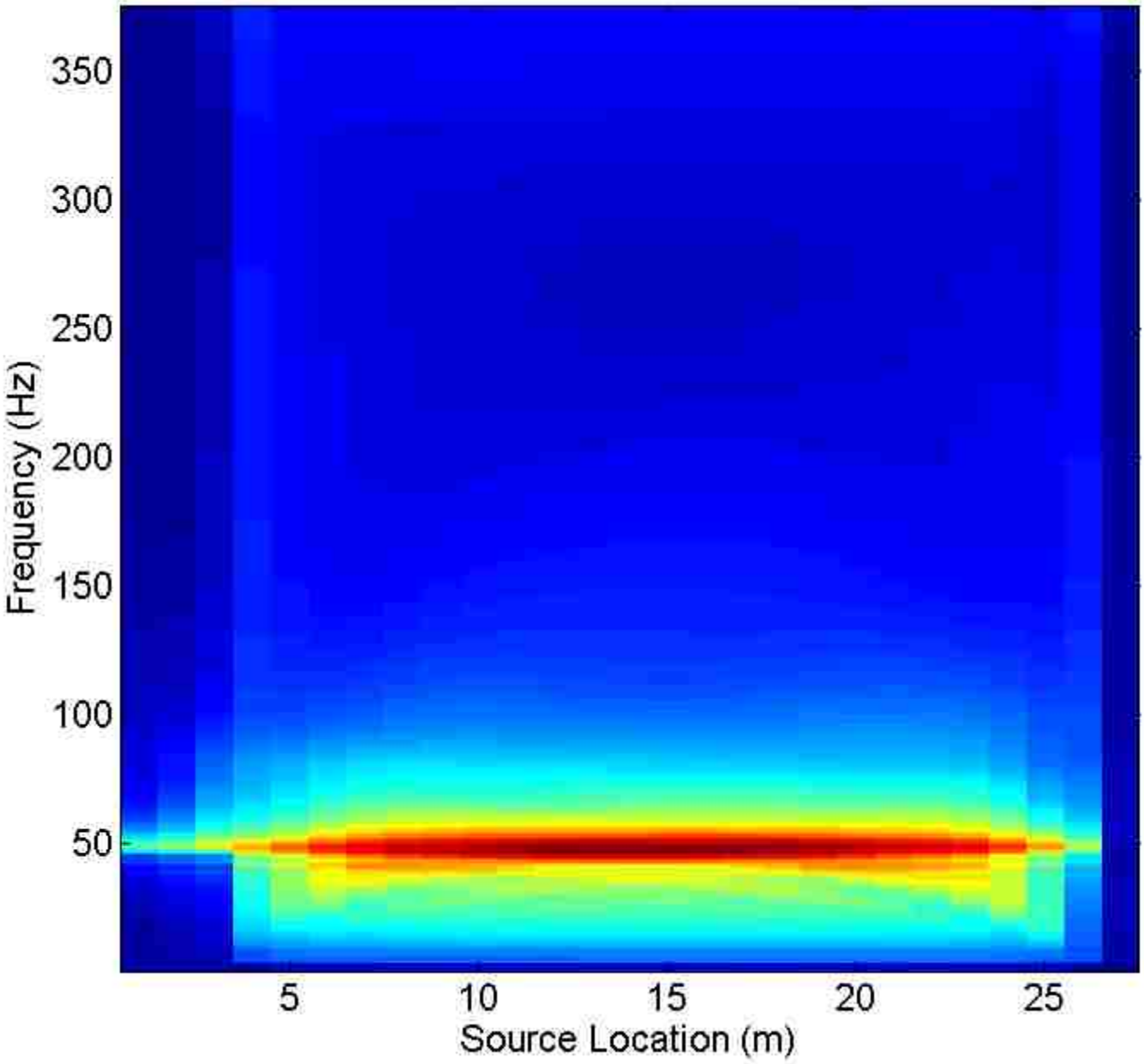

Figure A.1.c Stack of overtone images according to velocity using Model E with a 50 Hz Ricker wavelet source in multiple source locations. One on the *X* axis is the first source location, 27 on the *X* axis is the last source location.

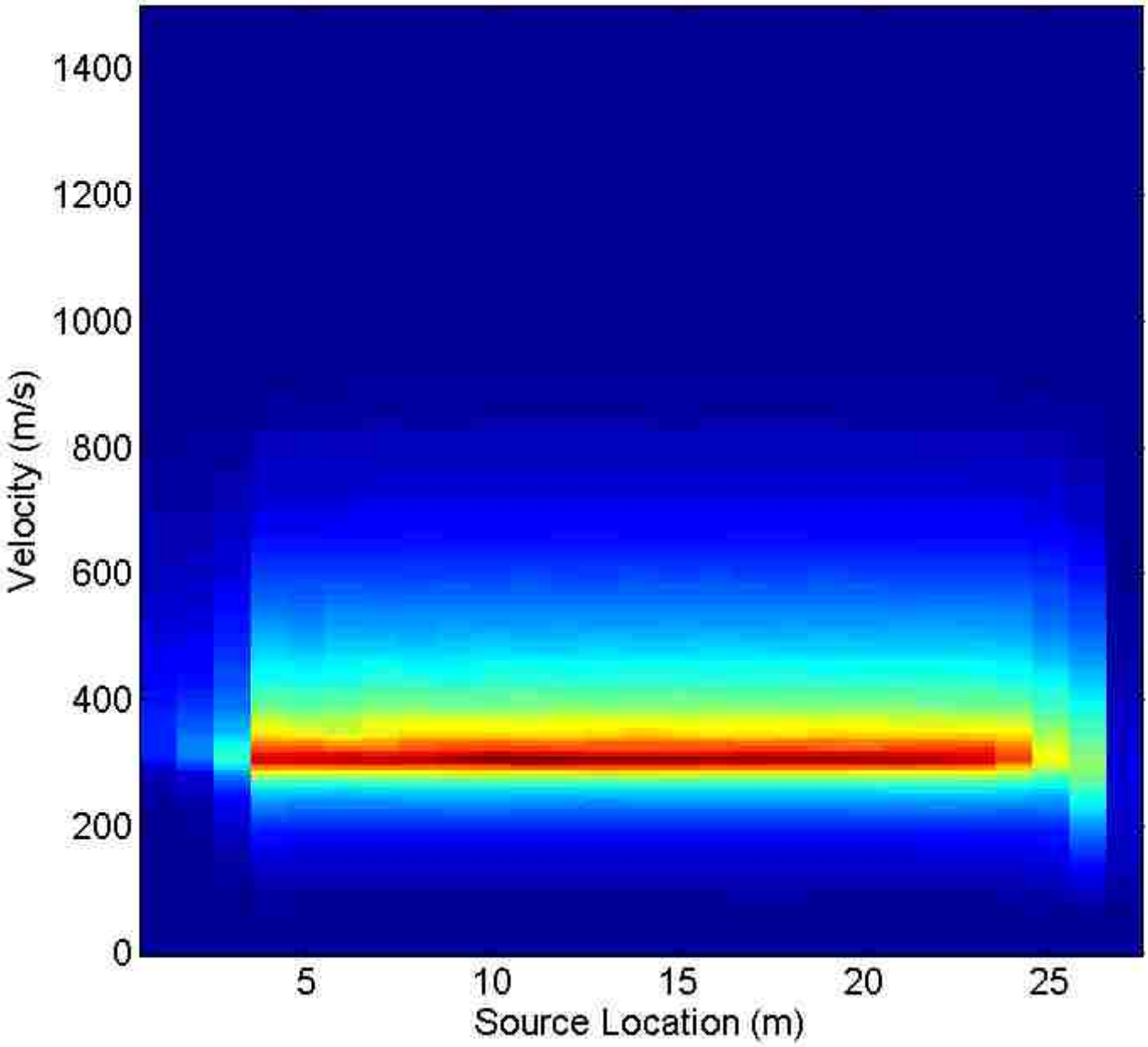

Figure A.1.d Stack of overtone images according to frequency using Model E with a 50 Hz Ricker wavelet source in multiple source locations. One on the *X* axis is the first source location, 27 on the *X* axis is the last source location.

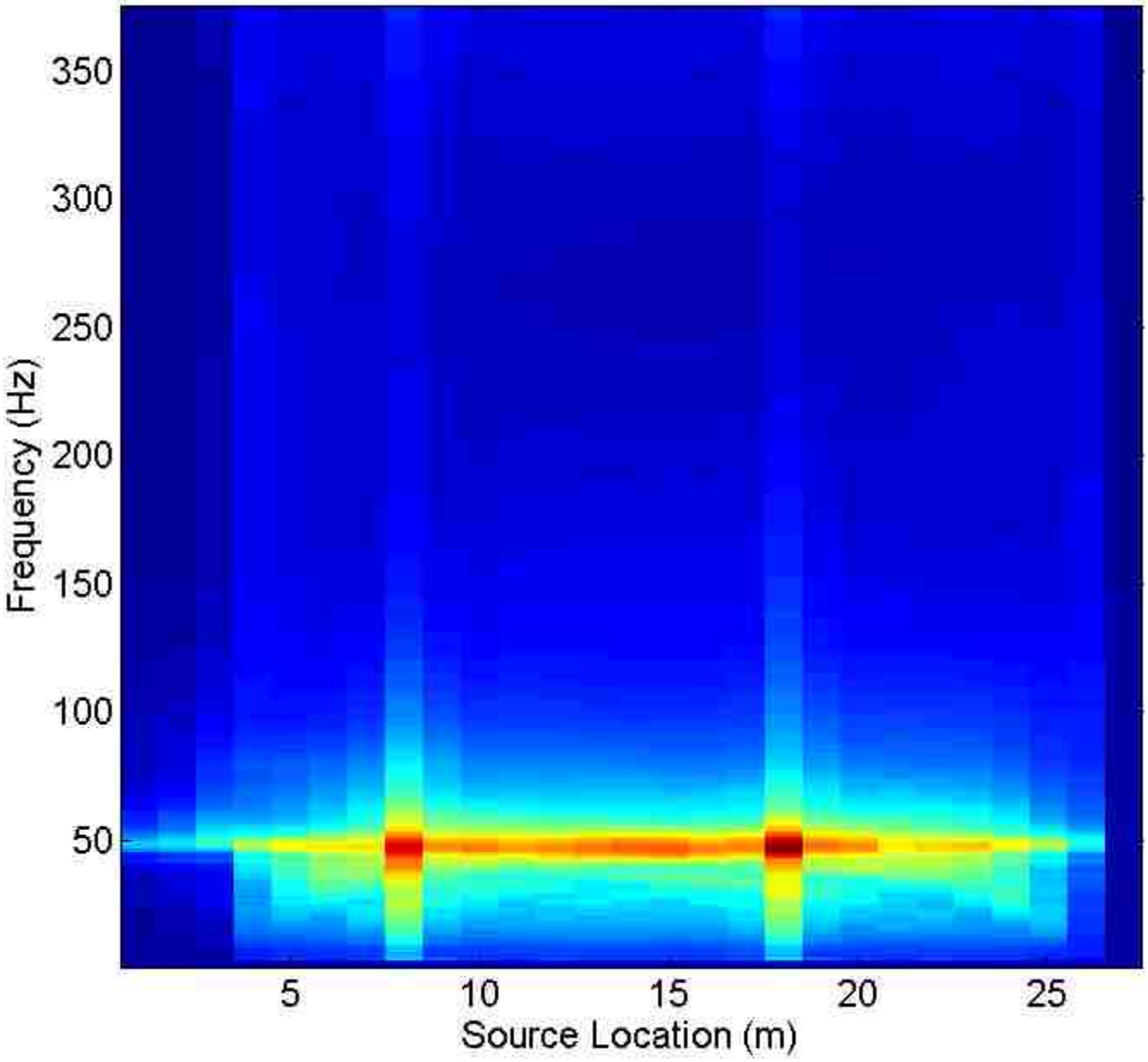

Figure A.1.e Stack of overtone images according to velocity using Model F with a 50 Hz Ricker wavelet source in multiple source locations and a pseudo-2D cavity. One on the *X* axis is the first source location, 27 on the *X* axis is the last source location. The cavities are located at source locations 8 at (10, 15.5, 1) and 18 at (20, 15.5, 1).

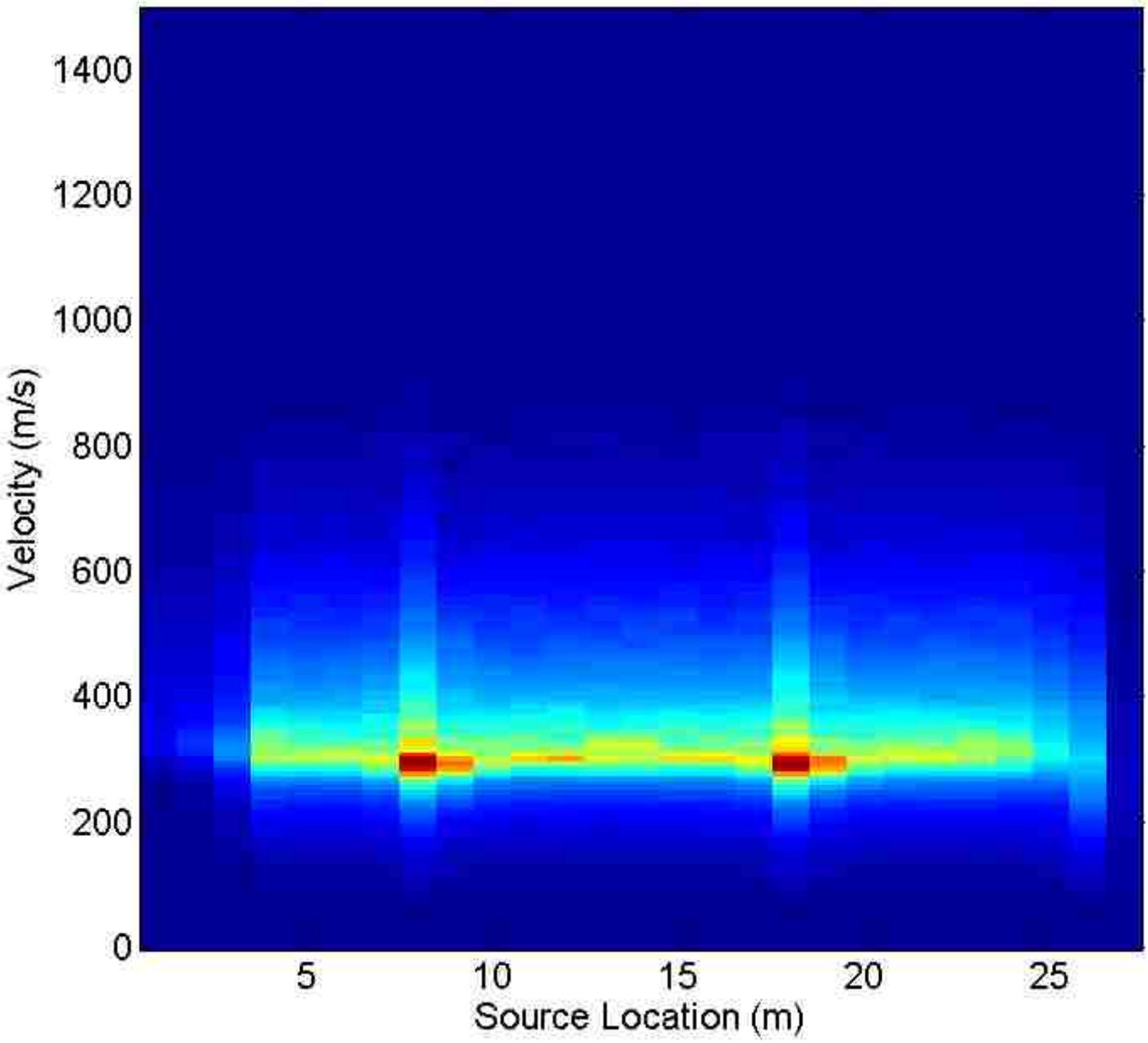

Figure A.1.f Stack of overtone images according to frequency using Model F with a 50 Hz Ricker wavelet source in multiple source locations and a pseudo-2D cavity. One on the *X* axis is the first source location, 27 on the *X* axis is the last source location. The cavities are located at source locations 8 at (10, 15.5, 1) and 18 at (20, 15.5, 1).

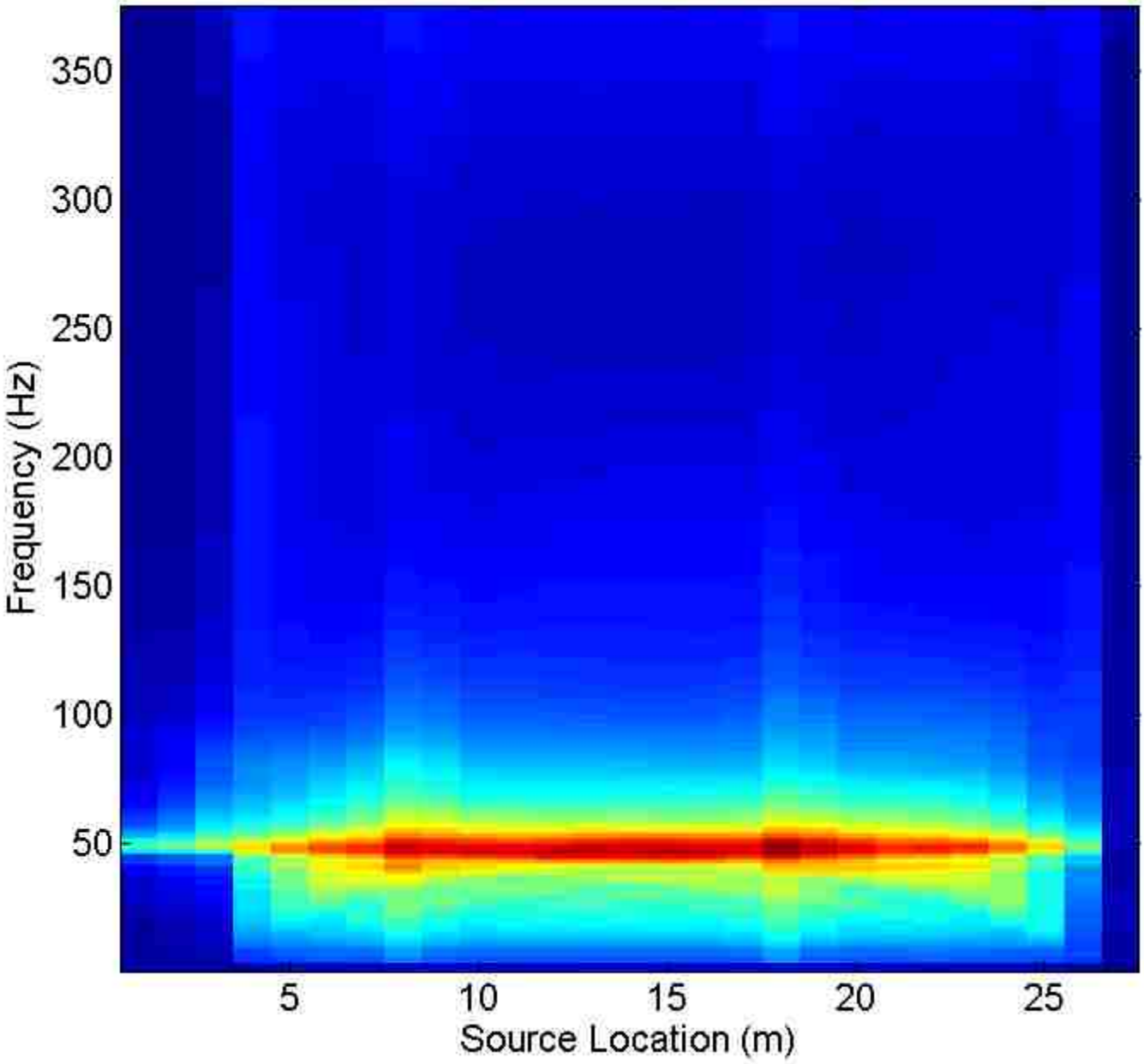

Figure A.1.g Stack of overtone images according to velocity using Model F* with a 50 Hz Ricker wavelet source in multiple source locations and a finite cavity. One on the *X* axis is the first source location, 27 on the *X* axis is the last source location. The cavities are located at source locations 8 at (10, 15.5, 1) and 18 at (20, 15.5, 1).

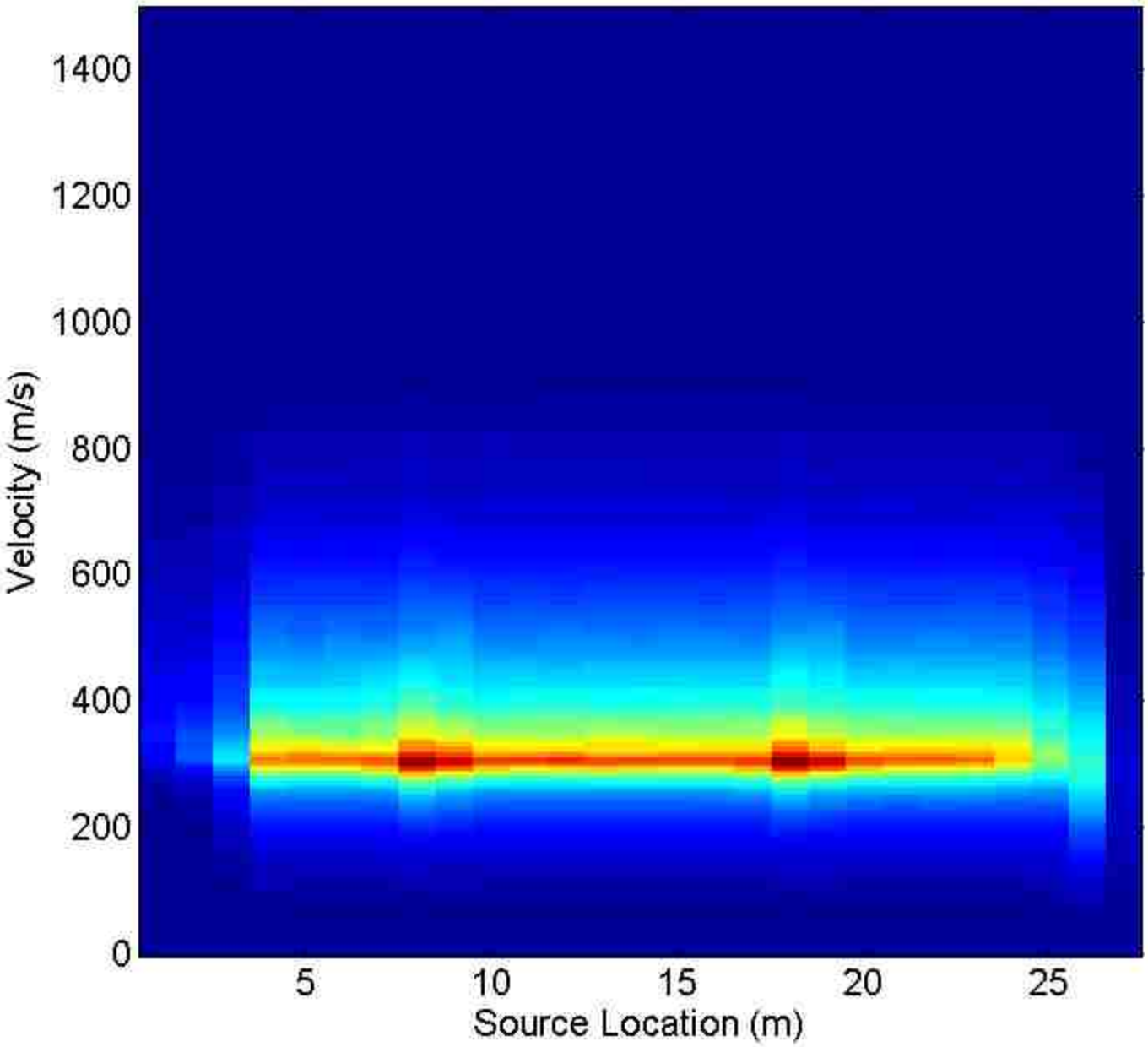

Figure A.1.h Stack of overtone images according to frequency using Model F* with a 50 Hz Ricker wavelet source in multiple source locations and a finite cavity. One on the *X* axis is the first source location, 27 on the *X* axis is the last source location. The cavities are located at source locations 8 at (10, 15.5, 1) and 18 at (20, 15.5, 1).

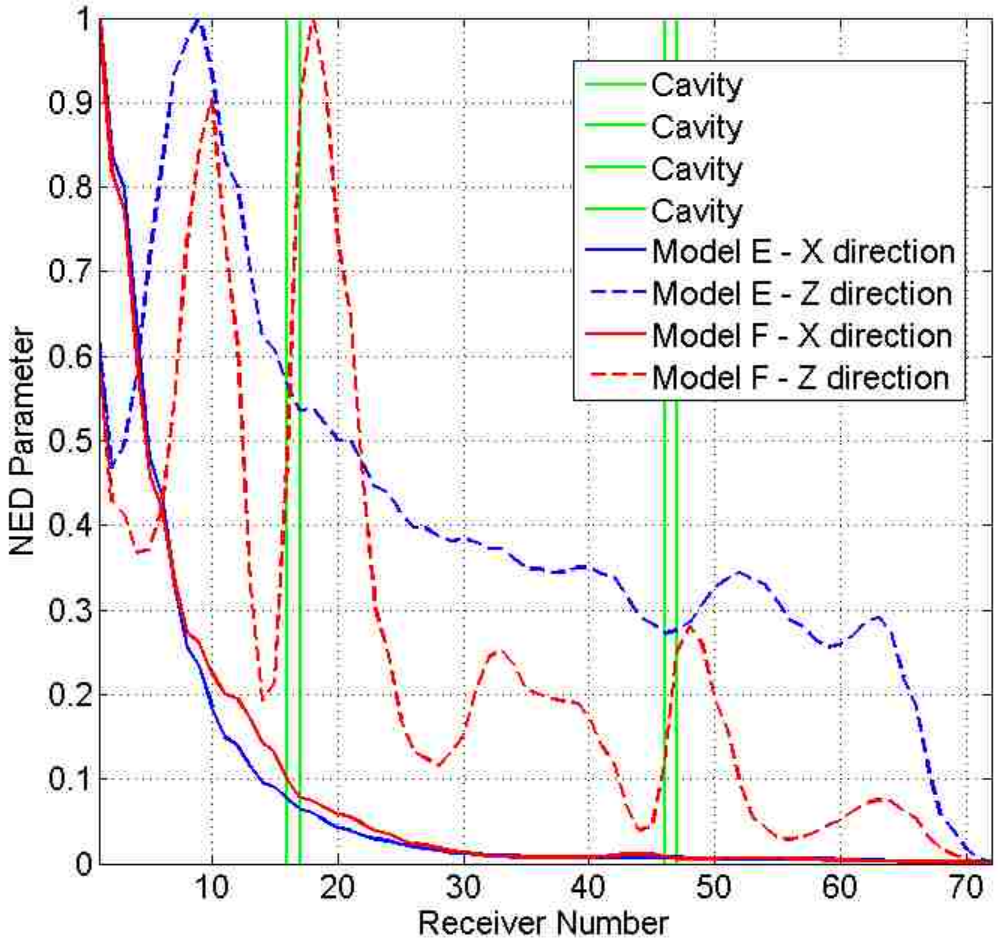

Figure A.2.1 Normalized Energy-Distance (NED) parameter for Model E and Model F.

A frequency range of 40 Hz to 80 Hz is used to evaluate the parameter.

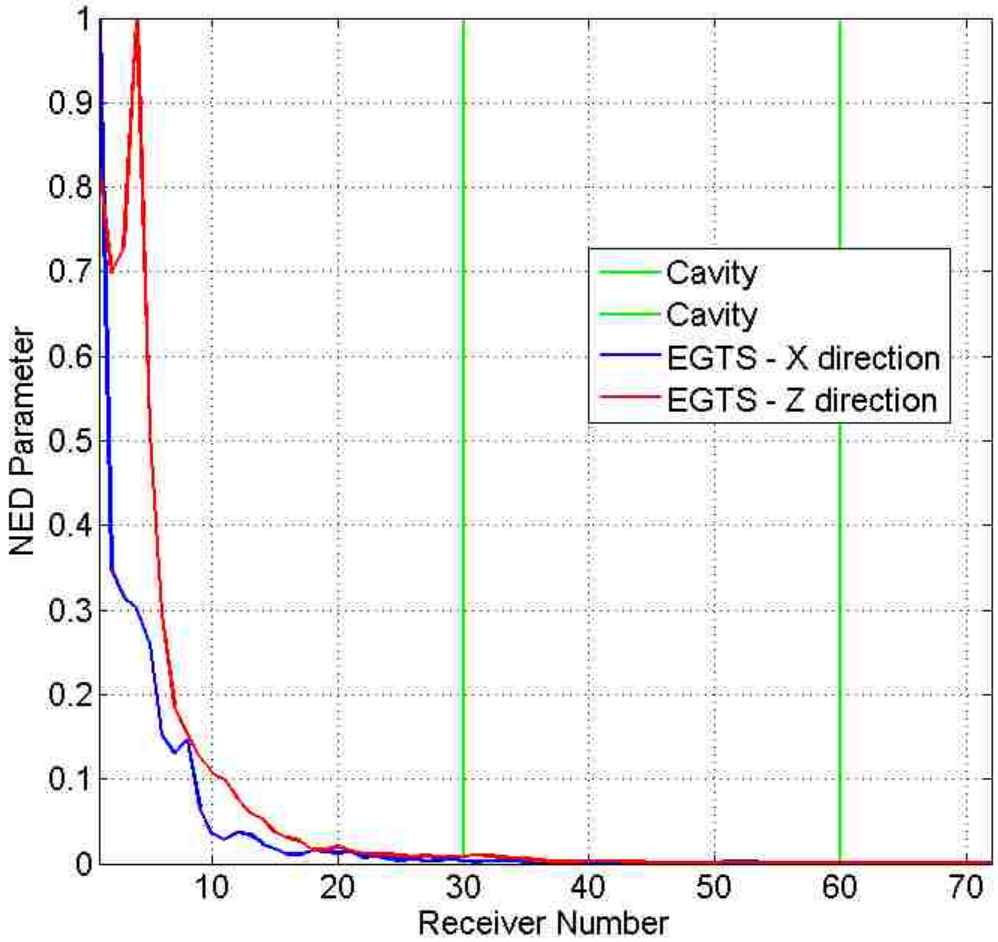

Figure A.2.2 Normalized Energy-Distance (NED) parameter for the Engineering Geophysics Test Site (EGTS) experimental data. A frequency range of 20 Hz to 60 Hz is used to evaluate the parameter.

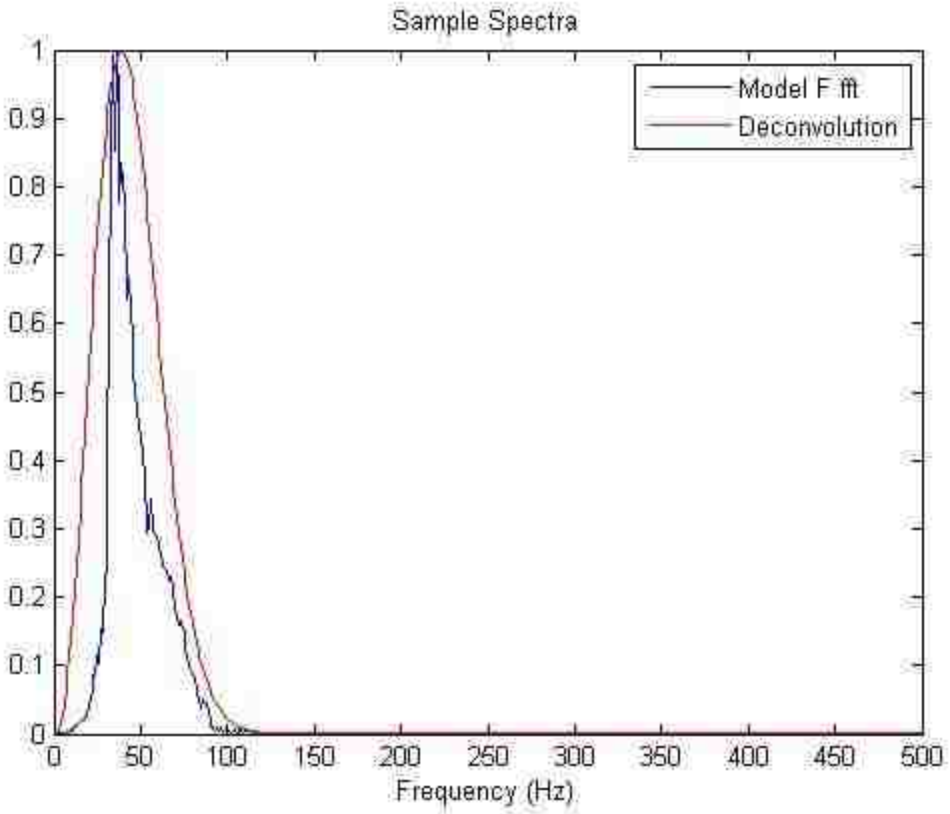

Figure A.13.1 Power spectrums of receiver number 10 from Model F and the Ricker wavelet used for deconvolution.

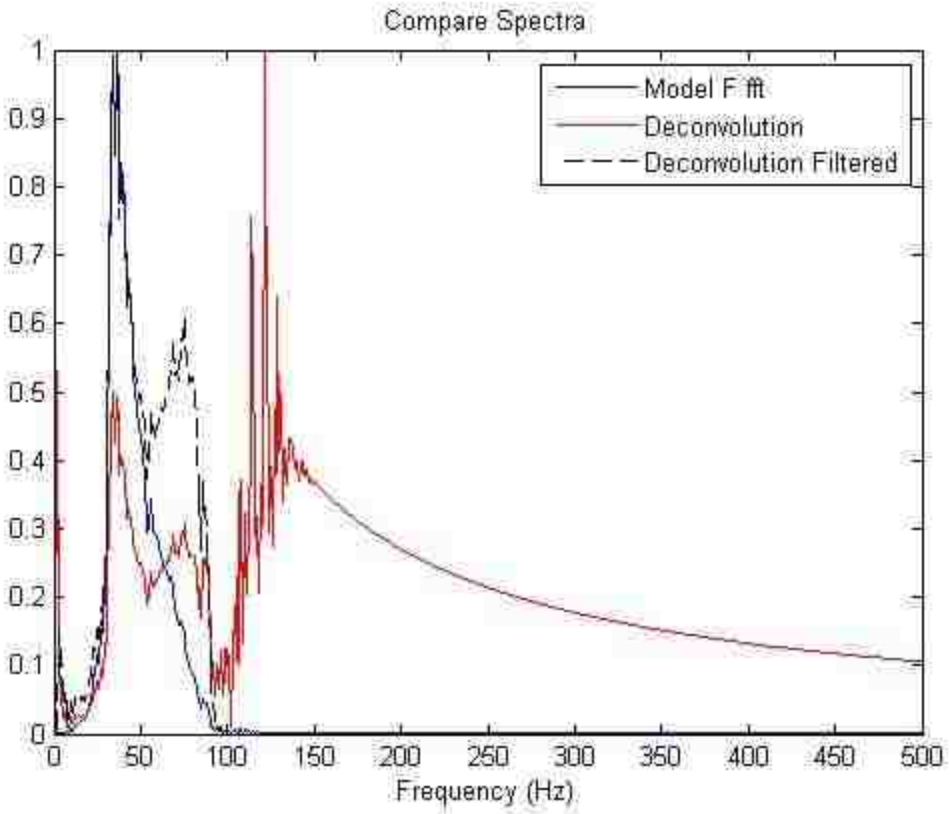

Figure A.13.2 Power spectrums of receiver number 10 from Model F, Model F after deconvolution, and Model F after deconvolution with filtering.

VITA

Graduate College

University of Nevada, Las Vegas

Heston Norcott

Degrees:

Bachelor of Science, Civil and Environmental Engineering, 2008

University of Nevada, Las Vegas

Thesis Title: FINITE DIFFERENCE MODELING OF SURFACE-WAVE SCATTERING FOR SHALLOW CAVITY DETECTION

Dissertation/Thesis Examination Committee:

Chairperson, Barbara Luke, Ph. D.

Committee Member, Carlos Calderón-Macías, Ph. D.

Committee Member, Moses Karakouzian, Ph. D.

Graduate Faculty Representative, Yi-Tung Chen, Ph. D.